Alma Mater Studiorum - Università di Bologna

DOTTORATO DI RICERCA IN

MECCANICA E SCIENZE AVANZATE DELL'INGEGNERIA

Ciclo 35

Settore Concorsuale: 09/A1 - INGEGNERIA AERONAUTICA, AEROSPAZIALE E NAVALE

Settore Scientifico Disciplinare: ING-IND/05 - IMPIANTI E SISTEMI AEROSPAZIALI

NAVIGATION DESIGN AND FLIGHT DYNAMICS OPERATIONS OF THE ARGOMOON CIS-LUNAR CUBESAT

Presentata da: Marco Lombardo

Coordinatore Dottorato

Lorenzo Donati

Supervisore

Paolo Tortora

Co-supervisore

Marco Zannoni

Esame finale anno 2023

To my dear family.

Author's Note

This thesis is continuously revised to correct all typos that are found during a never-ending revision process. To obtain the most updated version, please feel free to contact the author by sending an e-mail to: marco.lombardo14@unibo.it.
Some of the information contained in this document, including but not limited to spacecraft system specifications, trajectories, scientific and technical data are classified as confidential information. Therefore, this document shall not be disclosed to others than the authorized people until those information are disclosed to the public. For any other information related to the ArgoMoon mission that is not specifically reported in this thesis, please contact Argotec S.r.l. company based in Via Cervino, 52, 10155, Turin, Italy.

Navigation design and flight dynamics operations of the ArgoMoon cis-lunar CubeSat

Abstract

On November 16, 2022, the NASA's Space Launch System (SLS) has been launched for the first time in the context of Artemis-1 mission where, together with the Orion Multi-Purpose Crew Vehicle, a set of 10 CubeSats have been delivered into a translunar trajectory.

Among the small satellites deployed during Artemis-1 there is ArgoMoon, a 6U CubeSat built by the Italian company Argotec and coordinated by Italian Space Agency (ASI). ArgoMoon has been selected by National Aeronautics and Space Administration (NASA) with the mission objective of capturing relevant images of the Interim Cryogenic Propulsion Stage (ICPS) of SLS and provide a confirmation of the deployment of the other 9 CubeSats. The acquired pictures should then be used to support the NASA and payload communities in providing information regarding the status of the secondary payload deployment. The pictures of the ICPS also provide to the NASA community the opportunity to visually inspect the condition of the second stage as it completes the final phase of its mission. For the first 10 hours after the release, ArgoMoon performs target tracking and autonomous proximity-flight navigation around the ICPS making use of the on-board avionics and a complex image recognition algorithm based on machine learning and photographs captured on-board. The first phase of the mission ends along with the conclusion of the proximity operations around the target, enabling the start of the second phase of the mission, where the satellite will be commanded and navigated from ground through a highly elliptical geocentric orbit, with several encounters with the Moon. The end of the mission will occur approximately 180 days after the launch when a last fly-by of the Moon will dispose ArgoMoon into a heliocentric trajectory. During its 6-month journey, ArgoMoon will be an important demonstrator for the application of nano/small technologies in deep space

In order to successfully fly ArgoMoon along the designed cis-lunar trajectory, a ground-based navigation system has been developed exploiting the guidance techniques also used for regular deep space missions. The navigation process is subdivided into Orbit Determination (OD) and a Flight Path Control (FPC), and it is designed to follow the reference trajectory, prevent impacts with the Earth and the Moon, intensively test the navigation techniques, and guarantee the spacecraft disposal at the end of the mission. The work done in this thesis has accomplished the navigation of ArgoMoon, covering all aspects of the project life, from pre-launch design and analysis to actual operations. Firstly, the designed navigation process and the pre-mission assessment of its performance will be presented. In the context of the performance assessment, a covariance analysis have been performed to evaluate the expected performance of the OD, using the nominal setup. Moreover, extensive sensitivity analyses to evaluate the robustness of the navigation and the relevant characterizing parameters have been conducted. The results of the analyses show that

the designed trajectory can be successfully flown, and that the navigation performance is strongly dependent on the uncertainties of the ArgoMoon's Propulsion System (PS) and of the orbit injection.

The results of the ArgoMoon navigation operations performed after the launch in November 2022 will be described in detail by discussing the main encountered challenges and the adopted solutions. The results of the operations confirmed the robustness of the designed navigation which allowed to accurately estimate the trajectory of ArgoMoon despite a series of complex events. As expected from the pre-launch analysis results, navigating a CubeSat in deep space is challenging mainly due to the PS. ArgoMoon's chemical thruster was in fact not free from problems and having never been used in space before that moment, the unexpected events were difficult to manage. Moreover, frequent reboots of the on-board transponder and the presence of biases on the Doppler data had further complicated the navigation of ArgoMoon.

Acknowledgements

The work carried on in this PhD dissertation is the result of hard work, passion and sacrifice in pursuing my dream of being a flight dynamics engineer and navigate a satellite in deep space.

I want to firstly express my gratitude to Prof. Paolo Tortora and Prof. Marco Zannoni for giving me the opportunity to work on the navigation of ArgoMoon as main analyst trusting my abilities and passion for this research. Also, I want to thank them for the amazing experience had in navigating ArgoMoon and LICIACube and for all the wonderful experiences I had in various parts of the world in the context of this PhD. Furthermore, Prof. Zannoni proved to be a great teacher and mentor and often a good friend as well, so I want to thank him again for this.

I would like to thanks all my colleagues and friends at the Radio Science and Planetary Exploration Laboratory of the University of Bologna. A special thanks goes to Igor Gai, who shared with me the the beauties and the pains of working to CubeSats deep space navigation for the first time. Another special thanks goes to my colleague Luis Gomez Casajus, who has always advised and helped me since the beginning of my PhD.

I would also like to thank Biagio Cotugno, Spacecraft Operations Manager of Argotec S.r.l., for the pleasant and fruitful collaboration we had during the design phase of the ArgoMoon mission and later during the operational phases after launch.

The most important thanks comes now, and they are addressed to my family. None of the work and experiences I had since know would be possible without the love and support of my sweetheart Florida. In almost eleven years of sharing the life together she has never stopped giving me the strength and courage to do more and more and achieve my dreams. But above all she gave me Sofia, our beautiful, sweet and intelligent daughter who I want to thank for her patience and love in being close to me during the challenging years of my PhD. A beloved thanks to my parents Nicoletta and Francesco, to be proud of me and to believe in my capabilities, as well as providing me a continuous support in my life even if we live in different regions of Italy. Finally, thanks to my in-laws Mimoza and Myzafer, for being proud of me as if I were their son. I love you all, thanks for everything!

Acronyms

ADCS	Attitude Determination and Control Subystem
AMC	Advanced Media Calibrations
APL	Applied Physics Laboratory
ASI	Italian Space Agency
BS	Bus Stop
BP	Break Point
C/A	Closest Approach
CT	Count Time
CME	Close Moon's Encounter
COSMIC	Computer Optimization System for Multiple Independent Courses
CP	Control Point
CR3BP	Circular Restricted Three-Body Problem
DART	Double Asteroid Redirection Test
DCO	Data Cut-Off
DES	desaturation
DEC	Declination
DSN	Deep Space Network
DSS	Deep Space Station
ECSS	European Cooperation for Space Standardization
EME2000	Earth Mean Equator at J2000
EMO2000	Earth Mean Orbit at J2000
EOM	End of Mission
EOT	End of Tracking
EOP	Earth Orientation Parameters
EPS	Electrical Power Subystem
ESA	European Space Agency
ESTRACK	European Space Tracking
FOV	Field of View
FPC	Flight Path Control
GSFC	Goddard Space Flight Center

ICD	Interface Control Document
INS	Interferometric Narrowband Spacecraft
IRS	Image Recognition Software
ISL	Inter-Satellite Link
IMU	Inertial Measurement Unit
ITAR	International Traffic in Arms Regulations
IERS	International Earth Rotation and Reference Systems Service
ICPS	Interim Cryogenic Propulsion Stage
JHU	Johns Hopkins University
JPL	Jet Propulsion Laboratory
JAXA	Japan Aerospace Exploration Agency
HPBW	Half Power Beam Width
KOZ	Keep Out Zone
LAMBIC	Linear Analysis of Maneuvers with Bounds and Inequality Constraints
LEO	Low Earth Orbit
LEOP	Launch and Early Operations
LICIACube	Light Italian Cubesat for Imaging of Asteroids
LNA	Low Noise Amplifier
LOS	Line Of Sight
LTOF	Linearized Time of Flight
LUMIO	Lunar Meteoroid Impact Observer
MCC	Mission Control Center
MarCO	Mars Cube One
M-ARGO	Miniaturised Asteroid Remote Geophysical Observer
MONTE	Mission-analysis and Operations Navigation Toolkit Environment
MiPS	Micro Propulsion System
MSPA	Multi-Spacecraft Per Antenna
NASA	National Aeronautics and Space Administration
NAV	Navigation facility
NAVREQ	Navigation Requirement
NEA	Near Earth Asteroid
OBC&DH	On-Board Computer and Data Handling
OD	Orbit Determination
OICD	Operations Interface Control Document
OTM	Orbit Trim Maneuver
PL	Payload
PM	Proximity Maneuver
PPN	Parameterized Post-Newtonian

ProxOps	Proximity Operations
PS	Propulsion System
RA	Right Ascension
RSLab	Radio Science and Planetary Exploration Laboratory
RCS	Reaction Control System
REV	revolution
RF	Radio Frequency
RMS	Root Mean Square
RSS	Root Sum Squared
RTN	Radial Transverse Normal
RW	Reaction Wheel
S/C	spacecraft
SEP	Sun-Earth-Probe
SFTP	SSH File Transfer Protocol
SLS	Space Launch System
SNOPT	Sparse Nonlinear OPTimizer
SOI	Sphere of Influence
SOM	Spacecraft Operations Manager
SPA	Solar Panel Array
SPAD	Solar Pressure and Aerodynamic Drag
SPDS	Secondary Payloads Deployment System
SRP	Solar Radiation Pressure
SSPA	Solid-State Power Amplifier
STM	Statistical Trim Maneuvers
SKG	Strategic Knowledge Gap
TCA	Time of Closest Approach
TLI	Trans Lunar Injection
TSAC	Tracking System Analytical Calibration
TT&C	Telemetry Tracking and Command
UNIBO	University of Bologna
USO	Ultra Stable Oscillator
VLBI	Very-Long-Base-Interferometry
VPN	Virtual Private Network

Contents

Chapter 1

Introduction

Contents

1.1 Dissertation Introduction

The navigation in space is the fundamental process required for keeping track of the actual spacecraft (S/C) position during its flight as well as create orbital maneuvers to bring the S/C on its planned course. The use of CubeSats in deep space requires the development of navigation techniques and procedures that differ from the ones used in the near Earth CubeSats missions. The work carried on in this dissertation thesis aimed at designing, testing and validating a ground based navigation system for cis-lunar and deep space CubeSats, in particular for the lunar ASI's ArgoMoon mission [1]. The activities carried on during this dissertation's work have covered the entire life cycle of the ArgoMoon project, from Phase 0 up to Phase F.

The core of this research concerns the development of the ArgoMoon's navigation system in many aspects of the process mainly related to the navigation process and strategy, the navigation software and the flight dynamics operations. The navigation software developed as a set of general and mission specific toolkits on top of the NASA/Jet Propulsion Laboratory (JPL)'s software Mission-analysis and Operations Navigation Toolkit Environment (MONTE) [2]. The working steps followed in this research can then be depicted from a set of high level design process objectives:

- Evaluation of the state-of-the-art navigation results of deep space CubeSat missions.
- Evaluation of the ArgoMoon's mission to formalize the navigation requirements.

- Evaluation of the ArgoMoon's events and trajectory to shape the navigation concept.
- Preliminary design of a ground based navigation setup for cis-lunar missions.
- Optimization of the reference trajectory and design of the control strategy.
- Navigation expected performance assessment through a detailed covariance analysis.
- Organization of the flight dynamics operations and definition of the data interfaces.
- Perform the navigation of ArgoMoon after its launch on November 16, 2022.
- Evaluate the results and the performance of the conducted operations.

To cover the developed work and the obtained results, the dissertation has been organized as follows: Chapter 1 provides an introduction on the relevant deep space CubeSats missions as well as the fundamental topics regarding navigation method; the ArgoMoon mission, the S/C, and the trajectory are described in the Chapter 2; the navigation concept and setup are covered in the Chapter 3; the Flight Path Control (FPC) analysis, designed to control the trajectory, and the Orbit Determination (OD), needed to estimate and predict the orbital evolution, are covered in Chapter 4; the Chapter 5 provides a description of the conducted navigation operations as well as the obtained results. Finally, Chapter 6 summarizes the main findings and conclusions of this work.

1.2 CubeSats missions beyond the Earth

The CubeSat concept identifies a category of small satellites whose structure is based on an elementary form factor of 1 U which corresponds to a $10 \times 10 \times 10$ cm cube [3]. This standard has been proposed by the California Polytechnic State University during the 2000s as response to the trend of designing space mission in a "Smaller, Cheaper, Faster and Better" way [4][5]. The use of a small sized and light spacecrafts allows to reduce construction and launch costs without make compromising on scientific goals. The improvement of the space electronics in terms of size, capabilities, reliability and power consumption pushed forward the CubeSat utilization in near Earth orbit leading to over 1800 missions launched since 1998 [6]. These CubeSats missions have covered many different applications like Earth remote sensing, telecommunications, weather monitoring, and astronomy [7]. Many of the launched CubeSat were successful proving that this small satellites technology is also reliable for complex missions and not only for educational purposes or technological demonstrations. Thanks to these aspects, CubeSats are becoming attractive also for cis-lunar and deep space exploration, either as stand-alone missions or as complement to classical, larger spacecraft. However, outer space exploration poses additional challenges from the engineering point of view requiring to have a different design approach with respect to the near Earth missions. In fact, differently from their Earth-orbiting predecessors, the deep space CubeSats are required to have full functionality and active control systems like any regular spacecraft operating in deep space. Moreover, the CubeSat technology has not been intensively tested in deep space and then additional constraints and requirements can be required for such CubeSat missions.

1.2.1 Deep Space

Recently, the Mars Cube One (MarCO) of the JPL and Light Italian Cubesat for Imaging of Asteroids (LICIACube) of the ASI were the first CubeSats missions to have been

successfully performed in deep space. These two missions have involved either mother-daughter system architectures as well as the stand-alone operation further proving the reliability of such technology to perform complex and critical activities.

MarCO

The MarCO mission [8] was designed with the aim of using two identical 6U CubeSats as telecommunication relay for the NASA's InSight Martian lander. The two CubeSats were launched on May 5, 2018, sharing a ride on the Atlas V Centaur upper stage as secondary payloads together with the InSight lander. After the orbital injection, the MarCOs were independently navigated towards Mars with the aim of test their capabilities and validate the CubeSat technology in deep space [9]. After their interplanetary travel, the MarCOs performed a fly-by of Mars on November 26, 2018, successfully providing a real-time UHF relay for the InSight lander that was descending on Mars at the same time. The mission results showed that flying a CubeSat in deep space is feasible and performance expectations can be considerable. However, the MarCOs flight has also demonstrated that additional constraints and challenges can originate from subsystems like the orbital propulsion or the attitude control. For instance, the propulsion system was constrained by the power available to the S/C requiring the split of the orbital maneuvers into segments of not more than ten minutes of duration each. Furthermore, the navigation team identified an anomalous thrust the day after the launch in correspondence of the first momentum reduction burn performed by MarCO-B. The problem was related to the plenum valve that leaked causing the propellant condensation and an higher thrust level due to the expulsion of the liquid after the actuation of the thrusters' valves. This event is an important heritage for future deep space CubeSat missions allowing to carefully account for potential issues related to the employed miniaturized propulsion technology.

LICIACube

LICIACube has been the first European CubeSat mission (managed by ASI and entirely designed and operated from Italy) [10, 11, 12] to successfully fly in deep space in the context of the Double Asteroid Redirection Test (DART) mission [13] of NASA and the Applied Physics Laboratory (APL) of Johns Hopkins University (JHU). The DART mission was developed as a technological demonstration designed with the aim of evaluate an asteroid redirection by performing a controlled high velocity impact with a spacecraft. The impact's aimed target was Dimorphos, the 160 m secondary asteroid of the binary asteroids system (65803) Didymos [14]. The impact of DART was designed to occur at a velocity in between 6 km/s and 7 km/s with respect to Dimorphos in order to produce at least 73 s of variation in the Dimorphos' orbital period. LICIACube participated to this mission as a companion CubeSat of DART with the aim of capture detailed and relevant pictures of the impact of DART on Dimorphos. To achieve this objective, LICIACube was integrated into DART as secondary payload and it was released in space on September 17, 2022, approximately 15 days prior the expected impact epoch. Then, LICIACube has been navigated from the Earth by the Radio Science and Planetary Exploration Laboratory (RSLab) of the University of Bologna (UNIBO) towards Dimorphos to conduct a fly-by of the asteroid at approximately 55 km from the DART impact region [15]. In the night time of September 26-27, 2022, DART impacted Dimorphos as planned and the event has been successfully observed by LICIACube [16].

1.2.2 Cis-Lunar Space

The exploration of the Moon attracted a relevant international interest in the recent years. This interest led to the proposal and selection of many small satellites mis- sions to the cis-lunar space that are currently flying or will be launched in the next future (e.g., CAPSTONE [17], HORYU-VI [18]). Moreover, with the recent deployment in cis-lunar space of a CubeSat cluster during the Artemis-1 mission, the reconnaissance of the Moon has became a relevant testbed for the deep space smallsats technology.

Artemis-1

Artemis-1 is the first mission of the NASA's Artemis program to return astronauts to the Moon by 2024 [19]. The Artemis-1 mission was designed by NASA as an unmanned mission to the Moon to perform the first integrated flight test of the Orion S/C and SLS. In the context of the Artemis-1 mission, NASA selected ten CubeSats as secondary payloads of SLS based on their ability to return data or test technologies that will address the NASA's Strategic Knowledge Gaps (SKGs) related to exploration of the Moon and Mars [20, 21]. Nonetheless, the opportunity of deploying multiple CubeSats towards the Moon and beyond enabled the possibility of performing dedicated scientific experiments and relevant technological demonstrations. The ten CubeSats have been integrated on a non-interference, no harm basis way as secondary payloads into the Stage Adapter above the SLS's second stage named ICPS. The integration was performed on the adapter's ring through fourteen dispensers, Figure 1.1, capable of accommodating 6U and 12U CubeSats. The Artemis-1 integrated small satellites fleet was entirely composed by 6U CubeSats whose mission names and objectives are reported in Table 1.1. Essentially, the deployment of these CubeSats acted as the first de fact deep space CubeSat cluster.

The mission was successfully launched on November 16, 2022, carrying Orion towards its 25-day space mission with the aim of orbiting the Moon and coming back safely to the Earth. Approximately two hours later the launch, after the Trans Lunar Injection (TLI), the Orion S/C separated from the ICPS which started its preparation for the disposal maneuver. The last operation performed by the ICPS was to activate the Secondary Payloads Deployment System (SPDS) and start the countdown to deployment of the CubeSats. These secondary payloads have been released in space at a series of trajectory locations named Bus Stops (BSs). There were a total of six Bust Stops where in the first one a total of five CubeSats were scheduled for the deployment.

1.2.3 Future Missions

Actually, the increasing interest in the use of CubeSats in deep space and the obtained encouraging results led to the proposal and selection of many other missions that will be launched in the next future. For instance, by considering the cis-lunar space, the Lunar Meteoroid Impact Observer (LUMIO) mission planned for 2023 will bring a 12U CubeSat into a halo orbit around the Earth-Moon L2 point, with the aim of observe, quantify, and characterize the micro-meteoroid impacts on the Lunar far side [33]. In the case of LUMIO, the heritage from the navigation of cis-lunar CubeSats will be fundamental to successfully fly the S/C into its halo orbit which is well known to be a Circular Restricted Three-Body Problem (CR3BP) solution very sensitive to perturbations. In the exploration of the solar system, the European Space Agency (ESA)'s missions Hera [34] and Miniaturised Asteroid Remote Geophysical Observer (M-ARGO) [35] are two relevant examples of scientific deep space CubeSats missions planned for the next future. Together with DART and

Table 1.1: CubeSats integrated on the ICPS of SLS in the context of the Artemis-1 mission.

Mission	**Objectives**	**Propulsion**	**Payload**	**Operator**
ArgoMoon	Monitoring the status of ICPS and the release of the other CubeSats, and perform technological demonstrations [22].	Chemical	Autonomous target relative navigation.	ASI
BioSentinel	Astrobiology mission to study the effect of the impact of the deep space radiation on DNA repair over long time beyond low Earth orbit [23].	Cold gas	Radiation dosimeter, dedicated 3-color spectrometer.	Ames Research Center of NASA
NEA Scout	Reconnaissance of the NEA 2013 WA44 using a low-thrust solar sail propulsion system [24].	Solar Sail of 86 m^2	High resolution monochromatic camera.	JPL
CuSP	Orbiting the Sun to study the dynamic particles and magnetic fields to support the Space Weather Research [25].	Cold gas	Ion spectroscope, and a miniaturized electron and proton telescope.	Southwest Research Institute
EQUULEUS	Exploration of the Earth-Moon Lagrange points to study the Earth's plasmasphere [26].	Water Thursters	UV imager and a meteoroid impact detector.	JAXA
OMOTENASHI	Technological demonstration of the world's smallest semi-hard moon lander [27].	Solid / Cold gas	Radiation monitor and an accelerometer.	JAXA
LunaH-Map	Map the hydrogen enrichments in permanently shadowed regions at the lunar south pole [28].	Ion Engine	Miniaturized scintillation neutron detector.	Arizona State University
Lunar IceCube	Prospect, locate, and measure volumes and composition of water ice deposits and other volaties on the Moon [29].	Ion Engine [30]	Infrared high resolution spectrometer.	Morehead State University
LunIR	Collect spectroscopy and thermography for lunar surface characterization, remote sensing and site selection [31].	Electrospray	Miniaturized high temperature Mid-Wave Infra-Red sensor.	Lockheed Martin Space
Team Miles	Technological demonstration of deep space navigation using innovative plasma thrusters [32].	Hybrid plasma and laser	Software-defined radio operating in the S-band.	Fluid and Reason, LCC

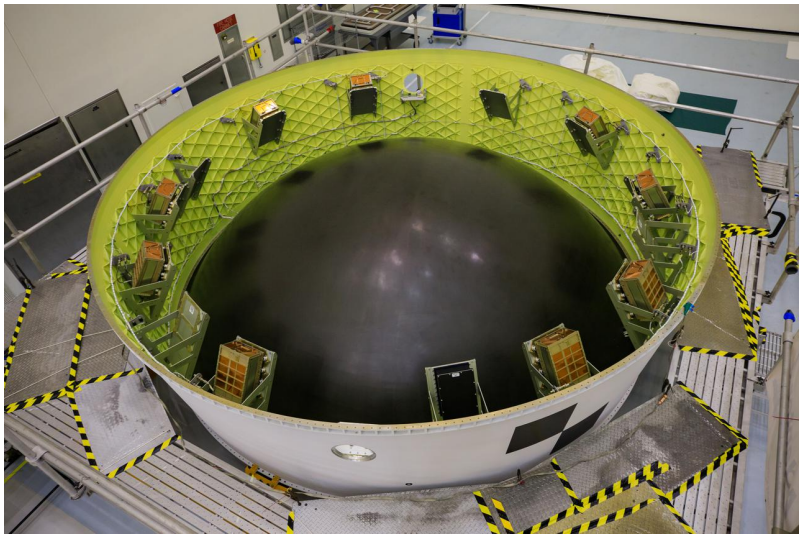

Figure 1.1: Orion spacecraft's stage adapter with nine out of ten CubeSats installed. Credits: NASA. Source: nasa.gov.

LICIACube, Hera is a planetary defense missions whose launch is planned for October 2024. The Hera mission foresees the exploration of the Didymos system and in particular the characterization of the DART's impact. In this mission there will be two additional CubeSats, named Juventas [36] and Milani [37], that will fly as companions of Hera to be deployed in orbit around the main asteroid of the Didymos system. Juventas and Milani will be used to improve the scientific return of the mission by carrying out dedicated independent experiments and also by exploiting the Inter-Satellite Link (ISL) used for the telecommunications of the CubeSats with Hera. Unlike the CubeSats companion missions introduced since now, the mission M-ARGO has been designed to be the first standalone deep space CubeSat that will perform a rendezvous with an Near Earth Asteroid (NEA). Furthermore, the M-ARGO mission will also be an important technological demonstrator since the S/C will be equipped with an high-efficiency electric propulsion system.

1.3 Deep Space Navigation

The navigation of a S/C is a fundamental part of the operations in space and it is critical for the success of the mission. It consists into the process of determining and controlling the S/C's trajectory in order to maintaining it within acceptable limits of the designed one [38]. Moreover, even if it is a task of the mission analysis, the trajectory design is directly connected to the navigation since it must be performed in accord to the capabilities of the S/C guidance system. For example, a trajectory that is too sensitive or complex may not be flown if the determination of the trajectory and its controllability are not accurate. S/C navigation is in fact a complex process that requires the acquisition of data containing information about dynamics of the vehicle (i.e., position and velocity), the definition of precise observational and dynamical models, the filtering and processing of the acquired datasets to estimate the trajectory, and the computation of the corrections for the trajectory dispersions that inevitably occur.

1.3.1 Orbit Determination

The OD is the part of the navigation process in which the actual and predicted trajectory of the S/C are computed. The OD problem can be formulated as follows: given a set of observable quantities related to the S/C, acquired at different epochs (e.g. the picture of a celestial body captured from a S/C on-board camera), determine the position and velocity of the S/C at a specific epoch so that it is possible to predict the trajectory in the future. The observable quantities are usually nonlinear functions of the state variables and then they cannot provide a direct observation of the S/C state. Moreover, the observations are also influenced by random and systematic errors and the used mathematical model is inexact. Therefore, the determination of the best estimate of a S/C's epoch state, with unknown initial conditions, noisy observations and uncertain mathematical model, is referred to as the OD process. Clearly, the concept of "best" estimate is related to the optimization in the statistical sense of the OD problem.

The OD process can then be described by the iterative process represented in Figure 1.2. The *modeled world* contains the dynamical model required to perform the numerical integration to obtain the S/C trajectory. The designed dynamical model should include all the forces expected to act on the S/C. The numerically integrated trajectory is then used to compute the so called *predicted observables*, or *computed observables*, with the designed observations mathematical model. Then, by making the difference between the *computed observables* and the *measured observables*, the so-called *residuals* are obtained. Theoretically, if the dynamical and observational models were perfectly known, the *residuals* would be characterized by a zero mean with an added white Gaussian noise due to uncorrelated measurements errors. However, errors in the trajectory and the observable models introduce distinctive signatures in the residuals. Therefore, the *a priori* dynamical model is corrected in an iterative process to minimize the *residuals* by usually apply a linearized batch weighted least-square filter [39]. The estimated parameters include, as a minimum, the S/C initial state vector. Other estimated quantities may be the gravity field of celestial bodies, their orbits, the S/C orbital maneuvers, or, in general, several parameters included in the acceleration and observational models.

Estimation Process

The process of estimating the trajectory of a S/C requires an optimal way to combine a large number of observations to improve the accuracy of the final result. An example of optimal solution for the estimation process is the weighted leas square filter. This kind of filter selects the estimate of the state vector as that value that minimizes the sum of the squares of the computed observations *residuals* [41]. Now suppose that $\hat{\mathbf{x}}$ is an estimate or an *a priori* value of the true state vector of the S/C at a certain epoch t_0 identified as $\mathbf{x} = [\mathbf{r}(t_0), \dot{\mathbf{r}}(t_0)]$. The system of non-linear equations governing the dynamics of the S/C can be represented as $\mathbf{x}(t) = [\mathbf{r}(t), \dot{\mathbf{r}}(t)]$ with

$$\frac{d\dot{\mathbf{r}}(t)}{dt} = \sum_{i=1}^{m} \nabla U_i(\mathbf{r}(t) - \mathbf{r}_i(t)) + \mathbf{a}_\gamma(t) + \mathbf{a}_{ng}(t) \tag{1.1}$$

where $\mathbf{r}$ is the S/C position vector with respect to the system's barycenter in an inertial reference frame, $U(\mathbf{r} - \mathbf{r}_i)$ is the gravitational potential associated to the i-th celestial body located at the position $\mathbf{r}_i$, $\mathbf{a}_\gamma$ is the acceleration associated to the relativistic effects, and $\mathbf{a}_{ng}$ is the acceleration due to the other non-gravitational forces.

The improvement of the estimate $\hat{\mathbf{x}}$ is then performed by using a $p \times 1$ vector of

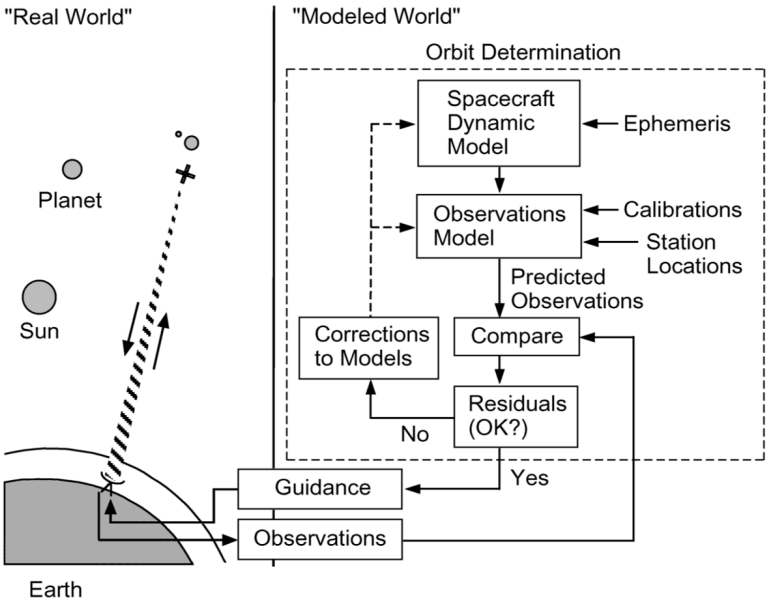

Figure 1.2: The iterative scheme of the navigation process [40].

observations $\mathbf{z}$ defined as

$$z_i = h_i(\mathbf{x}(t_i), t_i) \qquad i \in [1, ..., p] \tag{1.2}$$

where t_i are the time instants in which the observable is collected. As mentioned before, it is possible to see from Equation 1.2 that the observables do not provide a direct observation of the state variables but they are connected to them in a non-linear way. The first-guess trajectory is then numerically integrated using the designed dynamical model at least up to epoch t_p. Then, the *predicted observables* are computed at the time instants t_i and collected in the vector $\hat{\mathbf{z}}$ of the *computed observables* which is function of the current estimated state $\hat{\mathbf{x}}$. By considering only the position and velocity of the S/C, the state vector $\mathbf{x}$ is a 6×1 matrix but in general it is possible to define an n-dimensional vector containing also other parameters to be estimated (i.e., celestial body mass, orbital maneuvers, ...).

As mentioned before, the weighted least square filter is based on the minimization of a cost function defined as the weighted average of the norm of the residuals

$$J(\hat{\mathbf{x}}) = [\mathbf{z} - \hat{\mathbf{z}}(\hat{\mathbf{x}})]^T W [\mathbf{z} - \hat{\mathbf{z}}(\hat{\mathbf{x}})] \tag{1.3}$$

where W is a p-by-p weight matrix and $\mathbf{z} - \hat{\mathbf{z}}(\hat{\mathbf{x}})$ is the residuals vector. Therefore the estimation $\hat{\mathbf{x}}$ is the one that minimize the cost function J. Usually, the weight matrix W can be designed as the inverse of a diagonal matrix whose values are the standard deviations σ_i of the i-th observable corresponding to the measurements noise.

The minimization of J is obtained by solving the equation

$$\frac{\partial J}{\partial \hat{\mathbf{x}}} = \left[\frac{\partial J}{\partial \hat{r}_1} \; \frac{\partial J}{\partial \hat{r}_2} \; \frac{\partial J}{\partial \hat{r}_3} \; \frac{\partial J}{\partial \hat{v}_1} \; \frac{\partial J}{\partial \hat{v}_2} \; \frac{\partial J}{\partial \hat{v}_3} \right] = -2(\mathbf{z} - \hat{\mathbf{z}})^T W \frac{\partial \hat{\mathbf{z}}}{\partial \hat{\mathbf{x}}} = 0 \tag{1.4}$$

where the partial derivative of the computed observables $\hat{\mathbf{z}}$ with respect to the estimated state $\hat{\mathbf{x}}$ are organized in a p-by-n matrix denoted as A. The observation partials matrix is then linearized with a first order approximation to be used in the linear corrector scheme.

Finally, through the inverse of the Equation 1.4 is possible to define the differential correction as

$$\hat{\mathbf{x}}^{(k+1)} - \hat{\mathbf{x}}^{(k)} = -G'[\hat{\mathbf{x}}^{(k)}]^{-1} G'[\hat{\mathbf{x}}^{(k)}] = (A^T W A)^{-1} A^T W[\mathbf{z} - \hat{\mathbf{z}}(\hat{\mathbf{x}}^{(k)})] \tag{1.5}$$

which is an iterative scheme that adjusts the parameter vector, or estimated state vector, in order to minimize the norm of the residuals. So the iteration scheme is repeated until the residuals cease to become smaller with further iterations.

By introducing ${P_0}^{-1}$ as the *a priori* information matrix (i.e. the inverse of the *a priori* covariance matrix) and $\tilde{\mathbf{x}}$ the *a priori* state vector correction, the iteration scheme becomes

$$\delta\hat{\mathbf{x}}_k = (A^T W A + P_0^{-1})^{-1}(A^T W \delta\hat{\mathbf{z}} + P_0^{-1}\tilde{\mathbf{x}}) \tag{1.6}$$

where $\delta\hat{\mathbf{x}}_k = \hat{\mathbf{x}}^{(k+1)} - \hat{\mathbf{x}}^{(k)}$ and $\delta\hat{\mathbf{z}} = \mathbf{z} - \hat{\mathbf{z}}(\hat{\mathbf{x}}^{(k)})$.

An important instrument to analyze the accuracy of this estimation process is the error covariance matrix P. This matrix is retrieved from the first term on the right side of the Equation 1.6 as

$$P = (A^T W A + P_0^{-1})^{-1} = E[\delta\hat{\mathbf{x}}\delta\hat{\mathbf{x}}^T] \tag{1.7}$$

with $E[]$ ensemble average operator and $\delta\mathbf{x}$ error of the converged estimate.

Each element on the main diagonal of P is correlated to the formal uncertainty σ of the corresponding element of the state vector through the following expression:

$$\sqrt{P_{ii}} = \sigma_i \tag{1.8}$$

The off-diagonal elements of the P matrix identify the covariance of the i-th and j-th parameters of the estimated parameters as follows:

$$P_{ij} = \rho_{ij}\sigma_i\sigma_j \tag{1.9}$$

where ρ_{ij} is the correlation coefficient between the i-th and j-th parameters. In general, if the magnitude of the elements of P increase, the estimation loose accuracy.

Up to the point where subsequent iterations no longer result in decreasing residuals, the entire procedure is repeated. The described differential correction process, in its simplest form, is an iterative procedure that modifies the parameter vector in order to reduce the residuals' norm.

Observables

A crucial aspect of navigation is the capability to measure quantities that mathematically relate to the S/C dynamic of motion [42]. Such quantities are called observables and in the general OD application it is possible to identify two different types of common used observations: optical and radar. The optical quantity is based on the direct observation of a target body with respect to the fixed stars. Since the stars' positions are precisely known, it is feasible to calculate the direction between the observer and the target, but not the distance itself. The radar observations, the fundamental and principal quantities in the deep space navigation, overcome to the problem of measure the relative distance and velocity. These observations exploits the radio signals exchanged between a ground station (or from another object in space) and a spacecraft equipped with a transponder. The amplitude and phase of an electromagnetic wave that establishes a radio link between the S/C and the Earth are basic radiometric observables. The last three basic radiometric data types are then used to derive additional values more closely tied to the S/C's dynamics: Range, Doppler and Very-Long-Base-Interferometry (VLBI).

Based on the source of the reference signal and the number of intervening stations, there are essentially three different tracking link configurations:

Table 1.2: Uplink and downlink frequencies with their relative turn-around rations (M_2) for deep space communications [40, 42].

Band	Uplink (MHz)	Downlink (MHz)	M_2 (S)	M_2 (X)	M_2 (Ka)
S	2110-2120	2290-2300	$\frac{240}{221}$	$\frac{240}{749}$	$\frac{240}{3599}$
X	7145-7190	8400-8450	$\frac{880}{221}$	$\frac{880}{749}$	$\frac{880}{3599}$
Ka	34200-34700	31800-32300	$\frac{3344}{221}$	$\frac{33440}{749}$	$\frac{3344}{3599}$

- One-Way: down-link tracking only where the carrier of the signal is generated onboard the S/C, using an appropriate oscillator.

- Two-Way: the ground station generates the carrier of the signal using the station's master frequency standard. The uplink signal is then acquired by the S/C and coherently retransmitted to ground by an onboard transponder.

- Three-Way: the tracking process is identical to the two-way case except that the transmitting and receiving antennas are different. Given that the usage of two independent antennas creates different uncorrelated noise sources and latencies, this type of link offers less accuracy than the two-way scenario. However, this link configuration becomes necessary when the S/C is at very long distance from the Earth causing the signal round-trip light time to be greater than the visibility time of the ground station.

Internationally designated frequency bands, which are displayed in 1.2, are used for communications between Earth and S/C and vice-versa. Moreover, in the two-way case, the frequencies of the up-link and down-link signals are different to prevent interference between them since they may be traveling at same time when the link is established. The differentiation between up-link and down-link frequencies is performed using the turn-around ratio (M_2), 1.2, which is defined as the ratio of the transmitted down-leg frequency at the S/C to the received up-leg frequency at the S/C.

Range The ranging is the measurement of the light time that the signal takes to travel at speed of light between the ground station and the S/C or between two S/Cs that orbiting the same body. In the two-way range the measurement is done by evaluate the time delay τ defined as follows

$$\tau_d = \frac{\rho_u + \rho_d}{c} \tag{1.10}$$

where ρ_u is the uplink range, ρ_d is the downlink range and c is the speed of light. It is important to note that the range is the measurement of the time of flight of the photons and not the effective distance of the involved objects. Generally, the ranging is carried out by modulating a predetermined sequence (the ranging code) into the uplink carrier frequency at the ground station. Then, the range signal is demodulated and re-modulated onto the down-link carrier when the S/C receiver locks to the carrier. Finally, the sent ranging signal is recovered by the ground receiver as a noise-corrupted, time-delayed (and hence phase-shifted), version, and the time difference between the communicated and received signals is then determined.

Doppler (Range-rate) The Doppler observables exploit the Doppler shift affecting the exchanged signals to recover and information about the line-of-sight velocity of the S/C with respect to the ground station (or in general between a source and a destination). Assume now that a flying S/C sends a signal to a ground station the time t_1 with a given frequency f_1. Then, the ground station receive this signal at the time t_2 with a received frequency f_r. As first approximation, the frequency shift f_D affecting the signal received at the ground station is defined as

$$f_R = \left(1 - \frac{\dot{\rho}}{c}\right) f_T \tag{1.11}$$

The aforementioned equation is just used to demonstrate how Doppler tracking works. In order to accurately simulate the Doppler observables, the extraction of the Doppler frequency has a more convoluted derivation in practice. In practice, after the extraction of the Doppler tone from the differencing of f_R and f_T, a cycle counter measures the total phase change of the Doppler tone during a chosen Count Time (CT) interval T_C. Then, it is possible to observe that the signal's propagation distance has grown by one wavelength when the received signal's phase shifts by one cycle with respect to the transmitted signal's phase. Therefore, rather than providing an immediate measure of the range-rate, the Doppler count measures range change throughout T_C.

It is possible to distinguish the formulation of the Doppler measurements into *integral* and *differenced*. The former is a first order approximation of the range-rate during the count interval and it is defined as

$$F = \frac{M_2 f_T}{T_C}(\rho_{end} - \rho_{beg}) \tag{1.12}$$

where ρ_{beg} is the round-trip light time for a signal received at the beginning of the count interval and ρ_{end} is the one at the end. The *integral* version of the Doppler formulation is defined as

$$F = \frac{1}{T_c}\int_{\bar{t}-T_c/2}^{\bar{t}+T_c/2}(f_{ref} - f_T)dt \tag{1.13}$$

where $\bar{t}$ corresponds to the midpoint epoch of the count interval and f_{ref} is an arbitrary reference frequency, usually $M_2 \cdot f_T$. This causes the observable to shift in a manner that is proportionate to the change in range along the light path during T_c. The Doppler observables are frequently identified by the NASA's Deep Space Network (DSN) as F1, F2 and F3 for one-way, two-way and three-way Doppler, respectively.

Error Sources

The OD accuracy is constrained by a number of noise sources in Doppler and range acquisition [40]. For instance, in the case of the presented tracking data types (Doppler and range), there can be inaccuracies due to the Radio Frequency (RF) system, such as clock instability and instrumental signal delays. Moreover, the transmission media causes dispersion and path delays into the signals. Further limiting the capacity to predict S/C position are the imperfect definition of the tracking geometry as well as the dynamical mismodelling. Regarding the radio-tracking observables, the most relevant sources of noise are the following:

- *Clock Instability*: the signals transmitted by the ground station or the S/C require a stable clock in order to have a precise reference frequency. Any deviation of this reference frequency from the actual transmitted frequency will result in a range rate

error. Most of the current space-qualified Ultra Stable Oscillators (USOs) have an Allan variance [43] in the order of 10^{-13} over an average interval of 1000 seconds [44]. However, the use of two-way tracking allows to reduce the effects of the clock instability since the transmitted and received frequency standards are the one of the same ground station and then highly stable clocks, like the hydrogen maser (Allan variance down to 10^{-15} [45]), are typically used.

- *Instrumental Noise*: the RF equipment of the ground station and the S/C are affected by random and systematic errors resulting from thermal effects and uncalibrated delays in the electronics. The random noise due to the thermal effects can be mitigated by lowering the system operating temperature. If not properly calibrated, the instrumental effects can contribute to an error up to 0.003 mm/s to Doppler measurements acquired with a CT of 60 s [40].

- *Transmission Media*: the signals exchanged between the ground station and the S/C have to travel in medias that can introduce undesired delays. The term *path delays* is used to describe these delays that can be frequency dependent or not. The frequency dependent are the delays induced by dispersive medias where the charged particles decay with the inverse squared of the carrier frequency. The use of higher frequencies allows to reduce the effect of the dispersive medias where the multi-frequency link calibrations allow to correct the induced path delay [46]. The Earth's ionosphere can be also calibrated with high precision using GNSS-based methods in the absence of a multi-frequency connection . An example of dispersive sources are the Earth's ionosphere or the solar plasma. An example of not frequency dependent media, also called non-dispersive media, is for instance the Earth's troposphere. The effects of the Earth's troposphere are subdivided into a dry component and a wet one. The dry component contributes about 95% of the total zenith delay, it is stable and dependent to the station location on the Earth due to its proportionality to the surface pressure. The wet part is proportional to the atmosphere's water content along the antenna-S/C line of sight, and it produces an highly unstable delay with a magnitude smaller then the one of the dry part [47]. To mitigate the effect of the tropospheric path delays, a calibration is performed with the Tracking System Analytical Calibration (TSAC) and Advanced Media Calibrations (AMC) [48, 49].

- *Dynamical Mismodelling*: the observables and the dynamical models are not perfectly known. This flaw causes errors in the integration of the S/C's trajectory, in particular for non-gravitational accelerations and attitude motion. Consequently, the computation of the observables, which is based on the integrated trajectory, is affected by errors both from their mathematical model and the one of the S/C's dynamics.

1.3.2 Flight Path Control

The actual trajectory of a S/C cannot be expected to exactly match the designed one. Moreover, the OD process allows to recover the actual S/C trajectory providing only a best estimate solution that has an associated uncertainty. Therefore, deviations with respect to the reference trajectory must be expected thus requiring the design of a proper control strategy. Some of the principal errors causing dispersion on the S/C trajectory, as well as on the OD solution, can be summarized as follows:

- *Launcher performance*: the deployment of a S/C in space takes place at the end of a complex ascent flight performed by a launcher. In case of a deep space mission,

additional launcher's upper stages are used to perform such orbital maneuvers required to inject the payload into a cis-lunar or interplanetary trajectory. Then, the uncertainty on the performance with which the launcher injects the payload into the designed orbit causes a dispersion on the S/C initial state. Such dispersion is described by the so called *injection covariance* and it is also used in the OD as the *a priori* covariance for the S/C initial state.

- *Maneuvers performance*: the S/C's thrusters commit errors in performing orbital maneuvers and desaturation maneuvers. When the S/C performs an orbital maneuver, a variation of the velocity vector is obtained. The errors made by the propulsion system translate then into a velocity vector dispersion, which consequently causes an increment of the trajectory dispersion at the downstream aimpoint. The performance of the thrusters cannot be fully characterized before the launch, and then the propulsion system has to be calibrated during the flight.

- *OD errors*: the uncertainty in the prediction of the S/C trajectory causes a trajectory dispersion in the execution of an orbital maneuvers. The correction maneuvers are always computed using a selected optimal OD solution. Thus, if the predicted position of the S/C at the target is far from the truth, the computed correction maneuver will increase trajectory dispersion rather than reducing it.

The FPC purpose is to control and mitigate the trajectory dispersion in order to make the S/C following the designed path. The typical trajectory control is performed by targeting specific aimpoints using orbital correction maneuvers.

In general, the former trajectory control is based on solving a nonlinear constrained optimization problem. An optimization problem for a deep space correction maneuver can be stated, in a high-level way, as follows: find the correction to the S/C velocity vector $\mathbf{v}$, at the time of the maneuver, such that the error at the target is less than the tolerance ϵ and the velocity correction magnitude is minimized. To have a more detail comprehension of the introduced FPC problem, a mathematical statement is provided.

Let's assume that $\mathbf{s} = \mathbf{f}(\mathbf{x}) = (f_1(\mathbf{x}), f_2(\mathbf{x}), ..., f_m(\mathbf{x}))^T$ is the vector of the m target's variables (i.e., a subset of the S/C's state coordinates at certain epoch), where $\mathbf{f}(\mathbf{x})$ is the vector of the goal functions, and $\mathbf{x} = (x_1, x_2, ..., x_n)^T \in R^n$ is the independent control variables vector (i.e., the $n = 3p$ velocity components of the p optimized maneuvers) [50]. The optimization problem requires then to find the vector $\mathbf{x}$ such that

$$|\mathbf{f}(\mathbf{x}) - \mathbf{q}| < \mathbf{e} \tag{1.14}$$

where $\mathbf{q} = (q_1, q_2, ..., q_m)^T$ is the vector of the desired values of $\mathbf{s}$, and $\mathbf{e} = (e_1, e_2, ..., e_m)^T$ is the convergence criteria vector. The stated optimization problem is represented in the scheme of Figure 1.3 where the trajectory search concept can be depicted. The solution to the Equation 1.14 can be found by solving the approximate equation

$$\mathbf{r}(\mathbf{x}) = (r_1(\mathbf{x}), r_2(\mathbf{x}), ..., r_m(\mathbf{x}))^T = \mathbf{f}(\mathbf{x}) - \mathbf{q} \simeq \mathbf{0} \tag{1.15}$$

where $\mathbf{r}(\mathbf{x})$ is the residual vector. The minimization problem for the Equation 1.15 is defined as

$$\min_{\mathbf{x} \in \Re^n} h(\mathbf{x}) = \frac{1}{2} \sum_{i=1}^{m} (\mathbf{r}(\mathbf{x}))^T \mathbf{r}(\mathbf{x}) \tag{1.16}$$

which is a least square minimization of the residual vector $\mathbf{r}$.

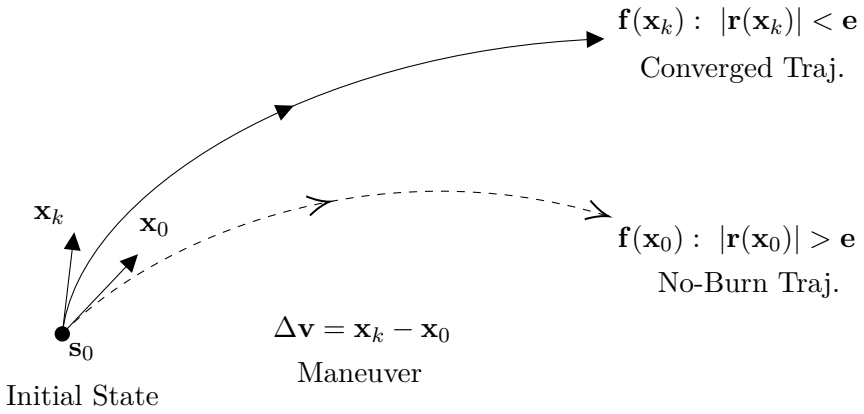

Figure 1.3: Optimal search of a maneuver's $\Delta\mathbf{v}$ vector to arrive at the target $\mathbf{f}(\mathbf{x})$ [50].

The described optimization problem can be solved iteratively with the linear Gauss-Newton method whose the k-th iteration can be computed as

$$\mathbf{x}_{k+1} = \mathbf{x}_k - (A^T(\mathbf{x}_k)A(\mathbf{x}_k))^{-1}A^T(\mathbf{x}_k)\mathbf{r}(\mathbf{x}_k) \tag{1.17}$$

where $A(\mathbf{x}) = \partial\mathbf{f}(\mathbf{x})/\partial\mathbf{x}$ is the partials derivatives matrix of the goal functions with respect to the control variables. In the proposed case where the control variables are the maneuver's components, the matrix $A(\mathbf{x})$ actually describes the sensitivity of the selected target with respect to a variation in the S/C's velocity at the maneuver's epoch. In case of a matrix A that doesn't have full column rank, than the method should be modified with a complete orthogonal factorization or singular-value decomposition. The iterative scheme of Equation 1.17 is then repeated until the convergence criteria of Equation 1.14 is not satisfied.

The Gauss-Newton method may not be locally convergent in case of large residuals or if the problem is significantly nonlinear. The trajectory of a S/C in deep space rarely behaves linearly and then an improvement of the solver is required. For instance, if the Hessian matrix of $h(\mathbf{x}) = A^T(\mathbf{x}_k)\mathbf{r}(\mathbf{x}_k)$ is available, the iteration of the Newton quadratic model can be evaluated as

$$\mathbf{x}_{k+1} = \mathbf{x}_k - H^{-1}(\mathbf{x}_k)\mathbf{g}(\mathbf{x}_k) \tag{1.18}$$

where $H^{-1}(\mathbf{x}_k)$ is the inverse of

$$H(\mathbf{x}_k) = A^T(\mathbf{x}_k)A(\mathbf{x}_k) + \sum_{i=1}^{m}\mathbf{r}_i(\mathbf{x}_k)\nabla^2\mathbf{r}_i(\mathbf{x}_k). \tag{1.19}$$

In case this method is used with a small residual vector or in a linear problem, the Equation 1.19 can be reduced to the Equation 1.17 essentially because the second-order information of the Hessian matrix is negligible:

$$\sum_{i=1}^{m}\mathbf{r}_i(\mathbf{x}_k)\nabla^2\mathbf{r}_i(\mathbf{x}_k) \ll A^T(\mathbf{x}_k)A(\mathbf{x}_k). \tag{1.20}$$

However, there are other optimal methods that better manage the second-order information of the Hessian matrix and behave efficiently with the nonlinear least-square problems. For instance, the Hanson-Krogh algorithm [51] exploit the use of a trust-region algorithm

with boxes for optimally solving constrained nonlinear least-squares problems. In this case, the cost function to be minimized is the Euclidean norm of

$$\mathbf{m}(\mathbf{x}_k) = -\mathbf{r}(\mathbf{x}_k) + \frac{\partial \mathbf{r}(\mathbf{x}_k)}{\partial(\mathbf{x})}(\mathbf{x}_k - \mathbf{x}_{k+1}) + \frac{1}{2}\sum_{j=1}^{q} \mathbf{a}_j \left((\mathbf{x}_k - \mathbf{x}_{k+1})^T \nabla_j \mathbf{x}_k\right)^2 \tag{1.21}$$

subject to the linear constraints $\mathbf{c}_k - \hat{\nu} \leq \frac{\partial \mathbf{c}(\mathbf{x}_k)}{\partial(\mathbf{x})}(\mathbf{x}_k - \mathbf{x}_{k+1}) \leq \mathbf{c}(\mathbf{x}_k) - \hat{\mu}$ and the bounds $\mathbf{x}_k \in T \cap S$, where $\mathbf{c}(\mathbf{x}_k)$ is the constraint function, $\mathbf{a}_j$ are the vector coefficients of the quadratic model terms, μ and ν the limits of the domain $T = \{\mathbf{x} | \mu_j \leq \mathbf{x}_j \leq \nu_j, j = 1, .., N\}$, and S is a trust-region box.

Therefore, if the cost function either encounters a value below the set tolerance or a local minimum, or if its norm experiences a change below the tolerance, the search for $\mathbf{x}$ ends. However, the convergence is not guarantee and then a maximum number of iterations should be provided, for both Gauss-Newton and Hanson-Krogh methods.

After an optimal control vector $\mathbf{x}$ is found, a validation of the result must be performed using the last OD solution. For instance, if the control vector regard an orbital maneuver, it must be considered that the execution of this maneuver will increase the uncertainty of the trajectory prediction at the target. Therefore, the validation of the optimized maneuver is required to evaluate if the target is correctly reached and if the increased uncertainty is still compatible with the requirements.

1.3.3 Trajectory Optimization

In the context of the navigation process, the trajectory optimization is typically used for the *reoptimization* of the S/C reference trajectory rather than a complete trajectory design cycle. The reoptimization can be required if there are significant differences between the navigation high-fidelity model and the dynamical model used for the reference trajectory design. The former task is performed before the launch and it is used to prevent additional mismodelling errors, especially if the trajectory is complex [52]. Moreover, in case of unexpected issues during the mission, a reoptimization of the trajectory may be required to face such problems and save propellant as well as satisfy the navigation requirements. For instance, the Cassini-Huygens mission had a major problem with the Huygens lander's telecommunication relay. The problem was found during the interplanetary cruise and it was related with an unexpected behavior of the Huygens receiver onboard the Cassini orbiter. The bit synchronizer of the receiver was found to have a design issue because its bandwidth was too narrow to accommodate for the relay signal's Doppler shift [53]. The Cassini's navigators contributed to the recovery by reoptimizing the Cassini's trajectory to reduce Doppler shift between the orbiter and probe during the data relay period [54].

The trajectory optimization problem can be described as the research of a S/C trajectory that satisfies certain initial, intermediate and final conditions while minimizing or maximizing a performance index [55]. Typically, the optimization of a trajectory is performed by minimizing the total fuel consumption, thus maximizing the S/C's mass for the scientific payloads. In other cases, the performance index may also be the time of flight or other quantities like a geometrical configuration of a fly-by.

The high-level mathematical statement of the trajectory optimization objective can be written in the Bolza form as

$$J_{\mathbf{u}(\cdot)} = \phi(\mathbf{x}(t_f)) + \int_{t_0}^{t_f} L(\mathbf{x}(t), \mathbf{u}(t))dt \tag{1.22}$$

with

$$\dot{\mathbf{x}}(t) = \mathbf{f}(\mathbf{x}(t), \mathbf{u}(t)) \tag{1.23}$$

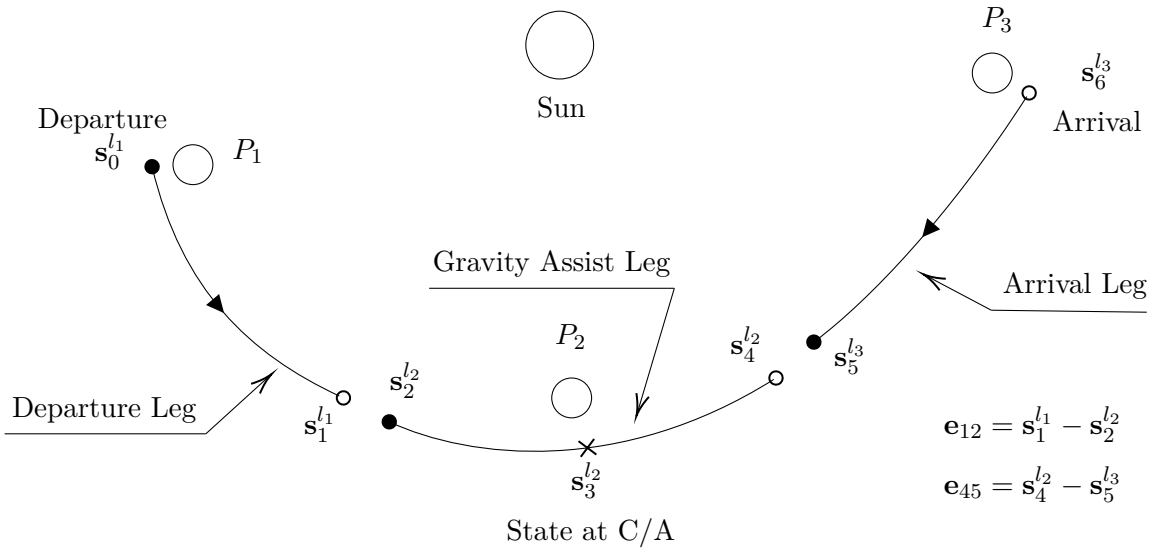

Figure 1.4: Optimization problem structure for an interplanetary trajectory from planet P_1 to P_3 with an intermediate gravity assist from the planet P_2.

where $\mathbf{x}(t) \in \mathbb{R}^n$ is the trajectory time-dependent function, $\mathbf{u}(t) \in \mathbb{R}^m$ is the vector of the control variables (e.g. the epoch of an orbital maneuver and its $\Delta\mathbf{v}$ components), $\phi(\mathbf{x}(t_f))$ is the terminal penalty, and the integral of the Lagrangian L expresses a cost incurred during the entire trajectory. Moreover, the optimization cost function of Equation 1.22 is subjected to the boundary conditions

$$\mathbf{x}(t_0) \in S_0, \qquad \psi(\mathbf{x}(t_f)) = 0 \tag{1.24}$$

where t_0 is the initial time and t_f the terminal time.

For instance, the introduced trajectory optimization problem can be applied to the case of an interplanetary trajectory in which a S/C has to travel from the Earth to another planet of the Solar System exploiting the gravity assist from another body [56]. Let's assume that an initial guess of the optimal trajectory is available and it has been obtained by exploiting the Lambert problem and the patched-conic method [57]. This initial trajectory can then be subdivided into three interdependently propagated legs where a set of selected components of each initial states compose the vector of the control variables $\mathbf{u}(t)$. The overall structure of the optimization problem can be depicted from Figure 1.4. The control vector is composed by the components (or just a subset of them) of the initial states $\mathbf{s}_0^{l_1}$, $\mathbf{s}_3^{l_2}$ and $\mathbf{s}_6^{l_3}$, which can be called *control points*. For example, the control point related to the departure state could be composed by the following three orbital elements: characteristic energy C_3, right ascension λ and declination δ of the departure asymptote. Then, for each single leg, the trajectory propagation is performed as follows:

- Departure Leg: forward from $\mathbf{s}_0^{l_1}$ to $\mathbf{s}_1^{l_1}$.
- Gravity Assist Leg: backward from $\mathbf{s}_3^{l_2}$ to $\mathbf{s}_2^{l_2}$ and forward from $\mathbf{s}_3^{l_2}$ to $\mathbf{s}_4^{l_2}$.
- Arrival Leg: backward from $\mathbf{s}_6^{l_3}$ to $\mathbf{s}_5^{l_3}$.

The constraints $\mathbf{e}_{12} < \epsilon$ and $\mathbf{e}_{45} < \epsilon$, where *epsilon* is the tolerance vector, describe the error between the states in correspondence of the location in which the legs has to be connected. In such way, the constraints, which are also called *break points*, are imposing a

continuity condition between the independent legs. By assuming that two maneuvers $\Delta\mathbf{V}_1$ and $\Delta\mathbf{V}_2$ are placed in correspondence of the *break points* $\mathbf{e}_{12}$ and $\mathbf{e}_{45}$, the constraints can be limited to only imposing the continuity in the position. The cost index J of such problem could be defined as function of the mission's total $\Delta V = |\Delta\mathbf{V}_1| + |\Delta\mathbf{V}_2|$ and the imposed constraints $\mathbf{e}_{12}$ and $\mathbf{e}_{45}$. In conclusion, the optimization of the introduced problem will aim at the minimization of the cost index J by controlling the initial S/C states of each leg.

The algorithms to solve this kind of problems must be able to perform nonlinear optimization subject to constraints, and bounds on the control variables. Usually, such kind of algorithms exploit the use of the Hessian matrix in the iterative computation of the correction to the controls vector. For example, thanks to its well proven efficiency in solving sparse nonlinear optimization problems, the Sparse Nonlinear OPTimizer (SNOPT) algorithm is frequently used in the context of the trajectory optimization [58].

1.3.4 Operative Software

The navigation is performed through the use of sophisticated computer software or set of multiple specific toolkits. Usually, the navigation software implements the entire process described in the previous sections as well as many other routines and subsystems required for secondary tasks like the pre-processing of the radiometric data. Moreover, the navigation toolkit may also include features dedicated to the mission analysis activities like the trajectory design. Typically, the same software is used from the mission design and analysis phase up to the operative one. This is mainly required by the fact that deep space missions cannot be "standardized" often requiring to adapt the navigation software to the specific scenario.

The deep space navigation software selected and used in the work of this dissertation is MONTE. It is a NASA/JPL's signature astrodynamic computing platform that has been employed for over a decade of operational use on the NASA's most demanding deep space robotic missions [59, 60], for radio science experiments data analysis [61, 62, 63], and recently for the deep space navigation of ArgoMoon [1] and LICIACube [64].

MONTE is a versatile group of programs and libraries that supports the design, analytical, and operational processes necessary for deep space missions. Its primary function is to provide operational OD and FPC including the high-fidelity modeling and integration of solar system bodies and forces. Additionally, it enables the processing, conditioning, and editing of navigation tracking data as well as the estimation of spacecraft and solar system parameters and maneuver design and optimization.

The user interface of MONTE is presented to as a Python-language package, giving rise to the nickname MONTE-Python [65]. This software's toolkit is used as a library from which users create unique, stand-alone Python apps to address specific deep-space navigation cases.

Chapter 2

The ArgoMoon mission

Contents

2.1 Introduction

ArgoMoon is an ASI's mission that has been selected by NASA to be part of the the Artemis-1 secondary payloads opportunity (Section 1.2.2) as an important technological demonstrator in the context of the NASA's SKGs program for the exploration of the Moon and Mars. The mission's space segment is based on a 6U CubeSat platform developed and integrated by the Italian's company Argotec [66], whose ground based navigation has been designed and performed by the RSLab of UNIBO [1]. Together with other 9 CubeSat, ArgoMoon has been integrated into the adapter's ring of the SLS' upper stage ICPS, Figure 1.1, and it has been one of the first secondary payloads deployed in space. ArgoMoon has been the first European CubeSat to flight in the cis-lunar space and the second full-italian mission in deep space.

The mission's primary objectives were to autonomously fly the ArgoMoon CubeSat around the ICPS, take detailed and significant pictures of the stage, and verify the deployment of the other CubeSats within the first six hours of the mission [22]. Then, the mission foresees to fly the S/C for 180 days in a highly elliptical geocentric orbit with several encounters with the Moon. The CubeSat platform and ground operations, including navigation, are intensively tested and rigorously validated during this phase as a technological demonstration.

The greatest challenges in the ArgoMoon mission are related to the operations beyond the Low Earth Orbit (LEO) and the Proximity Operations (ProxOps) near the ICPS constrained by strict requirements imposed by the SLS's program [67]. Moreover, the ArgoMoon S/C has to operate outside the Earth's magnetic field, crossing the Van Allan

radiation belts several times during its flight. Therefore, all the S/C subsystems have been designed to sustain the radiation, thermal and operational loads that are typically experienced in a deep space mission.

The ProxOps activities consist into a phase where the S/C autonomously tracks the ICPS and performs orbital maneuvers to control the relative distance, without involving any human intervention from the ground. To perform this activity, the ArgoMoon CubeSat has been equipped with an Image Recognition Software (IRS) capable of tracking a target that is within the Field of View (FOV) of the used camera. Moreover, a laser rangefinder has been integrated into ArgoMoon to provide a confirmation that the target is effectively inside the camera's FOV as well as provide relative distance measurements.

Apart for the ProxOps activities, the ArgoMoon S/C is operated and commanded from the Earth through the NASA's DSN for the telecommunications, in particular by using the 70 m and 34 m antennas [68]. The exchange of data between the S/C and the Argotec's Mission Control Center (MCC) located in Turin (Italy) is performed with a dedicated real-time internet connection to the DSN's ground stations. All the S/C operations have been performed by Argotec from their MCC, and the navigation has been conducted by the UNIBO's team from the flight dynamics control room of the RSLab in Forli (Italy).

The ArgoMoon mission will be an important demonstrator for the CubeSat flight in deep space providing a relevant heritage for future missions.

In this chapter an overview of the ArgoMoon mission is provided. The first section provides a description of the S/C subsystems of main interest for the work carried on this dissertation. Then, a detailed description of the mission timeline is provided in the second section with a special focus on the characteristics that are relevant for the navigation. Finally, a final section is dedicated to the reference trajectory of ArgoMoon which is one of the most important aspects of the designed navigation strategy.

2.2 The Spacecraft

ArgoMoon is a 6U CubeSat (Figure 2.1) based on the HAWK-6 platform developed and assembled by the aerospace company Argotec [69]. The platform has been designed to be scalable and flexible, have an efficient radiation hardness (up to 20 Krad) and provide

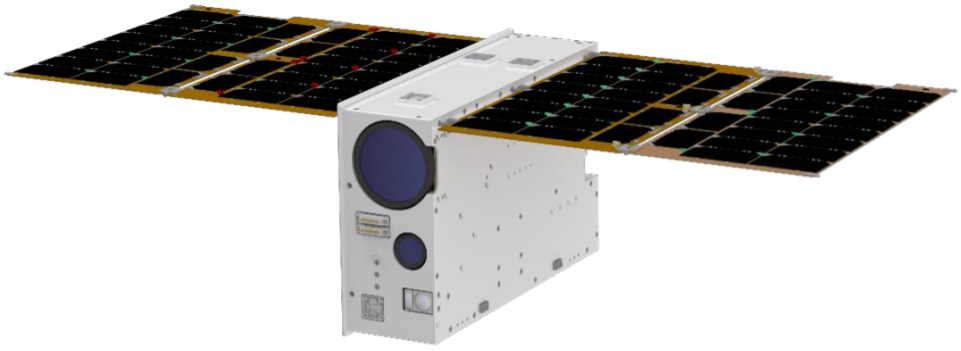

Figure 2.1: Exterior rendering of the ArgoMoon CubeSat. Courtesy of Argotec.

a drastically reduced failure rate if compared to other traditional CubeSat buses. The platform total mass is 14 kg, and it is powered by a Solar Panel Array (SPA) designed as a couple of double-side retractable wings that provides up to 80 W. The HAWK-6 is customizable and it can accommodate a payload with mass up to 3 kg, a volume of maximum 3.5 U, and a maximum peak power of 40 W. The orbital PS can be chemical or electrical providing different maximum ΔV values.

2.2.1 Subsystems Specifications

The ArgoMoon CubeSat is a specific customized HAWK-6 platform whose subsystems has been chosen based on the planned mission objectives [12]. In this section the ArgoMoon S/C subsystems will be briefly described by providing also the technical data of primary interest for this dissertation work. The subsystems' key hardware components are represented in Figure 2.2 where the rendering of the assembled S/C interior can be depicted.

Bus The satellite structure is made of aluminum alloy 7075-T651 and it is designed as 6U CubeSat standardized shape. The size of the body is of $36.6 \times 23.9 \times 11.6$ cm when the SPA is stowed and of $91.1 \times 36.6 \times 23.9$ cm when the solar panels are deployed. To radiate heat into space and passively control the internal satellite's temperature, the back side of the SPA and the Bus have been covered with a specific thermal paint. The reflection coefficients associated to the structure's surface with the thermal paint are collected in Table 2.1. The S/C wet mass at the launch epoch was of 13.261 kg.

Table 2.1: ArgoMoon surface reflection coefficients of the Bus and the SPA.

Component	Specular	Diffusive
Bus (Front/Back/Top/Bottom)	0.0	0.75 ± 0.02
SPA Front	0.23 ± 0.01	0.0
SPA Back	0.0	0.75 ± 0.02

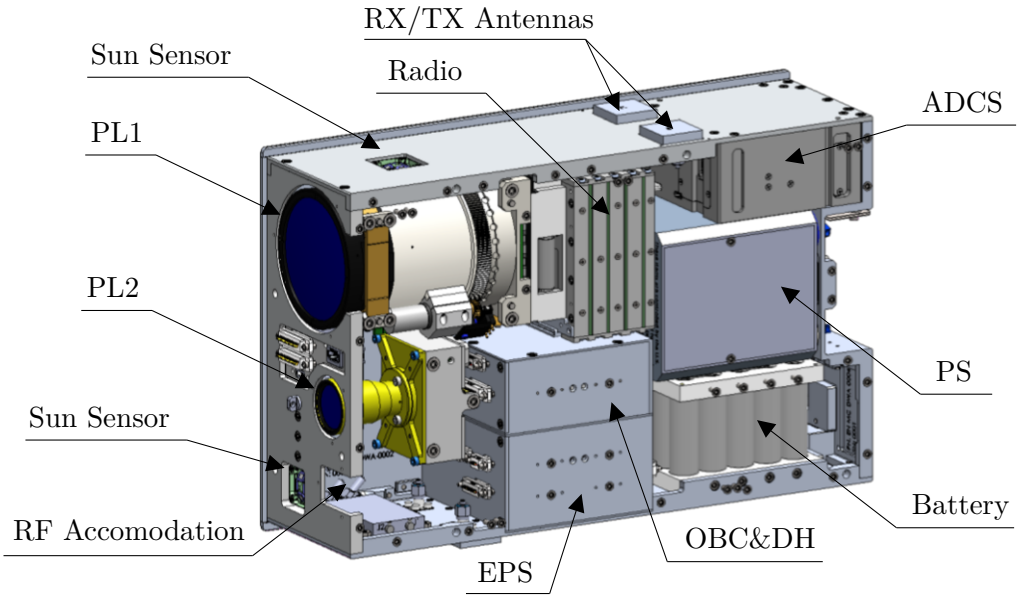

Figure 2.2: Interior rendering of the ArgoMoon CubeSat. Courtesy of Argotec.

Payload (PL) The ArgoMoon's PL is composed by two narrow and wide FOV optical cameras and a laser RF. The cameras are the core sensors used by the onboard IRS to recognize, track, and point different objects (i.e., the ICPS, Earth or Moon) lying in the FOV of the cameras (a detailed explanation of the IRS algorithm can be found on [66]). The narrow angle camera, named PL1, is characterized by a FOV of ±2.05 deg and its primary use is to capture high detailed pictures of the tracked target. The wide-angle camera, named PL2, has a FOV of ±32.5 deg and, since it can capture a bigger section of the sky, it is used to rapidly scan the space looking for the target to be tracked. The two optics have a total weight of 1.2 kg and occupy a volume of 1.5 U. The cameras technical specifications are summarized in Table 2.2. The RF is capable of measuring the distance from a target up to 5 km with an expected accuracy of 1 m. As well as the two cameras, the RF is exploited by the autonomous tracking algorithm to evaluate the distance from the tracked target.

Table 2.2: ArgoMoon cameras parameters.

Parameter	PL1	PL2
Focal Length	393.00 mm	22.42 mm
Diagonal FOV	±2.05 deg	±32.5 deg
Wavelength Range	450-700 mm	
F/N	5.2	4
Distortion	<1%	
Vignetting	<10%	
Relative illumination	<80%	>50%
Sensor	CMV12000	
Sensor's size	4096 × 3072	
Color filter	Bayer Filter	

Telemetry Tracking and Command (TT&C) The telecommunication subsystem of ArgoMoon is based on the miniaturized X-Band IRIS transponder of NASA/JPL [70]. The IRIS is a reconfigurable software-defined radio that has been designed for mission requiring to communicate with the NASA's DSN using X-band frequencies (1.2). The transponder is packed in a 1.2 kg package with a volume of 0.5 U and performs conventional uplink and downlink communications while supporting radiometric tracking with the DSN to deliver navigational products for precise OD. Then, the IRIS is connected to a Solid-State Power Amplifier (SSPA) and a Low Noise Amplifier (LNA) to provide the power and signal to the four patch antennas placed on two opposite sides of the ArgoMoon S/C (top and bottom faces). The TX antenna has a 3-dB beam-width of 80 deg with a gain of 7 dB where the RX one has 85 deg beam-width with a gain of 6.2 dB. The use of patched antennas allows to relax the constraints on the S/C pointing accuracy.

The ArgoMoon's transponder characterization performed on ground before the launch has provided a measurement of the average transponder delay of 6883.7 ± 30 ns. This information is fundamental for the OD since the transponder delay contributes to produce a bias on the range measurement. The measured transponder delay, if not properly considered, can produce a bias on the range measurements of 2.081 km.

Furthermore, during the characterization process, it has been that the IRIS is affected by a bias on the Doppler measurements. This bias was also already seen during the MarCO mission and it was safely managed by considering its value in the navigation filter [9]. The

total Doppler bias is expected to be originated by two different contributes:

- **Constant Doppler Bias**: it is originated from a quantization error which is a function of the uplink channel frequency and strictly related to the IRIS design methodology. The expected value for the ArgoMoon's IRIS was of -0.124 Hz. However, this bias is constant and it can be calculated and considered in the OD.
- **Varying Doppler Bias**: it is caused by a misconfigured turn-around ratio resulting in a scale-error which leads to a systematic, slowly varying bias if the scale-error is large. This contribute was expected to be smaller than the constant one and it has been assumed to be function of the IRIS internal temperature.

Moreover, the described constant Doppler bias was expected to be bigger at the power up of the radio. However, the use of a specific IRIS settings reset command named *POKE* allows to remove this bias falling back to the smaller one described above. Therefore, at each reboot of the IRIS radio a *POKE* command must be performed to correct this additional increment. The calculated Doppler bias that was expected to be present during the mission is then summarized in Table 2.3.

Table 2.3: ArgoMoon calculated Doppler bias characteristics.

Parameter	At IRIS power UP	After POKE command
Bias	+1.334 Hz	-0.124 Hz
Scale Error	6.53591×10^{-15} [Hz/Hz]	-1.45831×10^{-10} [Hz/Hz]

Propulsion System (PS) The PS of ArgoMoon is based on the VACCO's hybrid Micro Propulsion System (MiPS) based on a combined green mono-propellant (LMP-103S) and cold gas (R134a) propulsion system of 1.8 kg of mass and a volume of 1 U [71].

The main mono-propellant thruster is used for orbital maneuvering and it can provide up to 0.1 N of thrust with a specific impulse of 192 s. The thruster is capable of performing a single continuous maneuver with a duration up to 1000 s before requiring a cool-down period. However, the maximum duration of the single impulse has been limited to 800 s for safety reasons. The conservative cool-down period that has to be allocated between two continuous impulses is of 10 minutes. By considering that the maximum mass of ArgoMoon was of 14 kg, the maximum expected ΔV that the monopropellant thruster can provide to the S/C is 57 m/s.

The cold gas system, integrated together with the main engine, is used for attitude control and it is designed as four double-canted cold-gas thrusters with 0.057 N of nominal thrust. This PS is similar to the one used in the MarCO mission and, due to a leak experienced by the MarCO-B S/C during the execution of desaturation maneuvers, a particular attention has been paid to the estimation performance and robustness analyses about the maneuvers.

Attitude Determination and Control Subystem (ADCS) The attitude is determine and controlled with a 3-axis stabilization system equipped with a star tracker, sun sensors, an Inertial Measurement Unit (IMU), three Reaction Wheels (RWs), and a Reaction Control System (RCS). The IMU is used to support the reconstruction of the satellite's attitude when the star tracker cannot be used in case of S/C rotational speed greater than 2 deg/s) or when the Sun or Earth are inside the sensor's keep out zone. The

cold-gas system of the MiPS of the PS compose the RCS which is mainly used for the attitude control during the execution of an orbital maneuver or to perform a desaturation of the reaction wheels. In the case of ArgoMoon, the expected maximum spin rate of the RWs is 18 deg/s. The ADCS unit has a mass of 0.8 kg and a volume of 0.5 U where the expected pointing accuracy that the system should be able to ensure is of ±0.003 deg.

Electrical Power Subystem (EPS) The power generated by the SPA is collected by the EPS that manage the power demands from the other subsystems as well as the storing of the power in the battery pack. The maximum power that can be collected by the SPA during a full Sun exposition is of 80 W. The battery pack has a capacity of 120 Wh with a mass of 0.9 kg and a volume of approximately 0.7 U. The most power demanding operative mode is expected to be when the S/C is communicating with the Earth, both uplink and dowlink, producing a consumption of 57.3 W.

On-Board Computer and Data Handling (OBC&DH) The ArgoMoon S/C monitoring and control is performed by the flight core software that runs on the on-board computer. The interfaces between all the other subsystems take place in the OBC&DH as well as the persistent memory for storing all the S/C's data. This subsystem is responsible for the management of the telemetries and commands and it also hosts the autonomous navigation software based on the IRS.

2.3 Mission Timeline

In this section a description of the high-level ArgoMoon mission timeline is provided. The timing of events is provided relative to the generic launch date as the Artemis-1 mission has been shifted several times. The conceptual mission profile can be depicted from Figure 2.3, where summary of the relevant mission events timeline described in this section is reported in Table 2.4.

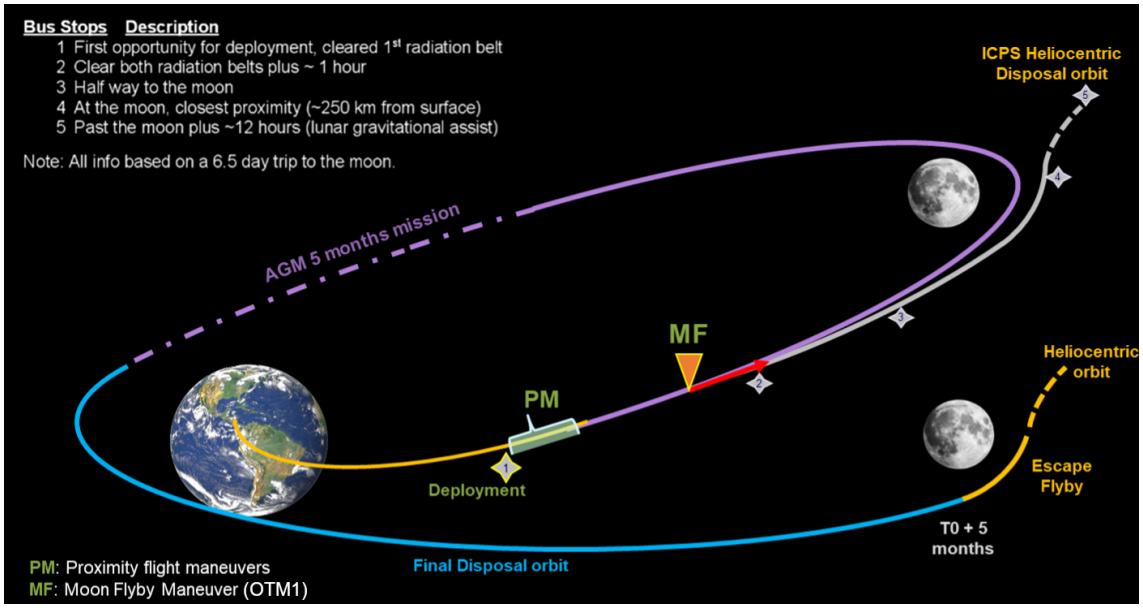

Figure 2.3: Scheme of the ArgoMoon conceptual mission profile. Courtesy of Argotec.

The launch of ArgoMoon in space has been performed by sharing a ride as one of the secondary CubeSat payloads of the SLS that carrying the Orion S/C for the Artemis-1 mission. The Artemis-1 mission timeline begins with the launch of SLS from Launch Pad 39B at NASA's Kennedy Space Center. After reaching the Earth's orbit, the ICPS provides the powerful thrust the payloads need to depart Earth's orbit and move toward the Moon. The former maneuver brings the Orion S/C and the secondary payloads into a trans-lunar trajectory with a fly-by of the Moon five days after the launch. Approximately 2 hours after the launch, Orion separates from the ICPS to continue the Artemis-1 mission towards the Moon. Then, at 3 hours and 48 minutes after the launch, the ICPS starts the countdown for the deployment of the CubeSats.

The mission of ArgoMoon begins at the moment in which the S/C leaves its dispenser mounted on the ICPS ring's adapter. ArgoMoon has been scheduled for the deployment at the BS1, approximately at 3 hours and 54 minutes after the launch. The mission has been subdivided into three main phases, each lasting a different amount of time. The Launch and Early Operations (LEOP) phase, named also Phase 1, lasts for the first day of flight and covers in particular the deployment, the automatic ProxOps close to the ICPS, and the first signal acquisition from the ground. Then, a Phase 2 begins once the first commanded orbital maneuver is performed to target the first fly-by of the Moon. This second mission's phase covers up to 20 days after the S/C deployment, and it is considered critical for the navigation since the quality of the fly-by characterize the resulting geocentric trajectory and the ΔV cost for the rest of the mission. Finally, the Phase 3 starts 20 days after the deployment, and it covers the rest of the mission. The disposal of the S/C is performed through a last fly-by of the Moon to enter into a graveyard heliocentric orbit.

2.3.1 Phase 1

At the moment in which ArgoMoon leaves the dispenser (T_D) the SPA are automatically deployed and the separation switches trigger the power drain to the EPS allowing the S/C to turning on its subsystems approximately in 10 seconds. In this phase the S/C follows the release path without activating the PS and the TT&C yet for safety reasons. The ICPS dispenser mechanism releases the ArgoMoon S/C with a resulting ΔV of 1.4 ± 0.07 m/s. However, the deployment direction is not exactly known since the ICPS is spinning.

At T_D+10 s, the ArgoMoon's systems are powered on and the ADCS can starts to recover the S/C's attitude. However, it has been expected that ArgoMoon may acquire a tumbling velocity probably around multiple axis due to the deployment event. The attitude reconstruction and the detumbling activity should require at least 1 minute to be performed, depending on the criticality of the tumbling motion. Then, the S/C perform a rotation of 180 deg using the RW in search of the ICPS using the two payload cameras and the IRS. The searching activity had to last at least 80 s to have the ICPS properly tracked and located inside the FOV of the cameras.

In the case that the release, boot up and ICPS tracking operations are performed nominally, ArgoMoon continues to follow its baseline ProxOps plan. Nominally, it has been planned to keep ArgoMoon on the side of the ICPS along the deployment direction in order to guarantee the capture of the desired pictures as well as to safely fly the S/C in the NASA's allowed region. In principle, to manage the aforementioned flight plan, the baseline ProxOps scenario foresees three PMs that are described in Table 2.4.

PM1 is performed to stop the drift of the S/C from the ICPS by using only the RCS thrusters since the mono-propellant orbital engine requires 15 minutes to be ready to operate. Then, once the main orbital engine has became ready to operate, the PM2 is performed to bring the S/C below the 500 m limit from the ICPS to start capturing

Table 2.4: ArgoMoon summary mission timeline with respect to the launch date.

Event	**Epoch**	**Details**
Launch	T_0	Epoch of the Artemis-1 launch
BS1 (T_{BS1})	$T_0 + 3$ hours 54 min	Begin of the first CubeSats dispensing phase
Deployment (T_D)	$T_{BS1} + 6$ min	Release of ArgoMoon from the ICPS
BS2 (T_{BS2})	$T_0 + 6$ hours 59 min	Begin of the last CubeSats dispensing phase observed by ArgoMoon
PM1	$T_D + 11$ min	Reduce the deployment induced drifting velocity with respect to the ICPS
PM2	$T_D + 23$ min	Counteract the drifting velocity to approach the ICPS
PM3 (KOZ)	$T_D + 75$ min	Drift away from the ICPS to remain outside the KOZ region
OTM1	$T_D + 20$ hours	Maneuver to trim the first fly-by of the Moon (M0)
M0	$T_D + 5.2$ days	First fly-by of the Moon
Pi $i = 0, \ldots, p-1$	N/A	Epoch of ArgoMoon's i-th perigee (with p as total number of perigees)
Ai $k = 0, \ldots, a-1$	N/A	Epoch of ArgoMoon's k-th apogee (with a as total number of perigees)
M$(n-1)$	$\sim T_D + 180$ days	Last fly-by of the Moon (with n number of total Moon encounters)
EOM	$\sim T_D + 200$ days	End of the mission (heliocentric disposal)

high-resolution pictures. The 500 m limit has been set in order to consider the PL2 camera resolution and the relative IRS performance. Finally, a KOZ maneuver should be performed in the opposite direction of the PM2 to make ArgoMoon drifting away from the ICPS.

The first acquisition of the S/C's signal has been planned to occur at 30 minutes after the deployment, when the S/C turns on the IRIS transponder. At that moment, the allocated 34 m antenna of DSN is pointing in the direction of the ICPS searching for the carrier of the ArgoMoon's signal. The research of the carrier signal is performed by the ground antenna through a series of four frequency sweeps requiring up to 20 minutes. After the locking of the S/C's carrier, the link is established and the S/C on-board time is updated. Then, after activating the start tracker and checking the status of all the other subsystems, the download of the acquired ICPS photos is performed. However, due to the 256 kbps downlink data rate limit, the download of the images may require several communication passes to complete.

The ProxOps are considered finished approximately at T_D+6 h, that is the time in which it is expected that the S/C will be too far away from the ICPS to acquire others visible pictures of the target. The profile of the S/C's distance with respect to the ICPS and the planned PMs of the baseline ProxOps scenario are reported in Figure **??**. Phase 1 ends approximately at 22 hours after the deployment, when ArgoMoon is ready to perform the first orbital maneuver before the fly-by of the Moon.

2.3.2 Phase 2

Phase 2 begins when the S/C is ready to perform the first commanded OTM, named OTM1. This maneuver has been planned to be executed not earlier than 22 hours after the deployment. The OTM1 is required to place ArgoMoon on the designed path toward the Moon. Approximately 5 days after the maneuver, the S/C performs the first fly-by of the Moon, identified as M0, with a Closest Approach (C/A) at an altitude lower than 10000 km. The correct execution of the M0 encounter is fundamental to maintain ArgoMoon in orbit around the Earth without escaping in a heliocentric orbit. Furthermore, during the M0 encounter ArgoMoon is flying close to the far side of the lunar surface while it is illuminated. Therefore, the opportunity to acquire high-resolution images of the Moon during this encounter event is of relevant importance for the mission's outcome.

Then, the M0 fly-by injects the S/C into a geocentric orbit whose first perigee occurs approximately 3 days after the previous encounter with the Moon. During Phase 2, ArgoMoon's flight activities are oriented towards capturing images of the Earth and the Moon, as well as intensively testing the S/C's subsystems and the operations, including navigation. Phase 2 ends 20 days after the beginning of the mission, approximately when the S/C completes half of his second revolution around the Earth.

2.3.3 Phase 3

Phase 3 starts after the end of the Phase 2, and lasts for the rest of the mission. This last phase encompasses most of the geocentric trajectory where also other distant encounters of the Moon may occur, depending on the launch date. In any case, these intermediate fly-bys are exploited as an additional opportunity for scientific observations of the Moon as well as for testing the S/C's payload. During the last week of the Phase 3, not earlier than 5 months after the deployment, a last fly-by of the Moon has been planned to inject ArgoMoon into a heliocentric orbit for its final disposal. Finally, the EOM will occur when the S/C will reach the heliocentric orbit and the tracking activities will be terminated.

2.4 Reference Trajectory

The reference trajectory for the ArgoMoon mission has been developed with the intention of flying the S/C throughout the cis-lunar space. The design of the ArgoMoon's trajectory has been performed by Argotec using the **GMAT!** (**GMAT!**) software. The main requirements that driven the design were the duration of the mission, the disposal of the S/C at the EOM into a specific heliocentric orbit, and the opportunity to have several encounters with the Moon during the flight.

According to the Artemis-1 mission profile, the SLS already places the Orion S/C and the CubeSats in a translunar orbit with the aim of performing the M0 close encounter [72]. By taking advantage of this first fly-by, the ArgoMoon's geocentric trajectory has been optimized such that it would allow for a new encounter with the Moon after at least 5 months. Moreover, the designed baseline trajectory may had close intermediate encounters with the Moon or just only distant passes at the limit of the Moon's Sphere of Influence (SOI). This approach led to an highly elliptical geocentric orbit whose period is a fraction of the Moon's orbital period. However, such kind of orbit is very sensitive to the initial conditions due to the gravitational attractions of the Moon and the Sun.

For each Artemis-1 launch date provided by NASA in the period 2020-2022, a new slightly different ArgoMoon's reference trajectory was then computed. Furthermore, for each launch date there were at minimum two reference trajectories referred to the opening and closing times of the launch window. In any case, NASA has planned the launch windows to always provide compatible orbital geometries, making the translunar trajectory leg almost independent of the chosen launch date. The robustness of NASA's orbital insertion with respect to the launch date allowed to obtain compatible ArgoMoon's reference trajectories even for different launch dates.

The ArgoMoon's trajectory begins at T_D, Table 2.4, with an initial state vector equal to the one of the ICPS at that epoch. The ArgoMoon's exact initial state vector after the deployment cannot be fully characterized *a priori*. The reason behind this characterization problem is that the ICPS is uncontrollably spinning around its principal inertia axis before initiating the dispensing activities. The introduced deployment direction problem with all the related known quantities is represented in Figure 2.4. However, the dispersion of the ICPS with respect to the Earth at T_D, Table 2.5, is predominant with respect to the dispersion introduced by the unpredictable direction of deployment. Therefore, it was acceptable to discard the deployment dynamics and assume that the orbital injection vector of ArgoMoon is equal to that of ICPS.

Table 2.5: Orbital injection covariance (3-σ) of the ICPS in the Earth-RTN frame at T_D.

Axis	Radial	Transverse	Normal
Position (km)	30.0	60.0	15.0
Velocity (m/s)	2.1	2.7	4.2

The ProxOps activities have not been modeled in the design of the reference trajectory because the PMs cannot be computed before the launch as their direction and duration depends on the actual deployment direction and magnitude. However, the impact of the ProxOps on the initial trajectory dispersion is negligible when compared to the ICPS injection covariance of Table 2.5 as in the case of the deployment.

The trajectory design setup optimizes the last fly-by conditions while minimizing the ΔV cost of the OTM1. The admissible range for the conditions of the last fly-by originated from the disposal requirement. This requirement depends on the launch date and requires

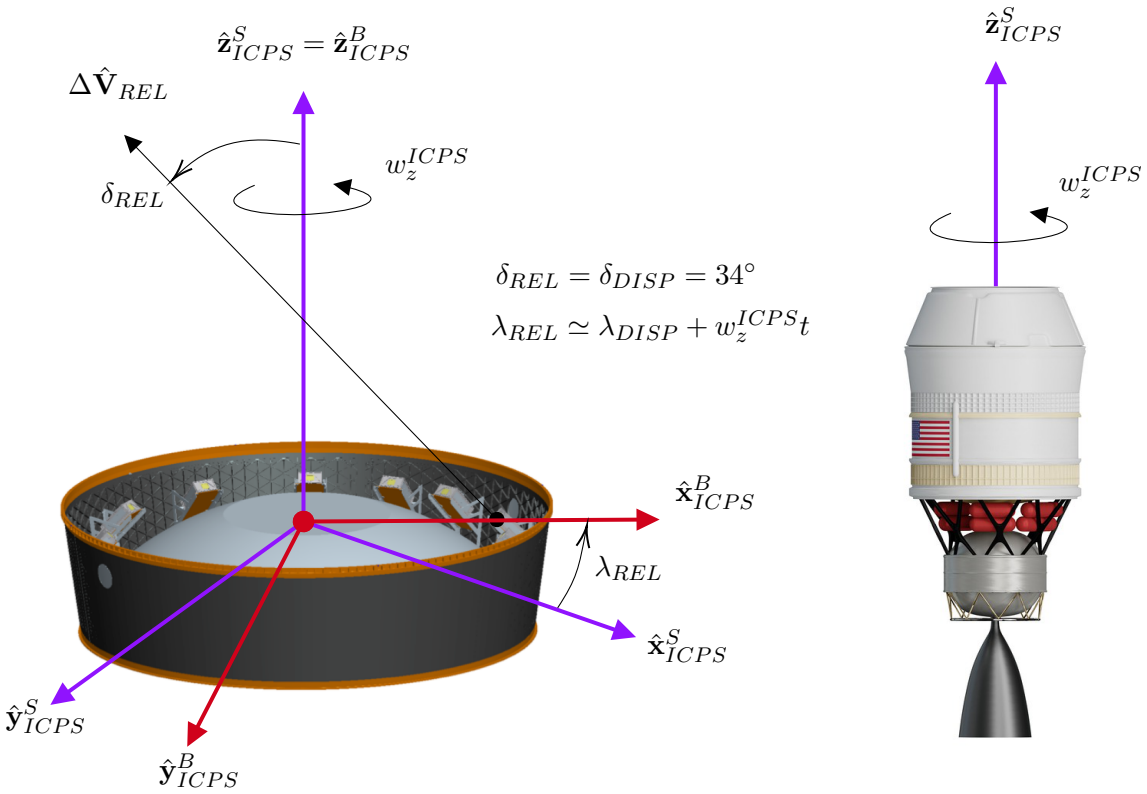

Figure 2.4: Representation of the ICPS secondary payloads deployment direction given the dispenser (DISP) location. The red frame identifies the ICPS body frame and the purple one is the ICPS non-spinning body frame.

having a heliocentric orbit with negligible probability of intersecting the Earth's SOI in the next 25 years. The OTM1 has been maintained fixed at $T_D + 22$ hours since it has been seen to be an optimal location as a compromise between ΔV cost and operational readiness time. In fact, the ΔV cost drastically increase by moving towards the fly-by making the OTM1 to be cheaper if moved back in time. However, it would be too risky or inconvenient for operational reasons to move the OTM1 too close to the ProxOps.

After the OTM1, the trajectory is purely ballistic and no other deterministic maneuvers are planned. However, as well described in the Chapter 4, the placement of the correction maneuvers must be carefully assessed to correct the errors that may affect the actual S/C trajectory.

The geocentric trajectory is composed by a slightly variable number of revolutions (REVs) around the Earth, depending on the launch date, where the perigees and apogees are identified using the capital letters P and A followed by an incremental number starting from 0 (i.e., P0 is the first perigee, A2 is the apogee of the second REV). A REV can be then defined as the trajectory's leg between two successive perigees (i.e., REVi goes from Pi to P$(i+1)$), except for the REV0 where the beginning of the leg coincides with the ICPS state at T_D. Moreover, an additional REVn (with n total number of REVs) identifies the trajectory's leg defined from the last perigee Pn up to the EOM.

The summary of the main characteristics, in particular the number of REVs and Moon's encounters, of all the ArgoMoon's reference trajectories can be depicted from Table 2.6. The plots in the XY plane of the Earth Mean Orbit at J2000 (EMO2000) frame of all the former trajectories are reported in Figure 2.5 and Figure 2.6. At the time

Table 2.6: Summary of the main characteristics of the ArgoMoon's reference trajectories computed for each opening launch windows dates. The Close Moon's Encounter (CME) is intended as a fly-by whose C/A is within the Moon's SOI radius (whose assume value is 66000 km).

Launch Date	**REVs**	**CMEs**	**Max. Apogee Range**	**Min. Perigee Range**
2020/06/28	12	4	1332659 km	38926 km
2021/11/23	11	2	1835965 km	25719 km
2021/12/21	11	3	1013660 km	30485 km
2022/02/12	10	2	1050266 km	38836 km
2022/03/12	9	2	1106835 km	38844 km
2022/06/06	10	2	1151622 km	37380 km
2022/08/03	12	3	967946 km	19548 km
2022/08/29	10	3	998029 km	32299 km
2022/09/02	10	3	866479 km	33786 km
2022/09/05	10	3	1053473 km	39251 km
2022/11/14	10	3	1147578 km	22030 km
2022/11/16	10	2	1080740 km	38841 km

of the navigation feasibility assessment described in the next chapters, the most recent reference trajectory was the one with launch on June 6, 2022.

The last released reference trajectory is the one corresponding to the actual ArgoMoon's launch on November 16, 2022. However, as can be seen from the trajectories plots and the characteristics summary, all the solutions have a similar number of REVs and Moon's encounters. The reference trajectory used in the analysis is the one with launch on 2022/06/06 and it has a total number of 10 REVs, two close encounters with the Moon (M0 and M3), and two distant encounters with the Moon (M2 and M3) with C/A less than 90000 km.

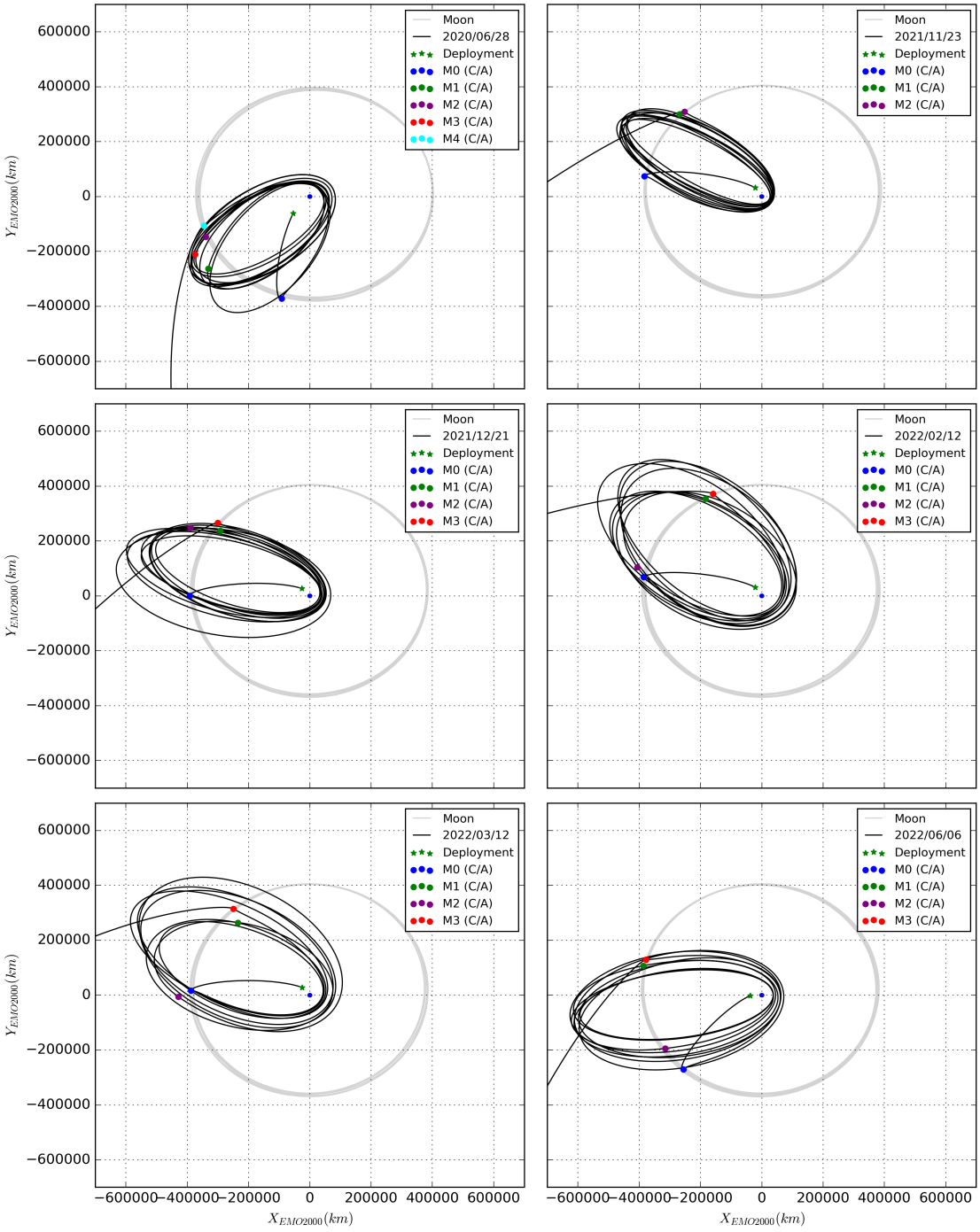

Figure 2.5: ArgoMoon reference trajectories plot in the XY plane of EMO2000 frame for each launch windows dates from 2020/06/28 to 2022/06/06. The colored dots (i.e., M0, M1, M2) identify the Moon encounters within 1.5 times the Moon's SOI radius.

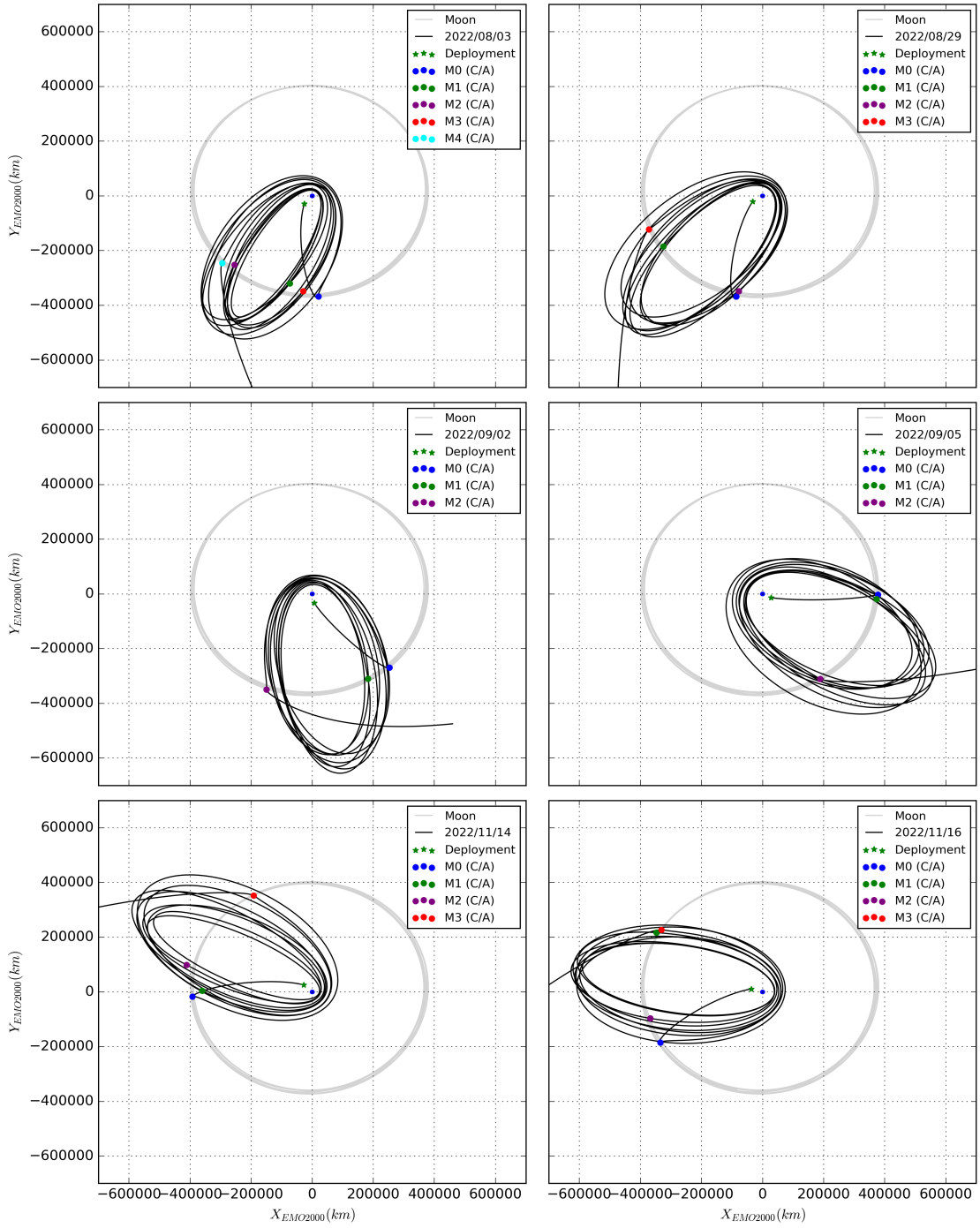

Figure 2.6: ArgoMoon reference trajectories plot in the XY plane of EMO2000 frame for each launch windows dates from 2022/08/03 to 2022/11/16. The colored dots (i.e., M0, M1, M2) identify the Moon encounters within 1.5 times the Moon's SOI radius.

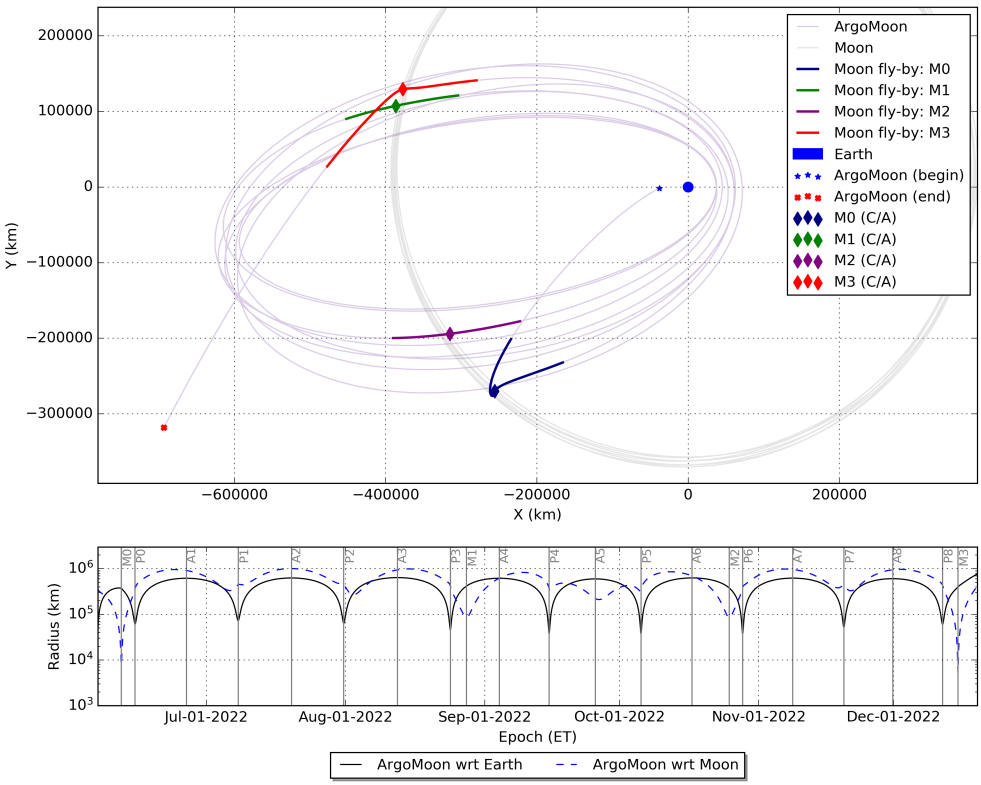

Figure 2.7: ArgoMoon reference trajectory with launch on 2022/06/06 in the XY plane of EMO2000 frame, and the distance of the S/C with respect to the Earth and the Moon. The Moon encounters within 1.5 times the Moon's SOI radius are identified by the colored arcs, while the C/A of the fly-bys are identified with the colored diamonds.

Chapter 3

Navigation Design

Contents

3.1 Concept

The navigation strategy of ArgoMoon has been designed on the basis of the typical techniques adopted in the deep space navigation of the regular probes that travel through the Solar System. Deep space navigation cannot be easily automated due to the complex dynamical environment in which the S/C operates. Therefore, the navigation process is performed from the Earth by a specific team, namely the navigation team, using a dedicated navigation software. ArgoMoon's navigation is ground-based, and, as described in Section 1.3, is subdivided into OD and FPC, as it is done in the regular deep space missions. In this section an introduction to the principal characteristics of the ArgoMoon's navigation system is provided.

3.1.1 Objectives and Procedures

The main objectives of the ArgoMoon's OD are the routinely reconstruction and prediction of the S/C's trajectory, the characterization of the performance of the PS and RCS, and

the production of a covariance study report after the delivery of an orbital solution. After acquiring the observables of the S/C, each navigation operator performs the reconstruction and prediction of the trajectory allowing to have independent solutions. The comparison of the different independent orbital solutions is then performed during the acceptance phase allowing an evaluation of the robustness of the consolidated solution. The OD products, which contain the best estimate of the S/C trajectory, are used in the FPC process to compute the trajectory correction maneuvers required to follow the planned path.

The main objectives of the ArgoMoon's FPC are the computation ot the correction maneuvers necessary to make the S/C follow the designated path, and the re-optimization of the trajectory if the mission requirements cannot be satisfied with the actual solution. Usually, the main sources of errors affecting the S/C trajectory are the launcher performance, the S/C thrusters' performance, the dynamical mis-modelling, and the OD errors. As a result of the non-deterministic nature of the former sources of errors, the corrective maneuvers are purely statistical and cannot be compute *a priori* before the beginning of the mission. Thus, the ArgoMoon's orbital maneuvers have been distinguished into OTMs and Statistical Trim Maneuverss (STMs). As seen before, an OTM is a deterministic maneuver that has been computed *a priori* by the mission analysis in the design of the reference trajectory. On the other side, a STM is an orbital maneuver scheduled before launch through the navigation analysis, whose nominal ΔV is zero, and the real value can only be computed during the operations.

The trajectory estimated by the OD and is also used to update the on-board S/C ephemeris and used by the DSN to properly point the antennas. Finally, the STM computed during the FPC are processed by the MCC operators and converted into telecommands for the S/C. The entire process have a duration that cannot be exactly determine since it depends on the quality of the data, on the problems affect the S/C and his trajectory, and on the human factor. Therefore, between the beginning of the OD process and the delivery of the FPC products for correcting the trajectory, a conservative amount of time is allocated. The epoch at which the collection of data is stopped to start the process is usually called DCO and it is described in Section 3.1.3.

Finally, the ArgoMoon navigation is performed by the dividing the trajectory into single arcs, encompassing a single REV, to be processed sequentially. The sequential process consists into considering only the most recent OD solution at the beginning of a new REV ignoring all the data before that time (whose information should be already contained in the selected *a priori* OD solution). Then, each mission's REV should have several intermediate coarse OD solutions, theoretically one for each increment of the observables dataset, and just several consolidated solutions corresponding to the computed STMs. The navigation system, the pre-launch analysis, and the operations have been designed and performed using the NASA/JPL's navigation software MONTE.

3.1.2 Observations

The main observables implemented in the OD of ArgoMoon are two-way coherent Doppler and two-way range, and one-way Doppler. The acquisition of the radiometric observables is performed by the DSN using the Deep Space Stations (DSSs) with dish diameters of 34 m [73, 68]. The DSN antenna complexes are located in Madrid (Spain), Goldstone (California, United States), and Canberra (Australia), for a total of 16 DSSs. The tracking of the S/C is a process that is performed in parallel with the downlink/uplink activity at each communication pass, or *tracking pass*. Thus, whenever a link is established between the ground station and the satellite, navigational observables are also obtained. The ArgoMoon's tracking passes schedule has been designed by means of a dedicated agreement

between DSN and ASI. Doppler accuracy level achievable using the IRIS transponder by tracking from the DSN antennas is expected to be in the order of 0.1 mm/s, at 60 s integration time [40, 74]. The radiometric data are then corrected for the path delay due to the Earth's troposphere and ionosphere using standard GNSS-based calibrations provided by the DSN [48].

3.1.3 Data Cut-Offs (DCOs)

The ArgoMoon's navigation routine foresees to nominally perform the OD process after each tracking pass, when a new data set is available. However, the consolidation and delivery of an OD solution is performed only after a DCO, which is identified as the epoch of the last measurement of the dataset used in the analysis. The DCOs are used as checkpoints to end the data collection for the start of a precise and reliable reconstruction procedure. Therefore, all the observables acquired after a DCO will not be considered for the solution delivered at that time. Usually, the DCOs are placed in strategic epochs of the mission with the aim of maximize the dataset size for the OD and the operational time before the delivery deadline. In the case of ArgoMoon, the DCOs placement rationale consists into having a new consolidated navigation solution, thus a new DCO, in correspondence of the following cases:

- Computation of a new scheduled STM.
- Update of the trajectory to guarantee the proper pointing of the ground antenna.
- Contingency events concerning also the navigation.

The DCOs should nominally be at 4 days prior the event's epoch to provide the a conservative amount of time for the operations [75]. However, in certain moments of the mission, the operations timeline may be too compressed to fulfill the former requirement. Therefore, in these cases the DCO should be at minimum 1 day prior the event to provide sufficient time for executing the whole navigation process and, in the case of a maneuver, generate and validate the telecommands to send to the S/C.

3.2 Requirements

As stated in Chapter 2, the primary goals of the mission are to safely fly ArgoMoon around the ICPS in order to gather comprehensive visual data of the upper stage, thoroughly test the CubeSat platform, and dispose of the S/C in heliocentric orbit at the EOM. Without directly involving the navigation team, the ArgoMoon autonomous flight control algorithm will primarily guarantee the ProxOps and the picture acquisition around the ICPS. Furthermore, there are no other specific requirements for the remaining portion of the mission. Therefore, a series of Navigation Requirements (NAVREQs) were identified with the aim of guaranteeing the navigability of the designed reference trajectory.

The following outlines the four OD and FPC related requirements that have been identified during the design process:

- **NAVREQ-1 Impact Avoidance**: the S/C shall not fly below the threshold altitudes of 1000 km with respect to the Earth and 100 km with respect to the Moon. The criterion is applicable throughout the whole mission and might be important during perigees and Moon's encounters. The requirement should be satisfied by also including the 3-σ uncertainty associated with the trajectory estimated by the OD.

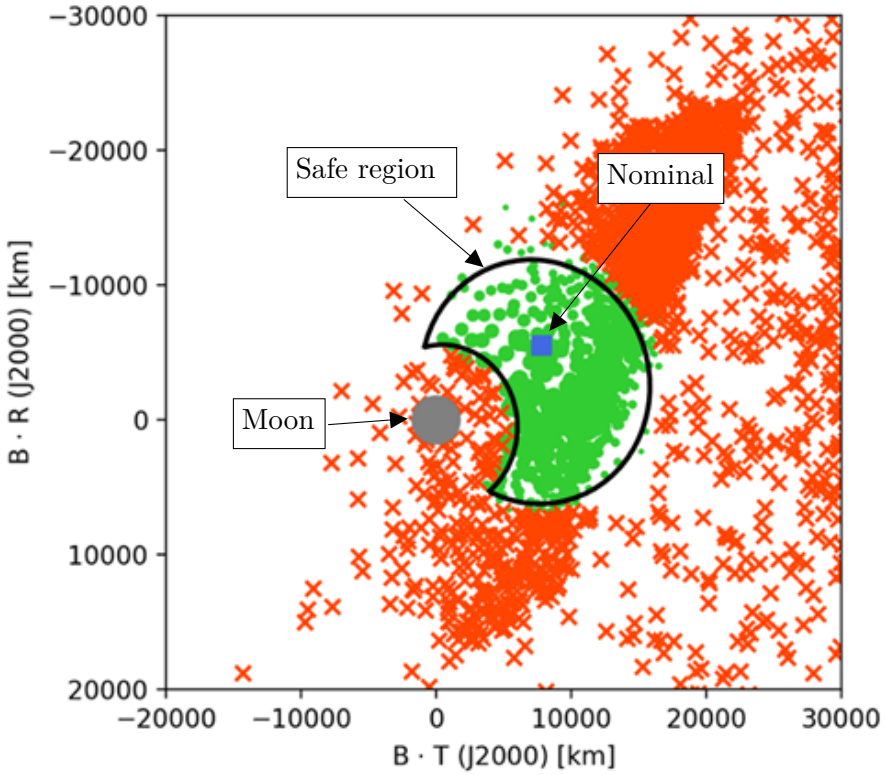

Figure 3.1: B-plane (Appendix A) admissible region for the last Moon's encounter of the trajectory with launch on June 6, 2022.

- **NAVREQ-2 Heliocentric Disposal**: the S/C shall be able to reach the heliocentric disposal orbit by exploiting the last fly-by of the Moon a couple of weeks before the EOM. With the criteria of having a low probability of crossing the Earth's SOI in the following years, the tolerance limits for the disposal were established by the mission analysis team through a Monte Carlo study for each new launch date. The requirement is represented as a region of confidence for the B-plane coordinates $(B.T, B.R)$, Appendix A, associated to the last encounter with the Moon. The disposal requirement relative to the most recent reference trajectory at the time of the navigation analysis is reported in Figure 3.1. The green dots are the samples with a correct disposal and the red crosses are the ones that do not satisfy the requirement.

- **NAVREQ-3 DSN Pointing Requirement**: to ensure the link with the 34 m DSSs, the pointing uncertainty due to S/C's OD shall be lower than 0.031 deg, that corresponds to half of the Half Power Beam Width (HPBW) of the antenna at X-band [76]. During the first day of the mission, the pointing requirement is relaxed to 1.05 deg, which is half of the HPBW of the 1.2 m aided acquisition antenna mounted above the subreflector of the DSS-24, DSS-34, and DSS-54 [76].

- **NAVREQ-4 Maximum Maneuver Duration and Cool-Down**: a single continuous maneuver cannot be longer than 800 s (roughly corresponding to a ΔV of 6 m/sec) due to the technical specification of the ArgoMoon's PS as described in Section 2.2.1. Moreover, two contiguous maneuvers must be separated by a cool-down period of at least 10 minutes.

- **NAVREQ-5 Maximum** ΔV: the trajectory control through the whole mission must be performed without exceeding the 57 m/s allocated to the navigation.

All conditions must be met with a 3-sigma confidence level, or greater than 99% if the distribution is not Gaussian. The NAVREQ-1 and NAVREQ-2 concern the OD and FPC since the trajectory has to be properly determined and controlled to fulfill that requirements. In fact, in the event of loss of trajectory controllability due to failure of the S/C's PS, the two previous requirements cannot be satisfied. The NAVREQ-3 concerns only the OD activities since the pointing do not require the trajectory control but only the knowledge of the S/C's position. Furthermore, due to the close range of ArgoMoon with respect to the Earth, NAVREQ-3 was expected to be the most critical requirement for the OD.

3.3 Tracking Schedule

The communication between the S/C and the ground is not performed continuously due to the power budget of the S/C and the time availability of the DSN allocated to each flying probe. The time interval in which the S/C is in view of a DSS, and the tracking is performed, is called tracking pass. Usually, the radiometric observables are acquired in almost all the passes in which the S/C establishes a link with a ground station. The DSN, as well as any other network of deep space antennas on the Earth, has to organize the tracking time of each managed mission by considering the maximum network capacity [77]. Therefore, each mission whose satellite is tracked by the DSN has its own agreement and tracking schedule planned before the launch. Tracking of new S/Cs without affecting the ones already tracked is major challenge since the scheduling process depends on peer-to-peer negotiation for modifications, with multiple iterations [78].

The definition of the mission tracking time is an iterative process that starts from an initial high-level proposal which is then analyzed and optimized by the navigation team. Through this step, the navigation team identifies the critical tracking passes that must be guaranteed (i.e., tracking during an orbital maneuver) and evaluate the optimal distribution of the tracking time for the navigation operations. Then, after several iterations between the navigation team, other mission's teams, and the DSN, a final optimized tracking schedule is consolidated. The actual schedule used for the operations is confirmed by the DSN a few days before the beginning of the mission. This final schedule will be compliant with the designed one but tailored by the DSN to fit it into the global schedule of all the other tracked missions.

The ArgoMoon DSN agreement initially foresaw two main time allocations: four hours per day for the first days of the mission (Phase 1 and Phase 2) and maximum four hours per week for the rest of the mission (Phase 3). Based on this high-level agreement, a distribution of the allocated tracking time into several passes was performed to better cover the trajectory. Nevertheless, the subdivision was maintained to a minimal number of passes necessary to capture the essential events such as a Moon fly-by, an orbital maneuver, and the DCOs epochs. The major drawback in the design of the ArgoMoon's tracking schedule was the potential overlapping of the first day's activities with 8 of the other CubeSats released by the ICPS. As introduced before, the tracking schedule described in this section should be considered as a baseline configuration since the DSN can limit or increase the actual tracking time.

During the first day after the CubeSats deployment, the DSN allocated one 34-m DSS per complex to track the ICPS and the deployed CubeSats. The 34-m DSS can provide

uplink to only one S/C at a time, while the downlink can be simultaneously performed up to four S/Cs lying in the same antenna's HPBW using the Multi-Spacecraft Per Antenna (MSPA) configuration [79]. In that way, the schedule complexity can be drastically reduced from the telemetry acquisition point of view. Conversely, the ArgoMoon's navigation relies on two-way tracking data, which means both uplink and downlink signals are required. Therefore, it was initially proposed by the DSN to have continuous MSPA downlink during the first mission's pass, and 30 minutes of two-way tracking per CubeSat at each pass during the first day. At the time of the navigation feasibility assessment, the tracking schedule of ArgoMoon foresaw 30 minutes of two-way tracking time per pass during the Phase 1 (ignoring the downlink one-way data that are not considered for the ArgoMoon's navigation). However, in the last months before the launch, the ArgoMoon's two-way tracking time was extended up to 2 hours per pass thanks to a reorganization of the CubeSats activities of the first day of Artemis-1. To further increase the tracking time during the first hours after the CubeSats deployment, the DSN and JPL proposed the use of differenced one-way Doppler observables, also called Interferometric Narrowband Spacecraft (INS) tracking data [80]. This kind of observable is evaluated by computing the difference between one-way Doppler observables acquired simultaneously by two DSN stations that are tracking the same S/C. The accuracy of the INS is greater than the one-way Doppler and it can provide much earlier trajectory accuracy improvement after the launch. Anyway, this measurement requires to have the S/C in view of two stations from two different DSN complexes on the Earth. However, INS tracking was only proposed as a support for the first hours of the operations and it was not officially confirmed to be available, therefore it was not considered for the ArgoMoon's navigation strategy.

The tracking schedule during Phase 2 consists of two tracking passes per day of two hours each. These two passes are conveniently placed in the morning and the other in the evening (European time) to support the navigation team's shifts. In correspondence of the launch tentative of December 2021, the DSN expected a drastic reduction of the ArgoMoon tracking time of the first 7 days due to the overlapping with the NASA's flagship missions Psyche and James Webb Space Telescope. Even though the Artemis-1 and Psyche launch attempts of December 2021 have been scrubbed, the ArgoMoon's tracking time has been conservatively assumed to be a maximum of one hour per day for the entire REV0 to keep account for further potential overlapping with other missions.

The four hours of tracking available every week during Phase 3 have been distributed into two passes of two hours each. The rationale behind this decision is that it is better to have more observables distributed throughout the trajectory rather then concentrated in a short amount of time. To improve the coverage of critical events, the two tracking passes per week have then been strategically placed in correspondence of DCOs and STMs. In fact, it is fundamental for the navigation to have an orbital maneuver covered by a tracking pass in order to accurately reconstruct it. Therefore, each STM has to be performed during a tracking pass and 4 days before, at the DCO, another pass maximizes the data before initiating the OD process. The number of STMs and their positioning logic is described in detail in Section 4.2.

The described tracking schedule was then provided to DSN as baseline for the actual communication and navigation activities. The specification of the interface characteristics between the DSN, the S/C and the MCC is provided through a dedicated Operations Interface Control Document (OICD) [79]. However, a list of critical passes requiring an elevated support must be provided to DSN to prevent such passes from being lost in the event of a schedule variation. In the case of ArgoMoon, an L3 elevated support has been required for the tracking passes of the first day of the mission and in correspondence of

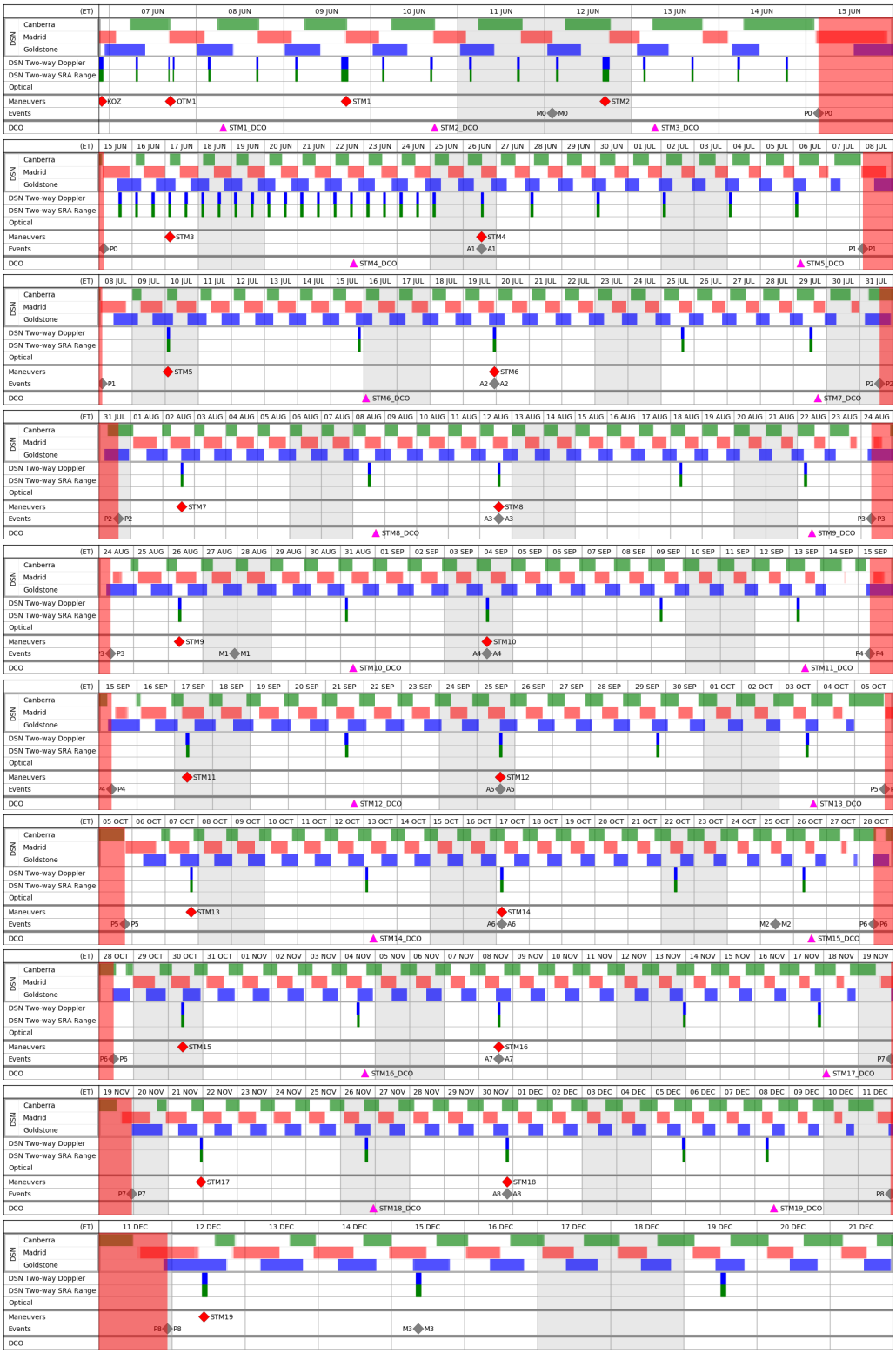

Figure 3.2: Designed tracking schedule and navigation timeline related to the launch on 2022/06/06. Each table is related to one single REV and it reports the DSN coverage on the first row, the scheduled tracking passes on the second and third row (Doppler and range data), the orbital maneuvers timeline on the fourth row, DCOs on the fifth row, and the fundamental trajectory events on the last row. The red bands identify the part of the timeline that does not belong to the REV.

the planned orbital maneuvers. The L3 passes receive real-time support by the DSN as well as a full redundant configuration [79].

The most recent nominal tracking schedule at the time of the feasibility assessment, that has been used also for the simulations described in Chapter 4, is the one related to the launch on June 6, 2022. A representation of the former timeline associated with the navigation activities is provided in Figure 3.2. As can be seen from the latter schedule, the tracking time is greatest during REV0 and half of REV1 in accordance with the high-level agreement, and is distributed such that a tracking pass always covers critical events such as maneuvers, DCOs and encounters. The location of the maneuvers and the DCOs is described in detail by Chapter 4.

3.4 Spacecraft Dynamical Model

The success of deep space navigation relies also on the proper definition of the S/C dynamical model. The dynamical model comes to play in the numerical integration of the participating bodies (i.e., the S/C, asteroids, satellites) when the OD and FPC are performed as well as in the trajectory re-optimization. As described in Section 1.3.1, if the developed dynamical model could perfectly describe the accelerations acting on the S/C, the OD would provide an almost exact reconstruction and estimation of the S/C trajectory. Therefore, the design of an high-fidelity dynamical model has been a fundamental part of the ArgoMoon navigation.

3.4.1 Accelerations Budget

In the implementation of the forces acting on the S/C, it is fundamental to take into account also the computational time and the complexity of the models. Taking all the possible forces into account in the model would be superfluous as many of them could be of very small magnitude and negligible if compared to the others. Moreover, as rule of thumb in the frame of the OD, given the smaller expected noise level of the considered observables, if an acceleration produces and effect on the trajectory that is lower than the noise level, then this acceleration may be negligible or less predominant for the navigation. In the case of ArgoMoon, the minimum noise expected on the Doppler (which is the observable carrying the most information about the S/C's accelerations) is 0.1 mm/s which corresponds to an order of magnitude of 10^{-13} km/s^2 if considered as minimum level in the acceleration observability.

The accelerations acting on the S/C that have been evaluated for the ArgoMoon's navigation model are the following:

- Newtonian gravitational point-mass acceleration due to the following bodies: Sun, Earth, Moon, the planetary systems, and Pluto.
- Newtonian gravitational acceleration due to the spherical harmonics of the following bodies:

  Earth: EIGEN-GL04C [81] model. Maximum degree and order: 20.

  Moon: GL0660B [82] model. Maximum degree and order: 20.
- Newtonian gravitational tides due to the Earth and the Moon.
- Relativistic perturbative accelerations due to Earth, Sun and Jupiter.
- Solar Radiation Pressure (SRP).

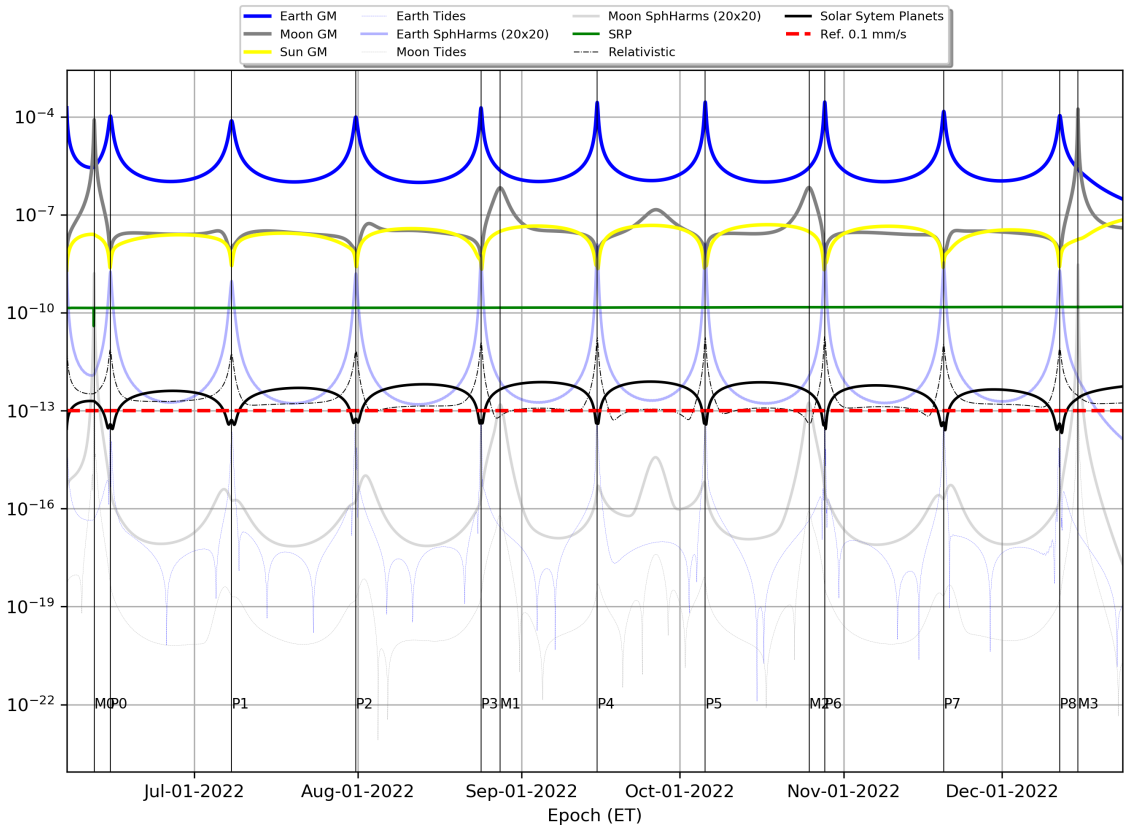

Figure 3.3: ArgoMoon's acceleration budget through the whole mission using the reference trajectory with launch on June 6, 2022.

The positions and masses of the point-mass bodies are retrieved from the JPL's planetary ephemerides DE430 [83]). The trajectory of the Earth and the Moon are not propagated since the JPL's ephemerides already provides very accurate information that cannot be improved by the ArgoMoon's orbital reconstruction.

The Figure 3.3 represents the ArgoMoon's acceleration budget through the whole mission based on the reference trajectory with launch on June 6, 2022. As described in Section 2.4, all the ArgoMoon's reference trajectories have compatible geometries and characteristics which make the previous acceleration budget valid for all of them. The major evidences obtained through the acceleration budget are the following:

- The predominant acceleration during the whole mission is the point-mass gravity due to the Earth.
- The point-mass gravity of the Moon becomes predominant during the closest approaches (encounters M0 and M3).
- The point-mass gravity accelerations due to the Moon and Sun are almost of the same order during the geocentric arcs.
- The SRP is the third predominant acceleration of the mission, as expected for small satellites such as CubeSats.
- The Newtonian gravitational acceleration due to the spherical harmonics of the Moon is greater than the Doppler noise reference only during the close encounters.

- The accelerations due to the Earth and Moon tides are the smallest and, even if they are included in the dynamical model, they may be irrelevant in the navigation. However they were included to be consistent with the adopted gravity models of Earth and Moon.

The evidence concerning the spherical harmonics of the Earth and the Moon allowed to limit the maximum degree and order to 20 drastically improving the computational time. However, this limitation had already been implemented following the suggestion provided by the European Cooperation for Space Standardization (ECSS) regarding missions in cis-lunar space [84]. Finally, the accelerations due to the Earth's atmosphere, primary and secondary albedo, thermal emissions and thermal recoil pressure are neglected due to their too low magnitude and consequently meaningless implementation from the point of view of the navigation process.

3.4.2 Accelerations Models

Newtonian Point Mass

The Newtonian Point Mass acceleration model that is derived from the Newton's universal law of gravitation. It consider the body that is exerting the gravitational force, called central body, as a point in the space with all the mass concentrated on it. The mathematical representation of the model is the following:

$$\mathbf{a}_{GM} = -\frac{GM}{r^3{}_s}\mathbf{r}_s \tag{3.1}$$

where $\mathbf{a}_g$ is the acceleration at the time t in the integration frame or reference, G is the gravitational constant, M is the mass of the central body, r_s is the distance from the central body to the spacecraft and $\mathbf{r}_s$ is the vector from the central body to the spacecraft in the integration coordinate frame.

Gravitational Potential

The gravitational acceleration exterted by a non spherical body is evaluated through the gradient of the body's gravitational potential U:

$$\mathbf{a}_U = \nabla U(\mathbf{r_s}) \tag{3.2}$$

The gravitational potential of an isolated body, with a generic shape and internal structure, can be described through the Poisson's integral

$$U(\mathbf{x}) = -\int_{R^3} \frac{G}{|\mathbf{x} - \mathbf{r}_{cg}|}\rho(\mathbf{r})dV \tag{3.3}$$

where $\mathbf{x}$ is the position with respect to the body's center of mass at which the potential is computed, $\rho(\mathbf{r})$ the density of the elementary volume, $\mathbf{r}_{cg}$ is the distance of the elementary volume element from the body's center of mass, and G is the gravitational constant. Since the gravitation potential must satisfy the Laplace's equation

$$\nabla^2 U = 0 \tag{3.4}$$

in any region exterior to the attracting mass, the potential is said to be an *harmonic function*. Then, the potential can be conveniently expanded, by considering $\mathbf{x} = \mathbf{r}$, where

$\mathbf{r}$ is the S/C position with respect to the body, in series of spherical harmonics of degree l and order m:

$$U(\mathbf{r}) = \frac{GM}{r}\left\{1 - \sum_{l=2}^{\infty}\sum_{m=0}^{l} P_{lm}(\sin\phi)\left(\frac{R}{r}\right)^{l}\left[C_{lm}\cos(m\lambda) + S_{lm}\sin(m\lambda)\right]\right\} \tag{3.5}$$

where M is the total mass of the body, $P_{lm}(sin\phi)$ are the un-normalized Legendre polynomials of degree l and order m, ϕ is the geocentric latitude, λ the longitude, R is the body's mean equatorial radius, r is the S/C distance from the body, C_{lm} and S_{lm} are the un-normalized spherical harmonics coefficients. Nonetheless, the spherical harmonics coefficients are frequently normalized as follows:

$$\bar{P}_{lm} = N_{lm}P_{lm} \quad S_{lm} = N_{lm}\bar{S}_{lm} \quad C_{lm} = N_{lm}\bar{C}_{lm}$$

where the normalization factor is

$$N_{lm} = \sqrt{(2-\delta_{m0})(2l+1)\frac{(l-m)!}{(l+m)!}}, \quad \text{with} \quad \delta_{m0} = \begin{cases} 1 & \text{if} \quad m = 0 \\ 0 & \text{if} \quad m \neq 0 \end{cases} \tag{3.6}$$

Gravitational Tides

The gravitational tide can be described as a force that stretches the body with respect to the center of mass due to the gradient of the gravitational field of another body. For instance, the tides on the Earth are raised due to the perturbation of the Moon and Sun.

The tidal potential is created by the presence of a secondary body and it changes the shape and mass distribution of the primary body. As a result, variations in the structure of the primary body result in variations in the gravitational potential previously described. Thereafter, the tides are modeled as a time varying corrections of the normalized spherical harmonics coefficients of the perturbed body. The spherical harmonics corrections due to the tides mode are modeled following the International Earth Rotation and Reference Systems Service (IERS) formalism [85]:

$$\Delta\bar{J}_n = -\frac{k_{l0}^{r}}{2l+1}\sum_{j}\left[\frac{GM_j}{GM}\left(\frac{R}{r_j}\right)^{l+1}\bar{P}_{lo}(u_j)\right] \tag{3.7}$$

$$\Delta\bar{C}_{nm} - i\bar{S}_{nm} = \frac{k_{lm}}{2l+1}\sum_{j}\left[\frac{GM_j}{GM}\left(\frac{R}{r_j}\right)^{l+1}\bar{P}_{lm}(u_j)(s_j - it_j)^m\right] \tag{3.8}$$

where M is the mass of the perturbed body, M_j is the mass of the perturbing body, R is the mean equatorial radius of the perturbed body, r_j is the distance between the two bodies, and

$$k_{lm} = k_{lm}^{r} + ik_{lm}^{i} \tag{3.9}$$

are the Love numbers of degree l and order m. The Love numbers are parameters that characterize the overall elasticity of the body under the effect of the tidal forces [86].

In the ArgoMoon case, the Love numbers used for the tides mode correction of the Earth and Moon spherical harmonics are reported in the Table 3.1.

Table 3.1: Love numbers for the tides correction of the Earth and Moon spherical harmonics models [82][85].

l	m	Earth		Moon	
		k^r_{lm}	k^i_{lm}	k^r_{lm}	k^i_{lm}
2	0	0.3019	0.00000	0.02405	0.0000
2	1	0.2983	-0.00144	0.02405	0.00000
2	2	0.30102	-0.0013	0.02405	0.00000
3	0	0.093	0.00000	0.0089	0.00000
3	1	0.093	0.00000	0.0089	0.00000
3	2	0.093	0.00000	0.0089	0.00000
3	3	0.093	0.00000	0.0089	0.00000

Relativistic Perturbation

The relativistic perturbative acceleration of a body due to other bodies of the Solar System is computed using the Parameterized Post-Newtonian (PPN) metric, in particular with the parameters β and γ [87]. This method can be applied to the cases in which the gravitational fields are weak and produced by bodies that moving slowly with respect to the speed of light, as in the case of S/Cs, planets, moons, etc.

The relativistic perturbation is then modeled as an additional perturbative acceleration to be summed up with the Equation 3.1. The mathematical representation of the acceleration is the following:

$$\begin{aligned}\mathbf{a}_{\beta,\gamma} = -\sum_{j\neq i}\frac{\mu_j \mathbf{r}_{ij}}{r_{ij}^3}\Bigg\{ & -\frac{2\,(\beta+\gamma)}{c^2}\sum_{l\neq i}\frac{\mu_l}{r_{il}} - \frac{2\beta-1}{c^2}\sum_{k\neq j}\frac{\mu_k}{r_{ik}} + \gamma\left(\frac{\dot{s}_i}{c}\right)^2 \\ & +(1+\gamma)\left(\frac{\dot{s}_j}{c}\right)^2 - \frac{2(1+\gamma)}{c^2}\dot{\mathbf{r}}_i\cdot\dot{\mathbf{r}}_j - \frac{3}{2c^2}\left[\frac{\mathbf{r}_{ij}\cdot\dot{\mathbf{r}}_j}{r_{ij}}\right]^2 - \frac{1}{2c^2}(\mathbf{r}_{ij}\cdot\ddot{\mathbf{r}}_j)\Bigg\} \\ & + \frac{\mu_j}{r_{ij}^3}\left\{\mathbf{r}_{ij}\cdot[(2+2\gamma)\mathbf{r}_i - (1+2\gamma)\mathbf{r}_j]\right\}(\dot{\mathbf{r}}_i - \dot{\mathbf{r}}_j) + \frac{3+4\gamma}{2c^2}\sum_{j\neq i}\frac{\mu_j\ddot{\mathbf{r}}_k}{r_{ij}}\end{aligned} \tag{3.10}$$

where $\dot{s}_j^2 = \dot{\mathbf{r}}_j\cdot\dot{\mathbf{r}}_j$, c is the speed of light, and $\mathbf{r}_{ij} = \mathbf{r}_i - \mathbf{r}_j$ is the position of the perturbed body i with respect to the relativistic body j. The position, velocity and acceleration vectors of the participants i, j, k and l, as well as the gravitational constant $\mu = GM$ of a given body, are referred to the Solar-System barycentric frame of reference.

Solar Radiation Pressure

The SRP origins from the electromagnetic radiation coming from the Sun that impact on the S/C. It describes the momentum transferred per unit of time on a unit surface immersed in a radiation field. The resultant of the SRP force acting on the S/C Sun-exposed surface produces an acceleration on the center of mass that create an effective orbital perturbation. The implemented mathematical model of the SRP is defined as follows:

$$\mathbf{a}_{SRP} = \frac{SfC}{mr_{\odot}^2}\mathbf{F}_N \tag{3.11}$$

Table 3.2: ArgoMoon elementary parts and surface properties implemented in the dynamical model. The normal vector of each elements pointing outward the surface in the S/C body-fixed frame.

Component	**Area** (m^2)	**Orientation** (S/C Frame)	**Reflection Coefficients**	
			Specular	Diffusive
Bus Top	$W \times D = 0.038$	$[-1, 0, 0]$	0.0	0.75 ± 0.02
Bus Bottom	$W \times D = 0.038$	$[+1, 0, 0]$	0.0	0.75 ± 0.02
Bus Side (Y+)	$H \times D = 0.087$	$[0, +1, 0]$	0.0	0.75 ± 0.02
Bus Side (Y-)	$H \times D = 0.087$	$[0, -1, 0]$	0.0	0.75 ± 0.02
Bus Front	$W \times H = 0.025$	$[0, 0, +1]$	0.0	0.75 ± 0.02
Bus Back	$W \times H = 0.025$	$[0, 0, -1]$	0.0	0.75 ± 0.02
Solar Arrays Front	$2L_{SA} \times D = 0.286$	$[-1, 0, 0]$	0.0	0.23 ± 0.01
Solar Arrays Back	$2L_{SA} \times D = 0.286$	$[+1, 0, 0]$	0.0	0.75 ± 0.02

where f is the shadowing scale factor, S is a scaling factor [1], C is the solar flux at 1 AU, m is the mass of the S/C impacted by the solar radiation, $r_\odot$ is the distance between the S/C and the Sun, and $\mathbf{F}_N$ is the normalized force vector that depends on the geometry of the S/C. The vector $\mathbf{F}_N$ depends on the S/C's geometry and surface properties and it can be defined using the elementary flat plate approximation as

$$\begin{aligned} \mathbf{F}_N &= F_n \hat{\mathbf{u}}_n + F_r \hat{\mathbf{u}}_r \\ F_n &= -A \left[2\kappa_d \nu_d + 4\kappa_s \nu_s \cos(\alpha) \right] \cos(\alpha) \\ F_r &= -A \left[1 - 2\kappa_s \nu_s \right] \cos(\alpha) \end{aligned} \tag{3.12}$$

where A is the area of the surface exposed to the incoming radiation, $\hat{\mathbf{u}}_n$ is the unit vector normal to the surface, $\hat{\mathbf{u}}_r$ is the unit vector from the surface to the Sun, κ_d and κ_s are the diffuse and specular reflectivity degradation factors, ν_d and ν_s are the diffuse and specular reflectivity factors and α is the angle between the vectors $\hat{\mathbf{u}}_n$ and $\hat{\mathbf{u}}_r$. Then, the S/C's surface is approximated using elementary geometries, like plates or spheres, whose normal vector definition can be easily implemented. Therefore, Equation 3.11 and Equation 3.12 are computed for each S/C's component composing the total SRP acceleration.

3.4.3 Shape and Surface Properties

As seen in the previous section, the definition of the S/C's shape and surface properties is required for the computation of the accelerations due to the SRP. The ArgoMoon's shape was modeled as a collection of elementary plates each with his surface properties and orientation. The Figure 3.4 represents the basic shape of ArgoMoon and the body-fixed frame implemented in the dynamic model. The body-fixed frame has the z-axis pointing in the same direction of the ArgoMoon's cameras boresight, the x-axis points towards the bottom side of the S/C, and the y-axis completes the orthonorma frame. The geometrical and surface properties of each shape's elementary plates are reported in Table 3.2.

3.4.4 Orbital Maneuvers

The orbital maneuvers performed by the S/C, both OTMs and STMs, were implemented using both the impulsive and the finite models. The impulsive burn model was used

[1] Nominally $S = 1$ but it is estimated in the OD to account for geometrical mis-modelling.

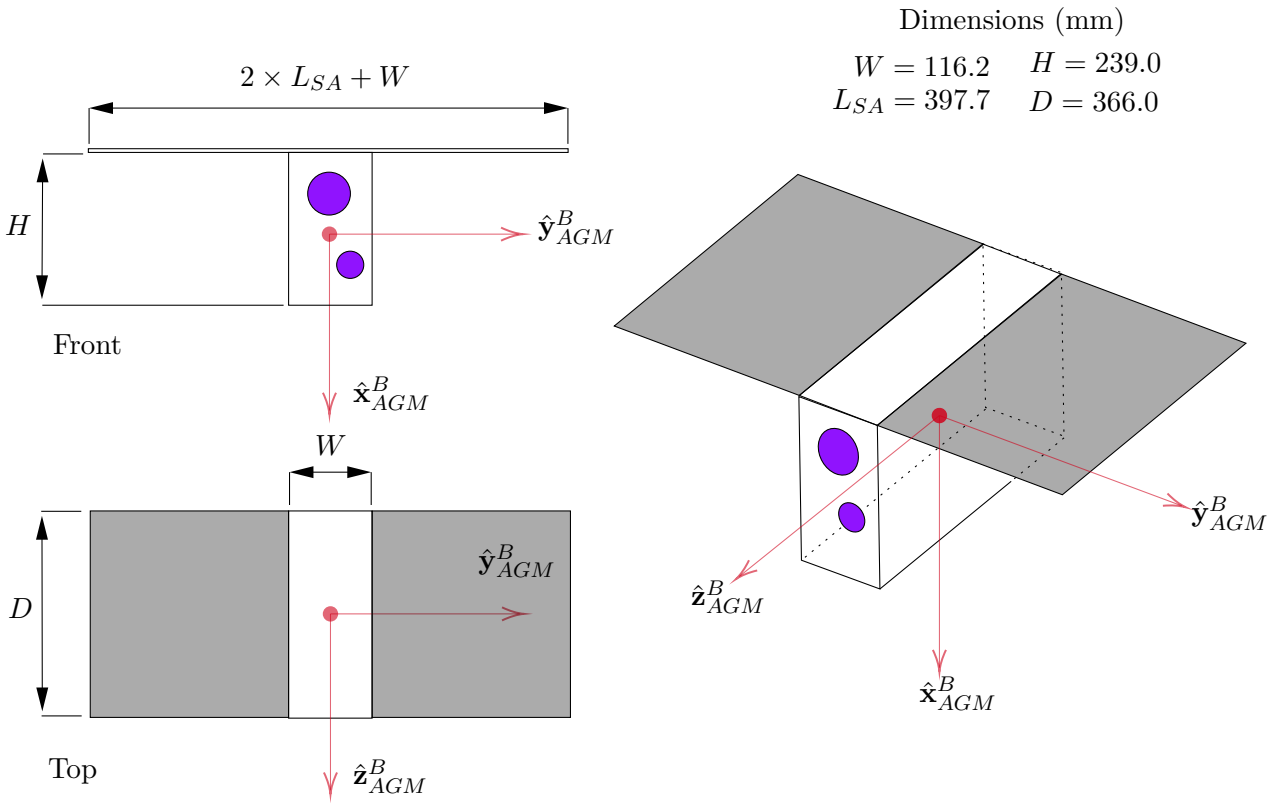

Figure 3.4: ArgoMoon simplified shape and body-fixed used in the navigation high-fidelity dynamical model.

during the analysis phase and it is modeled as an instantaneous change in the S/C's orbital velocity. The model is the following:

$$\Delta\mathbf{V}_I = R_f^I \Delta\mathbf{V}_f = R_f^I S \begin{bmatrix} \Delta V_x \\ \Delta V_y \\ \Delta V_z \end{bmatrix}_f \tag{3.13}$$

where R_f^I is the rotation matrix from the maneuver's frame to the integration frame, and S is a an overall velocity scaling factor. The variation in the S/C mass after the execution of the impulsive burn is computed as

$$\Delta m = m(t) \left(1 - e^{\frac{-|\Delta\mathbf{V}_f|}{I_{sp}g}} \right) \tag{3.14}$$

where $m(t)$ is the mass of the S/C at the burn epoch, I_{sp} is the engine specific impulse, and g is the gravitational acceleration at the Earth's surface.

The finite burn model has been used during the operations, in particular in the FPC for the delivery of the computed burns to be converted into telecommands for the S/C. The finite burn is implemented as acceleration defined as

$$\mathbf{a}_I^B(t) = R_f^I \left(\frac{D_c \mathbf{F}_f(t)}{m(t)} \right) \tag{3.15}$$

where $\mathbf{a}_I^B$ is the inertial acceleration due to the maneuver, $\mathbf{F}_f(t)$ is the force model associated with the thruster, D_c is the maneuver's duty cycle (whose value is in between 0 and

1). The variation in the S/C mass is obtained through

$$\frac{\partial m}{\partial t} = D_c \frac{F(t)}{I_{sp} g} \tag{3.16}$$

which is the mass flow of the maneuver at the time t with $F(t)$ as the magnitude of the force model of Equation 3.15. The force model can be implemented as a polynomial whose coefficients are initially taken from a pre-launch characterization of the engine.

In the case of ArgoMoon, the I_{sp} has been set to 192 s for the main engine and 46 s for the RCS. For the finite maneuvers model a constant force profile has been chosen. The main engine constant force has been set to 0.1 N and 0.177 N for the RCS. The former values have been provided by the MiPS constructor after the pre-launch tests performed on ground.

3.4.5 Stochastic Accelerations

To account for unmodeled accelerations or mismodelling, the addition of stochastic accelerations is usually performed. In the context of the OD, the stochastic parameters are treated as piecewise constant within discrete time intervals called batches. The stochastic accelerations are considered null by default but they are free to change in an uncorrelated way at each batch interval. The way in which their value changes depends on the associated covariance and result of the filtering process. Based on the duration of the batch intervals, the stochastic accelerations tends to absorb the signatures on the residuals that cannot be fitted with the assumed dynamical model. For instance, unpredictable events like the leakage of a thruster or the outgassing usually occur for a finite time interval and then cease and reappear at a later time. Therefore, the use of accelerations that can change differently at each batch interval allow the identification of such events [88].

In the case of ArgoMoon, the stochastic accelerations have been modeled as 8 hours time-batched white random noise with a standard deviation of 10^{-11} km/s^2. The assumed standard deviation corresponds to 20 times the ones observed in the reconstruction of the complete Cassini's trajectory [89]. However, during the navigation operations the stochastic accelerations batch time and noise can been conveniently changed in function of the quality of the data and the observed problems.

3.5 Reference Trajectory Re-optimization

Usually, in the design of the reference trajectory, the mission analysis team use his own software, dynamical model and integration scheme that may be different from the ones used by the navigation team. Therefore, when a new reference trajectory is provided, the navigation team reintegrates it compare the differences between them. Typically, errors between the two trajectories are present and, based on the entity of such errors, a proper correction has to be performed to avoid waste of propellant during the navigation [90]. For instance, the navigation team could perform a constrained re-optimization of the reference trajectory using the navigation high-fidelity model. Nonetheless, the two trajectories will always have differences provided that the mission and navigation requirements remain fulfilled.

3.5.1 Dynamical Model Differences

The ArgoMoon's reference trajectory was designed by the Argotec's mission analysis team using a dedicated software. Since the beginning of the design activities, critical differences

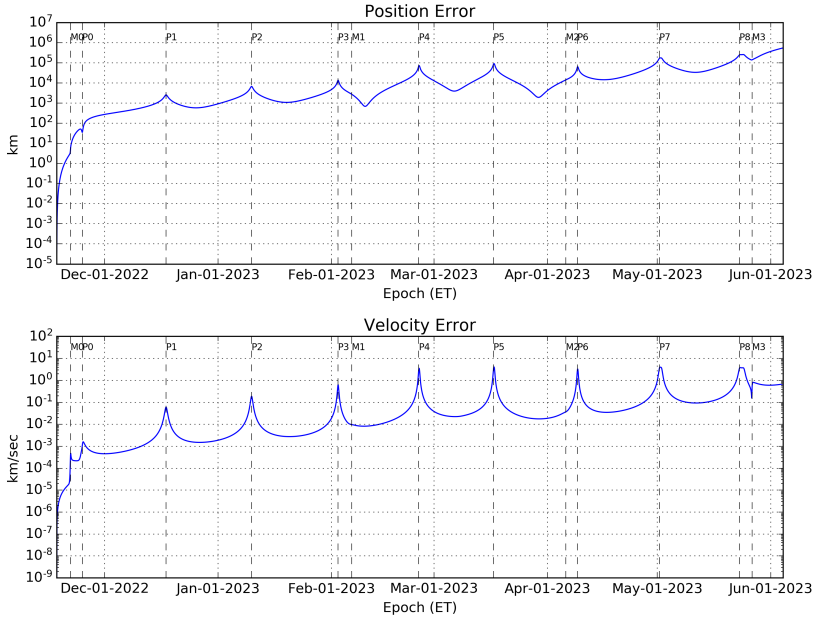

Figure 3.5: Trajectory differences between mission design and navigation for the last reference trajectory before the actual launch on November 16, 2022.

were seen between the software used by the navigation team, MONTE, and the one used by the mission analysis team. As first iteration, the differences between the two dynamical models have been smoothed out by using the same extended body gravity fields, ephemeris, planet masses, and similar integration schemes. However, models like the S/C's shape, the relativistic perturbation and the space time were differently implemented in the two software making difficult the matching of the reference trajectories. For instance, in the software used by Argotec the S/C's shape can be represented by using the simple cannonball model or by using the Solar Pressure and Aerodynamic Drag (SPAD) model [91]. The latter model has been developed internally by the Goddard Space Flight Center (GSFC) and it describes the SRP acting on a S/C by exploiting a pre-computed table of normalized force vectors. On the contrary, as seen in the previous section, MONTE adopt the elementary geometries collection for the computation of the SRP. Therefore, in that case, the two dynamical models of mission analysis and navigation were different and cannot be configured in the same way. Moreover, differently from MONTE, the software of the mission analysis team does not perform the change of the center of integration when the S/C moves between different SOIs and only one spherical harmonics field can be used at a time. The differences between mission design and navigation for the last reference trajectory before the actual launch are reported in Figure 3.5. As can be seen from the former plots, the high-fidelity trajectory computed with MONTE tends to diverge from the reference one. Therefore, an assessment of the ΔV cost to correct these differences shall be performed.

Nonetheless, as described in Section 2.4, the ArgoMoon's reference trajectory is very sensitive to the initial conditions and small perturbations as expected for a three-body problem. As a result, relevant errors occur in the end part of the trajectory reintegrated with the high fidelity navigation model due to the differences with the mission analysis software. In any case, precisely because the sensitivity to small perturbations, small corrections to the OTM1 and the first fly-by would sufficient to remove the errors.

3.5.2 Re-optimization Method

To correct the errors due to the differences between the mission analysis and navigation software a re-optimization of the reference trajectory is performed using the navigation high-fidelity model. The re-optimization of the ArgoMoon reference trajectory consisted into correct the OTM1 and the first fly-by of the Moon to exactly match the mission analysis' trajectory at the last encounter of the Moon at the EOM. Usually, further constraints and requirements are imposed but in the case of ArgoMoon the unique trajectory-related requirement was to guarantee the disposal of the S/C after the last fly-by. Therefore, it was not an issue if the mission analysis and navigation trajectories were slightly different in between the beginning of the mission and the last Moon's encounter.

The re-optimization of the trajectory was performed by using the Computer Optimization System for Multiple Independent Courses (COSMIC) tool of MONTE together with the SNOPT optimization algorithm. The COSMIC tool allows the user an intuitive timeline of maneuvers, Control Points (CPs) and Break Points (BPs) to describe the trajectory optimization problem. This timeline is then used by COSMIC to define controls and constraints as well as the cost of the optimization. Based on the requirement of having an exact match of the state at the last encounter with the Moon, the re-optimization timeline was then structured as follows:

- **CP0**: S/C injection state taken from the reference trajectory provided by the mission analysis team. This point is fixed meaning that it is not controlled by the optimization algorithm as it corresponds to the S/C orbital injection which, in the case of ArgoMoon, is not controllable. From this control point a forward trajectory propagation departs to BP1.

- **OTM1**: impulsive burn controlled in direction and magnitude and fixed in time. As for the initial state, the first guess value comes together with the reference trajectory provided by the mission analysis. This maneuver is maintained fixed in time as its location was constrained by the operations schedule and the mission analysis.

- **BP1**: first trajectory continuity constraint, both in position and velocity, placed two days before the encounter M0.

- **CP1**: S/C state at the C/A of the encounter M0. From this point a backward trajectory propagation depart to BP1 and forward propagation to BP2. The optimization algorithm controls all the six components of the state using the B-plane coordinates.

- **BP2**: second trajectory continuity constraint, both in position and velocity, placed at two days before the last fly-by of the Moon.

- **CP2**: S/C state at the C/A of the last encounter with the Moon. To satisfy the mission and navigation requirements, this control point has been configured to match the designed B-plane coordinates ($B.T, B.R, LTOF$) of the last fly-by. The other three coordinates, which are related to the orbital velocity and complete the definition of the CP2 state, are free to be controlled by the optimization algorithm. However, to maintain an acceptable disposal after the fly-by, these last three coordinates are bounded by a small range around their nominal value. Finally, from this control point a backward trajectory propagation depart to BP2 and forward propagation up to the EOM.

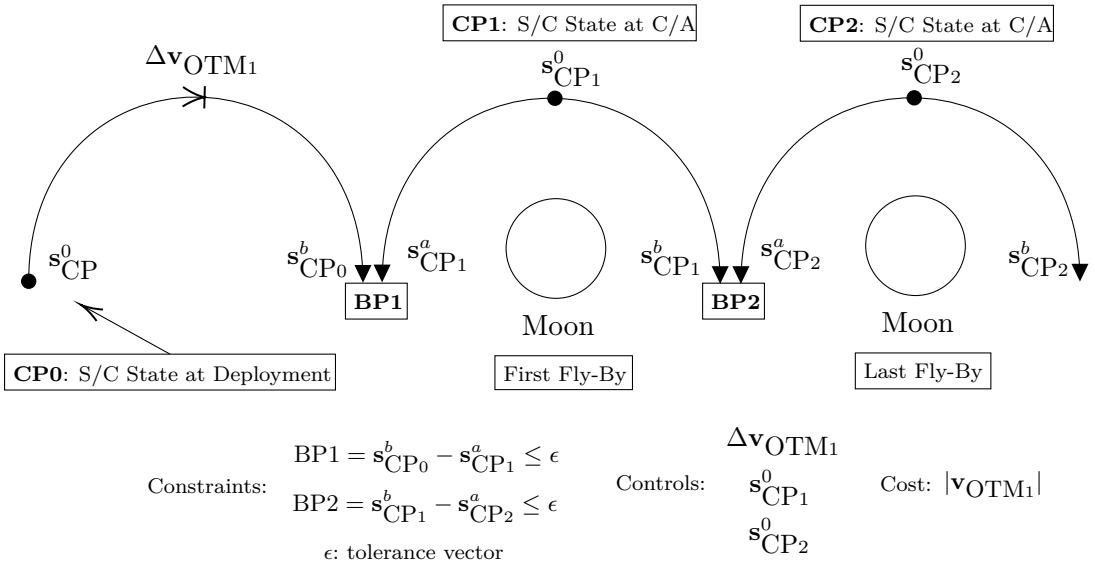

Figure 3.6: ArgoMoon reference trajectory re-optimization scheme implemented in COSMIC.

A schematic representation of the described re-optimization scheme is presented in Figure 3.6. The cost function for the minimization of the problem based on the previous timeline is the total ΔV of the OTM1. The vector of the controls is then composed by nine elements, the right ascension, declination and magnitude of the OTM1, and the six state coordinates of the M0 encounter. The constraints vector is composed by twelve elements that are the six state continuity errors at BP1 and the other six at BP2. Since the high-fidelity model is quite complex, the optimization may require several minutes before reaching convergence. Moreover, the convergence is not always guaranteed but depends on the configuration of the SNOPT solver and the scaling factors of controls and constraints. However, by carefully inspecting the results in case of failure, one may find that the algorithm tends to converge but the tolerances may were too tight. In the case of ArgoMoon tolerances of 10^{-3} km and 10^{-6} km/s were set for position and velocity on the break points, and they have been correctly satisfied by the optimized solutions.

The errors after the re-optimization for the last reference trajectory before the actual launch of November 16, 2022, are reported in Figure 3.7 . As can be seen from the former results, the errors are much lower than before the re-optimization and are below the imposed tolerances at the last Moon's encounter. As expected, due to the high sensitivity of the trajectory to the small perturbations, the ΔV of the OTM1 after the optimization remained close to the one of mission analysis, as can be seen from Table 3.3. In conclusion, these differences are a result of each teams own software and dynamical model, and produces an acceptable additional cost in the overall ΔV budget.

Table 3.3: Comparison between the OTM1 provided by the mission analysis and the one re-optimized using the navigation high-fidelity model, for the last reference trajectory related to the actual launch of November 16, 2022.

Maneuver Parameters	Mission Analysis	Re-optimization
Epoch	17-NOV-2022 12:00:17 UTC	
ΔV (m/s)	12.78	12.49
Right Ascension (RA) (deg)	207.34	204.45
Declination (DEC) (deg)	-9.12	-9.62

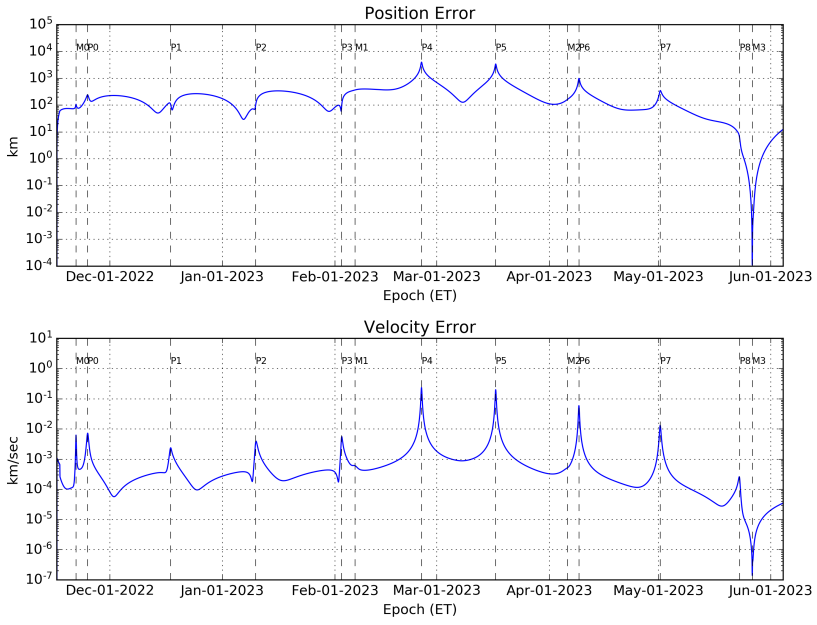

Figure 3.7: Trajectory differences after the re-optimization based on the navigation high-fidelity model of the reference trajectory for the actual launch of November 16, 2022.

Chapter 4

Navigation Simulations

Contents

4.1 Introduction

After the study and development of the ArgoMoon's navigation system, FPC and OD feasibility assessments were performed to evaluate the expected performance and the capability of met the navigation requirements with the conceptualized system. Firstly, the design of a trajectory control strategy was performed to identify the proper targets and maneuvers schedule to be used in the FPC. Then, multiple simulations were conducted to validate the developed FPC strategy and evaluate the feasibility in terms of total statistical ΔV cost.

The optimal maneuvers schedule obtained from the FPC analysis was used to consolidate the tracking schedule described in Section 3.3. After that, in-depth OD covariance analyses were carried out to quantify the expected formal uncertainties throughout the entire mission in order to verify the navigation requirements under various operational scenarios. Additionally, robustness analyses were carried out to examine the sensitivity of the OD to all key factors and to determine the most appropriate operations timeline for the mission.

The first section of this chapter provides a detailed description of the design and analysis of the FPC strategy. This section begins with an overview of the errors expected

to be relevant for the ArgoMoon trajectory dispersion and their evaluation through a a simulated uncontrolled trajectory dispersion.Then, an explanation of the methodology used to design the optimal control strategy and obtain the nominal STMs schedule is provided. Finally, the results of the FPC simulations based on the designed optimal control strategy are discussed.

The second section covers the entire OD analysis performed for the feasibility and performance assessment using the validated FPC strategy. As for the FPC analysis, the second section provides a technical discussion about the OD covariance analysis and the assumptions made for having a realistic but also conservative scenario of the ArgoMoon's OD. Then, the section is concluded by presenting the simulation results of the baseline OD scenario.

The last section of the chapter presents an overview of the conducted sensitivity analysis both for FPC and OD. The results discussed in at the end of this section allows to have a comprehension of the most relevant parameters expected to affect the performance of the ArgoMoon's navigation.

It is fundamental to point out that the analyses described in this section are related to the ArgoMoon reference trajectory with launch on June 6, 2022, as it was the most recent trajectory at the time of the feasibility assessment. However, all the analyses were also conducted for the trajectories before the latter one and the results were compatible proving the robustness of the developed navigation system. Therefore, the feasibility assessment results here described were still valid including the last reference trajectory delivered for the launch on November 16, 2022.

4.2 Flight Path Control

Evaluating the quantity of propellant required to correct the errors that can potentially impact the trajectory is necessary for determining whether navigation is feasible. The statistical errors must then be corrected using an optimal trajectory control strategy without exceeding the ΔV allocated to the navigation. The FPC analysis described in this section was performed with the aim of design a control strategy that significantly reduces the dispersion with respect to the reference trajectory while minimizing the number of maneuvers and the total required ΔV. The control strategy was a fundamental part in the design of the ArgoMoon navigation also because of its importance in the fulfillment of the navigation requirements.

4.2.1 Methodology

The study was initially conducted using a linear analysis to test different maneuvers schedule, aimpoints and targets' coordinates [92]. After the optimal solution was found, a non-linear analysis was performed to validate the trajectory dispersion as well as the ΔV. The linear method evaluates the dispersion and controllability of the selected targets using the covariance mapped to future times. The non-linear approach is based on the numerical propagation of the trajectory using the same high-fidelity model described in Section 3.4. Both simulations were performed using the Monte Carlo method, which samples from the covariances designed to describe the expected sources of errors. Each Monte Carlo was performed using a total number of 10000 samples which was ten times the minimum number of samples that was seen to be sufficient to characterize the statistics.

Following careful preliminary testing, it was discovered that both methodologies' results were consistent with negligible discrepancies except for the uncontrolled dispersion

that will be treated later. The consistency between the two methods allowed the linear approach to be validated and used to quickly and confidently analyze thousands of maneuver combinations, as well as aiming points and targeted coordinates.

The linear method was employed through the Linear Analysis of Maneuvers with Bounds and Inequality Constraints (LAMBIC) algorithm [93] (which is also directly integrated in MONTE) that has been used and validated in the FPC analysis of relevant deep space missions [52, 94, 95, 96]. Both linear and non-linear methods exploit the covariance propagation to simulate the dispersion on the trajectory due to the modeled sources of errors. A schematic representation of the linear covariance propagation for the statistical maneuvers analysis is provided in Figure 4.1. By considering a 6×6 covariance matrix P related to the 6 elements of S/C's state at the time t_0, the linear propagation of P to a time t is performed as

$$P(t_0|t) = \Phi(t_0, t)P(t_0|t_0)\Phi^T(t_0, t) \tag{4.1}$$

where

$$\Phi(t_0, t) = \frac{\partial \mathbf{x}(t)}{\partial \mathbf{x}(t_0)} \tag{4.2}$$

is the state-transition matrix defined as the partial derivatives of the state vector $\mathbf{x}$ at the time t with respect to the state vector at time t_0. The state-transition matrix is approximated to the first order leading to the linearization of the problem. The quantities and the scheme represented in Figure 4.1 are then described as follows:

- $P(t_0|t_0) = P_0$ is the initial covariance matrix representing the dispersion at the beginning of the propagation. The mapping of this covariance at the time t_0 is equal to the covariance matrix itself because $\Phi(t_0, t_0) = I$ where I is a 6×6 identity matrix.

- $\mathbf{x}_0$ is the initial state vector from which the propagation is performed towards the target. This state can be tough as the S/C state observed in a OD solution before the target.

- $P(t_0, t_T) = \Phi(t_0, t_T)P_0\Phi^T(t_0, t_T)$ is the initial covariance matrix propagated up to the target's time t_T. This covariance describes the uncontrolled trajectory dispersion at the target and it is useful to evaluate if the trajectory control is required or not.

- $P(t_{DCO}, t_T) = \Phi(t_{DCO}, t_T)P_{DCO}\Phi^T(t_{DCO}, t_T)$ is the covariance matrix at the maneuver's DCO mapped to the target's time t_T. The P_{DCO} is the estimated covariance matrix obtained by the OD solution at the time t_{DCO}.

- $P(t_T, t_T) = P_T$ is the actual covariance matrix that describe the trajectory dispersion at the target's time t_T after the application of the correction maneuver.

- $\Delta\mathbf{v}(t_B)$ is the computed maneuver's vector based on the difference between the observed random state vector $\mathbf{x}_{OD}$ and the desired one $\mathbf{x}_T$, both at the time t_T, plus the error sampled from $P(t|t)$. The maneuver's vector is computed at the maneuver's time t_B where the final ΔV magnitude is function of t_B.

- $\mathbf{q}_{err}$ is the maneuver's error vector which is function of the computed $\Delta\mathbf{v}$ vector.

- $\mathbf{x}_1$ is the actual S/C state at the target's time t_T after the entire propagation process. Then, the state $\mathbf{x}_1$ and the covariance P_T become the initial conditions for another analysis with respect to a downstream target after t_T.

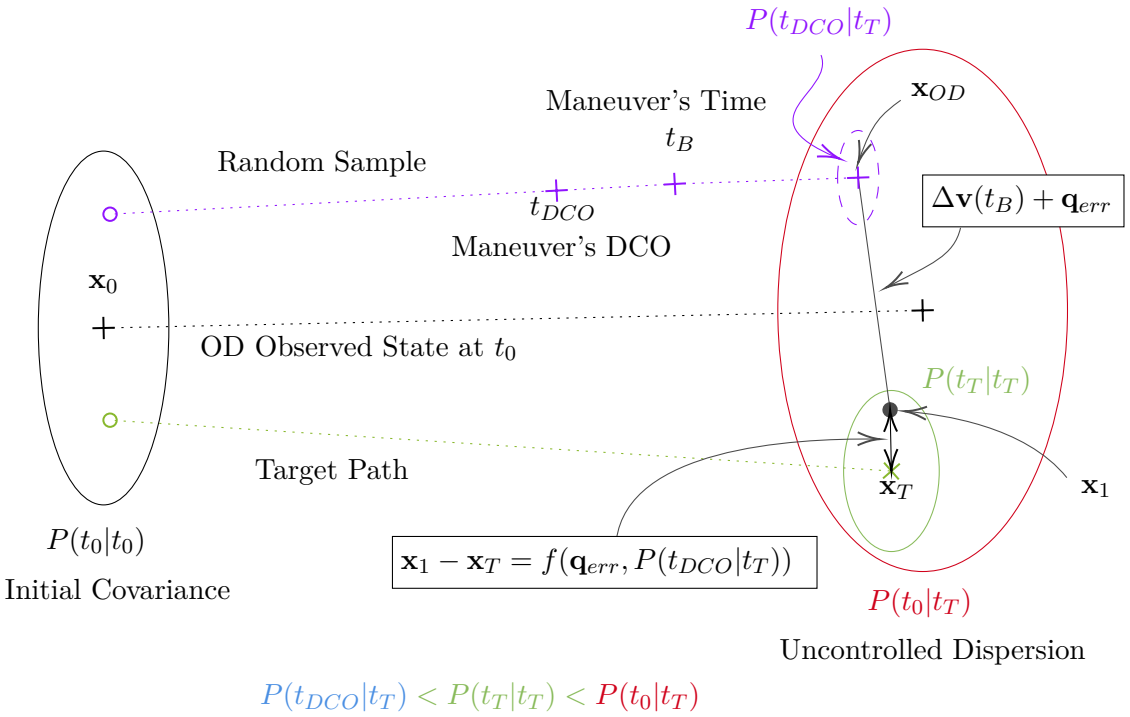

Figure 4.1: Representation of the statistical maneuvers analysis method based on the linear covariance propagation.

Typically, the described process is performed in a chain for each selected targets to which belong one or multiple planned maneuvers. Therefore, the results related to the downstream targets will depend on the maneuvers and dispersion of the previous ones.

The non-linear method simply exploits the covariances previously described to sample the errors used to perturb the numerical propagation of the single Monte Carlo sample. Moreover, in this method the maneuvers are computed using exactly the same approach as the operational FPC using a differential correction. However, the non-linear method was much slower than the linear one due to the higher computational time required by the high-fidelity propagation of each Monte Carlo sample. Therefore, the latter was used only to validate the strategy found using the linear method.

4.2.2 Errors Assumptions

The actual S/C trajectory can't be expected to be equal to the designed one since there are obvious uncertainties and errors in the assumed dynamics and initial conditions. For example, if a launcher deploys a S/C kilometers away from the expected position and with a slightly different velocity, the resulting trajectory will clearly not be the same as the reference one. This is a problem of uncertainty on the initial conditions that is derived from the performance of the launcher and the complexity of the ascent flight. This kind of uncertainty is described by the so called *injection covariance* that is usually provided by who designed the launcher and the ascent trajectory. Usually, the injection covariance is also employed in the OD as *a priori* uncertainty on the S/C initial state. Therefore, the uncertainties related to the S/C dynamics affects both the FPC the OD generating a statistical dispersion on the navigated trajectory.

In addition to the orbital injection covariance, the other relevant sources of errors considered in the ArgoMoon FPC analysis are the maneuvers execution error, the OD and

mis-modelling error. The error due to the execution of an orbital maneuver is derived from the uncertainty on the performance of the PS and ADCS. As a matter of fact, the S/C pointing during a maneuver is not perfect because it depends on the ADCS accuracy in reconstructing and controlling the attitude. Moreover, the ArgoMoon PS relies on a complex chemical system that cannot exactly generate the commanded ΔV. Consequently, these errors contribute into make orbital maneuvers that are actually different from the commanded one an then additional dispersion is generated on the S/C trajectory. The OD and mis-modelling error contribute to the dispersion since they affect the computation of the correction maneuver. In fact, during the operations it is evaluated whether or not to make a planned corrective maneuver on the basis of an OD solution. Therefore, since the OD solution is not exact and has a predicted uncertainty, the resulting trajectory retargeting will be inaccurate causing further dispersion in the execution of the orbital maneuver. The considered sources of error and the relative assumptions for the ArgoMoon FPC analysis are summarized in Table 4.1. The wide uncertainty on the SLS performance and ArgoMoon PS capabilities were expected to be the predominant sources of error.

Table 4.1: Trajectory statistical errors considered in the FPC analysis.

Error Source	**Model**	
Injection Covariance	ICPS state (Earth-RTN) uncertainty (3-σ) at disposal epoch:	
	Position (km)	30.0 / 60.0 / 15.0
	Velocity (m/s)	2.1 / 2.7 / 4.2
Maneuvers Execution	Gates Model applied to both OTMs and STMs.	
OD and Mis-Modelling	OD covariance mapped from the maneuver's DCO to the aimpoint.	

The described models are then implemented in the linear and non-linear method using the same approach. The dispersion on the S/C initial state is performed by sampling the position and velocity errors from the ICPS injection covariance. The maneuver's execution error is implemented using the Gates model [97] described in detail in the following paragraph. The OD error is simulated using the OD covariance mapped from the maneuver's DCO to the target's epoch to generate a randomly sampled error in the maneuver's target values. The mis-modelling is included in the OD error computation by estimating stochastic accelerations during the OD simulation.

Gates Error Model

The Gates execution error model generates randomly sampled execution errors for a specific commanded $\Delta\mathbf{v}$. Then, these generated errors can then be added to the commanded $\Delta\mathbf{v}$ to simulate the actual $\Delta\mathbf{v}_a$. For various maneuver magnitude ranges, different error statistics can be defined. The Gates model divides the execution error into two components: one parallel to the commanded $\Delta\mathbf{v}$ named magnitude error, and one called pointing error which is perpendicular to the $\Delta\mathbf{v}$ vector. These errors are further broken down into errors proportional to the ΔV and fixed errors independent of the maneuver size.

Let $\Delta\mathbf{v}$ be the commanded maneuver's vector with which the execution errors are to be generated. The Gates model compute the pointing error standard deviation as

$$\alpha = \sqrt{\sigma_\alpha^2 + \rho_\alpha^2 |\Delta \boldsymbol{v}|^2} \tag{4.3}$$

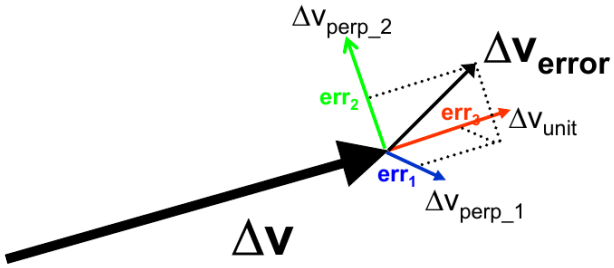

Figure 4.2: Schematic representation of the Gates error model. Source: Monte 149 help guide - JPL, Caltech.

and the one of the magnitude error as

$$\beta = \sqrt{\sigma_\beta^2 + \rho_\beta^2 |\Delta \boldsymbol{v}|^2} \tag{4.4}$$

where σ and ρ are the fixed and proportional magnitude error contribution of their subscript components. The error can be then expressed in a coordinate system with the z-axis aligned with the commanded $\Delta\mathbf{v}$ direction as presented in 4.2. Given three independent random realization ζ_1, ζ_2, and ζ_3, of a normal distribution $N(0,1)$, the maneuver error can be described as:

$$\boldsymbol{e} = \alpha \cdot \zeta_1 \cdot \hat{\boldsymbol{e}}_x + \alpha \cdot \zeta_2 \cdot \hat{\boldsymbol{e}}_y + \beta \cdot \zeta_3 \cdot \hat{\boldsymbol{e}}_z \tag{4.5}$$

being $\hat{\boldsymbol{e}}_z$ in the computed maneuver direction, $\hat{\boldsymbol{e}}_x$ and $\hat{\boldsymbol{e}}_y$ perpendicular to the computed maneuver. Therefore, the actual maneuver is simulated as $\Delta\mathbf{v}_a = \Delta\mathbf{v} + \boldsymbol{e}$ where the Gates error $\boldsymbol{e}$ is a representation of the $\mathbf{q}_{err}$ vector presented in Figure 4.1.

Usually, the standard deviations of the pointing and magnitude errors are empirically derived from the results of the PS characterization performed before launch. Later, during the actual flight, it may be possible to specialize the assumed Gates error parameters by analyzing the OD estimation results of the executed orbital maneuvers [97]. For the ArgoMoon mission, the assumed Gates error parameters (Table 4.2) were set to conservative values derived from a pre-launch analysis of the PS performed by the Argotec's engineers.

Table 4.2: Gates model assumptions for the maneuvers execution error (1σ coefficients).

		Error Component	ArgoMoon PS
Maneuvers Execution Error	Magnitude	Proportional (%)	3.5
		Fixed(m/s)	0.11
	Pointing	Proportional (deg)	1.1
		Fixed(m/s)	0.11

4.2.3 Uncontrolled Trajectory

Initially, a Monte Carlo analysis of the uncontrolled trajectory was performed to determine the trajectory's sensitivity to the initial conditions. Furthermore, the analysis enabled the evaluation of the Earth and Moon impact risks, as well as the heliocentric disposal capability, without performing any correction maneuvers.

Starting from the reference initial state, a total of 10000 trajectory samples were propagated with the high-fidelity model and perturbed using the assumed injection covariance.

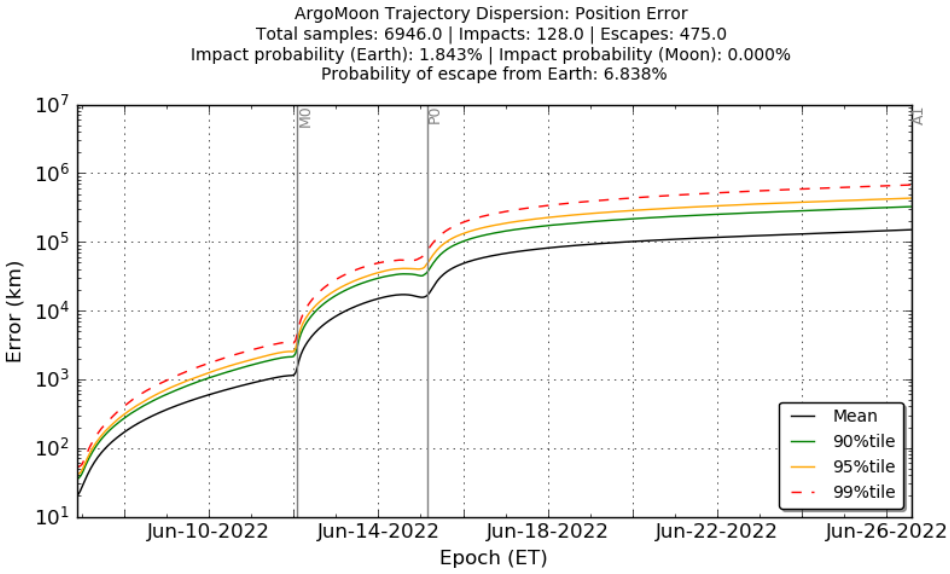

Figure 4.3: Statistics of the uncontrolled trajectory error with respect to the reference trajectory from the deployment up to the first apogee A1.

The OTM1 is then executed by adding the maneuver execution error, and the trajectory is propagated up to the EOM without any other correction maneuvers being simulated. To generate dispersion statistics, the position and velocity errors with respect to the reference trajectory are computed for each trajectory sample. The results in Figure 4.3 show the magnitude of the position error computed with respect to the nominal trajectory up to A1. Figure 4.4 reports the results of the trajectory dispersion mapped on the B-plane (Appendix A) of the fly-by M0. The plots have been limited only to the first relevant part of the mission due to the chaotic behavior of the solutions after P0.

After the closest encounters with the Moon (M0) and the Earth (P0), the initial error brought on by the injection covariance and the Orbit Trim Maneuver (OTM)1 execution error soon increases, and it then stays confined between 10^5 km and 10^6 km until the mission's end. The uncontrolled dispersion provided a probability of about 1.8% to fly below 1000 km of altitude with respect to the Earth, violating the NAVREQ-1. Moreover, due to the chaotic behavior of the propagated samples, the last fly-by with the Moon (M3) is never achieved. The trajectory is indeed particularly sensitive to the starting conditions, as expected for three-body issues, and the large dispersion after M0 is an indication that the mission's first fly-by is crucial. The Sun and the Moon's third body perturbations are actually more noticeable because of the geometry of the orbit, and as is well known for three-body problems, even a minor change in the initial conditions can result in a significantly different solution.

The B-plane dispersion shows that the linear method (dashed blue ellipse) and the non-linear one (red ellipse and scattered points) provides almost the same results. However, the non-linear dispersion after the first apogee A1 starts to diverge from the linear case meaning that the uncontrolled trajectory behaves fairly linear only during REV0 and part of REV1. As matter of fact, if the first Moon fly-by was skipped starting the dispersion one day after it, the differences between the linear and non-linear uncontrolled dispersions were negligible. This evidence can be expected from the fact that a cis-lunar orbit with an encounter with the Moon is highly non-linear by the very nature of the problem. Therefore, it was clear that the targeting analysis of the M0 encounter was the first fundamental step

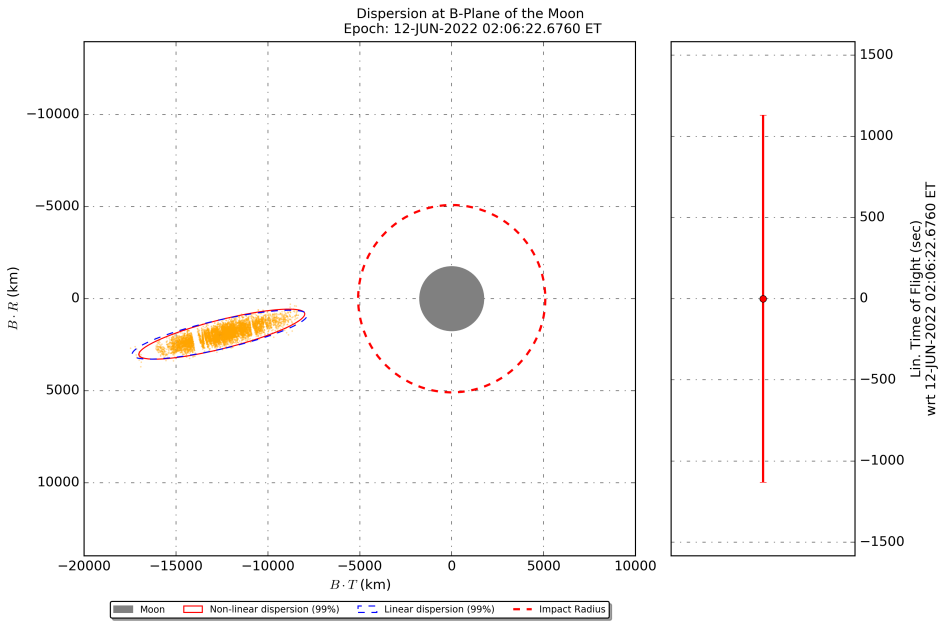

Figure 4.4: The 99$^{\text{th}}$ percentile of the trajectory dispersion on the B-plane of M0.

to proceed with the research of an optimal control strategy.

4.2.4 Optimal Control Strategy

The dispersion with regard to the reference trajectory must be reduced in order to meet the navigational requirements. This necessitated the search for a series of aimpoints to target via impulsive orbital maneuvers. The K-inverse method was used to evaluate the aimpoint selection and the location of the targeting maneuver [92]. As seen in Section 4.2.1, the state-transition matrix Φ plays an important role in the FPC since it can be used for mapping a perturbation of the state at the time t_0 to a different time t. Therefore, this matrix expresses the sensitivity of the state parameter to their variation along time, between two epochs. The K-inverse method exploits this characteristic of the state-transition matrix to evaluate the controllability of an aimpoint using a specific coordinate system. An orbital maneuver executed at a time t_B is effectively a variation of the three velocity components at that time. This variation in the orbital velocity produces a certain change in the state a next time $t_T > t_B$. Let's assume now that the state at the time t_T represents the aimpoint to target using the aforementioned orbital maneuver. Conceptually, the aimpoint state cannot be targeted in all its six components but only by a subset of three components as the number of components of the orbital maneuver. In that sense, the K matrix, which is the core of the K-method, is practically defined as a 3×3 block of the state-transition matrix, mapped to the aimpoint's epoch in the desired coordinate system, extracted as

$$K = \begin{bmatrix} \frac{\partial c_1(t_T)}{\partial \dot{x}(t)} & \frac{\partial c_1(t_T)}{\partial \dot{y}(t)} & \frac{\partial c_1(t_T)}{\partial \dot{z}(t)} \\ \frac{\partial c_2(t_T)}{\partial \dot{x}(t)} & \frac{\partial c_2(t_T)}{\partial \dot{y}(t)} & \frac{\partial c_2(t_T)}{\partial \dot{z}(t)} \\ \frac{\partial c_3(t_T)}{\partial \dot{x}(t)} & \frac{\partial c_3(t_T)}{\partial \dot{y}(t)} & \frac{\partial c_3(t_T)}{\partial \dot{z}(t)} \end{bmatrix} \tag{4.6}$$

where c_1, c_2, and c_3 are three targeted coordinates at the aimpoint epoch t_T and $\dot{x}(t)$, $\dot{y}(t)$, and $\dot{z}(t)$ are the S/C velocity components at an epoch $t < t_T$. Therefore, the K matrix represents the sensitivity of the targeted coordinates with respect to a change in the orbital velocity. Then, if $\Delta\mathbf{x}(t_T)$ represents a perturbation of the aimpoint coordinates c_1, c_2, and c_3, the variation in the acS/C velocity required to correct this perturbation can be computed by exploiting the inverse of K as follows:

$$\Delta\mathbf{v}(t) = K^{-1}\Delta\mathbf{x}(t_T). \tag{4.7}$$

As a result, finding the minimum of the K-inverse norm provides the optimal maneuver for minimizing the ΔV. Therefore, by recalling the quantities introduced in Section 4.2.1, the maneuver $\Delta\mathbf{v}(t_B)$ to correct the error at the target, assuming a realistic scenario with the OD in the loop, is computed as

$$\Delta\mathbf{v}(t_B) = K(t_T|t_B)^{-1}(\mathbf{x}_T - \mathbf{x}_{OD} + \Delta\mathbf{b}_{OD}). \tag{4.8}$$

where $\mathbf{b}_{OD}$ is a the OD error's vector sampled from the covariance matrix $P(t_{DCO}|t_T)$. The actual maneuver is then simulated by adding to the commanded vector $\Delta\mathbf{v}(t_B)$ the Gates error described before.

The use of this linear method has given the possibility to rapidly test many kinds of aimpoints and coordinates to be targeted, as well as the maneuver's location. To reduce the design space as much as possible, the fly-bys with the Moon (M0,M3) and the geocentric apoapses (A1, A2, ..., A8) were already considered as optimal aimpoints based on previous studies [92]. Moreover, the analysis of the uncontrolled trajectory was already providing a confirmation about the targeting of the fly-by of the Moon. Then, by performing the control of the first encounter M0, it was seen that the linearity after the fly-by was restored meaning that the analysis for the rest of the mission was widely supported by the linear method. In addition, to reduce the trajectory dispersion by improving the control on the S/C orbital velocity, the periapses (P1, P2, ..., P7) of the orbit around the Earth have been selected as further aimpoints.

As well documented from the experience of many deep space missions, the fly-bys with the Moon were targeted using the B-plane coordinates $(B.R, B.T, LTOF)$ whose detailed explanation is provided in Appendix A. The targeted coordinates of the apsides aimpoints are the cartesian position at the apogees and the cartesian velocity at the perigees. Then, to evaluate the location of the maneuvers targeting the chosen aimpoints, the K-inverse norm analysis was performed. Thus, given a fixed target downstream, the corresponding K-inverse norm can be rapidly calculated using Equation 4.7 at different times $t < t_T$. This produces a curve representing the evolution of the K-inverse norm, hence the ΔV order of magnitude, whose minimums are the optimal locations where to place a maneuver. In the case of the M0 encounter, the time interval in which the K-inverse norm was studied covered from the start of the mission up to the C/A of the fly-by. For the last Moon encounter M3, the time interval was from the penultimate perigee until the C/A of M3 as done for M0. For the geocentric apoapses and periapses, the chosen time interval covered the REV to which the aimpoint belong to (i.e., the K-inverse norm analysis for A1 was through the REV1). This last decision was based on the fact that two successive periapses or apoapses aimpoints are at most one REV apart. The Table 4.3 reports a summary of the selected aimpoints and targeted coordinates in particular for the reference trajectory with launch on June 6, 2022.

The K-inverse norm evolution for the fly-bys M0 and M3 are shown in Figure 4.5. Where the mission analysis team has positioned the OTM1 before M0 is about where the minimum of the norm is located. The norm then increases by approaching M0, making

Table 4.3: Selected aimpoints and targeted coordinates for the optimal control strategy applied to the reference trajectory with launch on June 6, 2022.

Aimpoints	Epochs	Target Coordinates		Center	Frame
M0	12-JUN-2022 02:06 UTC	B-plane		Moon	EME2000
M3	15-DEC-2022 08:55 UTC	B.T	km		
		B.R	km		
		LTOF	s		
P0 to P8	Perigees' epochs	Cartesian Velocity		Earth	EME2000
		VX	km/s		
		VY	km/s		
		VZ	km/s		
A1 to A8	Apogees' epochs	Cartesian Position		Earth	EME2000
		X	km		
		Y	km		
		Z	km		

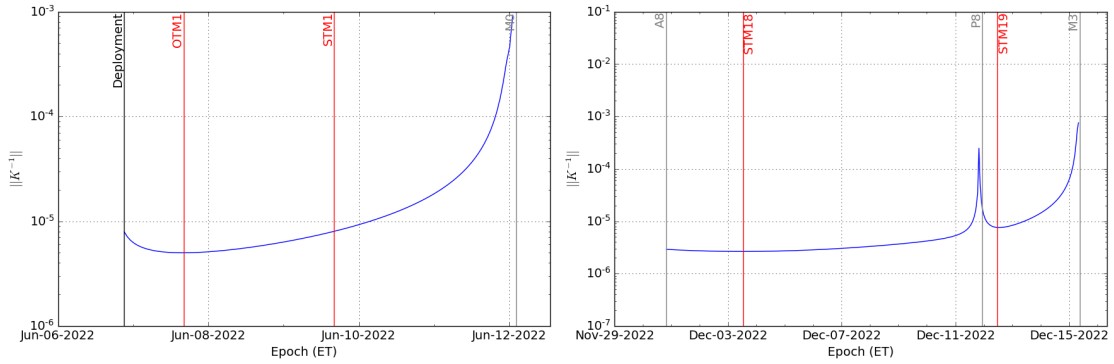

Figure 4.5: K-inverse norm evolution for the targeting of $(B.R, B.T, LTOF)$ coordinates of the B-plane for the fly-bys M0 (left) and M3 (right)..

any maneuvers near to the fly-by more expensive in terms of ΔV. Because of this, STM1 was scheduled 48 hours after OTM1, as early as possible, while still allowing for enough time to complete the navigation process. As mentioned before, the norm analysis of M3 was performed starting from the beginning of the revolution (REV)8 (corresponding to the second-last perigee until the C/A). The results about M3 show two local norm minima, one two days after the apogee A8 and one 12 hours after the last perigee P8, where the correction maneuvers STM18 and STM19 should be placed.

Figure 4.6 depicts the evolution of the K-inverse norm during REV1, aiming at the cartesian position at A1 and cartesian velocity at P1. The targeting of the cartesian position at A1 is optimal if performed at the local minimum two days after the perigee P0. Close to perigees and apogees there is a local maximum due to the 180-degree transfer singularity of the Lambert problem [92]. The norm evolution for the cartesian velocity at P1 shows a minimum close to A1, even if the curve is relatively flat. Close to the perigees, the norm increases because of the reduction of the orbital velocity. The same considerations apply to the orbits REV2 to REV8 as can be seen from the Figures 4.7 to 4.13 represent the evolution of the K-inverse norm during each REV from 2 to 8. Finally, Figure 4.14 reports an high-level schematic representation of the designed optimal strategy that apply to all the trajectories and not only to the one analyzed in this section.

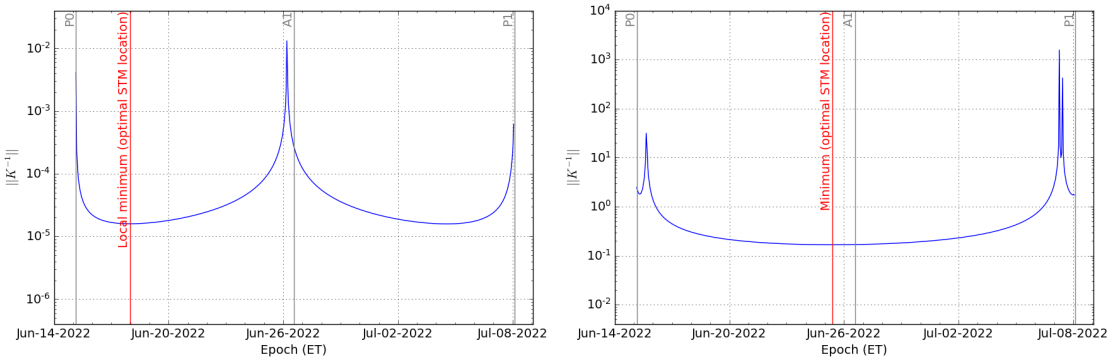

Figure 4.6: K-inverse norm evolution for the targeting of the cartesian position at the apogee A1 (left) and the cartesian velocity at the perigee P1 (right).

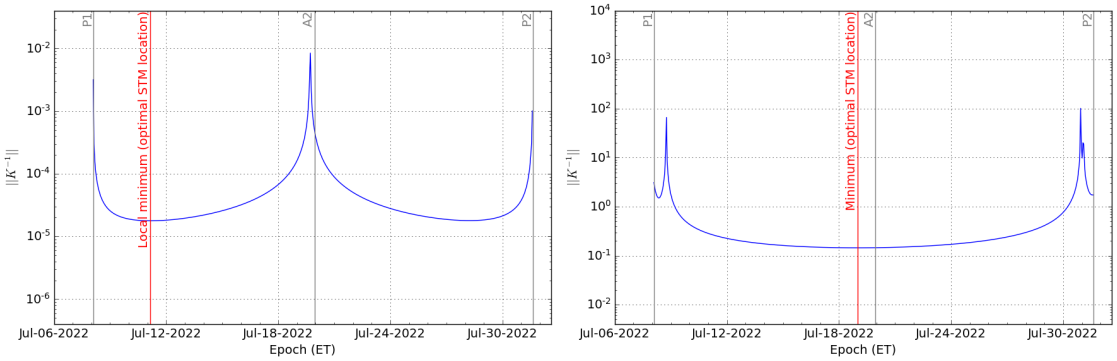

Figure 4.7: K-inverse norm evolution for the targeting of the cartesian position at the apogee A2 (left) and the cartesian velocity at the perigee P2 (right).

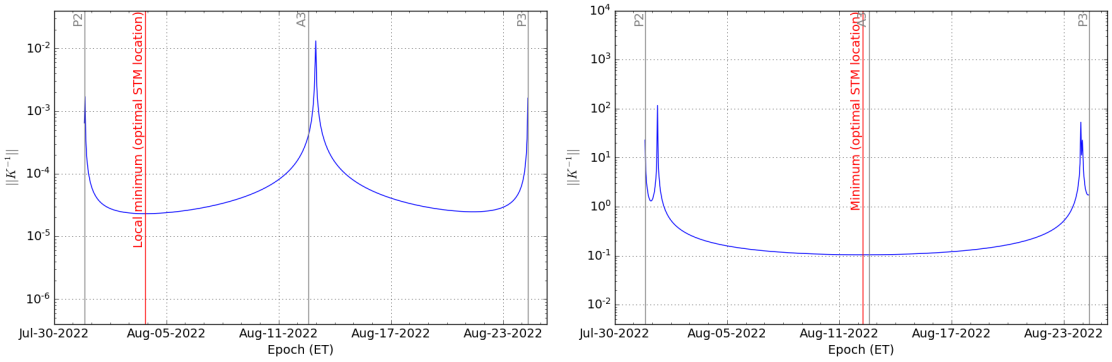

Figure 4.8: K-inverse norm evolution for the targeting of the cartesian position at the apogee A3 (left) and the cartesian velocity at the perigee P3 (right).

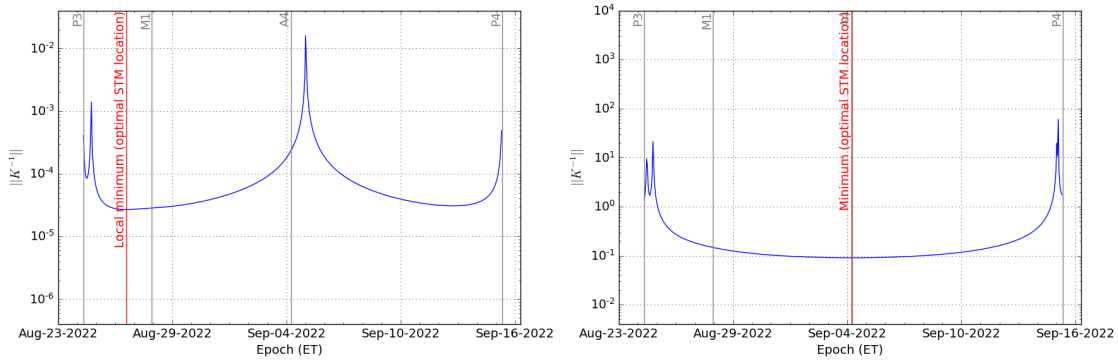

Figure 4.9: K-inverse norm evolution for the targeting of the cartesian position at the apogee A4 (left) and the cartesian velocity at the perigee P4 (right).

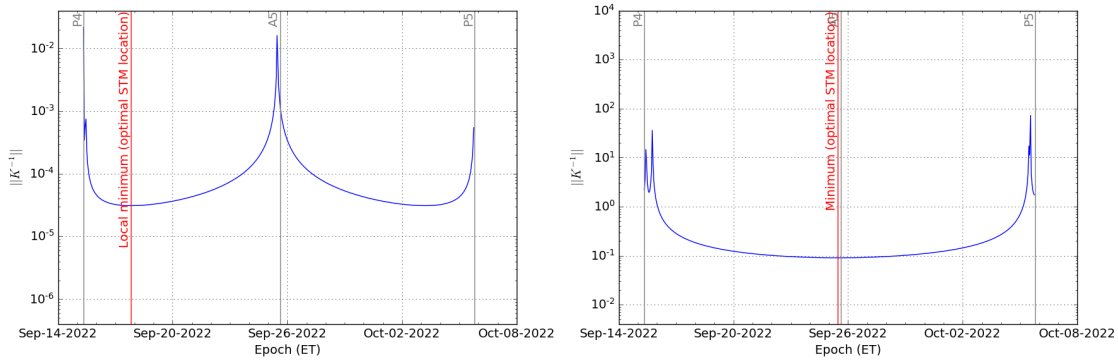

Figure 4.10: K-inverse norm evolution for the targeting of the cartesian position at the apogee A5 (left) and the cartesian velocity at the perigee P5 (right).

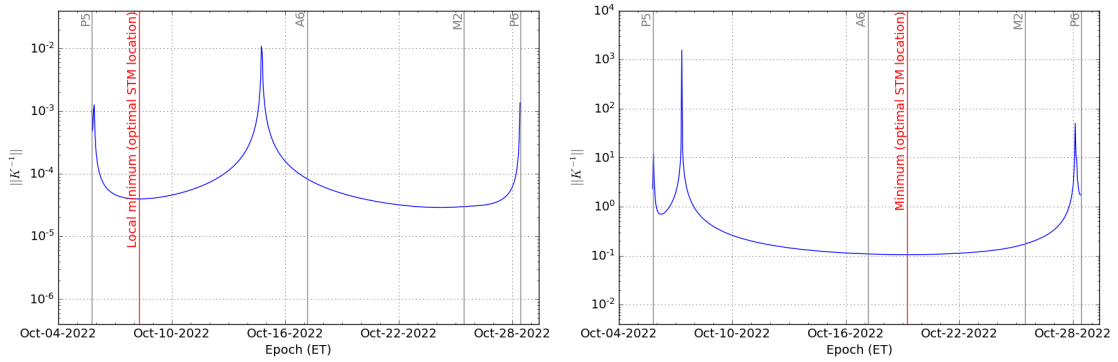

Figure 4.11: K-inverse norm evolution for the targeting of the cartesian position at the apogee A6 (left) and the cartesian velocity at the perigee P6 (right).

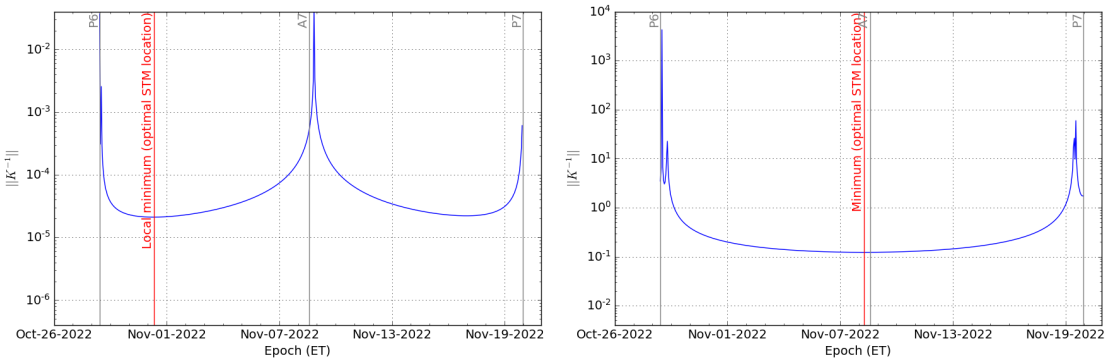

Figure 4.12: K-inverse norm evolution for the targeting of the cartesian position at the apogee A7 (left) and the cartesian velocity at the perigee P7 (right).

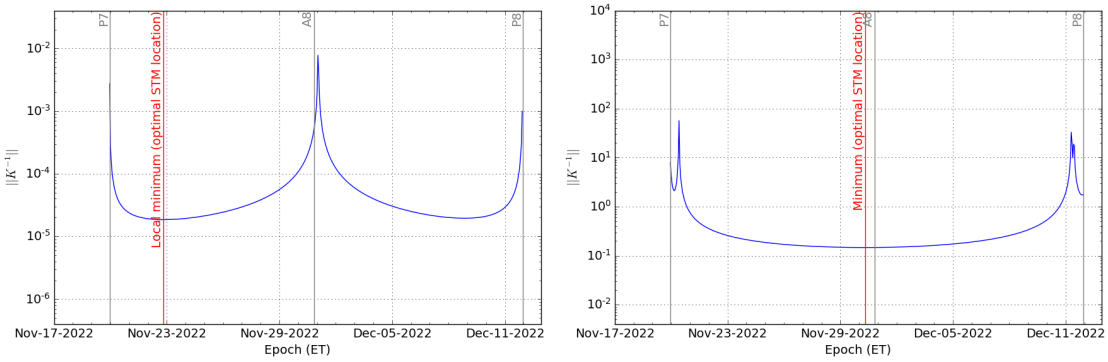

Figure 4.13: K-inverse norm evolution for the targeting of the cartesian position at the apogee A8 (left) and the cartesian velocity at the perigee P8 (right).

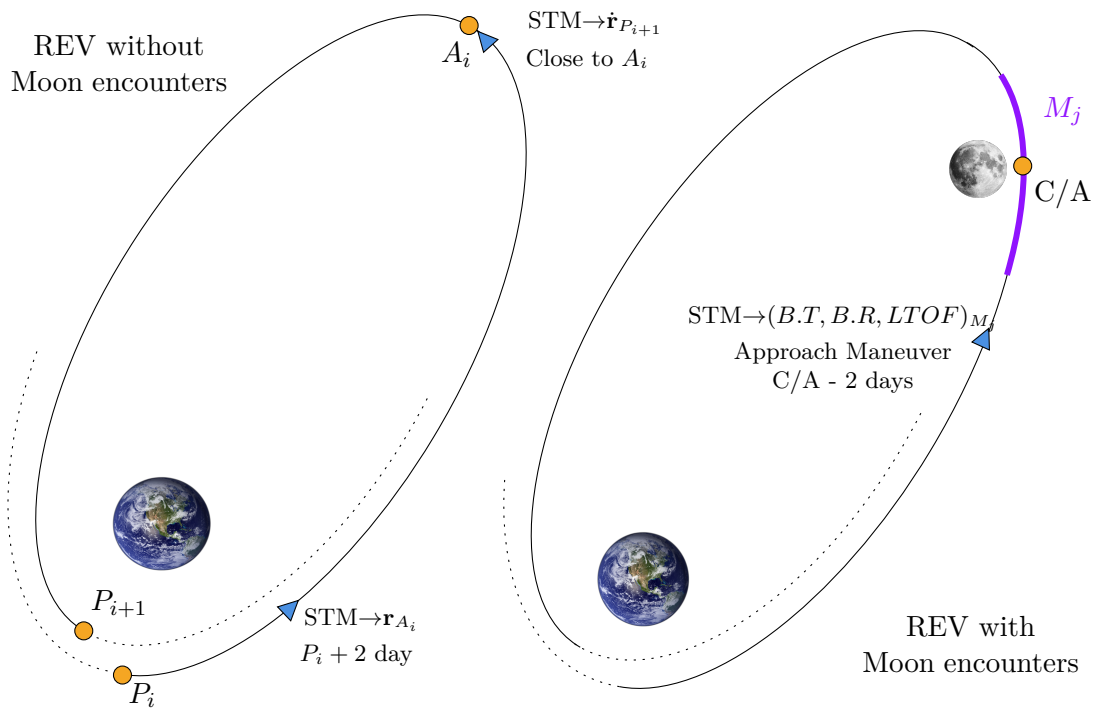

P: Perigee | A: Apogee | M: Moon Fly-By | STM: Statistical Trim Maneuver

Figure 4.14: Schematic representation (not in scale) of the ArgoMoon's optimal trajectory control strategy for a REV without a Moon encounter (left) and with a Moon encounter (right).

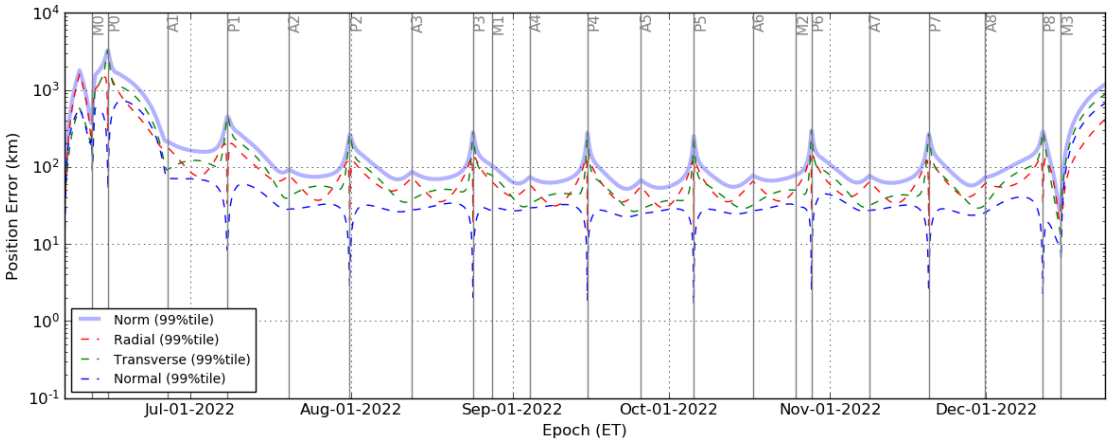

Figure 4.15: Controlled trajectory 99$^{\text{th}}$ percentile dispersion through the whole mission using the nominal control strategy. The error is computed with respect to the reference trajectory using the geocentric RTN frame.

4.2.5 Simulation Results

An evaluation of the expected statistical ΔV and controlled trajectory dispersion was done through a Monte Carlo non-linear analysis employing the discovered optimal STM locations and targets. In addition to the correction maneuvers, the OTM1 was simulated in open-loop (executed as provided by the mission analysis) with the addition of the maneuver's execution error. For the computation of the SRP, the attitude of the S/C was considered Earth-pointing during the scheduled tracking passes and Sun-pointing otherwise. The resulting statistical ΔV for the baseline scenario is reported in Table 4.4 in terms of mean, that is the expected value, and the 99$^{\text{th}}$ percentile, that is used for the validation of NAVREQ-5. The reported ΔV results show that STM1, STM2, STM3 and STM4 are the most expensive statistical maneuvers. According to the controlled dispersion of Figure 4.15, the position errors relative to the reference trajectory show a peak during REV0, especially after the M0 encounter, and reach a maximum value of around 3000 km at P0. After A1 and before M3, the dispersion remains always below about 400 km (at perigees), increasing again to 1000 km only at EOM, because of the disposal flyby M3. Thanks also to the fact that none of the reference trajectories had altitudes with respect to the Earth lower than 10000 km, the designed control strategy provides a final dispersion that widely satisfy the NAVREQ-1.

In addition, Figure 4.16 and Figure 4.17 show the trajectory dispersion on the B-plane of the M0 and M3 encounters. The dispersion at the M0 encounter is quite large after the OTM1 and drastically reduced after STM1 meaning that injection error shall be corrected prior the encounter's C/A. The dispersion at the M3 encounter is well contained in the NAVREQ-2 requirement region even at the STM18.

As expected, the injection covariance is the main cause of dispersion and M0 serves as an error amplifier. Unfortunately, as was evident from the K-inverse analysis, there was not enough time between the S/C deployment and M0 to include further correction maneuvers to target the fly-by. As a result, the ΔV needed to absorb the injection and maneuvers execution errors is distributed through the maneuvers up to the STM4. The majority of the remaining ΔV of the mission is needed to correct the OD and maneuvers' execution errors.

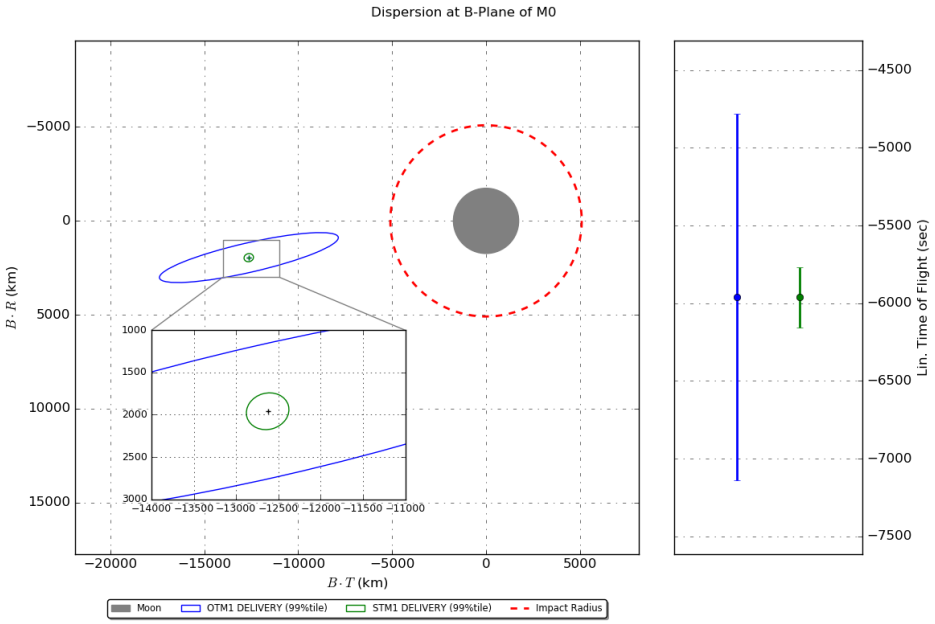

Figure 4.16: Trajectory dispersion (99$^{\text{th}}$ percentile) at the B-plane of M0 after OTM1 (blue ellipse) and STM1 (green ellipse).

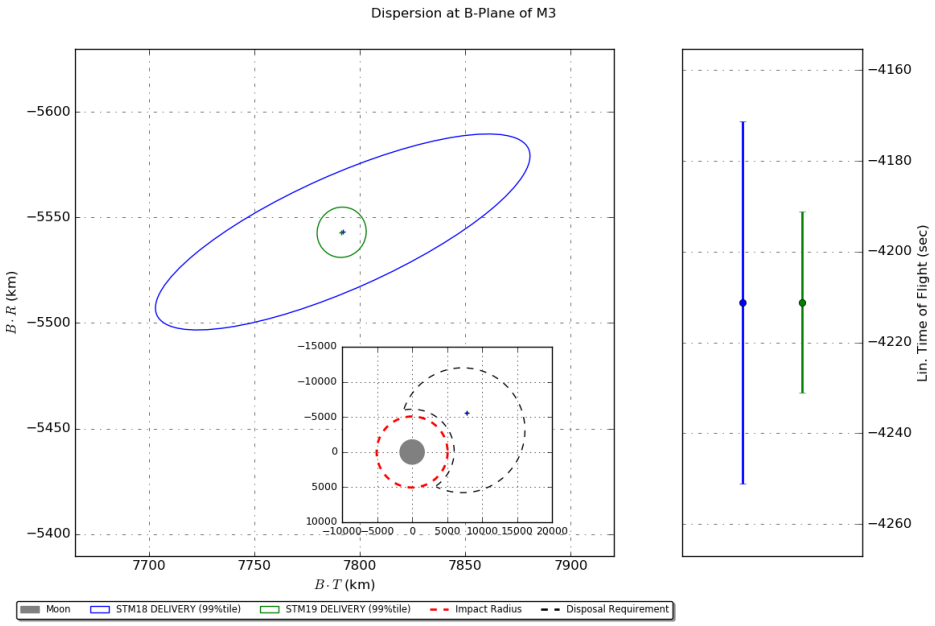

Figure 4.17: Trajectory dispersion (99$^{\text{th}}$ percentile) at the B-plane of M3 after STM18 (blue ellipse) and STM19 (green ellipse).

Table 4.4: Statistical ΔV from the non-linear analysis where the details about the aimpoints can be depicted from Table 4.3. The colored rows are referred to the STMs with the higher 99^{th} percentile ΔV of the mission.

Maneuver	**Nominal Epoch**	**Aimpoint**	**Mean (m/s)**	**Sigma (m/s)**	**90%tile (m/s)**	**95%tile (m/s)**	**99%tile (m/s)**
OTM1	TD + 71400 sec	N/A	11.03	0.38	11.51	11.66	11.92
STM1	OTM1 + 2 day	M0	5.72	3.73	10.84	13.05	17.27
STM2	M0 + 14 hour	A1	6.19	3.98	11.26	13.87	19.97
STM3	P0 + 2 day	A1	0.79	0.58	1.51	1.88	2.87
STM4	A1	P1	0.66	0.41	1.16	1.41	2.06
STM5	P1 + 2 day	A2	0.14	0.11	0.28	0.35	0.56
STM6	A2	P2	0.13	0.08	0.22	0.26	0.37
STM7	P2 + 2 day	A3	0.07	0.04	0.13	0.15	0.20
STM8	A3	P3	0.09	0.06	0.17	0.21	0.27
STM9	P3 + 2 day	A4	0.06	0.03	0.11	0.11	0.15
STM10	A4	P4	0.08	0.05	0.16	0.18	0.23
STM11	P4 + 2 day	A5	0.05	0.03	0.09	0.11	0.13
STM12	A5	P5	0.08	0.05	0.16	0.18	0.24
STM13	P5 + 2 day	A6	0.05	0.03	0.08	0.09	0.12
STM14	A6	P6	0.08	0.05	0.15	0.17	0.23
STM15	P6 + 2 day	A7	0.07	0.05	0.13	0.16	0.21
STM16	A7	P7	0.09	0.05	0.16	0.19	0.25
STM17	P7 + 2 day	A8	0.06	0.03	0.11	0.11	0.15
STM18	A8	M3	0.07	0.04	0.14	0.15	0.20
STM19	P8 + 12 hour	M3	0.15	0.09	0.27	0.31	0.42
	Total		23.29	7.34	35.07	40.01	49.44

4.3 Orbit Determination

The ArgoMoon OD expected accuracies and the fulfillment of the mission requirements were assessed through a *covariance analysis*. In this method the OD process is performed exactly as it will be done during the operations except for using simulated data generated with the same dynamical model adding a synthetic noise. The use of a realistic setup and assumptions allow to infer the expected accuracy of the estimation. Moreover, by tuning the setup (i.e., *a priori* uncertainties, tracking schedule, observable noise) used to generate and analyze the simulated measurements, it is possible to provide a better understanding of the effects of the main design parameters on the expected OD performances. However, the covariance analysis does not account for model errors meaning that the results are always aligned with their mean values. Therefore, the use of conservative assumptions and stochastic parameters allow to consider the mis-modelling effects in the computed uncertainties. The simulation procedure adopted for the OD analysis is structured in the following steps:

1. Setup of an high-fidelity dynamical and measurements models (Section 3.4).
2. Generation of the simulated observed measurements:
   (a) Computation of the S/C trajectory with respect to the Earth by numerically integrating the equations of motion.
   (b) Computation of the simulated observables based on the measurements model.
   (c) Computation of the *observed observables* by adding the assumed noise levels to the simulated observables.
3. Execution of the Orbit Determination process:
   (a) Computation of the *predicted observables* following the same procedure of 2b.
   (b) Generating pre-fit residuals as *observed observables* minus *predicted observables*. Because the same model is adopted for the two set of measurements, the residuals are given by the sum of the simulated noise and the numerical noise.
   (c) Cutting of the simulated observables to be considered for the assumed observation schedule.
   (d) Set the filter by defining the estimated and considered parameters, *a priori* covariances and stochastic properties.
   (e) Run least square filter to compute the estimated value and the covariance matrix of a set of solve-for parameters.
   (f) Covariance mapping to epochs and coordinate systems of interest.

4.3.1 Processing Assumptions

The ArgoMoon's OD was developed as a batch-sequential single-arc estimation where each arc encompasses a trajectory's REV. The batch-sequential approach consist into process each arc separately but in a sequential order such that an arc uses the estimated parameters and covariance of the previous arc as the *a prior* information. As a matter of fact, the numerical precision of the OD solution degrades considerably as the data arc length is extended to include two or more REVs where multiple Moon encounters are also present. With the batch-sequential approach it is therefore possible to consider only the data related to the processed arc by still including the information obtained from the

previous arcs. The numerical integration of the S/C's trajectory of each arc starts where the preceding arc ended so that the numerical errors are minimized. In the ArgoMoon case, the trajectory propagation covered 1.5 × REV because of the estimated covariance mapped to the next apogee epoch required to targeting it with the downstream STM.

The ArgoMoon's baseline OD scenario was modeled following on a set of conservative and important assumption. First of all, the S/C state *a prior* covariance at the beginning of the first arc (REV0) was assumed to be equal to the ICPS injection covariance introduced in Table 4.1. The dynamics of the unmodeled ProxOps during the first 30 minutes of the mission as neglected since it did not significantly increase the state covariance. For the other REVs, the S/C state *a priori* covariance was obtained mapping the S/C state estimated covariance of the previous arc, scaled by a safety factor of 4. To account for mis-modeling of small forces and evaluate their impacts on the expected uncertainties, the stochastic accelerations were simulated. Moreover, during the actual operations, the estimated stochastic accelerations are monitored to evaluate the quality of the estimation. As explained in Section 3.1.3, the DCO of an orbital maneuver was considered as the epoch after which no more data is exploited to compute the maneuver. The time between the DCO and the correspondent maneuver shall be sufficient to acquire the necessary data, generate the OD solution, compute the maneuver using the FPC, validate the navigation outputs, generate the S/C commands, and upload them through the DSN antennas, including the necessary margins. Based on these assumptions, the DCO of the STMs was set to be nominally of four days prior to the maneuver. However, the DCO of STM1 was only 32 hours before the maneuver because it could not be placed further away from the deployment, and so closer to the Moon flyby, due to ΔV cost reasons as discussed in Section 4.2.4. Therefore, in case of a contingency situation, a DCO of 1 day before the maneuver was considered the minimum time necessary to perform navigation safely as also assumed in other studies [98]. Finally, since ArgoMoon cannot activate the IRIS transponder during the execution of an orbital maneuver, no tracking data were simulated in correspondence of the maneuvers. By considering the 99^{th} percentile of the FPC analysis results in Table 4.4, the data cancellation on STM1 to STM4 was of ± 30 minutes around the maneuvers' epochs where for the other STMs a conservative value of ± 5 minutes was assumed. The introduced baseline assumptions for the OD process are then summarized in Table 4.5.

Table 4.5: Summary of the baseline OD assumptions.

Arc data	Tracking data of a single REV	
Tracking data X/X band	Doppler	2-way, 60 s of CT
	Range	2-way, 1 observable every 300 s
Data noise and weights	Doppler	0.1 mm/s at 60 s of CT
	Range	2 m
Stochastic accelerations	10^{-11} km/s^2 per axis, uncorrelated white noise 8 hours of batch time	
Orbital Maneuvers	DCO	96 hours before the maneuver's epoch (nominal) 24 hours before the maneuver's epoch (minimum)
	Tracking	No data during the maneuver execution
REV0 epoch state covariance	ICPS state (Earth-RTN) uncertainty (3-σ) at disposal epoch	
REV1 to REV9 epoch state covariance	Previous arc's mapped state covariance scaled by a safety factor of 4	

4.3.2 Observables Assumptions

In the simulation phase, the two-way Doppler and range measurements (X-Band) between ArgoMoon and the DSN were computed for each complex (Goldstone, Madrid and Canberra) every time the S/C is in view of a 34 m antenna. Then, the simulated data were trimmed using the tracking schedule of Section 3.3 to simulate the real tracking activities. This approach allowed to quickly vary the nominal tracking schedule to test different combinations without simulating the measurements again. The Doppler measurements were simulated with a CT of 60 s where the range was sampled every 300 s. During the generation of simulated observed measurements, a white Gaussian noise was added. In the filtering procedure, the data was weighted directly using the input noise level.

The expected noise level on the Doppler was evaluated using simplified models of the main noise sources [74]:

- plasma noise;
- tropospheric noise;
- antenna mechanical noise;
- ground station electronics;
- S/C's on-board electronics.

The plasma noise is a source that is mainly function of the carrier frequency at the X/X band the Sun-Earth-Probe (SEP) angle. The maximum noise contribution due to the SEP angle occurs in conjunctions, namely when SEP=0 deg, and is at minimum during oppositions when the SEP angle is 180 deg. The SEP angle throughout the ArgoMoon mission evaluated at the time of the OD analysis is represented in Figure 4.18a. The results shows that in the middle of the mission the SEP angle is lower than 30 degrees and an higher Doppler noise may be expected. An antenna mechanical noise of 0.005 mm/s was assumed from typical values for DSN where the one related to the typical S/C electronics noise was of 0.001 mm/s [74].

Tropospheric noise also depends on two key factors: the time, which is higher in the summer and lower in the winter, and the adopted calibration technique. A typical GNSS-based calibration was considered, which may calibrate up to 10-20% of the noise due to the Earth's troposphere. Figure 4.18b illustrates the total expected noise contribution for each considered source, while Figure 4.18c depicts the overall noise experienced during the ArgoMoon mission.

4.3.3 Filter Configuration

The OD filter nominal configuration of each arc is reported in Table 4.6 for the estimated parameters, and Table 4.7 for the considered ones. The filter parameters can be estimated and updated or have just their error considered in the estimated uncertainties. The full state covariance of the ICPS at its disposal epoch (Table 4.1) was used to generate the epoch state *a priori* uncertainty for the REV0. The filter's solution's epoch state covariance was then mapped to the following arc epoch and used as an a priori covariance for the upcoming OD arc, multiplied by a safety factor of 4, corresponding to a factor 2 in the sigmas. SRP uncertainty was compensated for by estimating in each arc a scale factor with a conservative *a priori* σ. The estimation of stochastic accelerations accounted for the mis-modeling of the SRP and other unmodeled forces. Because ArgoMoon's ADCS

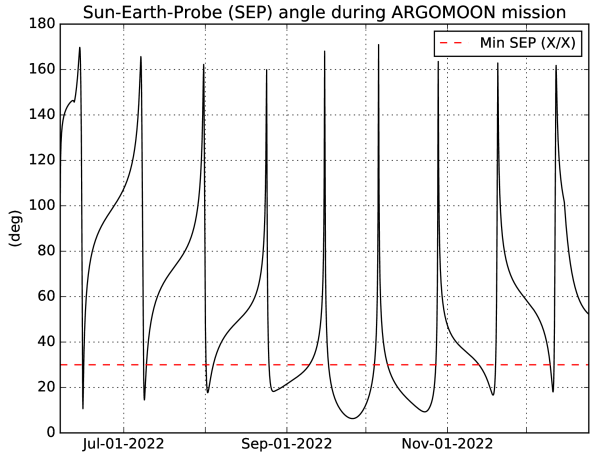

(a) *Sun-Earth-Probe angle.*

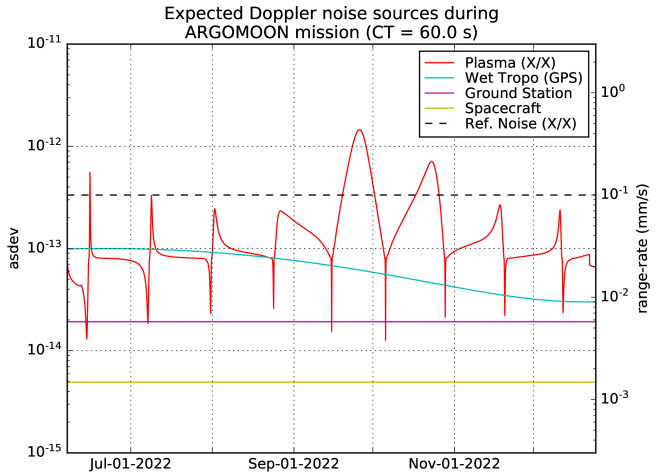

(b) *Doppler noise by source.*

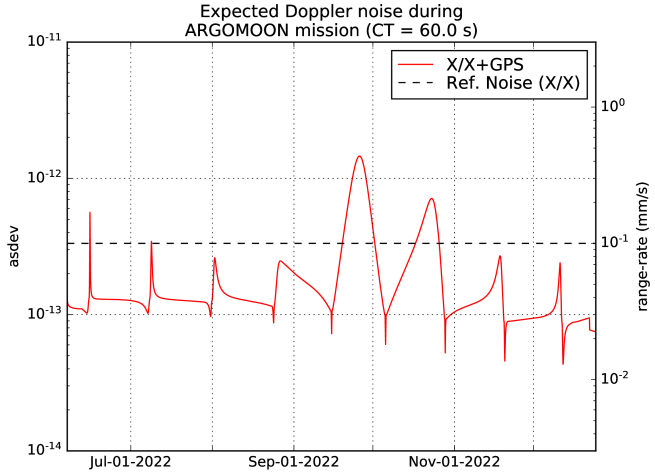

(c) *Total Doppler noise.*

Figure 4.18: ArgoMoon mission Doppler noise evaluation.

and PS have never been deployed in deep space, the orbital maneuvers were estimated with a high conservative *a priori* uncertainty. The latter orbital maneuvers uncertainties were consistent with the Gates error, Table 4.2, used in the FPC analysis. For each tracking pass and station, a stochastic uncorrelated range bias was estimated. Moreover, to account for the S/C transponder characteristic delay, a constant range bias was estimated. The filter considered the uncertainties inferred from the DE430 ephemeris about the masses of the Earth and Moon. The parameters related to the radiometric tracking observables, such as the UT1 time bias, Earth Polar Motion, atmospheric delays, and DSN station locations, were also considered in the filter.

4.3.4 Baseline Results

The evaluation of the OD simulation results was performed by mapping the solution covariance to times of interest and then evaluated in different coordinate sets. The main

Table 4.6: Baseline filter setup for the estimated parameters adopted in the simulations.

Parameter	**Unit**	***A priori* Uncertainty**	**Comments**
S/C Epoch State (REV0)			
Position (1-σ)	km	30.0 / 60.0 / 15.0	Diagonal covariance matrix in geocentric RTN frame.
Velocity (1-σ)	m/s	2.1 / 2.7 / 4.2	
S/C Epoch State (REV1-REV9)			
Position	km	-	4 × estimated covariance mapped from previous arc.
Velocity	m/s	-	
SRP			
Scale Factor	-	50%	Details on Section 3.4.
Deterministic Burns (OTM)			
Δv	m/s	10%	
Ra	deg	1.1	
Dec	deg	1.1	
Δt	s	3.0	
Statistical Burns (STM)			
Δv_x/ Δv_y/Δv_z	m/s	0.011	
Δt	s	3.0	
Observables Bias			
Per-Pass Range	m	2	Ground stations delay.
Constant Range	m	500	IRIS transponder delay.
Constant Doppler	Hz	0.0124	10% of IRIS Doppler bias.
Stochastic Accelerations			
X/Y/Z	km/s^2	1×10^{-12}	Stochastic, assumed from [89] multiplied by a factor of 2.
Time Batch	hours	8	

Table 4.7: Baseline filter setup for the considered parameters adopted in the simulations.

Parameter	**Unit**	***A priori* Uncertainty**	**Comments**
Celestial Bodies GMs			
Earth	km^3/s^2	5×10^{-4}	From DE430 [83].
Moon	km^3/s^2	1.4×10^{-4}	From DE430 [83].
Station Locations			
DSN	cm	3	Per axis, assumed from [89].
Path Delays			
Troposphere (wet/dry)	cm	1/1	Assumed from [89].
Ionosphere (day/night)	cm	5/1	
Earth Orientation Parameters			
Polar Motion	deg	8.6×10^{-7}	Assumed from [89].
UT1 Bias	s	2.5×10^{-4}	

objective in the evaluation of the results was to assess the obtainable OD accuracy but most of all the verification of the requirements compliance. Then, the main quantities that were meant to be analyzed are the following:

- The expected uncertainty in the S/C state in the RTN frame centered on the Earth.
- The expected uncertainty int the S/C state at the Moon encounters in the B-plane.
- The DSN pointing uncertainty evaluated using the Root Sum Squared (RSS) of the latitude and longitude uncertainties of the S/C with respect to the DSN complexes.

The initial results of the OD analysis have demonstrated the importance of the DSN pointing uncertainty throughout the mission, especially during the first two days of flight. Unlike deep space missions to the Solar System, ArgoMoon's trajectory is relatively close to Earth, and the 34 m antennas' 3dB cone captures a smaller region of space around ArgoMoon when pointing at it. For instance, to track a S/C that is orbiting close to Mars, it would be sufficient to point the 34 m antenna towards the planet to be able to search the S/C's carrier signal. This means that when a S/C is flying trough the Solar System, the DSN pointing uncertainty should be less important as an higher uncertainty in the S/C trajectory is allowed. The large *a priori* covariance of the ArgoMoon's initial state causes the pointing uncertainty to be larger than the 34 m antenna's receiving HPBW but lower than the one of the 1.2 m aided acquisition antenna, that will be adopted during the first day of the mission. The optimal delivery schedule was determined by examining the expected pointing uncertainty at each tracking pass using different DCOs. The first delivery to DSN (DEL1) has to be performed after the OTM1 tracking pass to fulfill the NAVREQ-3 in view of the STM1. The DEL1 therefore needs a DCO after the mission's first tracking pass in order to provide enough time for OD processing. Then, the other deliveries to DSN (DEL2, DEL3, ..., DEL19) are made before the tracking passes of each STMs using the same DCO allocated to the maneuvers (i.e., DEL2 is performed in

correspondence of the STM1 tracking pass with the DCO 24 hours before the maneuver). In order to fulfill the NAVREQ-3 up to the EOM, a last delivery DEL20 should take place following the reconstruction of the last fly-by M3.

Bases on the developed DSN delivery schedule, Figure 4.19 and 4.24 depict the pointing uncertainty evolution during REV0 and REV9 (last part of the mission), respectively. Figures 4.20 to 4.23 give the pointing uncertainty evolution from REV1 to REV8 encompassing two REVs per figure. Throughout the mission, the pointing uncertainty exhibited a sequence of peaks around the perigees that violate the pointing requirement. This phenomenon is induced by the fast reduction in the S/C distance with respect to the Earth during the closest approaches. However, no tracking passes were planned at the perigees and by considering the uncertainty only at the epochs of the tracking passes (represented by the blue dots in the pointing uncertainty plots), the NAVREQ-3 was always satisfied, at a 3-σ level.

Figures 4.25 and 4.26 depict the S/C ephemeris uncertainties mapped on the B-plane of the fly-bys M0 and M3, respectively, using different DCOs. The results for M0 demonstrated that the NAVREQ-1 could not be satisfied when employing only the *a priori* uncertainty provided by ICPS dispersion. However, the impact requirement became satisfied even by exploiting just one tracking pass after the S/C release. The uncertainty improved, adding more data, and the DCO of the STM1 minimized the OD error. The expected uncertainties for M3 indicated that the NAVREQ-2 was always met since the OD error was always contained within the allowable zone at 3-σ.

Figures 4.27 to 4.31 depict the S/C ephemeris uncertainties evolution throughout the whole mission, from the deployment up to the EOM. The results revealed quickly increasing uncertainties following the orbital maneuvers due to the significant uncertainties assumed in the analysis, which is attributable to the lack of a comprehensive performance evaluation of the ArgoMoon PS. However, by inspecting the baseline results all over the mission, it was possible to see that the RSS of the position uncertainty is always below 30 km. In particular, during the initial part of REV1 (Figure 4.28), the ephemeris uncertainties were lower since the tracking schedule was denser than in the Phase 2. Based on this evidence, it could be confirmed that the assumed OD strategy and tracking schedule were able to fulfill the NAVREQ-1. The expected uncertainty of the reconstructed S/C ephemeris at the end of each OD arc, through the whole mission, is reported in Figure 4.32.

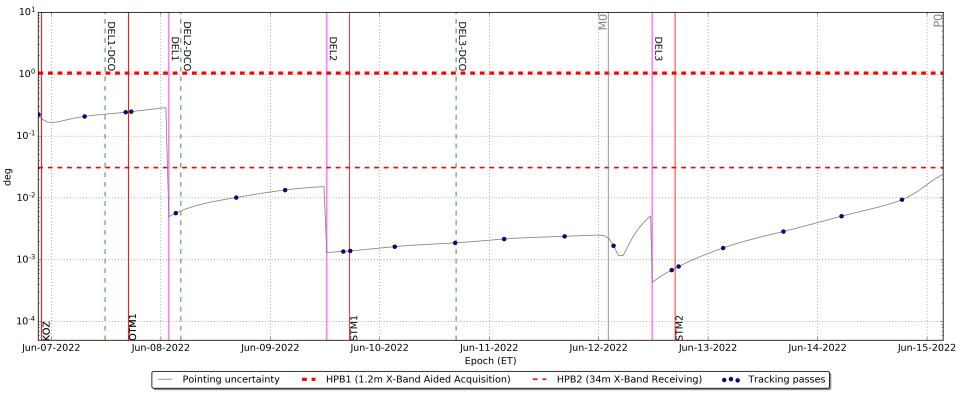

Figure 4.19: DSN to ArgoMoon pointing uncertainty evolution (3-σ), during REV0. The gray line is the uncertainty evolution using the designed delivery schedule, while the blue dots identify the tracking passes.

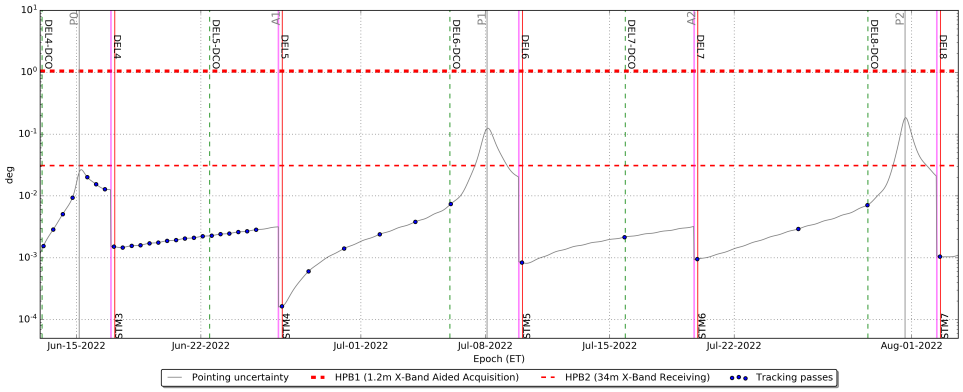

Figure 4.20: DSN to ArgoMoon pointing uncertainty evolution (3-σ), from P0 to P2 (encompasses REV1 and REV2). The gray line is the uncertainty evolution using the designed delivery schedule, while the blue dots identify the tracking passes.

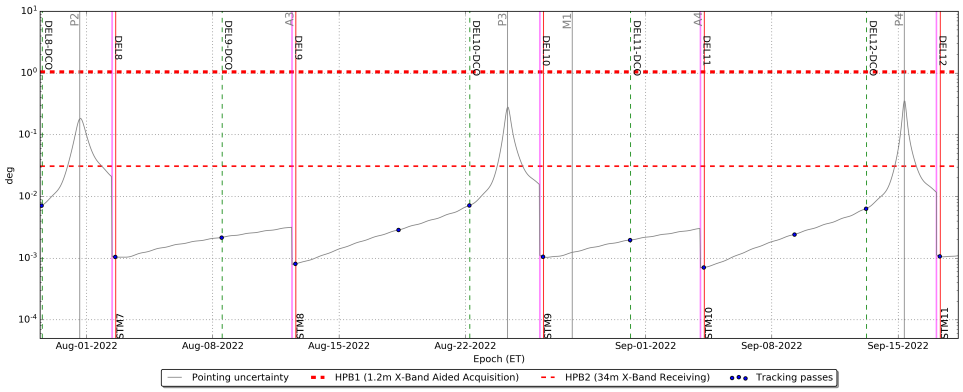

Figure 4.21: DSN to ArgoMoon pointing uncertainty evolution (3-σ), from P2 to P4 (encompasses REV3 and REV4). The gray line is the uncertainty evolution using the designed delivery schedule, while the blue dots identify the tracking passes.

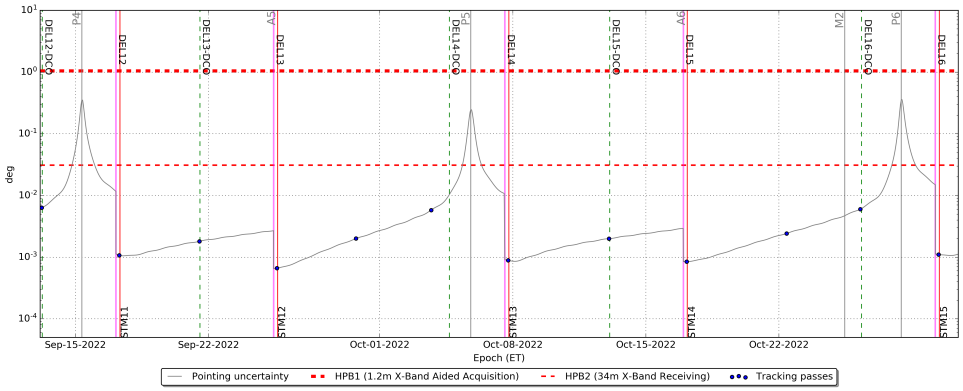

Figure 4.22: DSN to ArgoMoon pointing uncertainty evolution (3-σ), from P4 to P6 (encompasses REV5 and REV6). The gray line is the uncertainty evolution using the designed delivery schedule, while the blue dots identify the tracking passes.

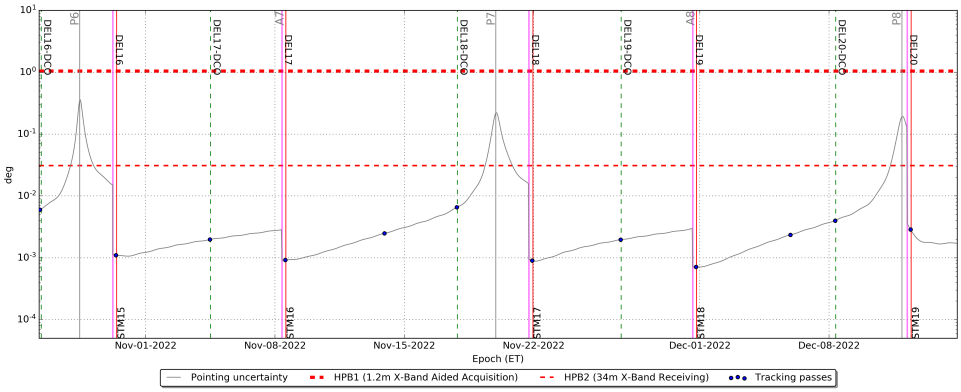

Figure 4.23: DSN to ArgoMoon pointing uncertainty evolution (3-σ), from P6 to P8 (encompasses REV7 and REV8). The gray line is the uncertainty evolution using the designed delivery schedule, while the blue dots identify the tracking passes.

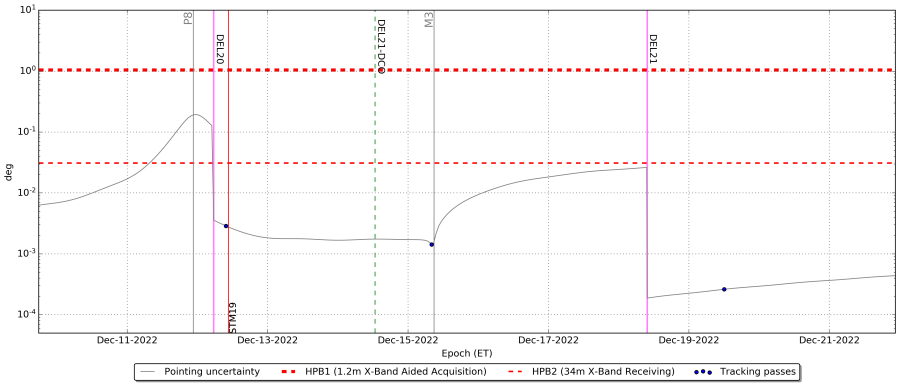

Figure 4.24: DSN to ArgoMoon pointing uncertainty evolution (3-σ), from P8 to the EOM. The gray line is the uncertainty evolution using the designed delivery schedule, while the blue dots identify the tracking passes.

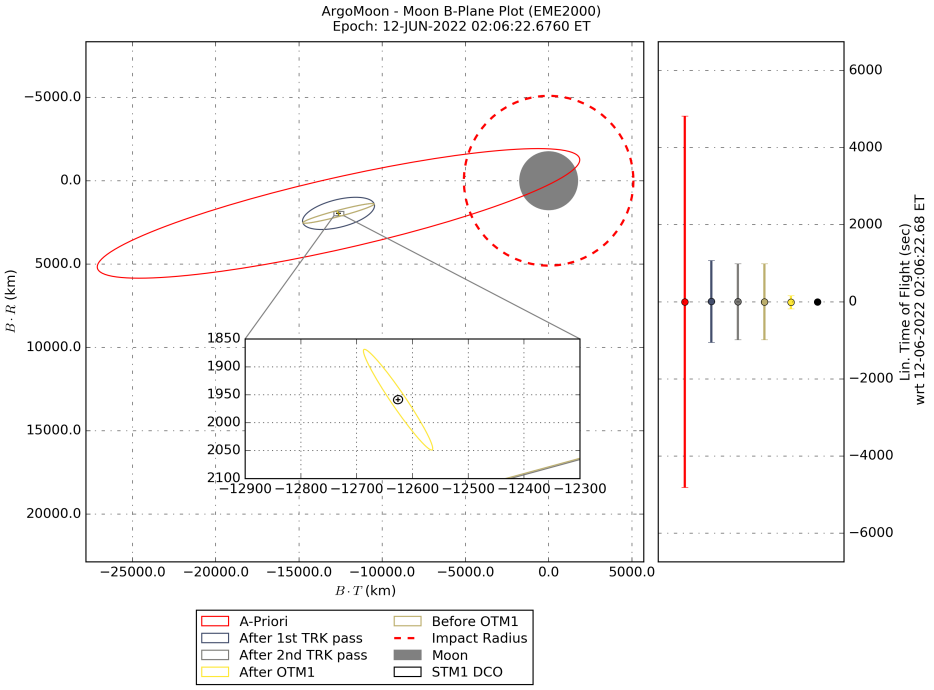

Figure 4.25: B-plane uncertainties (3-σ) for the fly-by M0 with DCO at the end of each tracking (TRK) pass up to the DCO of the STM1 (last maneuver before the fly-by).

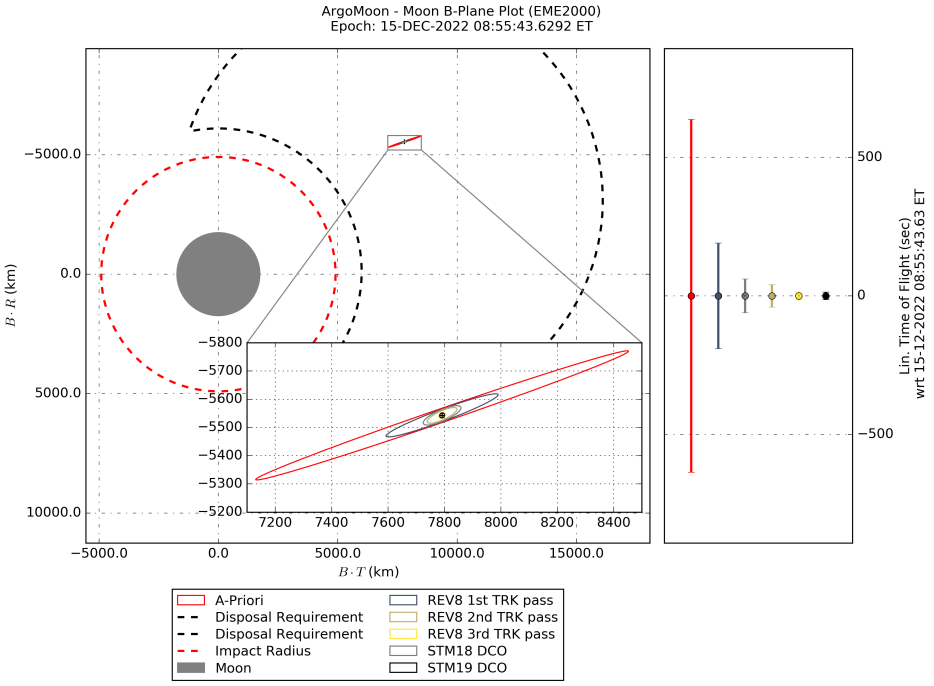

Figure 4.26: B-plane uncertainties (3-σ) for the fly-by M0 with DCO at the end of each tracking (TRK) pass up to the DCO of the STM19 (last maneuver before the fly-by).

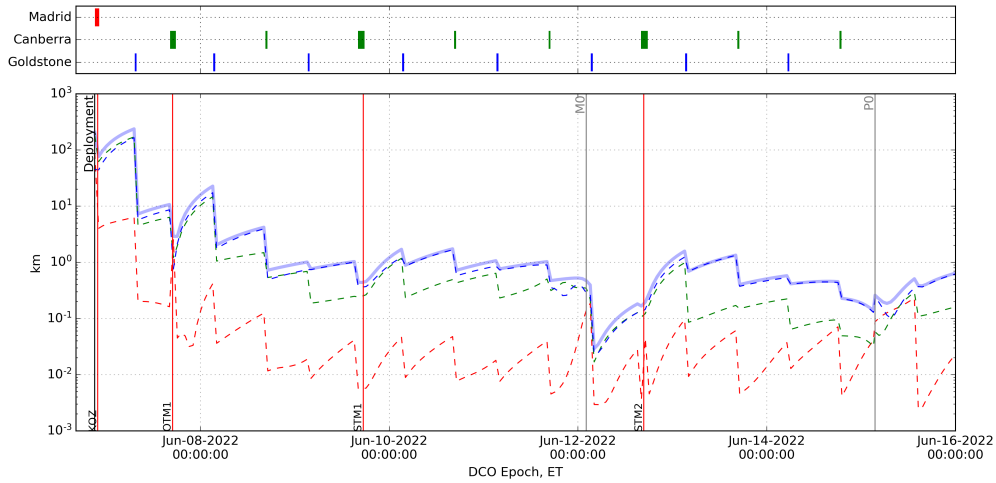

Figure 4.27: Position uncertainty evolution (3-σ) during REV0, in the Earth-centered RTN frame.

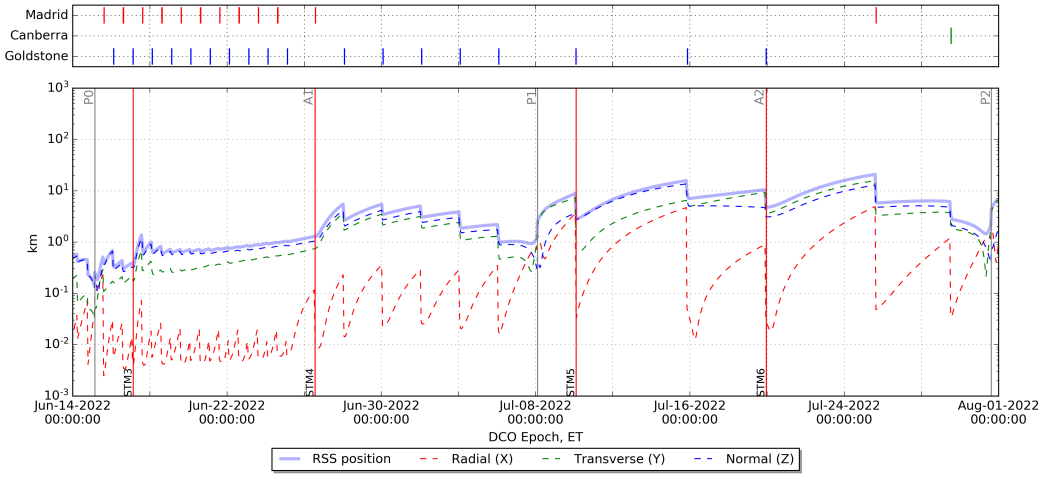

Figure 4.28: Position uncertainty evolution (3-σ) during REV1 and REV2, in the Earth-centered RTN frame.

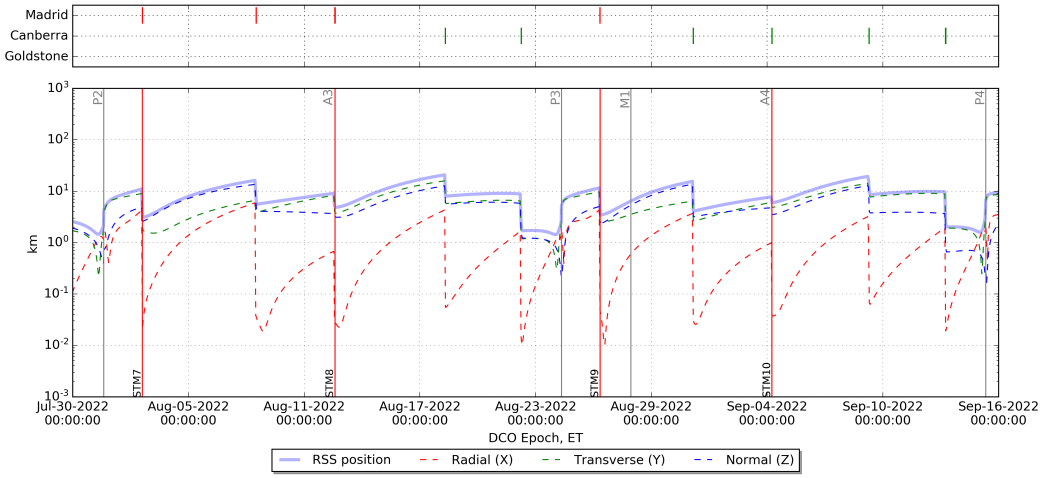

Figure 4.29: Position uncertainty evolution (3-σ) during REV3 and REV4, in the Earth-centered RTN frame.

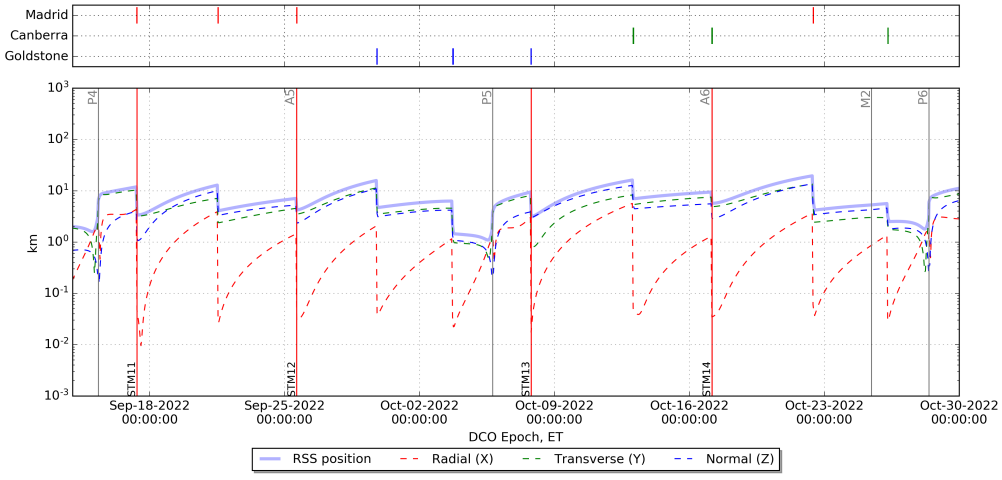

Figure 4.30: Position uncertainty evolution (3-σ) during REV5 and REV6, in the Earth-centered RTN frame.

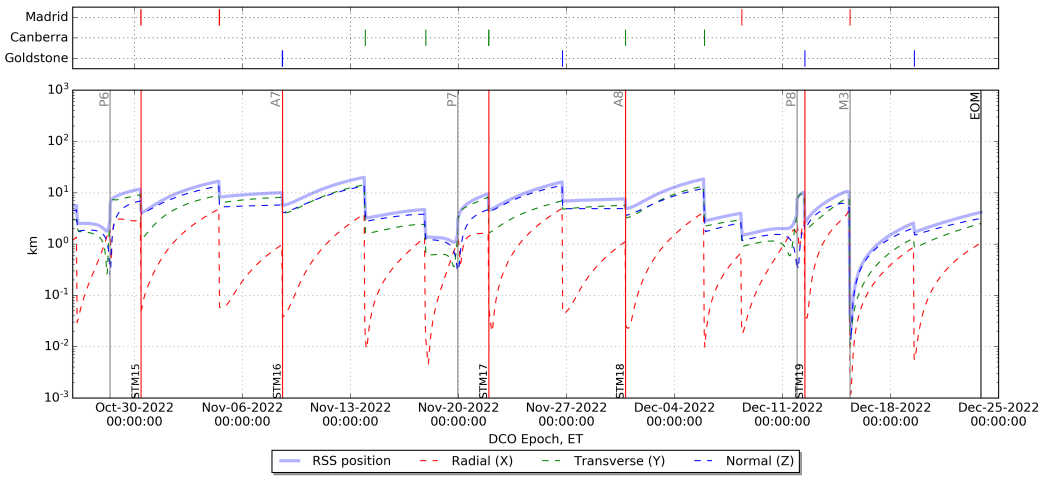

Figure 4.31: Position uncertainty evolution (3-σ) from the beginning of REV7 up to the EOM, in the Earth-centered RTN frame.

Figure 4.32: Evolution of the expected S/C ephemeris uncertainty (3-σ, Earth-centered RTN frame) through the whole mission after a REV by REV single-arc reconstruction.

4.4 Sensitivity Analysis

A parametric variation of the navigation setup described in Sections 4.3 and 4.2, such as *a priori* uncertainties and measurement acquisition schedule, was used to examine the robustness of the navigation performance. This sensitivity study of the FPC and OD allowed for the identification of the critical parameters that affect navigation results in terms of DSN pointing and disposal needs (OD), as well as ΔV cost and trajectory dispersion (FPC). As a result, it was demonstrated that for each of the tested cases, the dispersion and OD uncertainty were always able to widely satisfy the NAVREQ-1 always guaranteeing that there was no risk of impact with Earth and Moon. Furthermore, at the fly-by M3 the dispersion and OD uncertainty were always widely contained in the required area ,indicating that the variation in the parameters had no impact on the NAVREQ-2. The results of the OD sensitivity at the B-plane of M3 can be depicted from Figure 4.33. The sensitivity results related to the FPC dispersion at M3 are not reported since the dispersion ellipses on the B-plane were almost identical to the OD ones. The former evidence was meaning that the optimal trajectory control strategy was capable of minimize the trajectory dispersion at M3 to be at the same order of the OD.

The results of the total statistical ΔV are reported for each relevant case in Table 4.8. As shown in Figure 4.34, the majority of the ΔV cost is concentrated in the first four STMs, which are necessary to absorb the dispersion caused by injection uncertainty (as expected in the discussion of Section 4.2.5). The targeting of the fly-bys without using the *LTOF* coordinate (*No LTOF targeting* case) should allow to save almost 5 m/s at the 99^{th} percentile but at a cost of a slightly larger dispersion at the closest approaches with the Moon. The number of tracking passes constrained at the beginning of the mission, the loss of Doppler or range data, and the increase of the OTM1 *a priori* uncertainty had

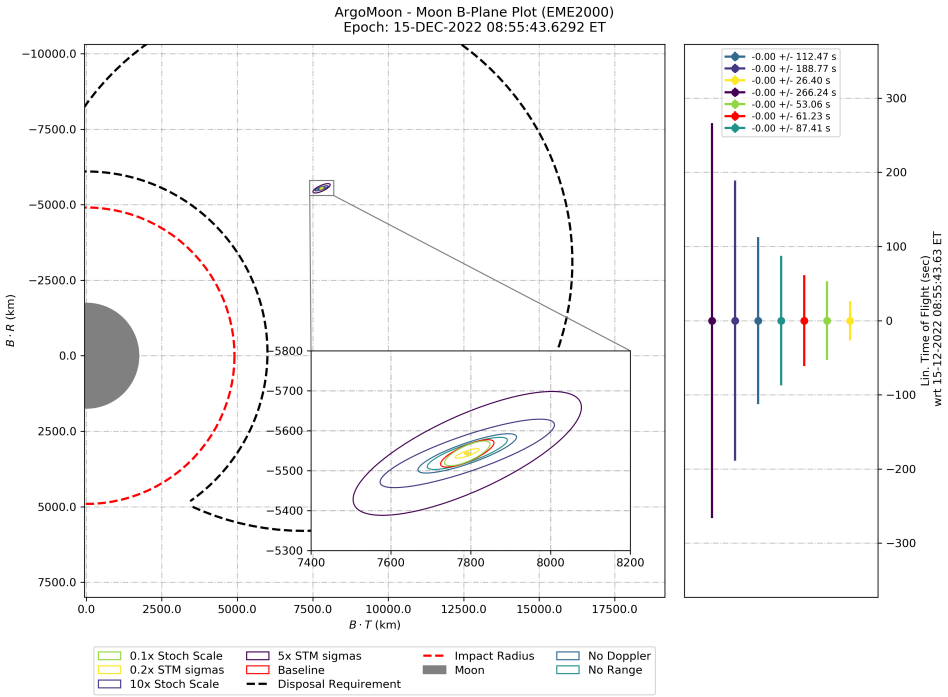

Figure 4.33: Relevant parameters variation effect on the B-Plane uncertainties (3-σ) of the last fly-by (M3) at the DCO of STM18.

Table 4.8: Full mission ΔV statistics for each FPC relevant sensitivity case.

Case	**Mean (m/s)**	**Sigma (m/s)**	**99% (m/s)**
Baseline	23.31	7.64	49.52
0.5×Injection Covariance	18.23	3.93	31.61
0.5×Maneuvers Execution Error	21.42	6.25	41.32
No LTOF targeting	22.15	7.26	46.64
5×OTM1 sigmas	23.34	7.77	49.51
Maximum 1 pass per day	23.42	7.63	49.62
No Doppler data	23.67	7.64	49.6
No Range data	23.55	7.66	49.86
10×Stochastic sigmas	24.48	7.68	50.37
5×STM sigmas	26.69	7.69	52.32
2×Maneuvers Execution Error	30.14	12.93	77.75
2×Injection Covariance	34.05	15.21	86.88

a little effect on the overall statistical ΔV.

On the contrary, the former cases did not allow to satisfy the DSN pointing requirement for certain passes during the REV0 and REV1 (in between the passes 0 to 40) as can be seen in Figure 4.35. Furthermore, while only adding 3 m/s on the total statistical ΔV, the amplification of the *a priori* uncertainties related to the stochastic accelerations and the STMs did not permit to satisfy the DSN pointing requirement on different tracking passes through the whole mission (i.e., the tracking passes 20, 46, 51, etc.).

Regarding the OD expected performance sensitivity not strictly related to the requirements, Figure 4.36 shows the ratio of the OTM1 uncertainties with respect to te nominal case throughout the REV0 for each relevant sensitivity case. In addition, Figure 4.37 represents the same nominal ratio but for the S/C position uncertainty at each mission's perigee and apogee. The results related to the OTM1 shown that the reconstruction of an ArgoMoon's orbital maneuver should be mostly affected by the lack of Doppler and range, the biases on the range measurements, and the stochastic accelerations. Based on

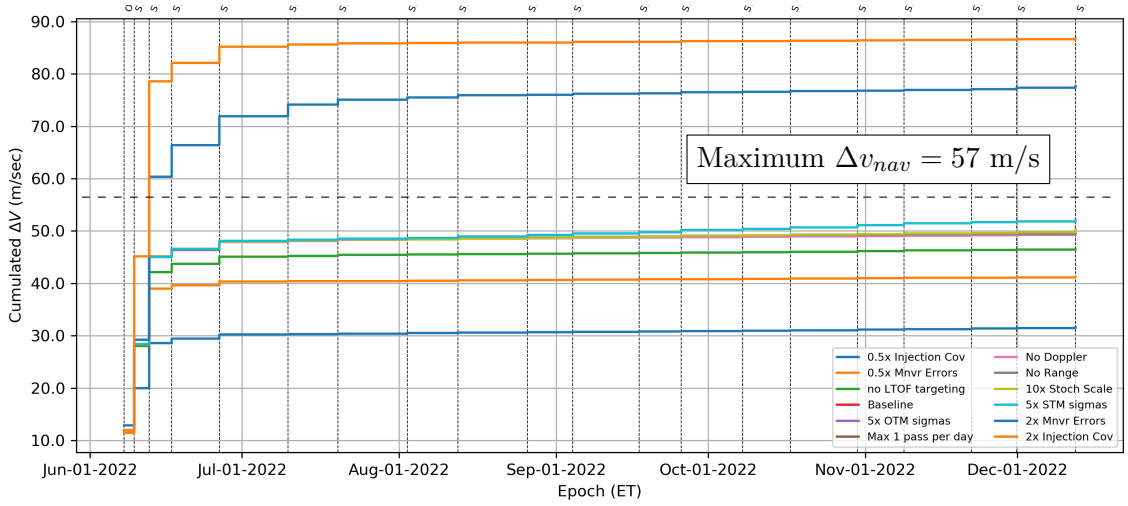

Figure 4.34: Full mission cumulated ΔV statistics plot for each FPC relevant sensitivity case.

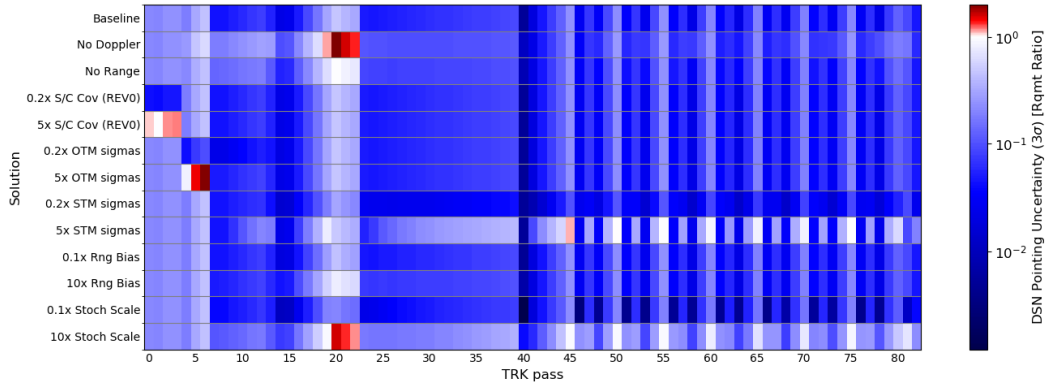

Figure 4.35: Full mission DSN pointing requirement ratio between the expected uncertainty and the NAVREQ-3, for each tracking (TRK) pass, with respect to each relevant sensitivity case.

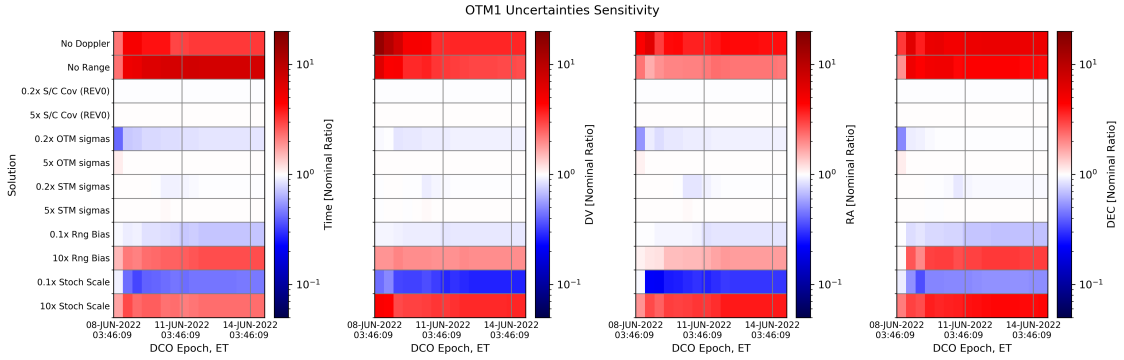

Figure 4.36: OTM1 expected reconstruction uncertainties through the REV0 for each relevant sensitivity case.

that, it was considered fundamental to have Doppler and range data before and after an orbital maneuver to properly reconstruct the event. The uncertainty on the S/C position at the apsides was mostly affected by the increment of the stochastic accelerations as well as the variation in the *a priori* uncertainties of the STMs.

Summarizing, the injection covariance and the maneuver execution error were the two critical case areas for the ArgoMoon navigation. The lack of Doppler data and the increment of mismodeling of S/C accelerations had an impact on the DSN pointing requirement as well. The uncertainty on the orbital injection is related to the SLS rocket performance and cannot be controlled, while the performance of the propulsion system was not fully characterized due to limited resources available to a CubeSat mission. For these reasons, baseline conservative values have been assumed for the injection covari- ance, the maneuvers uncertainties, and the stochastic accelerations. Since the Doppler observables are crucial for reconstructing orbital maneuvers, a DSN elevated support of Level-3 [79] was demanded for the tracking passes covering the expected maneuvers' execution. Thus, the cases that violate the ΔV constraint and DSN pointing requirement are only statistically marginal and were considered only to understand the effect of the critical parameters on the navigation performance.

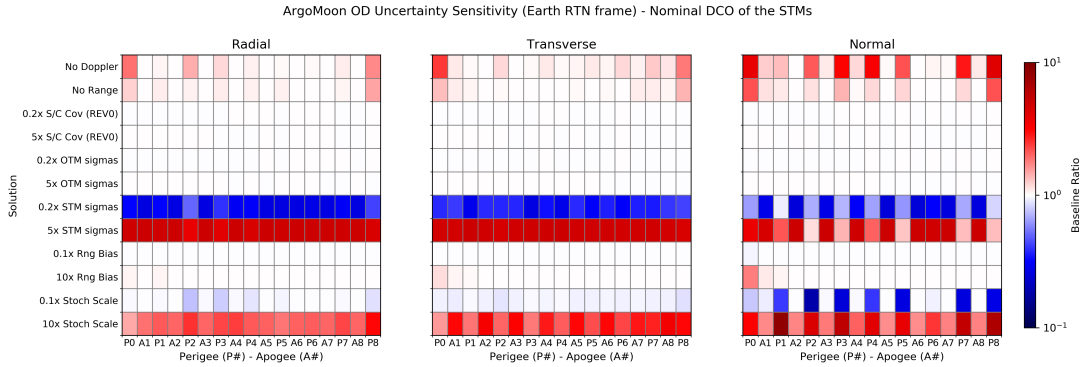

Figure 4.37: Ratio between the S/C position uncertainty of each relevant sensitivity case with respect to the nominal one, at each apogee and perigee of the mission.

Chapter 5

Navigation Operations

Contents

5.1 Introduction

This chapter aims to provide a general overview of the actual ArgoMoon's navigation operations from the pre-launch setup up to the results obtained during the flight. The first sections give an introduction about the interfaces and the nominal setup of the navigation system. Finally, the results of the performed navigation operations are presented and discussed for each delivered orbital solution.

Figure 5.1: Flight dynamics team in the control room at the RSLab in Forli (Italy), about one hour before the launch of ArgoMoon.

5.1.1 Mission Teams and Responsibilities

In this section a brief introduction of each teams and their relative responsibilities in the mission operations is provided. Moreover, each paragraph's title identify the acronym used during the operations to rapidly identify the former teams.

ARG The mission operations were in charge of Argotec that had its own MCC in Turin (Italy) where a team of engineers, S/C operators and managers were located. The MCC core is located in the *front room* where the Spacecraft Operations Manager (SOM) lead a team of operators that prepared and sent the telecommands to the S/C and monitored its status from the acquired telemetry. The MCC also has a *backroom* where a team of specialists, who also participated in the development of the S/C, were located to supervise the state of the subsystems and keep them performing correctly.

UBO The navigation of ArgoMoon was responsibility of a dedicated external team composed by fight dynamics specialists of the University of Bologna (UNIBO). The UBO team operated from the RSLab in Forli (Italy) with a dedicated control room always connected through a real-time video feed and voice loop with the Argotec's MCC. The equipment adopted by UBO for the execution of the navigation operations has been called Navigation facility (NAV). Figure 5.1 shows the flight dynamics team preparing for the operations in the navigation control room about one hour before the launch of ArgoMoon.

ASI The ArgoMoon mission was under the supervision of ASI. The decision-making responsibility for the critical aspects of the mission was of then in charge of the ASI team that maintained a constant monitoring of the activities. Moreover, ASI had also a key role in moderating the inter-team cooperation as well as providing support in the correct exchange of the critical information required for the success of the mission.

5.2 Setup

The ArgoMoon's operative navigation consisted into the practical application of the baseline system analyzed in the previous chapters. However, the navigation operations performance depends not only on the capabilities of the S/C and the navigation strategy but also on the correct organization of the human resources, interfaces and work routines. More-

over, the proper setup of hardware and software is fundamental to guarantee redundancy, accuracy and reliability of the given navigation service.

5.2.1 Staffing

The UBO team was composed by four to five members organized into work shifts. Such number of members was required to cover in real-time the operations during the first week as well as provide reliability, redundancy and allow some level of flexibility in case of personnel unavailability. During this initial period, two or three tracking passes per day were scheduled, leading to a dense activity period. Therefore, the work of the team was organized to have work shifts to cover the principal deliveries and conveniently also the tracking passes in the early morning. The UBO members were all engineers with advanced degrees in the aerospace engineering and several years experience in astrodynamics and orbit determination. The most trained member was the team leader with more than five years of experience in fight dynamics. He was in charge of leading the team and responsible for the navigation solution approval and delivery. Then, two junior analysts with a considerable preparation and training in the ArgoMoon setup were dedicated to the routine operations of OD and FPC. Another senior analyst with several years of experience in the OD was dedicated to the support of the management activities when the team leader was not present. Finally, another junior analyst was allocated as backup support and for the tracking pass monitoring activities.

5.2.2 Data Flow

The ArgoMoon navigation process foreseen two main originators of input data: the DSN and the MCC. The acquisition of the radiometric observables was performed by the DSN which then uploaded all the products onto a server accessed via a redundant Virtual Private Network (VPN) from the MCC. Then, the MCC had a shared dedicated server that was accessible from the NAV using the SSH File Transfer Protocol (SFTP). This server was used as a share point where all the navigation inputs and outputs were uploaded. The primary responsibility of the MCC as navigation data originator was to upload the tracking data and calibrations on the share point as soon as they were available on the DSN's remote server. Then, all the data of attitude, telemetry, maneuvers, events, trajectory and calibrations had to be uploaded from the MCC within the planned time frame. The data originated from the navigation process, like the estimated trajectory or the computed maneuvers, were uploaded by the UBO team from the NAV on the MCC share point to be available to the ARG and ASI teams.

The correct and reliable exchange of the data between the DSN, MCC, and NAV is a key aspect for the proper execution of the navigation. For example, if the data related to the attitude of the S/C or the maneuvers performed are not in the agreed format or are simply wrong, the processing of such data would fail leading to the impossibility of having a reliable estimate of the trajectory. Therefore, a dedicated Interface Control Document (ICD) was prepared by the UBO team with the aim of having a standard format and naming convention in the exchange of the navigation related products. The diagram of Figure 5.2 summarizes the data flow concepts described in this section.

5.2.3 Tracking

As introduced in Section 3.3, the configuration of the DSN tracking activities was managed through the OICD. This document usually includes all the parameters required to properly

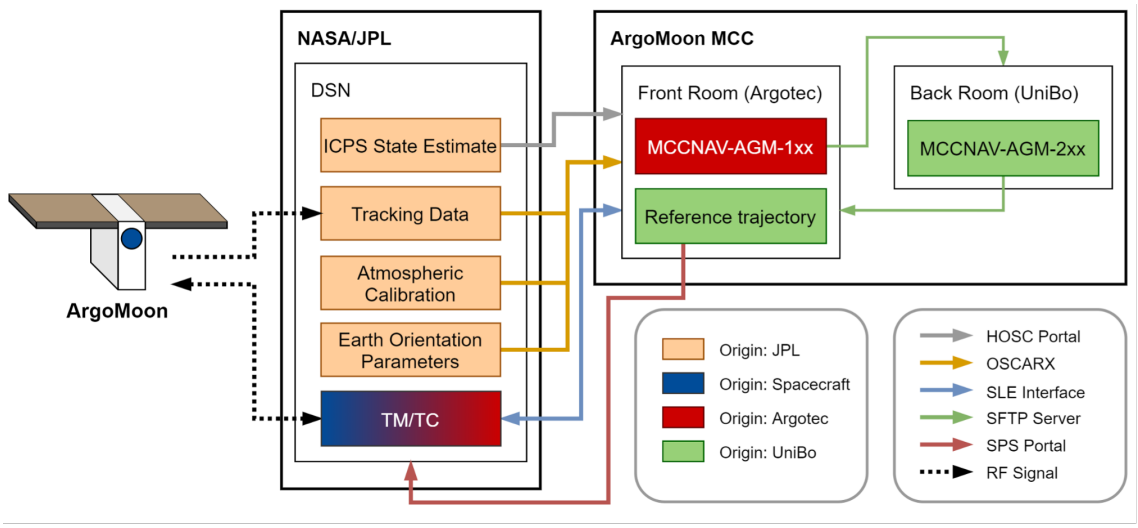

Figure 5.2: Data Flow and Communication of the ArgoMoon mission (courtesy of Argotec). The UniBo (UBO) navigation team was originally located in the back room but, for operation optimization reasons, the team actually operated its dedicated control room at the RSLab in Forli, Italy.

set the communication link with the S/C, including the tracking. The parameters that are critical for navigation are the Doppler's count time, the range acquisition frequency and the frequency with which the DSN has to provide the data to the MCC. The chosen value for the Doppler's count time was of 1 s to allow near real-time inspection of events as well as detectability of rapidly changing dynamics. The 1 s points can be conveniently compressed to 60 s during the OD process. The range acquisition frequency value was of at least 1 range measurement every 5 minutes as assumed in the feasibility assessment. The partials files frequency was of 15 minutes meaning that the DSN had to increment the tracking data file every 15 minutes with newly acquired data. In such way, the MCC always detected on the DSN shared server a single tracking data file with a size that increased every 15 minutes until the end of the tracking pass.

The ArgoMoon tracking schedule changed multiple times due to the shifting in the launch dates starting from the first launch attempt of August 29, 2022. However, the events were favorable to the ArgoMoon mission since the DSN was still able to maintain the baseline schedule and also add several additional tracking passes. In conclusion, the actual tracking schedule was be able to guarantee two-hours tracking passes twice per day. The final amount of tracking time was then widely in accord with the DSN agreement and it was four time the one assumed in the feasibility assessment for the first 7 days.

5.2.4 Processes

The navigation responsibility was to provide the reconstructed and predicted trajectory of ArgoMoon as well as compute the planned STMs if the correction was required. The navigation support was planned for the whole mission, from the launch up to the EOM, included the post-mission trajectory reconstruction and the archiving of the results. These high-level objectives originated then a set of routine actions and minor objectives in charge of the navigation team that are summarized as follows:

- Provide a real-time support during the tracking passes in correspondence of critical mission phases.

  - Critical phases are the mission Phase 1, in particular the first signal acquisition, the execution of an orbital maneuver, the close encounters of the Moon or the Earth, and critical events like an unexpected behavior of the S/C.

- Perform a basic and rapid OD after each tracking pass to monitor the predicted trajectory.
- Deliver a consolidated OD solution before each planned STMs or as soon as possible when a critical event occurs.
- Verify if the predicted trajectory in correspondence of a planned STM requires to be corrected.
- Compute and deliver the STM together with the consolidated OD solution if the correction was required.
- Provide a report of the estimated parameters and fulfillment status of the navigation requirements.

The process for operational navigation of ArgoMoon was organized on the basis of the assumptions and strategy originated from the design phase, as well as the objectives and actions described above, taking inspiration from the techniques adopted by JPL. The navigation team's working day usually began with the activities preparation in particular with the update of the timeline of the events, tracking, S/C attitude, maneuvers and small forces. The work of each team member was organized to understand the occurred events, prepare the OD setup for the daily analysis, organize the operations based on the upcoming deliveries and mission events, and perform the OD and FPC run in view of the next deadline. The amount of additional data available at the start of a shift was typically that of two tracking passes since the end of the previous shift. However, there could be also cases where no new data was acquired since the last process. As a result, the following actions list the usual process flow followed after a DCO:

1. Setup of a new OD case: a new working environment for the OD software is created daily by using the case of the previous day or by replicating the operations template if a new OD arc begun. As seen in Chapter 3, the ArgoMoon OD arc encompasses a single REV, thus the OD case should contain all the settings and data of the previous cases up to the beginning of the arc. Usually, an additional OD run is also performed to replicate the results of the previous solution to validate the new OD case.

2. Download of the data: the tracking data files, and the S/C data products required for the OD process are downloaded from the SFTP server of the MCC. Usually, the download is incremental meaning that all the previous data products had already acquired in the previous OD runs.

3. Pre-processing: this activity regards the conversion and parsing of all the downloaded data to be used in the navigation software. The conversion is performed through an automated process that in general do not involve a particular human intervention. However, the converted data are always checked for correctness and eventually cleaned of outliers or conversion errors. In the conversion of the Doppler data with CT of 1 s, a compression to a CT of 60 s is also performed to have the data ready for the later phases. The parsing of products like maneuvers or propagation

states is conducted with a semi-autonomous tool that required the navigator to select the right method of conversion as well as the output format. The pre-processing activity usually involves a quick OD run for the inspection of the quality of the data and the correctness of the parsed products.

4. Pass-through: the identification of unexpected events, as well as the inspection of the quality of the data and the correctness of the parsed products, is performed by computing the so-called pass-through residuals. The latter quantity is the difference between the pre-processed observables and those computed using the previous estimate model without involving any filtering process. If the pass-through residuals do not significantly deviate from zero and there are no major signatures, then the actual dynamical model is giving a good prediction and only minor corrections should be expected. The pass-through analysis allows to immediately notice if the previously estimated trajectory is reliable or if in the meantime there were unmodeled events that deviated the S/C from its path.

5. OD run: once the OD case is ready to work and all the data had been downloaded and pre-processed, the trajectory reconstruction and prediction could begin. The OD run is an automated routine that performs the propagation of the trajectory, computes the predicted observable, executes the filter correction, and updates the actual dynamical model with the obtained result. As describe in Section 1.3, the OD run may require multiple iterations before converging to a solution. The convergence is considered reached when the correction to the solve-for parameters is significantly smaller than their formal uncertainties.

6. Solution inspection: the converged OD solution is then inspected and analyzed by the analyst in terms of parameters estimation and residuals. This is usually a critical activity since it depends also on the expertise and capabilities of the analyst that has computed the OD solution. Typically, a potential good solution is firstly identified when there are signatures-free residuals and the ratio between the correction delta of the estimated parameters and their *a priori* uncertainties is significantly lower than 1. However, such optimal conditions are rarely met during the operations and then additional solution evaluations has to be performed. Therefore, a graphical report of the solution is generated with the aim of helping the navigators to evaluate the following quantities:

   - Representation of the predicted trajectory with respect to the reference one using different coordinate systems:
     - B-plane coordinates if the upcoming encounter is a fly-by of the Moon.
     - Cartesian position coordinates if the upcoming encounter is an apogee.
     - Cartesian velocity coordinates if the upcoming encounter is a perigee.
   - Plots of the estimated parameters and uncertainties with respect to their *a priori* values.
   - Plot of the antenna pointing difference between the new estimated trajectory and the latest delivery to the DSN.

   The former quantities are chosen also to evaluate the status of the selected solution with respect to the navigation requirements. The inspection of the solution may finally lead to a no-go and a reiteration of the OD run changing assumptions, data weights, *a priori* values and uncertainties.

7. Solution approval: after the previous points were all completed by each analyst, the supervisor collects all the converged good solutions to make a comparison and select the one to deliver. Usually, this process is required to be sure that all the analysts have found consistent solutions through their independent analysis meaning that the obtained results are reliable.

8. FPC run: if the predicted trajectory of the validated OD solution is not achieving the target aimpoint a STM is computed to correct the trajectory. This step is nominally performed only for the planned STMs whose schedule is described in Chapter 4.2.5. However, the FPC was planned to be executed also in contingency cases where an unplanned trajectory correction has to be performed or an OTM has to be reoptimized. The computation of the orbital maneuver is performed by means of a dedicated differential correction tool based on the Hanson-Krogh algorithm (Section 1.3.2). The dynamical model and the S/C initial state exploited by the FPC to compute the maneuver are taken directly from the accepted OD solution. The trajectory propagations performed in the differential corrector end 1 hour after the target's epoch such that the computational time is minimized. The target and goal coordinates are extracted from the reference trajectory based on the designed trajectory control strategy described in Section 4.2. The computed maneuvers are implemented in the FPC using the finite model as described in Section 3.4.4 where the control vector of the differential corrector was composed by the direction of the maneuver and its duration. Moreover, as requested by the NAVREQ-4, the computed orbital maneuver had to be subdivided into single burns of maximum 800 s of duration separated by 10 minutes of cool-down period. Therefore, the FPC routine was refined using the following algorithm:

   (a) Optimize a correction maneuver as a single continuous burn.

   (b) Subdivide the optimized burn into independent maneuvers as follows:

      - Each maneuver will be saturated to a duration of 800 s except the last one whose duration covers the remaining fraction of time.
      - The first maneuver starts from the same epoch of the continuous burn previously optimized.
      - The i-th maneuver start after the end of the previous plus 10 minutes of cool-down.
      - All the subdivided maneuvers share the same direction of execution.

   (c) Reoptimize only the last burn's duration and the global direction shared by the maneuvers.

   Following the described algorithm, the FPC returned a set of independent burns with a duration of 800 s except the last one whose duration was optimized together with the direction shared by all the burns of the set. In this way, the MCC could directly use the FPC outputs to generate the telecommands without carrying out further post processing.

9. Upload of the outputs: after the OD solution was selected by the supervisor, the generated outputs, and the computed maneuver are converted into the format agreed with the MCC. Then, the navigation products are uploaded to the SFTP server of the MCC so that the operators could generate the maneuvers telecommands to be sent to the S/C.

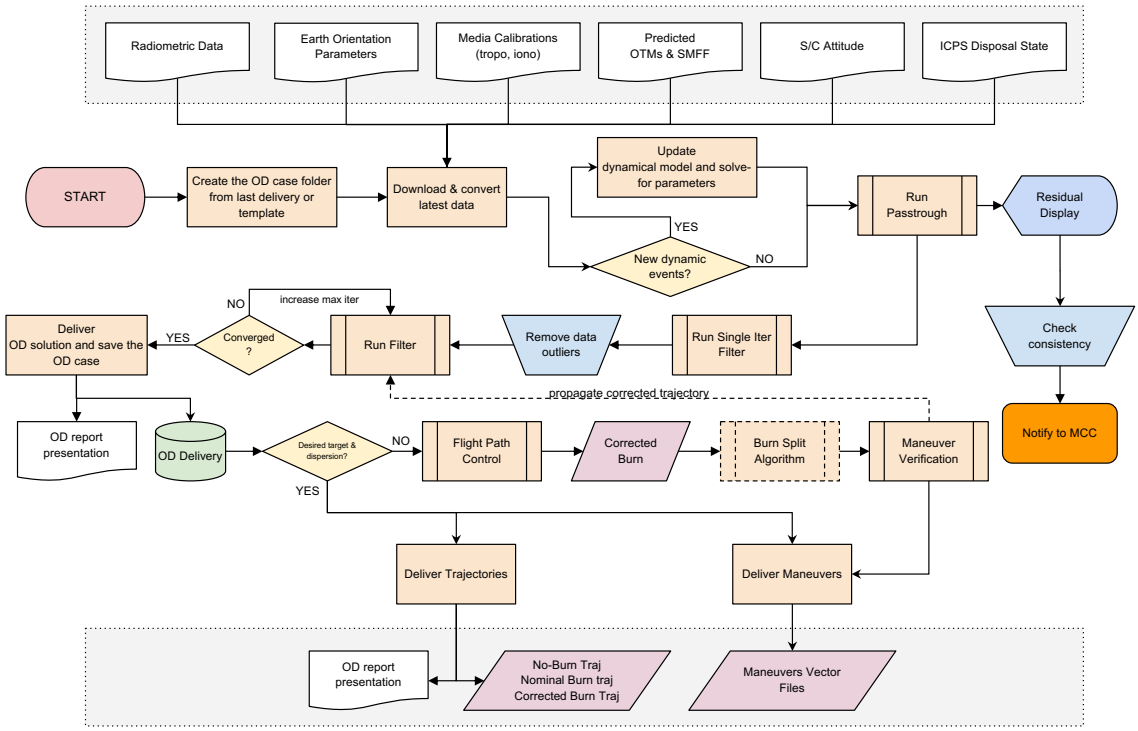

Figure 5.3: Flowchart of the ArgoMoon navigation routine based on the typical deep space navigation operations.

All the entire navigation routine described in the previous steps was performed when a consolidated solution had to be delivered. However, in correspondence of the intermediate tracking passes between planned deliveries, the routine was limited to the points 1 to 6, while the first point was skipped if the routine was repeated several times in the same day. Furthermore, during the phases where the real-time support was provided, the routine was limited to only the points 2 to 4. A detailed flowchart that summarizes the described routine is represented in Figure 5.3.

5.3 Navigation Results

The preparation of the navigation setup to the early operations begun the day before the launch. The UBO team took service with all the members one hour before the launch to fully support the LEOP. The first work shift was prepared to cover the operations up to the end of the launch day in view of the OTM1A scheduled for the next morning. Since no OD delivery was expected in the first day of the mission, the activities were focused on the quasi real-time inspection of the residuals and the execution of a preliminary OD to evaluate the status of the injection in orbit. However, in the case of failure of the ProxOps, one member of the team was dedicated to the contingency plan to evaluate the possibility of performing a safe rendezvous with the ICPS with the data available at that time.

5.3.1 Initial Conditions

The ArgoMoon orbital injection state was set to be equal to the one of the ICPS at its disposal epoch using the last reference state provided by NASA at that time. Anyway, as soon as NASA released the reconstructed Interim Cryogenic Propulsion Stage (ICPS)

state after the injection in orbit, the initial state of the S/C was updated with the latter, whose values are reported in 5.1. The expected mass of ArgoMoon at the deployment was updated to 13.261 kg by considering the losses due to the stocking period of almost 1 year inside the ICPS. The predicted attitude was initially assumed to be nominally Sun-pointing, and Earth-pointing when the S/C was supposed to be communicating with the ground.

Table 5.1: Initial state of ArgoMoon after the launch.

Parameter	**Epoch (UTC)**	**Center**	**Frame**	**Value**		
ArgoMoon Initial State	16-NOV-2022 10:23:38.921	Earth	EME2000	X	-35933.99753	km
				Y	8640.29677	km
				Z	8920.49489	km
				VX	-4.28744	km/s
				VY	-0.73689	km/s
				VZ	0.05055	km/s

The first signal acquisition was expected to occur within 30 minutes after the deployment of the S/C, depending on the actual launch time. Due to the characteristics of the ArgoMoon's IRIS radio described in Section 2.2, a constant Doppler bias of 0.124 Hz was implemented in the Doppler model and estimated in the filter. Moreover, due to the expected IRIS status at the first boot-up, an additional Doppler bias of -1.458 Hz was implemented but only for the first tracking pass of the mission. This because the MCC planned to send a POKE command during the second tracking pass to calibrate the IRIS radio and remove the previous bias. To account for the characteristic IRIS transponder delay of 6.8837×10^{-6} s measured on ground, a constant bias on the range measurements equal to 7325.6 Range Units (2.0564 km) was implemented and estimated in the filter. Furthermore, due to operational purposes, during the first tracking pass no range data was expected.

5.3.2 Baseline Filter

The baseline configuration of the estimation filter for the operations is reported in Table 5.2 and Table 5.3, for the estimated and considered parameters, respectively. The S/C epoch state *a priori* uncertainty was provided using the predicted injection covariance in geocentric RTN frame of the ICPS at the disposal epoch. Then, since the S/C epoch state was estimated in the integration inertial frame Earth Mean Equator at J2000 (EME2000), the ICPS diagonal injection covariance was rotated from the geocentric RTN frame to EME2000 using the assumed initial S/C state. Unfortunately, NASA had already communicated before the launch that it would not deliver an estimated ICPS covariance to the CubeSats teams as it was an information protected by International Traffic in Arms Regulations (ITAR). The mis-modelling of the SRP and other unmodeled forces were managed by estimating the stochastic accelerations and an SRP scale factor. For each tracking pass, a stochastic uncorrelated range bias was estimated. A correction to the IRIS transponder delay was estimated as a constant bias on the range measurements. The described baseline filter configuration was used in each OD process since the LEOP without performing particular changes. As described in the feasibility assessment chapters, in case of an orbital maneuver, the maneuver estimation was performed in magnitude and direction using 10% of uncertainty on the ΔV and 1.1 deg on the right ascension and declination.

Table 5.2: Baseline filter setup for the estimated parameters during REV0 operations.

Parameter	**Unit**	***A priori* Uncertainty**	**Comments**
S/C Epoch State			
Position	km	30.0 / 60.0 / 15.0	Diagonal covariance matrix in geocentric RTN frame.
Velocity	m/s	2.1 / 2.7 / 4.2	
SRP			
Scale Factor	-	10%	Details on Section 3.4.
Observables Bias			
Per-Pass Range	m	2	Ground stations residual delay.
Constant Range	m	500	IRIS transponder residual delay.
Constant Doppler	Hz	0.0124	10% of IRIS Doppler bias.
Stochastic Accelerations (S/C body frame)			
X/Y/Z	km/s^2	1×10^{-12}	X/Y/Z sigmas assumed from [89] and multiplied by 2.
Time Batch	hours	8	

Table 5.3: Baseline filter setup for the considered parameters during REV0 operations.

Parameter	**Unit**	***A priori* Uncertainty**	**Comments**
Celestial Bodies GMs			
Earth	km^3/s^2	5×10^{-4}	From DE430 [83].
Moon	km^3/s^2	1.4×10^{-4}	From DE430 [83].
Station Locations			
DSN	cm	3	Per axis, assumed from [89].
Path Delays			
Troposphere (wet/dry)	cm	1/1	Assumed from [89].
Ionosphere (day/night)	cm	5/1	
EOP			
Polar Motion	deg	8.6×10^{-7}	Assumed from [89].
UT1 Bias	sec	2.5×10^{-4}	

5.3.3 Launch and Early Operations

On November 16, 2022, at 06:47:44 UTC, Artemis-1 was successfully launched onboard the Block 1 variant of the SLS from Launch Complex 39B at the NASA's Kennedy Space Center, Florida, United States. At 06:55:59 UTC, the ICPS separated from the SLS core stage and 45 minutes later it performed the perigee raise maneuver to enter in orbit around the Earth. Then, after an successful TLI maneuver, the Orion S/C separated from the ICPS at the 08:45:20 UTC exposing the secondary payloads to the space for the first time. The ICPS executed the disposal burn at 10:09:20 UTC initiating the activities for the CubeSats deployment. At the 10:23:38.921 UTC /(*disposal epoch*), the ICPS became an uncontrolled body slowly spinning around its primary inertia axis with a rate of about 6 deg/s. The deployment of the CubeSats was automated by a countdown clock started at the disposal epoch and 6 minutes later the release of ArgoMoon was expected. At the same time, NASA delivered the estimated state of the ICPS at the disposal epoch to the CubeSats teams. Nevertheless, the ICPS injection covariance was not provided due to the ITAR imposed by NASA on the performance of SLS. However, since this was the most accurate ICPS state available at the ArgoMoon deployment, following the procedures it was used as the ArgoMoon initial state. Therefore, the quasi real-time pre-fit inspection during the first tracking pass was performed by exploiting the S/C trajectory propagated from the updated initial state.

As for many of the other CubeSats, the deployment of ArgoMoon was not completely free of drawbacks. The release of the S/C took place at 10:36:04 UTC and the first two-way Doppler points were acquired starting from 10:42:36 UTC by DSS 55 of Madrid's DSN complex. The early downloaded telemetry was telling that the S/C was not properly charging its batteries and it was tumbling with a global spin rate of about 11 deg/s. The tumbling was caused by the 6 deg/s spin rate of the ICPS plus a contribution of 5 deg/s due to the dispenser mechanism. The complete opening of the SPA was initially impeded by the satellite rotation, which caused a fast battery drain during this phase. To stop the tumbling motion and regain the control of the attitude, the S/C performed two desaturation (DES) maneuvers, named DES1 and DES2, at the 11:10 UTC and 11:16 UTC. Unfortunately, the detumbling took approximately 15 minutes during which the S/C was put in *safe mode*, and it was unable to safely perform the planned ProxOps. The End of Tracking (EOT) on the DSS 55 occurred at the 13:34 UTC. The main events from the launch up to the end of the first tracking pass are collected in Table 5.4.

Table 5.4: Summary of the main events during the first hours after the launch on November 16, 2022.

Event	**Time (UTC)**	**Comments**
Launch	06:47:44	Actual SLS launch epoch.
ICPS disposal	10:23:39	Last known orbital state of the ICPS.
Deployment	10:36:04	Release of ArgoMoon from the ICPS.
Signal acquisition	10:42:36	Beginning of the first tracking pass.
DES1	11:10:00	First maneuver to offload the RWs.
DES2	11:16:00	Second maneuver to offload the RWs.
EOT	13:34:00	End of the first tracking pass.

Figure 5.4 reports the very first pre-fit residuals of the mission computed from the first partial dataset received by the DSS 55 approximately 16 minutes later the signal acquisition. As can be seen from the local trend of the presented data, the S/C tumbling motion

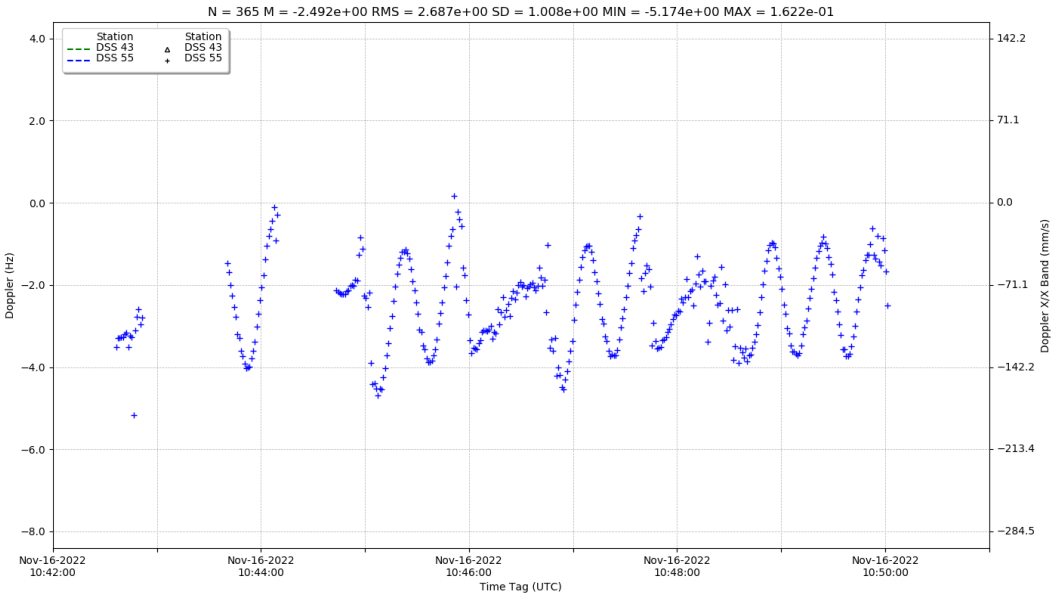

Figure 5.4: Pre-fit two-way Doppler residuals (CT = 1 s) of the first 15 minutes of data acquired by the DSS 55 after the S/C deployment.

was producing a clear and distinguishable signature. Such evidence was an important confirmation of the status of the S/C communicated by the telemetry. However, these events have made the initial data very difficult to process and use for the OD because the removal of the signatures requires the knowledge of the antenna phase center position in the body-fixed frame (can be estimated) and the attitude motion (not known). The complete pre-fit residuals of the first pass of the mission are reported in Figure 5.5. Inspection of the pre-fit residuals allowed to identify the Doppler steps due to the DES1 and DES2 as well as the frequent discontinuities in the data due to the loss of the carrier lock, probably as a consequence of the bad attitude. In principle, a DES maneuver should not produce a variation in the S/C's velocity, but the ArgoMoon's attitude control thrusters were not planar in the rear face; hence some parasitic thrust was also generated during the RWs desaturation. The execution of an orbital maneuver produces a single evident step in the pre-fit Doppler residuals. This residuals' step is two times (for two-way Doppler observables) the variation of the S/C velocity in the direction of the Line Of Sight (LOS) between the ground antenna and the S/C itself. Therefore, by analyzing this pre-fit residuals' steps, it is possible to preliminary evaluate the performance of an orbital maneuver and its effective ΔV. For DES1 and DES2, as can be seen in Figure 5.5, the Doppler steps were approximately 100 mm/s each, meaning that the ΔV along the LOS of each DES maneuver was about 50 mm/s.

Due to the events happened during the first tracking pass, the DSN required support from European Space Tracking (ESTRACK) to track ArgoMoon for approximately 1 hour before the next nominal tracking pass that was expected at the 19:20 UTC. This additional tracking pass was successfully performed by the ESTRACK's 35 m antenna of the Malargue complex in Argentina. However, since the communication through ESTRACK was not expected, the DSN personnel had to manually retrieve the tracking data from the ESTRACK's servers before uploading them on the DSN's share point. Therefore, due to the additional time required by the latter action, the Malargue's data was not available to the navigation team during the first day and then it was not possible to exploit them

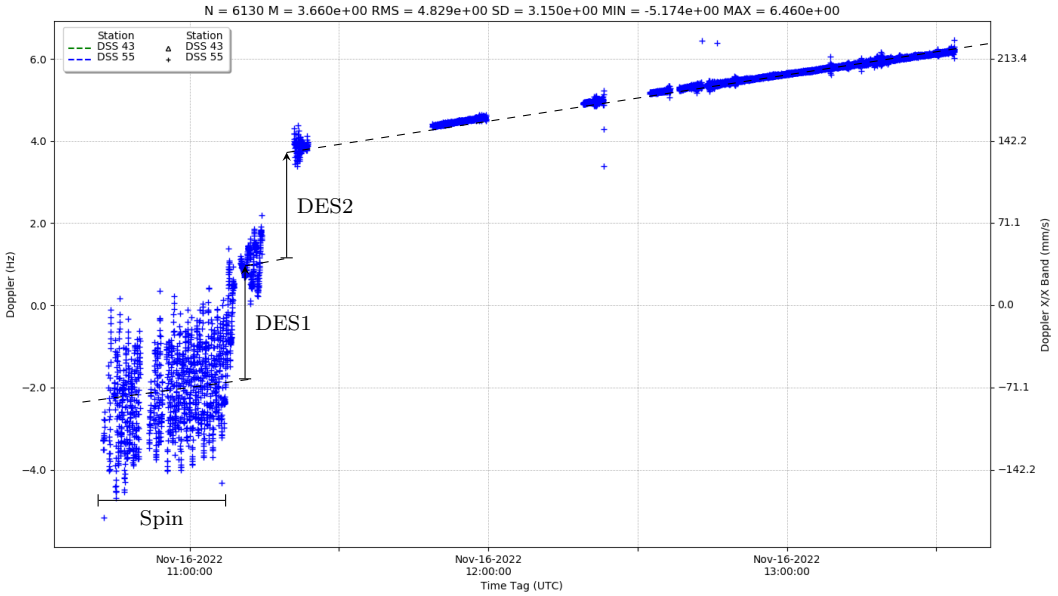

Figure 5.5: Pre-fit two-way Doppler residuals (CT = 1 s) of the first mission's tracking pass on the DSS 55.

in the evaluation of an initial OD solution.

The very first OD analysis was performed using all the data of the DSS 55 tracking pass compressed with a CT of 10 s and the outliers removed. To fit such noisy and disturbed data, a deweighting was necessary by dividing the pass into four separate batches where each of them had its own weight, as can be seen from Table 5.5. Moreover, as expected from the IRIS radio characterization described in Section 2.2, this first OD solution included the correction to the initial pre-POKE Doppler bias of -1.458 Hz plus the global one of 0.124 Hz. Unfortunately, no range data was available at that time since to acquire them an update of the IRIS settings was required. The update of the IRIS was scheduled on the second tracking pass of the mission to avoid the loss of the locking during the first communication pass. Therefore, without the range data, it was not possible to immediately constraint the S/C position with respect to the Earth. The estimation included the two DES maneuvers as well as the release dynamics modeled as an impulsive maneuver with no mass reduction. The release maneuver was modeled as described in Section 2.4 using the ICPS attitude provided by NASA at the disposal epoch. The uncertainty associated with the release direction was of 180 deg for the right ascension to account for the unknown spinning of the ICPS and of 10 deg on the declination (assuming the nominal inclination of the dispenser). In any case, such release was not observable and then the former modelization was later abandoned.

Table 5.5: Weights applied to single batches of the data of the first tracking pass of November 16, 2022, for the computation of the UBO001 solution.

Batch	From (UTC)	To (UTC)	Weight (Hz)	Comments
1	11:40	11:10	0.6287	Spin
2	11:10	11:15	0.3021	After DES1
3	11:15	11:25	0.0898	After DES2
4	11:25	13:34	0.0028	Remaining Data

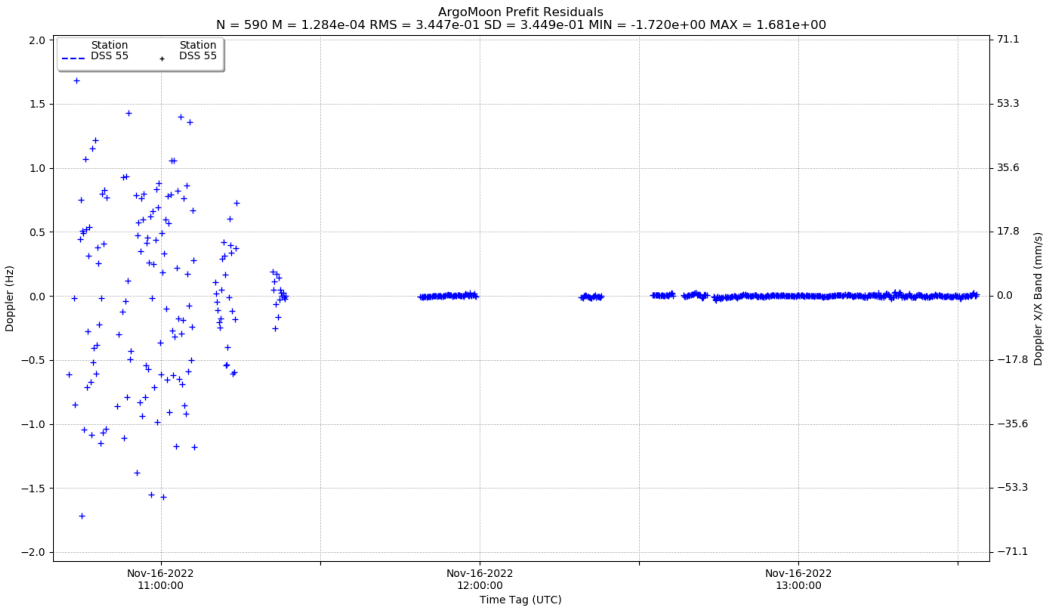

Figure 5.6: Post-fit two-way Doppler residuals (CT = 10 s) of the UBO001 solution.

The obtained solution, named UBO001, was very rough due to the corrupted data, the expected biases, and the lack of range data. However, this estimation was necessary to assess that the injection in orbit was not leading ArgoMoon to an impact with the Moon. Moreover, since the ProxOps were not performed, a contingency plan was activated, and it was necessary to also confirm if ArgoMoon could intercept the ICPS again for a rendezvous.

The UBO001 solution post-fit residuals are provided in Figure 5.6 while the trajectory estimation mapped on the B-plane of M0 encounter is reported in Figure 5.7. The UBO001 showed that the injection in orbit provided by the ICPS placed ArgoMoon in a trajectory that, if left uncorrected, would lead five days later to a Moon fly-by very close to the surface. In fact, the error ellipse mapped on the B-plane is very close to the impact radius (Appendix A) meaning that statistically there was a marginal impact risk and then further data was necessary to confirm this solution.

Regarding the ICPS rendezvous opportunity, no useful ArgoMoon-ICPS relative motion data was available after the deployment, making impossible to precisely estimate the trajectory of ArgoMoon with respect to the ICPS with only the noisy ground based data. Indeed, the ArgoMoon trajectory estimation mapped on the relative velocity plane of the ICPS, Figure 5.8, showed that the relative 3-σ position uncertainty with the ICPS was too large to fit within the admissible region and thus guarantee a safe rendezvous. Based on the results provided by the UBO001 solution, the navigation team recommended to not perform any rendezvous maneuver to intercept again the ICPS. In accordance with the recommendation, the final decision of ARG and ASI teams was to discard the contingency rendezvous with the ICPS to ensure the safe continuation of the ArgoMoon mission.

The UBO001 solution was not delivered as final due to the described problems and the lack of data to validate it at that time. The UBO001 estimated trajectory was then used as backup for the DSN pointing in case of carrier locking problems.

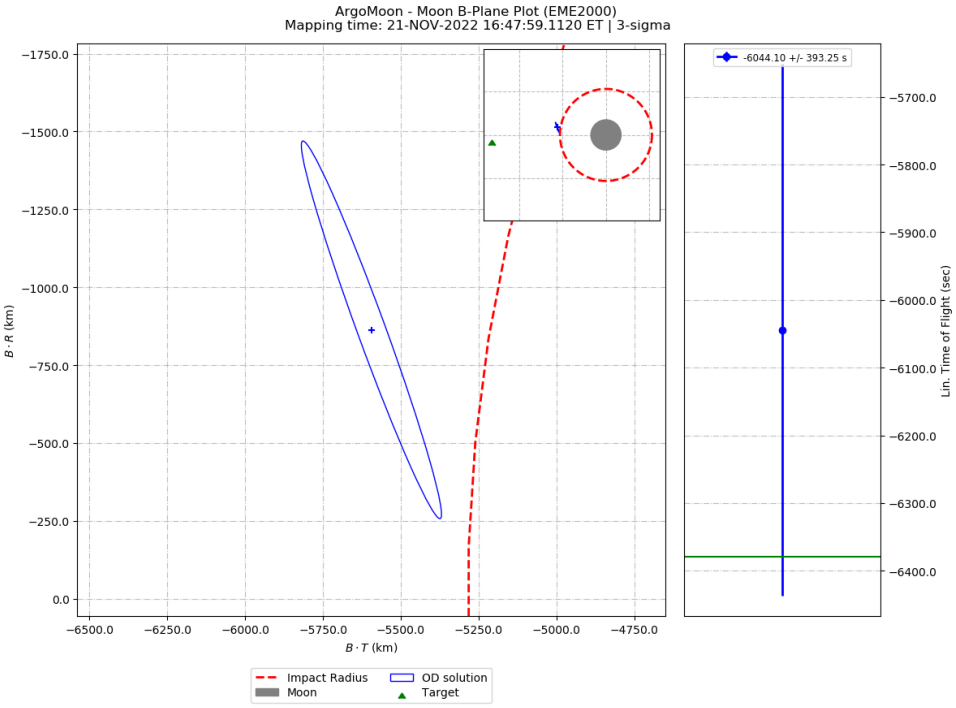

Figure 5.7: Predicted trajectory and 3-σ uncertainty mapped to the Moon B-plane after launch (UBO001 solution).

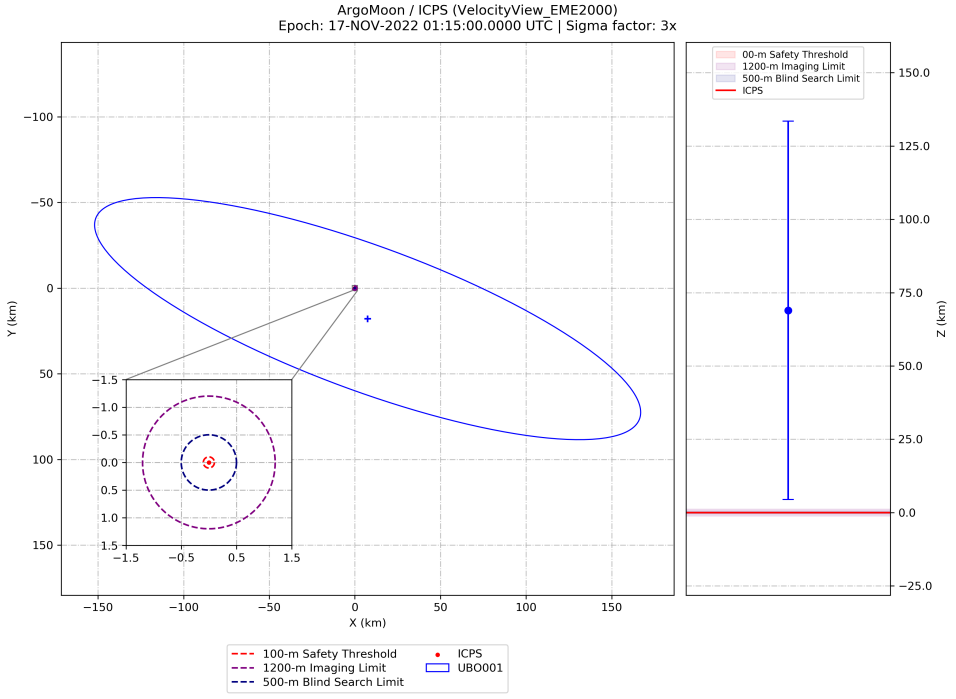

Figure 5.8: Predicted trajectory and 3-σ uncertainty mapped to the relative velocity plane of the ICPS (UBO001 solution).

5.3.4 Solution UBO002

In the early morning of the second day of operations, a new intermediate solution, UBO002, was determined using a DCO right after the third tracking pass of the mission. This third pass was provided by the DSS 43 while the data from the Malargue complex was still not available at that time. The UBO002 solution was computed to evaluate if the OTM1 had to be corrected, and to provide support to the DSN pointing in case of poor reception of the S/C's downlink signal. The pass-through of all the two-way Doppler data available for the UBO002 solution, generated using the UBO001 solution, is presented in Figure 5.9a, while a detail of only the data of the DSS 43 is provided in Figure 5.9b.

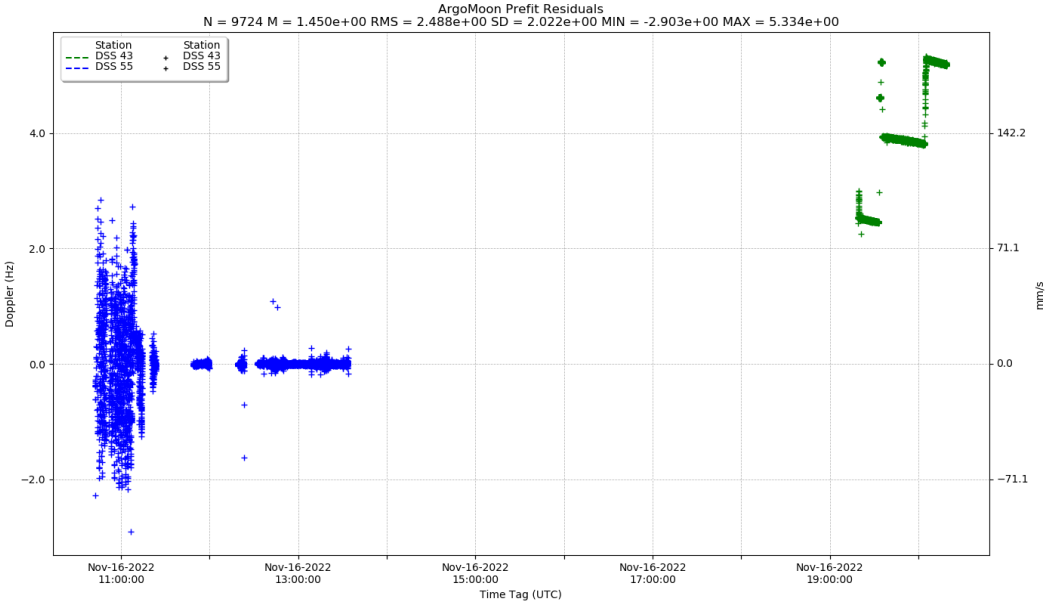

(a) *Data from DSS 55 and DSS 43.*

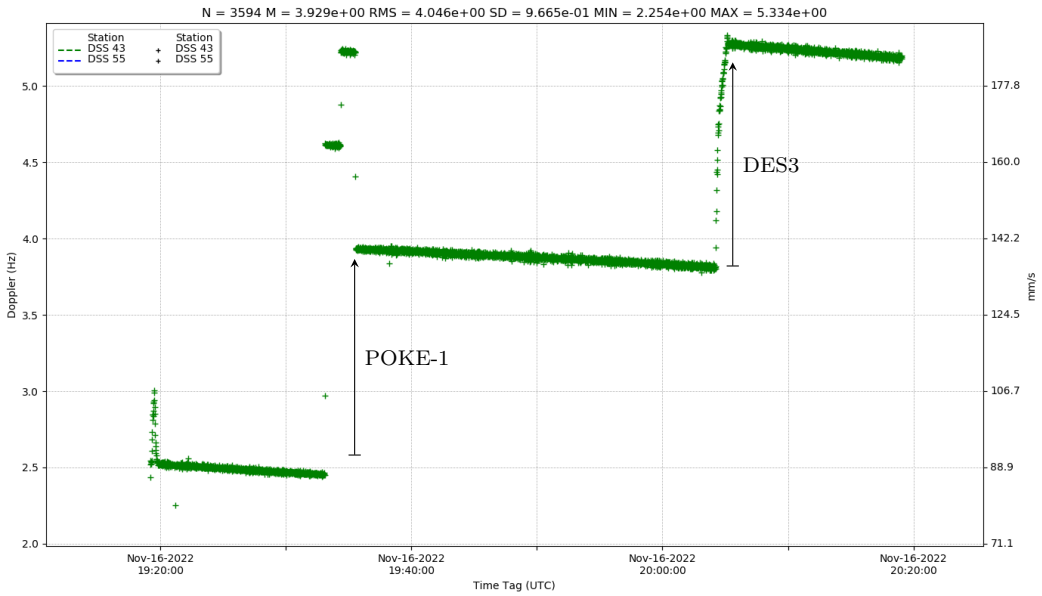

(b) *Detail of the data from DSS 43.*

Figure 5.9: Pre-fit two-way Doppler residuals (CT = 1 s) using the UBO001 solution.

During the pass on the DSS 43, a command identified as POKE-1 was performed to calibrate the IRIS radio at 19:35 UTC of November 16, 2022. In fact, by inspecting the pre-fit residuals, it is possible to see a step on the Doppler at that time of about 1.469 Hz (55 mm/s), meaning that the calibration was successful. Thanks to the radio calibration, the DSS 43 pass was also the first of the mission having the range measurements. Nonetheless, to reduce the spin rate of the RWs and ensure the satellite's operability, an additional maneuver named DES3 was performed at 20:04:10 UTC. This DES maneuver successfully helped to reduce the spin rate, but it further complicated the trajectory reconstruction and estimation. Therefore, in the computation of UBO002, it was decided the ignore all the data before the DES2 maneuver to improve the OD and reduce the number of unmodeled events. Furthermore, also the data acquired in the vicinity of the IRIS radio calibration and the DES3 were discarded. The removal of the release and DES1-2 maneuvers from the model was then absorbed by the S/C injection covariance in the fit of the residuals. In any case, the range was successfully acquired after the POKE-1 command and then further data to constrain the solution were available. It is fundamental to point out that the UBO002 was able to fit only by constraining the Doppler biases of the DSS 55 and pre-POKE DSS 43 passes to be equal. After POKE-1, the initial Doppler bias of -1.458 Hz was removed and then only the global Doppler bias was required to be estimated.

The UBO002 post-fit residual of both Doppler and range are reported in Figure 5.10, while the predicted trajectory and its related uncertainty mapped on the B-plane of M0 are represented in Figure 5.11. The analysis of the B-plane results confirmed that the injection was acceptable because the trajectory with nominal OTM1A was compatible with the target within 3-σ and then no additional FPC was required. The blue ellipse of the nominal burn solution is larger than the No-Burn one due to the maneuver's uncertainty.

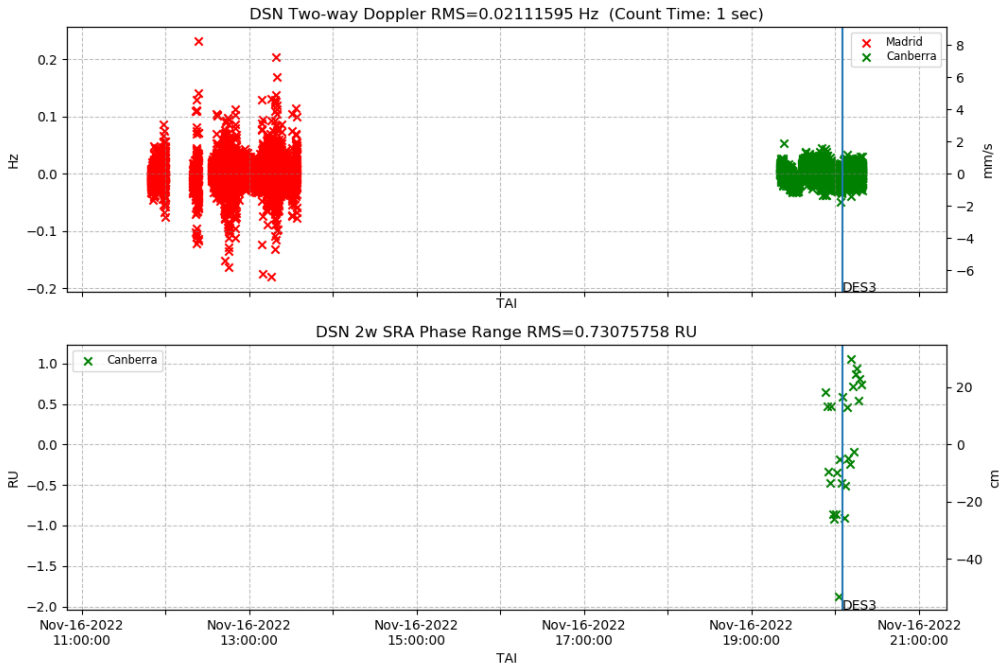

Figure 5.10: Two-way Doppler (top) and range (bottom) post-fit residuals of the UBO002 solution.

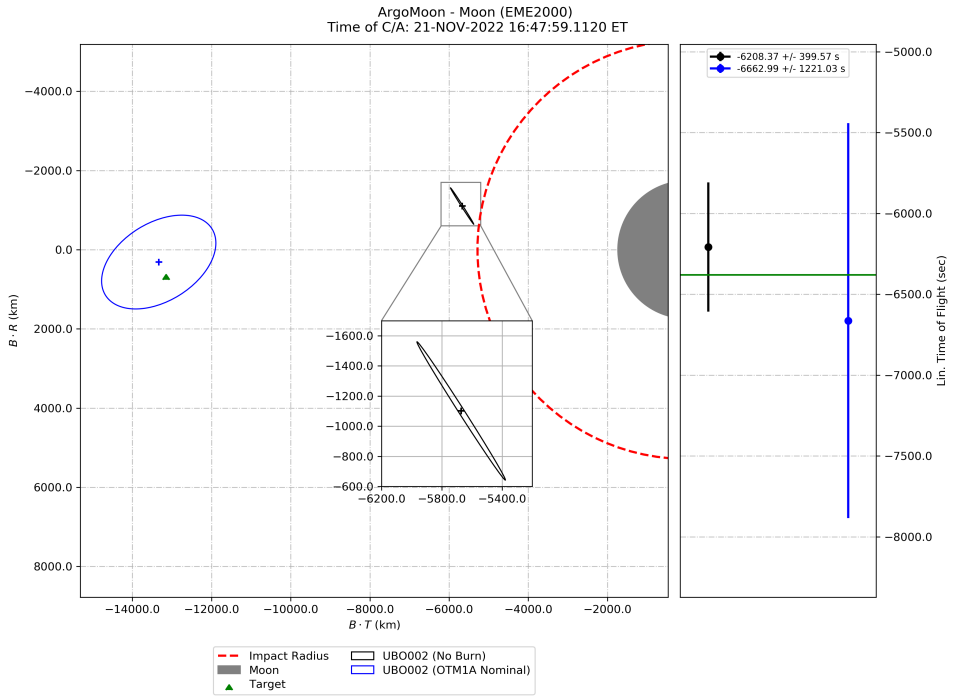

Figure 5.11: Predicted trajectories and 3-σ uncertainties of the UBO002 solution, with the nominal OTM1A in blue and No-Burn in black, mapped to the Moon B-plane.

5.3.5 Solution UBO003

The first orbital maneuver OTM1A was planned for the 11:43 UTC of November 17, 2022, with the aim of targeting the reference B-plane coordinates of the M0 encounter. As seen in the UBO001 and UBO002 solutions, if left uncorrected the path of ArgoMoon would lead to a dangerous close approach of the Moon and a successive escape into heliocentric orbit. The OTM1A was expected to occur during the third tracking pass of the mission in view of the DSS 53. However, the ARG team decided to scrub this maneuver and proceed with the backup maneuver OTM1B on the next pass. In that way it was possible to acquire more tracking data to have a more robust solution in view of the most important orbital maneuver of the mission. Moreover, the data of the Malargue station acquired during the first day was then available to the navigation team. The pass-through of the Malargue and DSS 53 passes using the previous UBO002 solution is reported in Figure 5.12a. Unfortunately, during the DSS 53 pass an unexpected reboot of the IRIS radio brought back the configuration to the pre-POKE one. Then, the reboot of the IRIS caused the Doppler bias of about -1.458 Hz to be present again as can be seen from the detail of the pre-fit data in Figure 5.12b. Furthermore, the IRIS reboot had again reset the settings for the correct acquisition of the two-way range that was not available anymore after that time.

For UBO003, the navigation team decided to use all the data since the DES2 maneuver, as done for UBO002. The Doppler data together with the new range data of the last two passes would certainly have improved the estimation and so they were used. Anyway, processing all data required constraining the Doppler bias to be the same before the POKE-1 command and after the reboot of the IRIS radio. In between the POKE-1 and the first IRIS reboot event, the estimated Doppler bias remained the global one. The

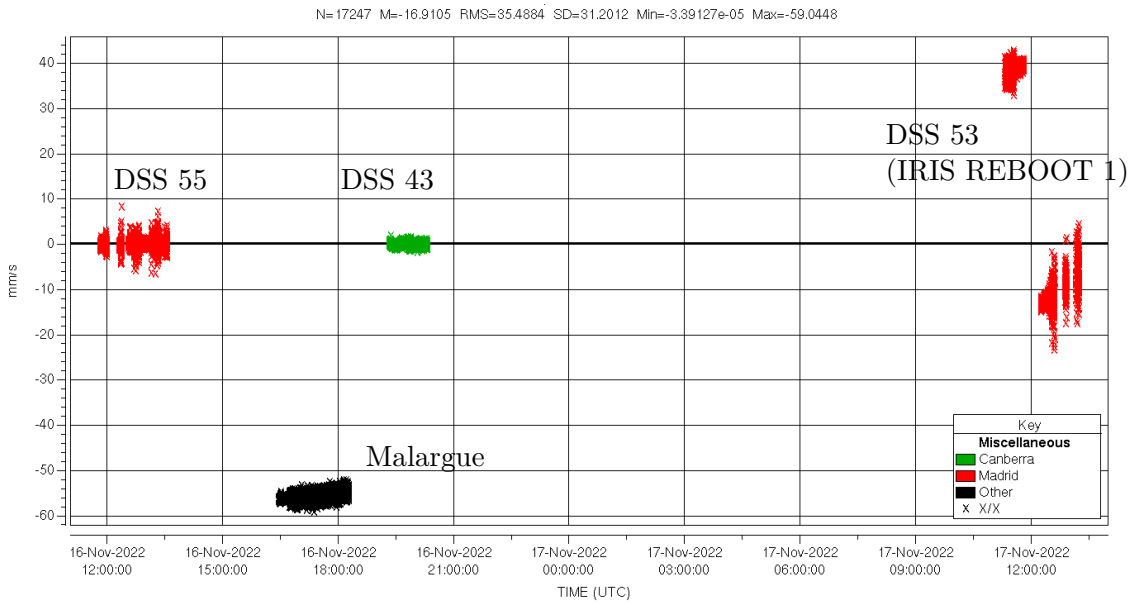

(a) *Data from DSS 55, DSS 43, Malargue, and DSS 53.*

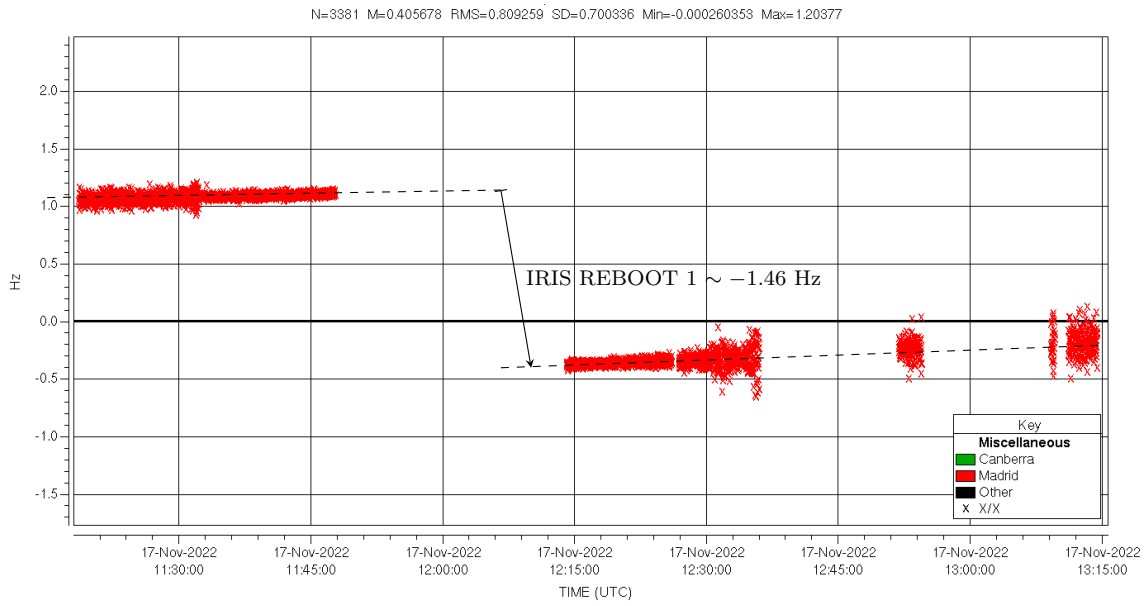

(b) *Detail of the effect of the first IRIS reboot on the data from DSS 53.*

Figure 5.12: Pre-fit two-way Doppler residuals (CT = 1 s) from Malargue (black) and DSS 53 using the UBO002 solution.

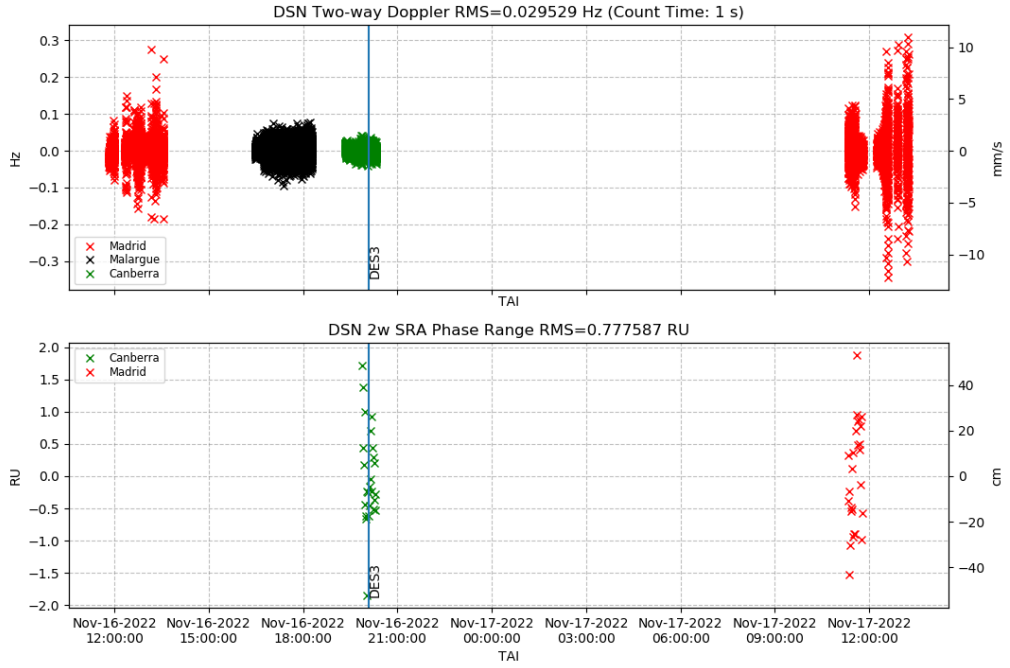

Figure 5.13: Two-way Doppler (top) and range (bottom) post-fit residuals of the UBO003 solution.

correction of the Doppler problem with that approach was named correlated per-pass Doppler bias estimation. The post-fit residuals of the UBO003 solution are shown in Figure 5.13. The UBO003 No-Burn trajectory uncertainty mapped on the B-plane of the M0 encounter is compared with the UBO001 and UBO002 solutions in Figure 5.14. The B-plane results show a lower estimated uncertainty for UBO003 whose nominal value was compatible to the previous solutions.

The UBO003 solution was particularly important since it was the first after which the FPC was performed. The OTM1B was planned in backup of the OTM1A and it was scheduled for the 23:50 UTC of November 17, 2022. The OTM1B was the backup of the unique deterministic maneuver of the mission and therefore had been calculated before launch. Even if the maneuver was only 7 hours away from the DCO, the navigation team was still able to provide an additional support by recomputing the OTM1B using the UBO003 solution. In fact, by looking to Figure 5.15, it becomes clear that the nominal OTM1B was off target by more than 3-σ, and the intervention of the FPC was important to save fuel. The computation algorithm of the FPC produced a corrected OTM1B composed by three single burns similarly as the nominal one. The detail of the computed maneuver and the comparison with the nominal one is reported in Table 5.6. The UBO003 and the corrected OTM1B were successfully delivered for the telecommands generation at 21:20 UTC of November 17, 2022.

5.3.6 Solution UBO004

Solutions UBO001 to UBO003 were computed using Doppler data at 10 s and 1 s of CT, which tend to mask the signatures due to unmodeled dynamics and events. When the

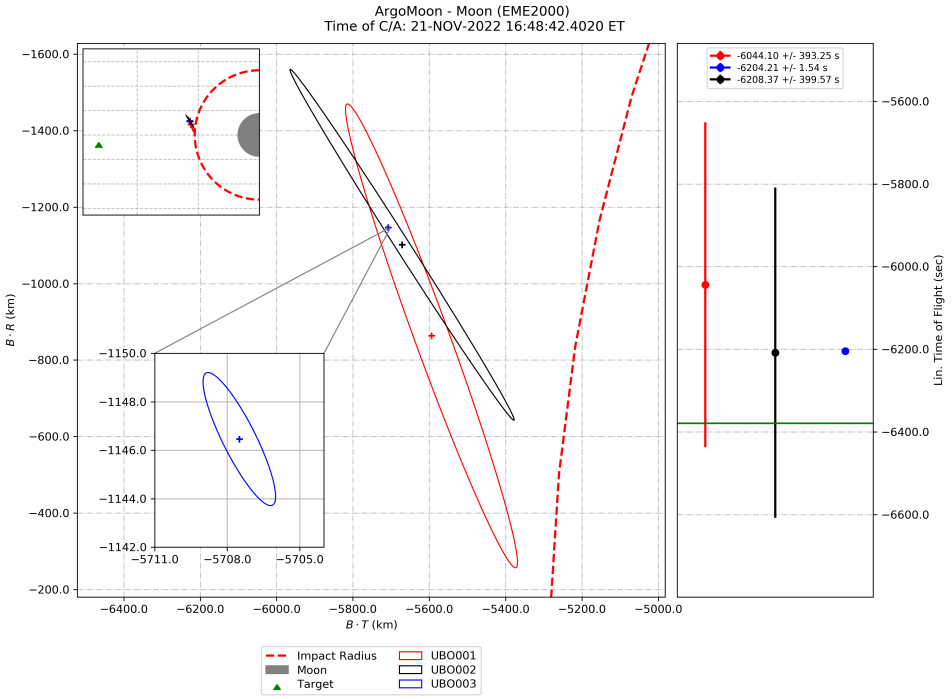

Figure 5.14: Comparison of the UBO001, UBO002 and UBO003 predicted trajectories and 3-σ uncertainties mapped to the Moon B-plane.

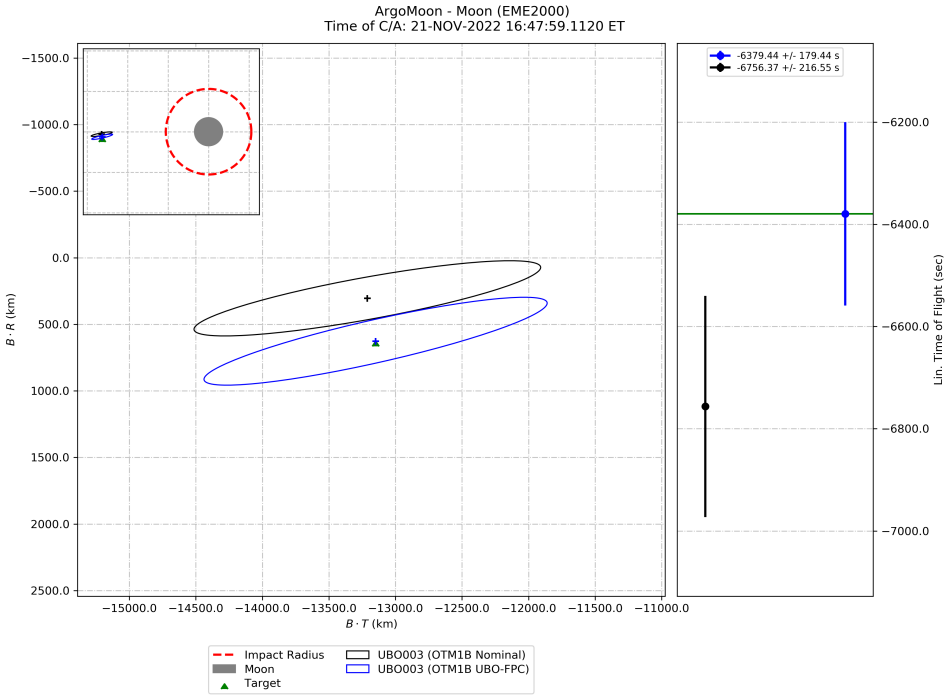

Figure 5.15: Predicted trajectories and 3-σ uncertainties mapped to the Moon B-plane for the UBO003 solution with the nominal OTM1B and with the one computed in the FPC.

Table 5.6: Comparison between the nominal OTM1B and the one computed through the FPC with the UBO003 solution.

Maneuver	**Burn**	**Time** (ET)	ΔT (s)	ΔV (m/s)	**Direction** (deg)	
					RA	DEC
OTM1B Nominal	1	17-NOV-2022 23:44:45	712.7	5.47	206.51	-8.43
	2	18-NOV-2022 00:06:36	712.3	5.48		
	3	18-NOV-2022 00:28:28	711.9	5.50		
	-	-	2136.9	16.45		
OTM1B UBO003	1	17-NOV-2022 23:44:45	800.0	6.04	209.46	-14.14
	2	18-NOV-2022 00:08:05	800.0	6.06		
	3	18-NOV-2022 00:31:25	583.18	4.43		
	-	-	2183.18	16.53		

Doppler data are compressed to 60 s the signatures becomes more evident and the OD process can be improved in terms of accuracy. The UBO004 solution was computed on November 18, 2022, using the Doppler data compressed at 60 s to obtain a more accurate and robust solution. The DCO of the UBO004 was at 07:30 UTC of November 18, 2022. A total of three tracking passes occurred after the delivery of the UBO003, where the first was on the DSS 36, the second on the DSS 43 and the last on the DSS 55 right before the DCO. Firstly, during the DSS 36 pass, the MCC sent a POKE-2 command at 21:20 UTC of November 17 to the IRIS radio for resetting the Doppler bias and enable the acquisition of two-way range data again. The DSS 36 pass ended just 20 minutes before the one on the DSS 43 where the OTM1B was planned. The execution of the maneuver, as computed from UBO003, was finally approved and the telecommands were sent by the MCC and successfully received by the S/C.

The first partial burn OTM1B1 started at 23:42 UTC of November 17 and lasted about 62 s resulting into a ΔV, reconstructed using telemetry data, of about 1.02 m/s. For operational and safety reasons, the ARG team decided to cancel the second partial burn and perform only the remaining OTM1B3. Even in this case, the S/C ignited the thruster at 00:27:27 UTC of November 18 and burned for 57 s of the expected 583.18 s. The pass-through of the UBO004 Doppler data with the UBO003 solution are reported in Figure 5.16. The pre-fit residuals of the DSS 43 were observed almost in real time by the navigation team, confirming the behavior of the engine.

The direction of the OTM1B was very close to the LOS with the Earth allowing to have an optimal observability of the performed ΔV. Through the analysis of the pre-fit residuals of Figure 5.16, the ΔV_{LOS} values were evaluated by measuring the steps in the residuals. Table 5.7 reports the LOS-ΔV values extracted from the telemetry and from the Doppler residuals of the UBO003 pass-through, compared to the commanded values.

Table 5.7: Comparison of the commanded and telemetry reconstructed values of the OTM1B with the one observed from the Doppler residuals.

Burn	**Commanded LOS-ΔV (m/s)**	**Telemetry LOS-ΔV (m/s)**	**Observed LOS-ΔV (m/s)**	**Telemetry LOS-ΔV angle (deg)**
OTM1B1	5.9612	1.0123	0.7815	170.5361
OTM1B3	4.3288	0.6809	0.6185	167.6574

The first tentative of fitting the new data with OTM1B was unsatisfactory and the correlation between the Doppler biases, the maneuvers and the SRP was starting to affect the convergence and the results. Then, provided also that the available time after the UBO004 DCO to the next pass was only 10 hours, it was necessary to adopt a safer and faster solution to fit the recent data and compute a new correction maneuver. As previously seen in the FPC analysis, the cost of the ΔV to target the B-plane of M0 rapidly increases as the fly-by approaches. Therefore, differently from what was planned, it was necessary to work faster without having the time of analyzing in detail all the events occurred since that time. The navigation team decided then to ignore the Doppler and range data before the POKE-2 command and in between OTM1B1 and OTM1B3 to improve the reconstruction. As for the UBO002 solution, all the uncertainties related to the previous events were absorbed in the estimation of the S/C initial state by enlarging the injection covariance by a factor of 3. The estimation of the burns 1 and 3 of the OTM1B was performed using the impulsive model as for the DES burns. Moreover, to reach convergence in the UBO004, the OTM1B *a priori* sigmas were increased by a factor of 3 leading to a 30% of uncertainty on the ΔV, 5.5 deg in the direction (both right ascension and declination), and 300 s in the execution time. In addition, only the global post-poke doppler bias was needed to be estimated since the Doppler data before the POKE-2 command were discarded. The converged UBO004 post-fit residuals are reported in Figure 5.17, while the uncertainty on the M0 B-plane is represented in Figure 5.18 together with the UBO002 and UBO003 solutions.

The UBO004 solution showed that the OTM1B approximately moved the $(B.T, B.R)$ of the S/C to -6340 km and -920 km respectively, where the effect on the $LTOF$ was negligible. However, the new B-plane aimpoint was approximately 6802 km away with respect to the reference target, thus still far from the nominal trajectory. Hence, together with ARG, the UBO team decided to compute for a correction maneuver, named STM0, to be executed and monitored in the next available communication window. The first available tracking pass in which perform such maneuver was in the evening of November 18, leaving only 10 hours to finalize the OD and perform the FPC. As expected, the computed STM0 had a ΔV magnitude bigger than the OTM1B and it was necessary to split the maneuver into four burns as from the NAVREQ-4. At the time of UBO004, it was decided together with the ARG team to continue with the targeting of the nominal B-plane conditions in the hope of being able to accumulate enough ΔV even with shorter burns. The parameters of the computed STM0 that was then uploaded on the S/C are reported in Table 5.8.

Table 5.8: Parameters of the STM0 computed through the FPC with the UBO004 solution.

Maneuver	**Burn**	**Time** (ET)	ΔT (s)	ΔV (m/s)	**Direction** (deg)	
					RA	DEC
STM0	A	18-NOV-2022 19:36:09	800.0	6.06	209.36	-11.97
	B	18-NOV-2022 19:59:29	800.0	6.08		
	C	18-NOV-2022 20:22:49	800.0	6.10		
	D	18-NOV-2022 20:46:09	501.17	3.83		
	-	-	2901.17	22.07		

As shown by Figure 5.19, the addition of the STM0 into the predicted uncertainty on the B-plane produced a bigger covariance ellipse with respect to the UBO003 solution with the computed OTM1B. The reason behind the worsening of the predicted uncertainty is due to the greater ΔV, thus a bigger uncertainty on its value, of the STM0 compared

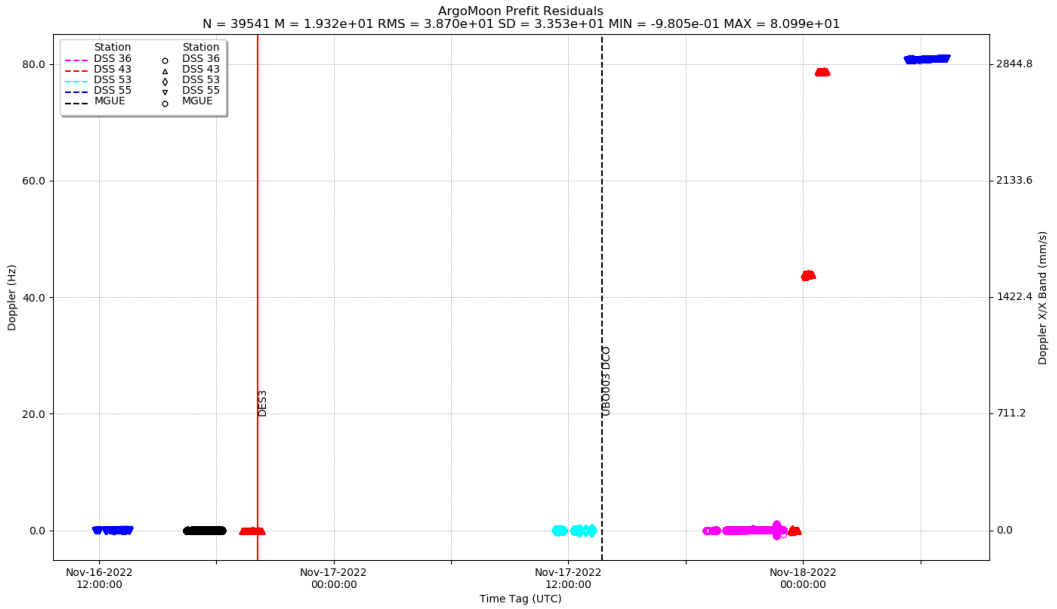

(a) *Data of UBO003 and the new one from DSS 36, 43 and 55.*

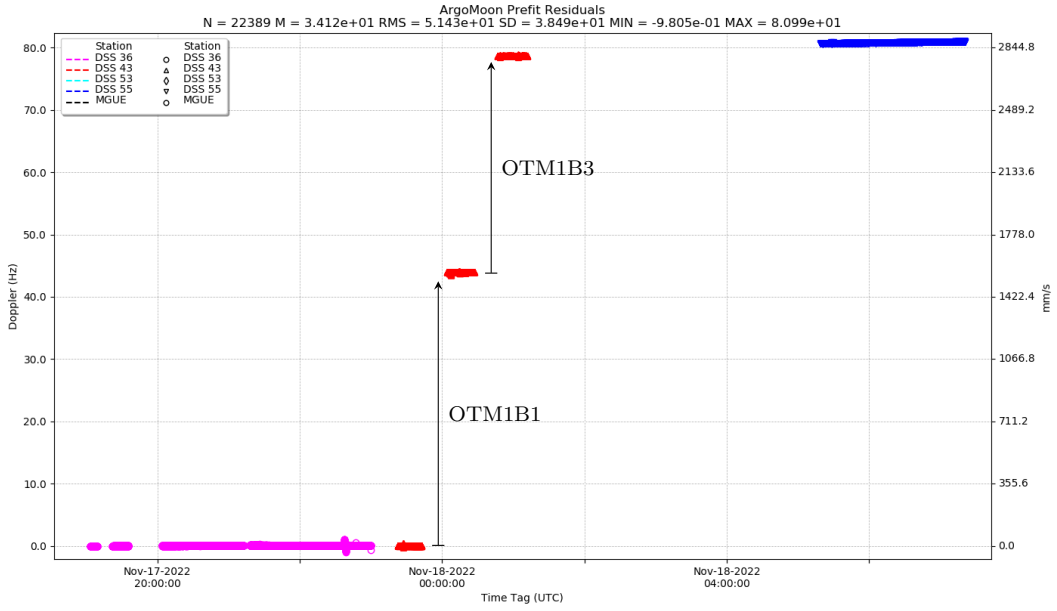

(b) *Detail of the new data with a focus on the effect of OTM1B on the residuals.*

Figure 5.16: Pre-fit two-way Doppler residuals (CT = 1 s) using the UBO003 solution.

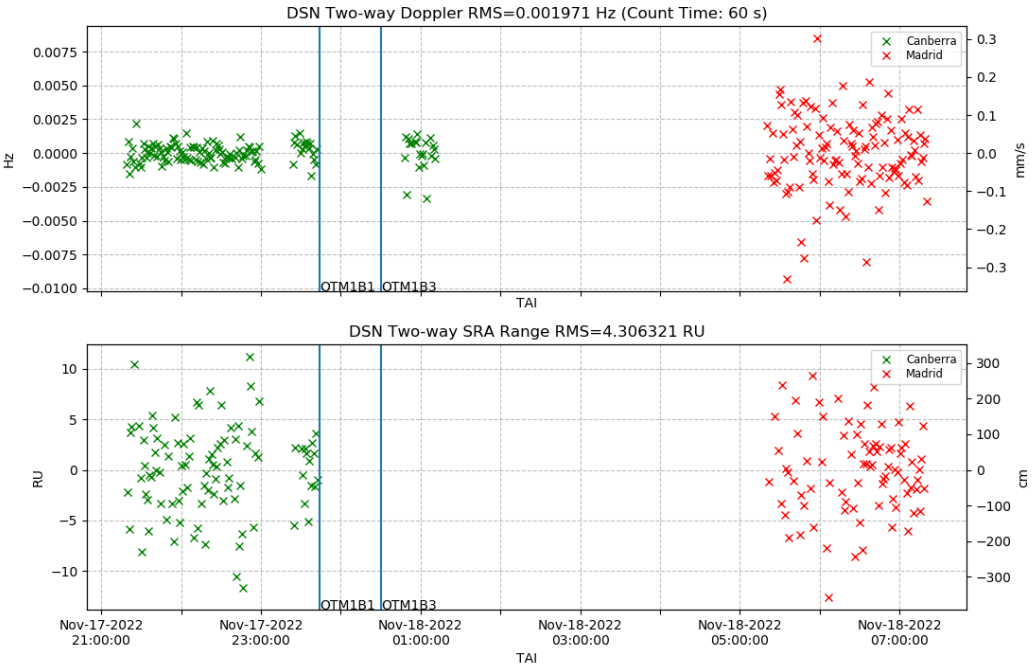

Figure 5.17: Two-way Doppler (top) and range (bottom) post-fit residuals of the UBO004 solution.

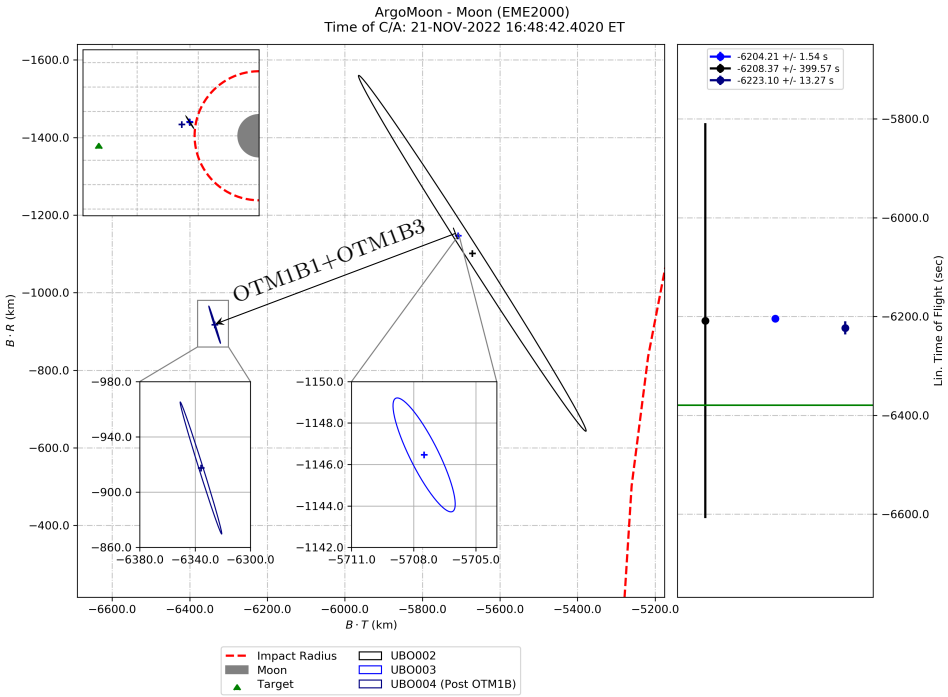

Figure 5.18: Comparison of the UBO002, UBO003 and UBO004 predicted trajectories and 3-σ uncertainties mapped to the Moon B-plane.

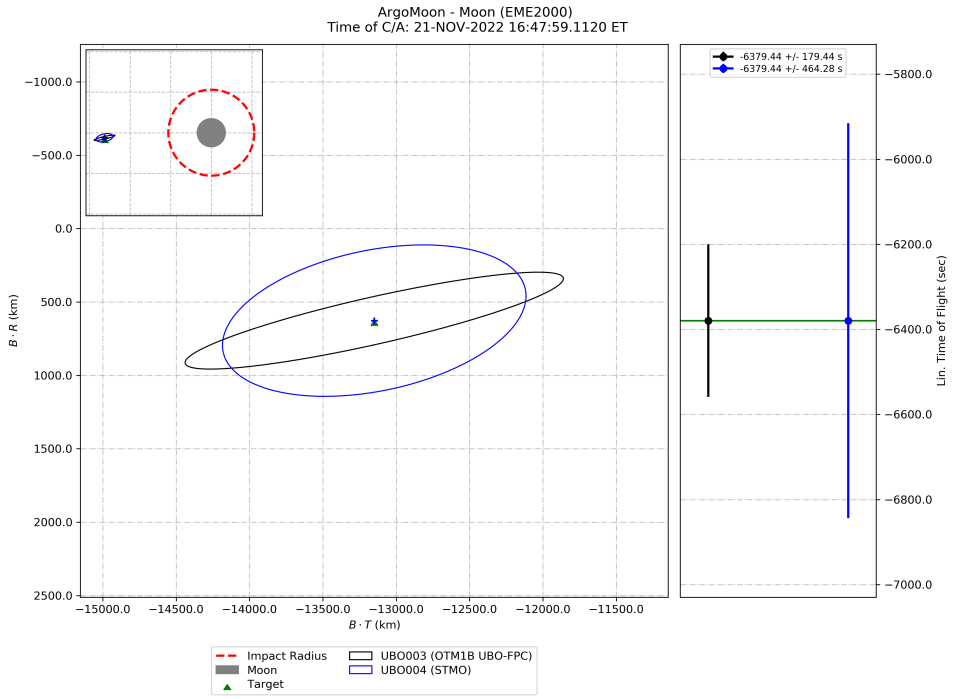

Figure 5.19: Comparison of the UBO003 and UBO004 predicted trajectory and 3-σ uncertainties mapped to the Moon B-plane after the FPC.

to the previous OTM1B. Moreover, since the UBO004 used less data than the UBO003, there was no possibility to further improve the predicted uncertainty.

5.3.7 Solution UBO005

The solution UBO005 was determined the day after UBO004 with the DCO at 00:00 UTC of November 19, 2022. The additional data available at the DCO was only the one from the tracking pass on the DSS 24 in which the execution of the STM0 was planned. The maneuver was successfully commanded and this time the S/C's telemetry was telling that each partial burn of the STM0 was correctly performed. However, by considering the S/C attitude provided by the telemetry, the inspection of the pass-through residuals computed using the UBO004 solution confirmed that the STM0 produced a total ΔV of about 5 m/s.

Figure 5.20a reports the pre-fit residuals of the new Doppler data using the UBO004 solution while Figure 5.20b provides a focus on the pre-fit residuals in correspondence of the STM0 execution during the pass on DSS 24. As can be seen from the pass-through, it was possible to observe only the Doppler steps due to the sum of STM0A and STM0B (named STM0A+B), and the sum of STM0C and STM0D (STM0C+D), because of the lack of data within the two pairs of burns. The observed Doppler steps were 7.6281 m/s for STM0A+B and 2.1721 m/s for STM0C+D, while the detailed results are reported in Table 5.9.

The pre-fit data presented in Figure 5.20 was compressed with a CT of 60 s and used for the computation of UBO004 solution. Unfortunately, the range data during the STM0 was not available and then only Doppler data was used for the reconstruction of the maneuver. STM0 was estimated as a single impulsive burn by removing the intermediate

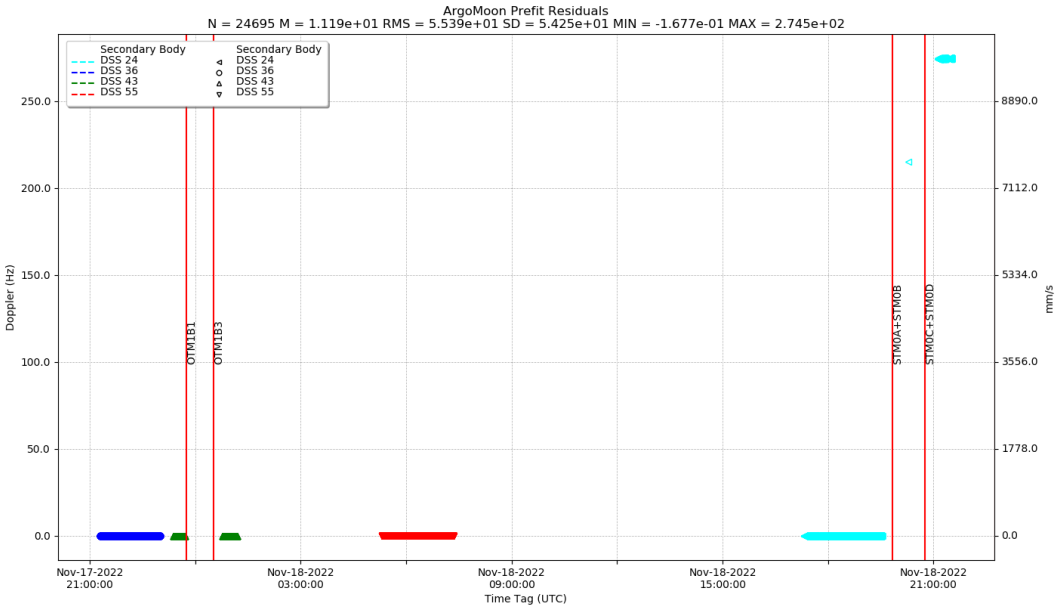

(a) *Data of UBO004 and the new one from DSS 24.*

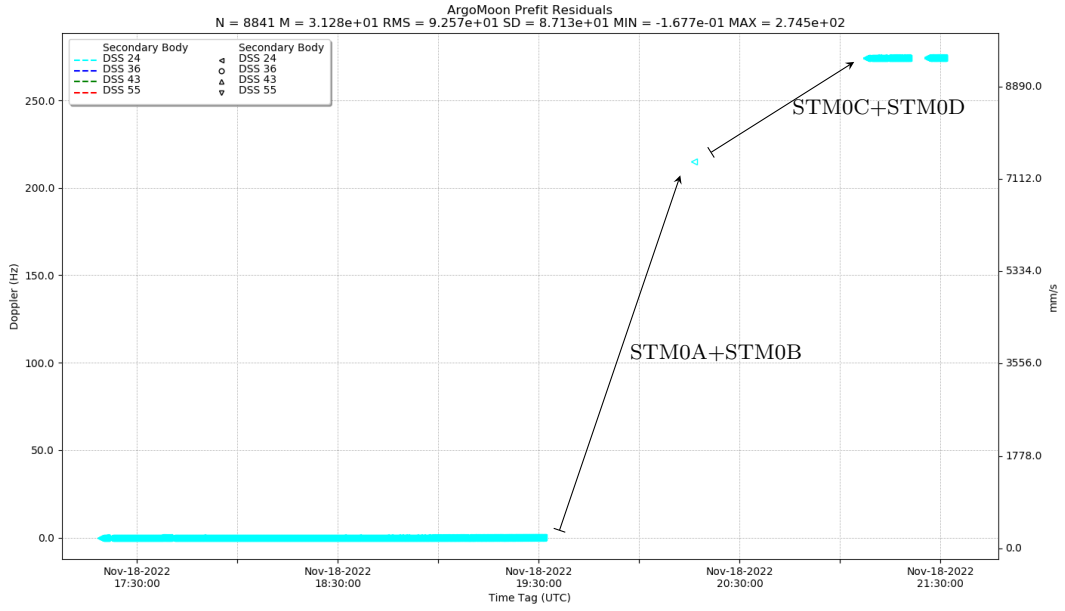

(b) *Detail of the new data from DSS 24 where the STM0 took place.*

Figure 5.20: Pre-fit two-way Doppler residuals (CT = 1 s) using the UBO004 solution.

Table 5.9: Comparison of the commanded and telemetry reconstructed values of the STM0 with the one observed from the Doppler residuals.

Burn	**Commanded LOS-ΔV (m/s)**	**Telemetry LOS-ΔV (m/s)**	**Observed LOS-ΔV (m/s)**	**Telemetry LOS-ΔV angle (deg)**
STM0A	5.9964	6.9602	N/A	171.4172
STM0B	6.0166	6.5589	N/A	171.4729
STM0A+STM0B	12.0131	13.5191	3.8140	N/A
STM0C	6.0371	6.6459	N/A	171.5283
STM0D	3.7925	3.1361	N/A	171.5831
STM0C+STM0D	9.8296	9.7820	1.0860	N/A

points between the two pairs of burns described before, to facilitate convergence. The UBO005 post-fit residuals are presented in Figure 5.21, while the predicted trajectory uncertainty mapped on the B-plane of M0 is shown in Figure 5.22.

Based on the results of the UBO005, the ARG and ASI teams decided to continue with the tentative of performing a correction maneuver at each tracking pass until the day of the M0 encounter. At the time of the contingency plan definition, there were three remaining tracking passes before the day of the fly-by on November 21, 2022.

Therefore, a new FPC was then performed using the UBO005 solution providing three new maneuvers named STM1, STM2 and STM3. The details about the computed maneuvers are reported in Table 5.10. As expected, by approaching the M0 encounter the cost of the ΔV rapidly increases. Thus, the last feasible maneuver was the STM3 with a ΔV of about 54 m/s, close to the limit of the NAVREQ-5.

Table 5.10: Parameters of the STM1, STM2 and STM3 computed through the FPC with the UBO005 solution. The last two maneuvers were not divided since it was not anymore needed by the MCC at that time.

Maneuver	**Burn**	**Time** (ET)	ΔT (s)	ΔV (m/s)	**Direction** (deg)	
					RA	DEC
STM1	A	19-NOV-2022 19:31:09	800.00	6.08	221.29	-7.55
	B	19-NOV-2022 19:54:29	800.00	6.10		
	C	19-NOV-2022 20:17:49	800.00	6.12		
	D	19-NOV-2022 20:41:09	800.00	6.14		
	E	19-NOV-2022 21:04:29	687.55	5.29		
	-	-	3887.55	29.72		
STM2	N/A	20-NOV-2022 07:31:09	5375.60	41.26	223.53	-8.09
STM3	N/A	20-NOV-2022 13:16:09	6582.05	54.65	225.69	-8.53

5.3.8 Solution UBO006

After the delivery of the UBO005, the MCC prepared and sent the telecommands for the STM1 to the S/C. The telemetry communicated that the first two burns A and B terminated before reaching the commanded duration, so the MCC decided to cancel the other burns C, D and E. Then, in the night of November 20, 2022, the tracking data

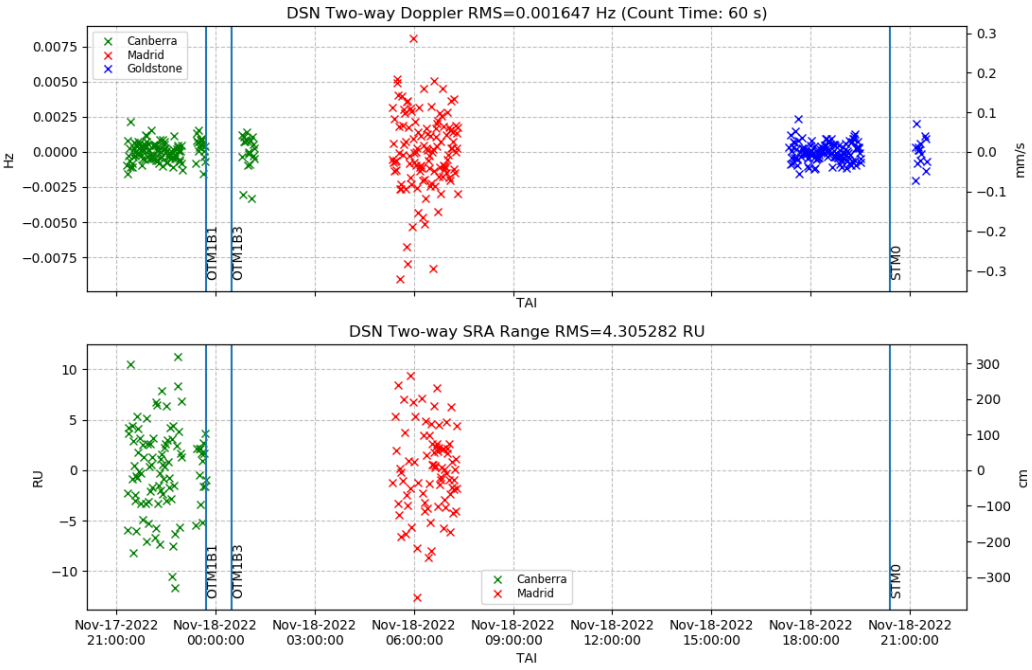

Figure 5.21: Two-way Doppler (top) and range (bottom) post-fit residuals of the UBO005 solution.

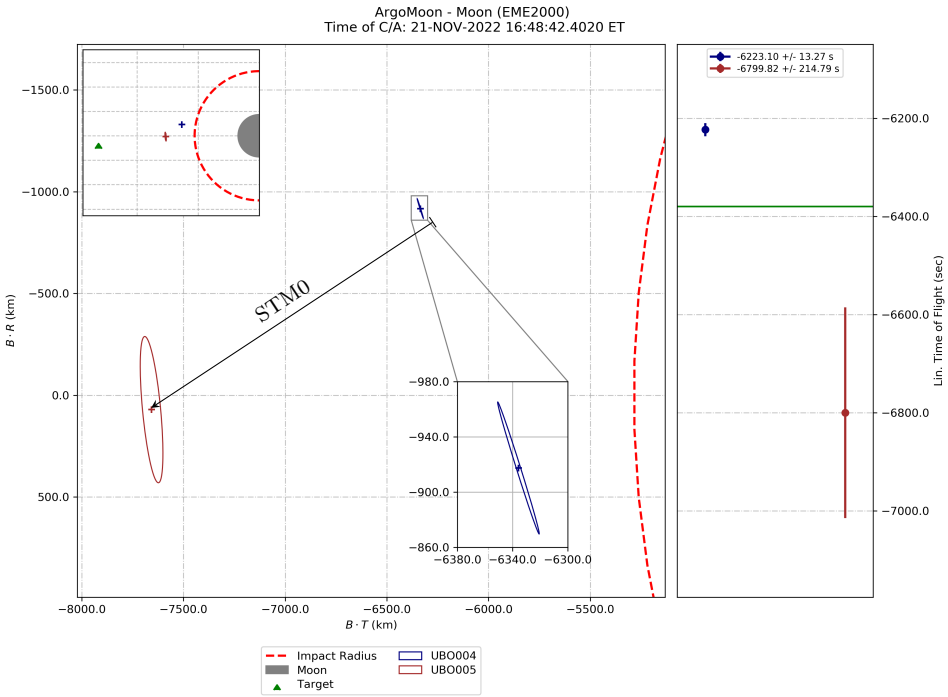

Figure 5.22: Comparison of the UBO004 and UBO005 predicted trajectories and 3-σ uncertainties mapped to the Moon B-plane.

acquired since the last DCO were analyzed by means of a pass-through using UBO005 solution. Since the DCO of the UBO005 a total of three tracking pass were acquired: the first pass was on the New Norcia station of ESTRACK, the second on the DSS 54, and the last one was on the DSS 25 during which the STM1 was executed. During the tracking passes of New Norcia and DSS 25, the S/C performed two automatic RWs offloading maneuvers named DES4 and DES5. Then, by evaluating the pre-fit residuals presented in the Figures 5.23a and 5.23b, it was possible to observe that the effective ΔV after the STM1 was significantly lower than the one requested by the navigation team.

The observed Doppler steps were 0.9531 m/s for STM1A and 1.6554 m/s for STM1B, much less than the commanded/telemetry ΔV as can be seen in the detailed results reported in Table 5.11. The observation of the Doppler step was not feasible for DES4 because it was performed before the beginning of the tracking pass. DES5 was executed right after the STM1B and before the re-acquisition of the signal, thus it was not directly observable. However, from the navigation point of view, the DES5 maneuver was considered part of the STM1B due to its proximity to the latter.

Table 5.11: Comparison of the commanded and telemetry reconstructed values of the STM1 with the one observed from the Doppler residuals.

Burn	**Commanded LOS-ΔV (m/s)**	**Telemetry LOS-ΔV (m/s)**	**Observed LOS-ΔV (m/s)**	**Telemetry LOS-ΔV angle (deg)**
STM1A	5.9632	1.4424	0.4765	168.5745
STM1B	5.8855	7.0141	0.8277	164.6432

Furthermore, the trend of the pre-fit residuals on New Norcia and DSS 54 with respect to the previous solutions was immediately telling that there were unmodeled accelerations. In the tentative of fitting the data for an UBO006 solution, it was assumed that the mismodelling effects were probably due to a leakage of the ArgoMoon's thruster. Furthermore, inspection of the stochastic accelerations estimation supported the hypothesis that an unmodeled acceleration was raised after the last ignition of the thruster. Based on this assumption, the leakage was modeled as a polynomial acceleration starting after the execution of the STM0. Unfortunately, that strategy was not able in providing satisfactory post-fit residuals and it was not possible to further investigate the problem in view of the M0 encounter. On the morning of November 20, 2022, no new OD solution was still available due the numerous problems that occurred, while in the meantime the S/C was executing the STM2 in a last attempt to recover the nominal fly-by of the Moon. Furthermore, during the DSS 53 pass where the STM2 was performed, five additional DES maneuvers took place to reduce the spin rate of the S/C and ensure its operativity. The STM2 was the last maneuver attempt since the ArgoMoon's thruster became definitively unusable approximately 6 hours later. The reason was due to the complete exhaustion of the RCS propellant needed to control the attitude during the execution of a maneuver.

By exploiting again the UBO005 solution, a pass-through of the tracking data from the DSS 53 during the which the STM2 was performed, and the obtained pre-fit results are reported in Figure 5.24. As already expected by analyzing the telemetry, the STM2 was not correctly performed and the inspection of the pass-through with UBO005 allowed to measure the actual ΔV as reported in Table 5.12. The DES6 and DES7 occurred one after the other at the beginning of the tracking pass showing a Doppler step of 10.7 mm/s. The DES8 was executed before the STM2 making it not directly observable and, like DES5

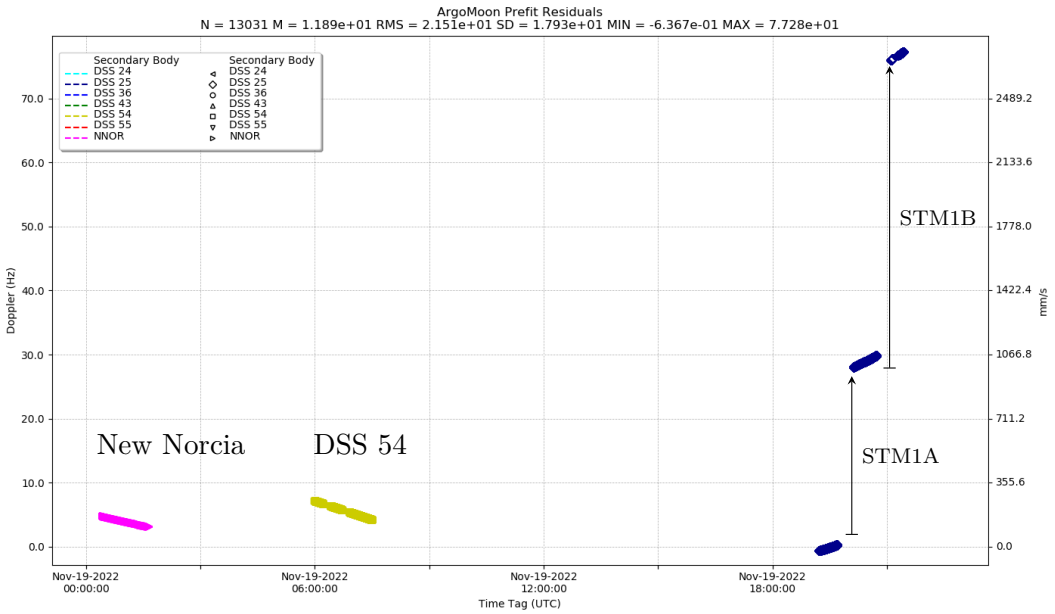

(a) *The data after the DCO of UBO005 up to the STM1 pass.*

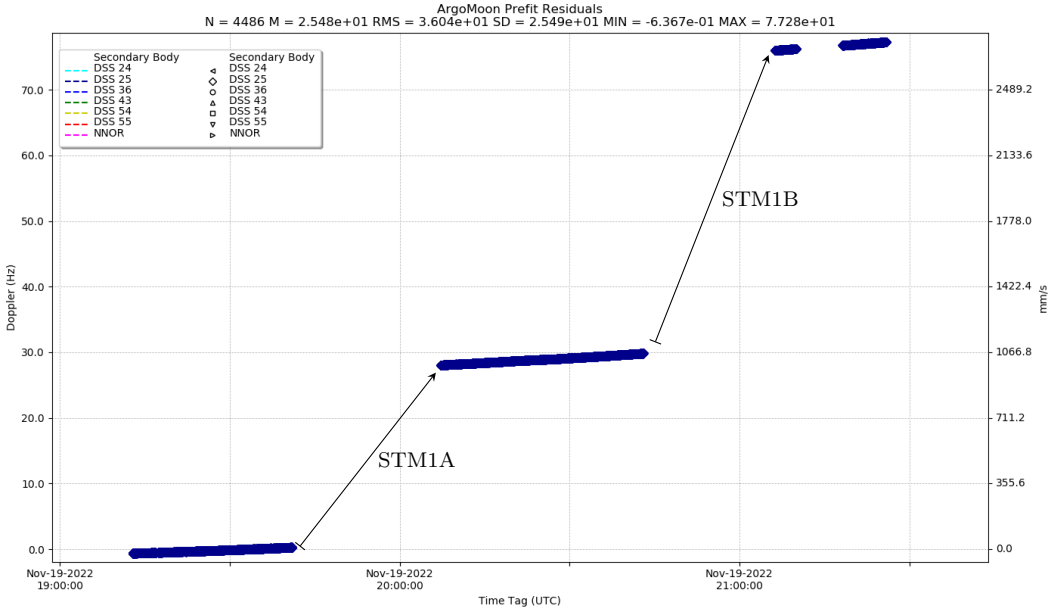

(b) *Detail of the new data from DSS 25 where the STM1 took place.*

Figure 5.23: Pre-fit two-way Doppler residuals (CT = 1 s) using the UBO005 solution.

Table 5.12: Comparison of the commanded and telemetry reconstructed values of the STM1 with the one observed from the Doppler residuals.

Burn	**Commanded LOS-ΔV (m/s)**	**Telemetry LOS-ΔV (m/s)**	**Observed LOS-ΔV (m/s)**	**Telemetry LOS-ΔV angle (deg)**
STM2	6.0836	6.7594	1.0237	179.5461

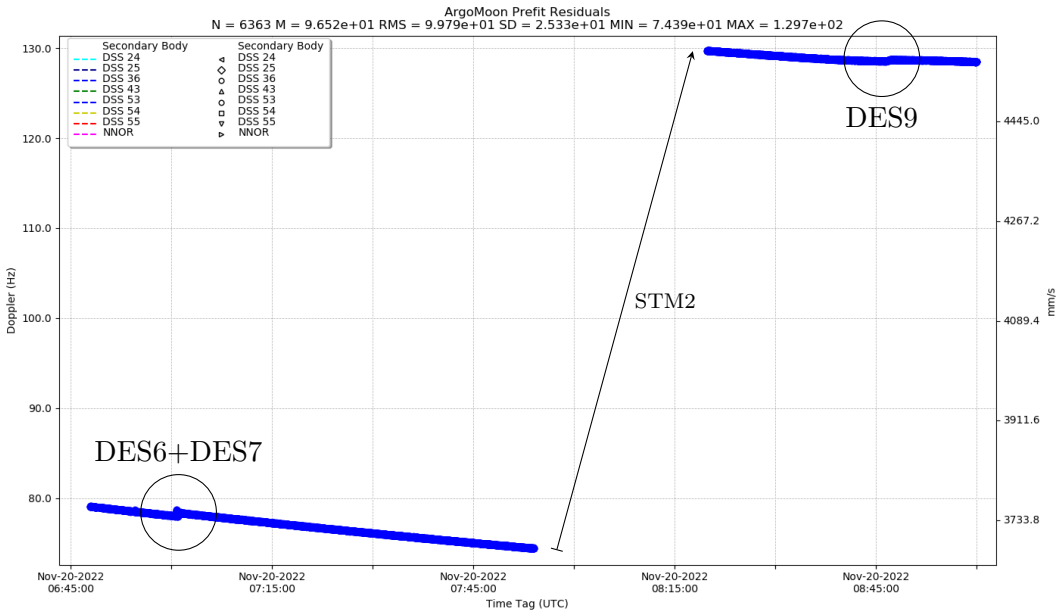

Figure 5.24: Pre-fit two-way Doppler residuals (CT = 1 s) in correspondence of the STM2 using the UBO005 solution.

with STM1B, it was considered part of the STM2. The DES9 took place during the end of the tracking pass and its observed Doppler step was 5.7 mm/s.

The UBO006 was computed by fitting only the STM2 tracking pass while all the rest of the data of the mission was neglected. The decision of ignore all the previous data was based mainly on the mismodelling problems related with the leakage. The result was a *safe* OD solution where the S/C initial state was taken from UBO005 at 22:00 UTC of November 19, 2022, a couple of hours after the STM1. The S/C state covariance presented in 5.2 was mutated to a simple diagonal matrix in the EME2000 frame with 5000 km of uncertainty on the position and 5 m/s on the velocity. The OD solution included the estimation of the observable DES maneuvers and the STM2. The resulting post-fit residuals are presented in Figure 5.25 where the Doppler data was compressed with a CT of 60 s. Due to the assumptions made, and the presence of multiple maneuvers, UBO006 resulted into a higher predicted trajectory uncertainty with respect to UBO005, as it can be seen in Figure 5.26.

5.3.9 Solution UBO007

At the time of the UBO006, the M0 fly-by was estimated to occur at 16:00 UTC of November 21, 2022, at 1993.18 km of altitude with respect to the Moon's surface. By considering

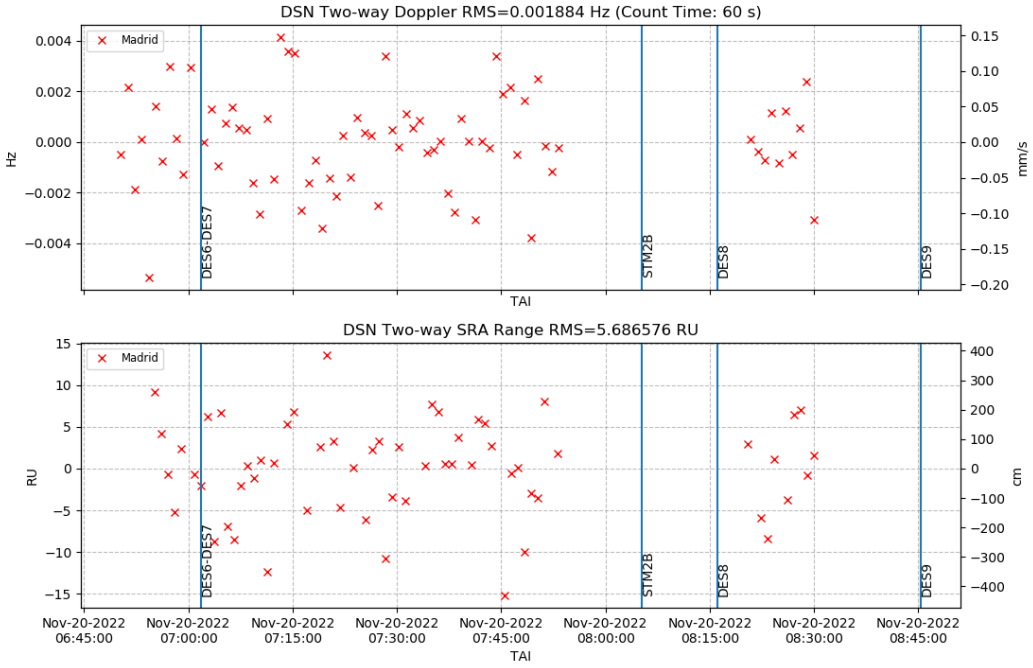

Figure 5.25: Two-way Doppler (top) and range (bottom) post-fit residuals of the UBO006 solution.

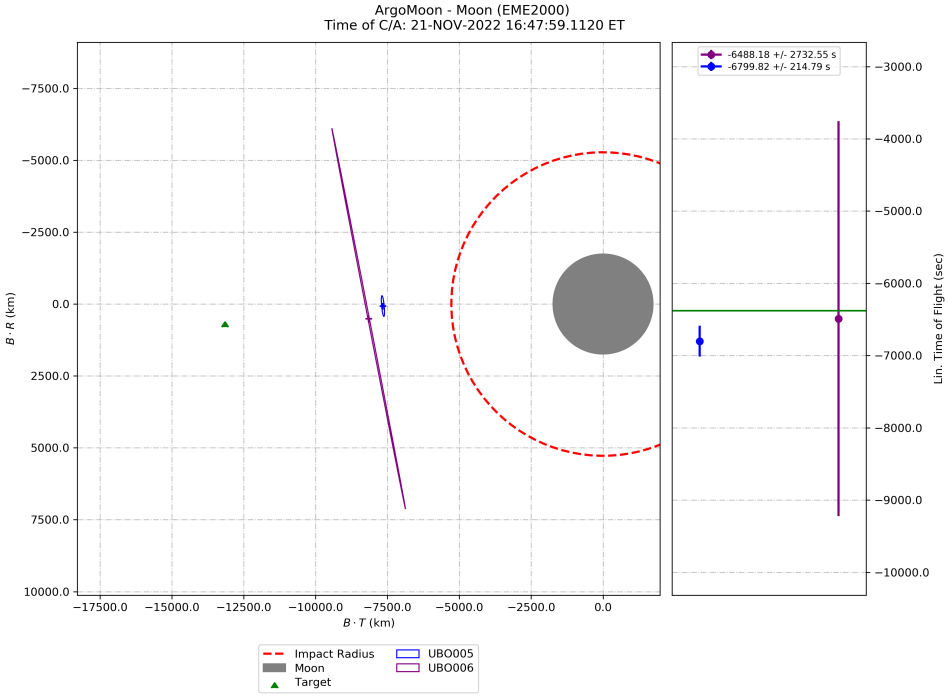

Figure 5.26: Comparison of the UBO006 and UBO005 predicted trajectories and 3-σ uncertainties mapped to the Moon B-plane.

the reference timeline with launch on November 16, the M0 had been anticipated of 47 minutes where the altitude was 4100 km lower than the desired one. Unfortunately, such predicted fly-by was leading ArgoMoon to a heliocentric trajectory after the first perigee P0. However, the orbit controllability was lost after STM2 and then the navigation routine was aimed at the reconstruction and prediction of the trajectory mainly for DSN pointing. Therefore, deliveries had to take place when there was a deviation from the DSN trajectory in order to guarantee the fulfillment of the NAVREQ-3.

Figure 5.27 reports the pre-fit residuals of the Doppler data acquired after the UBO006 up the 00:00 UTC of November 21. The residuals were providing again the evidence of an unmodeled acceleration that was probably originated by the thruster's leakage happened another time after the STM2. Accordingly, UBO006 and the subsequent data presented in Figure 5.27 were not reliable. On November 21, at 16:07 UTC, ArgoMoon performed the fly-by M0 and the contact with the S/C was re-established by the DSS 24 at 20:50 UTC of the same day. However, the DSS 24 had received only a weak signal form the S/C meaning that there might have been problems with the direction of pointing or with the S/C's attitude. It was then assumed that the UBO006 solution may not be correct or too inaccurate due to the occurred thruster leakage. Therefore, to avoid further problems with the pointing of the S/C, the navigation team decided to start a new analysis with a DCO at 22:00 UTC of November 21 using the new acquired tracking data. This new OD delivery was performed rapidly to correct any possible pointing issue. Then, due to the leakage occurred before the encounter, the navigation team decided to restart with a new OD solution using only the data after 00:00 UTC of November 21. The idea was that through the former method the reconstruction of M0 would be mismodelling-free since the leakage was supposed to be terminated. Therefore, the S/C initial state was retrieved from UBO006 at the epoch 07:00 UTC of November 21 and the data was considered only after the epoch of the initial state. Unfortunately, no range data was available during the M0 encounter and therefore the OD processing of UBO007 would have involved Doppler

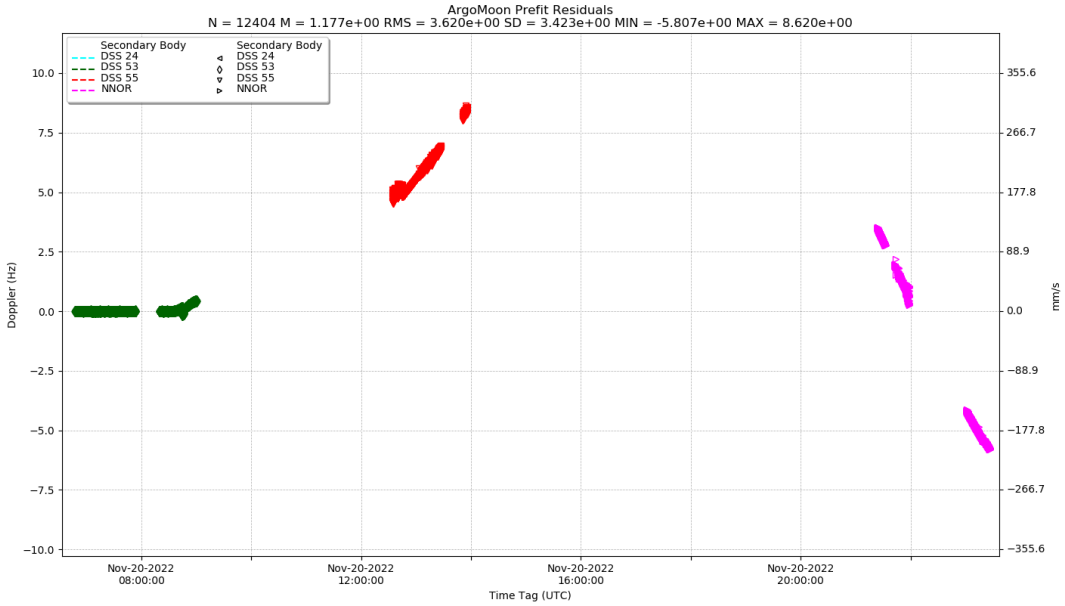

Figure 5.27: Pre-fit two-way Doppler residuals (CT = 1 s) up to 00:00 UTC of November 21, 2022, using the UBO006 solution.

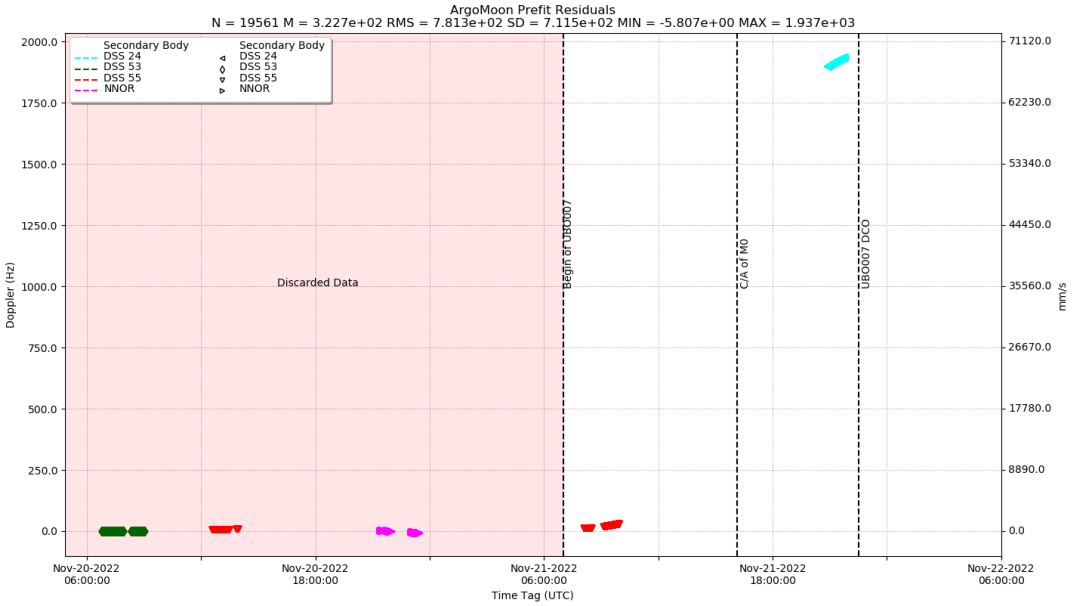

Figure 5.28: Pre-fit two-way Doppler residuals (CT = 1 s) up to 00:00 UTC of November 22, 2022, using the UBO006 solution.

data only. The pass-through residuals of the considered data using the UBO006 solution are presented in Figure 5.28.

UBO007 was successfully obtained by fitting the Doppler data compressed with a CT of 60 s. UBO007 was identified as the *fly-by* solution since it was based only on the data around the encounter to reconstruct the event and predict the post fly-by trajectory. The post-fit residuals of UBO007 are presented in Figure 5.29, while the reconstructed trajectory and the associated uncertainty on the Moon B-plane are shown in Figure 5.30. The angle between the UBO007 and UBO006 trajectories as seen from the DSN is reported in Figure 5.31. The results clearly showed that the angle between the two solutions was exceeding the HPBW of the 34 m antennas and then the UBO007 solution had to be delivered to DSN for the next tracking activities. The delivery of the solution was performed on 23:25 UTC of November 21, 2022, approximately 8 hours after the C/A with the Moon. After that time, the DSN would use the UBO007 trajectory to proper pointing the antennas towards ArgoMoon.

5.3.10 Solution UBO008

At the time of the UBO007 delivery, there were two additional tracking passes, respectively on DSS 35 and New Norcia, that had been scheduled for the night of November 22, 2022. During the tracking pass on the DSS 35 a substantial drop in power of the received S/C's carrier signal was seen again. Furthermore, the next pass on the New Norcia station was failed due to the loss of the carrier lock for the same power problems. However, in the night of November 2022, the MCC promptly notified the navigation team that on November 21, before the first tracking pass used for UBO007, a reset command was sent to the IRIS radio. Hence, all the tracking data around M0 used for UBO007 were affected again by the pre-POKE Doppler bias of -1.458 Hz. Thus, UBO007 was assumed to be not reliable for the DSN pointing and a new solution was required.

The UBO008 solution was then computed to update the trajectory for the DSN point-

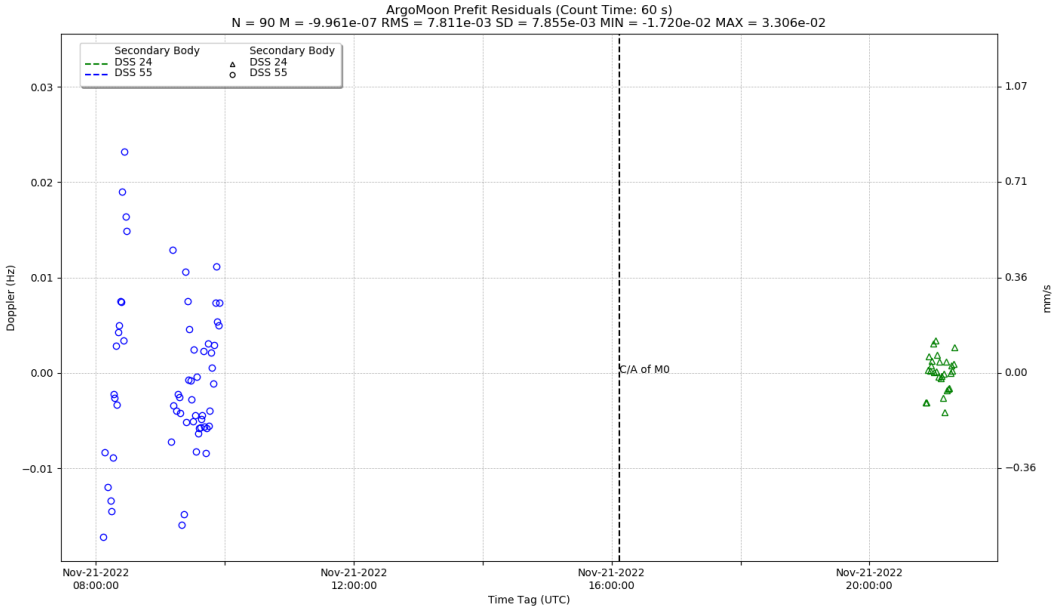

Figure 5.29: Post-fit two-way Doppler residuals (CT = 60 s) of the UBO007 solution.

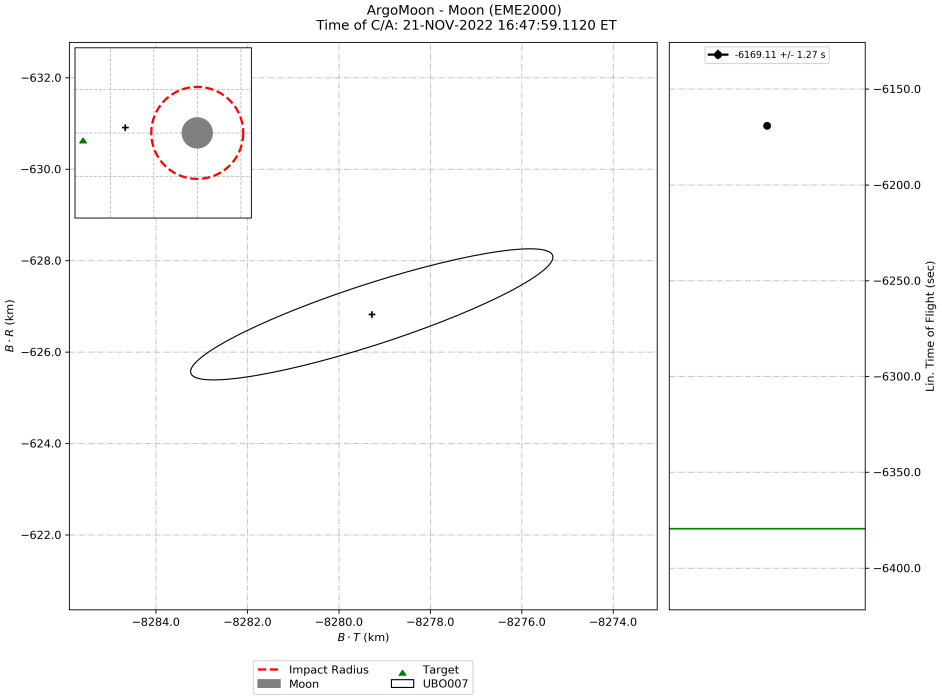

Figure 5.30: UBO007 reconstructed trajectory and 3-σ uncertainty mapped to the Moon B-plane.

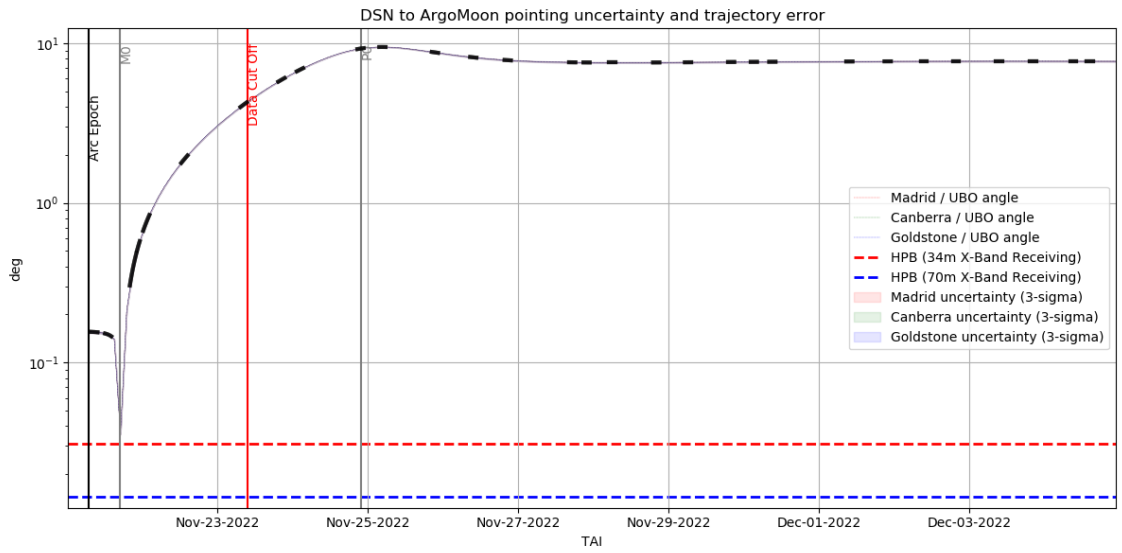

Figure 5.31: Angle between UBO007 and UBO006 trajectories as seen from the DSN with the associated pointing uncertainty shaded above the angle line. The black rectangles above the angle line represents the past and future tracking passes. The DCO epoch represented by the vertical red line refers to that of the UBO007 solution.

ing activities after the fly-by. The DCO of the UBO008 was at 15:00 UTC of November 23, 2022, where all the data before 13:00 UTC of November 22 was discarded, and the S/C's initial state was maintained the same as for UBO007. Moreover, at 13:30 UTC of November 22, the MCC sent a new POKE-3 command to restore the status of the IRIS radio and remove again the large bias on the Doppler data. The cancellation of all the data during the fly-by and before was to ignore the critical events happened in the previous days and focus only on the post fly-by trajectory prediction. In fact, as described in the UBO007 section, the navigation aim was mutated to mainly focus on the fulfillment of NAVREQ-3 for which it was acceptable to neglect the data acquired during and before the encounter M0.

Since the critical events had been removed, the S/C was no longer leaking, and the IRIS radio was reconfigured, the UBO008 post-fit residuals were good in fewer iterations than previous solutions. The estimated parameters were reduced to only the S/C's initial state and the SRP scale factor since no other maneuvers or events were expected to be present. The post-fit residuals of UBO008 are presented in Figure 5.32, while the reconstructed trajectory and the associated uncertainty on the Moon B-plane are reported Figure 5.33.

As it can be seen from the B-plane results, UBO007 and UBO008 solutions were close but, due to the amplification of small errors after a fly-by, the predicted trajectories could diverge with the risk of losing the correct pointing from the DSN. Figure 5.34 shows the angle between the UBO007 and the UBO008 as seen from the DSN ground complexes. The two solutions were in fact still compatible with the NAVREQ-3 up to the first perigee P0 after which the error would have exceeded the HPBW of the 34 m antennas. Therefore, the navigation team delivered UBO008 to the DSN on 23:00 UTC of November 23, 2022, to ensure the correct pointing activities for the weeks following the DCO.

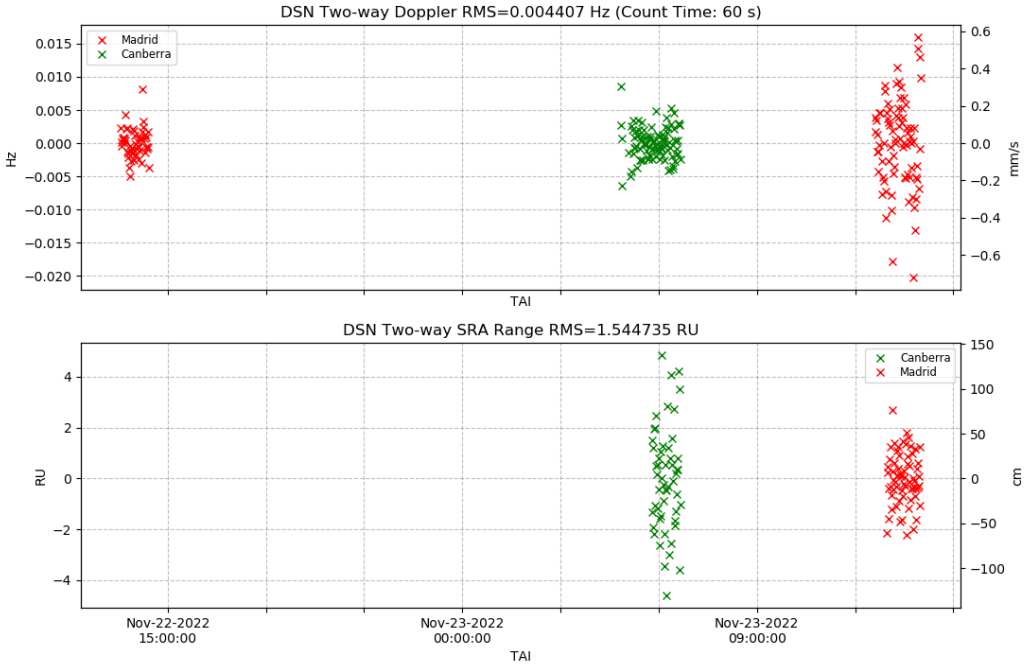

Figure 5.32: Two-way Doppler (top) and range (bottom) post-fit residuals of the UBO008 solution.

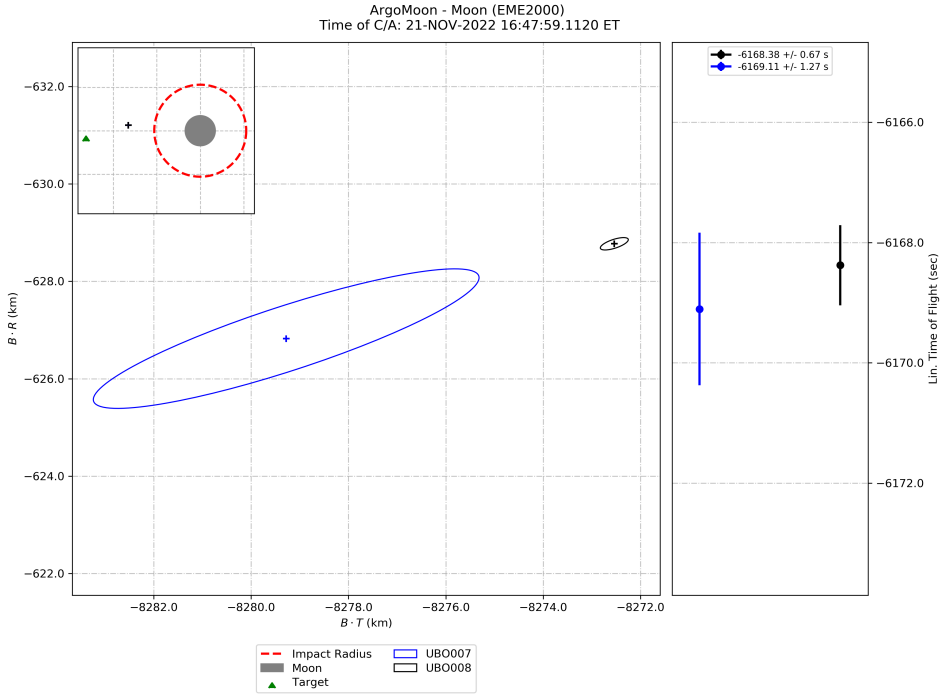

Figure 5.33: Comparison of the UBO008 and UBO007 reconstructed trajectories and 3-σ uncertainties mapped to the Moon B-plane.

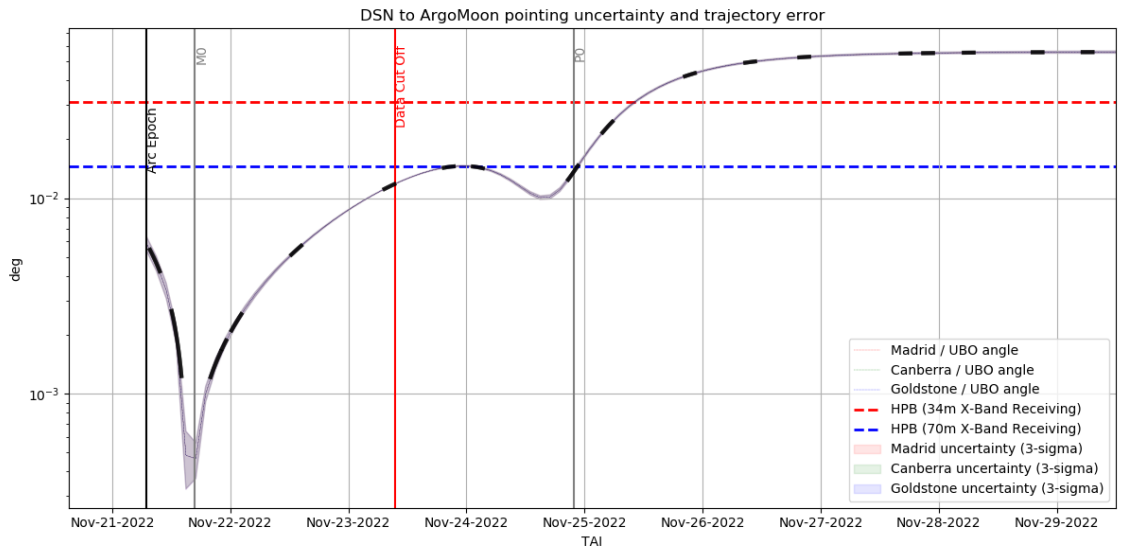

Figure 5.34: Angle between UBO008 and UBO007 trajectories as seen from the DSN with the associated pointing uncertainty shaded above the angle line. The black rectangles above the angle line represents the past and future tracking passes. The DCO epoch represented by the vertical red line is referred to the one of the UBO008 solution.

5.3.11 Solution UBO009

After UBO008, the navigation team monitored the DSN pointing status by observing the angle between the updated OD solutions after each tracking pass and UBO008. It was then seen that the NAVREQ-3 was still fulfilled after each OD update meaning that the UBO008 was a good and robust solution in the prediction of the ArgoMoon trajectory. Therefore, a new last OD delivery named UBO009 was performed simply by extending the UBO008 trajectory propagation up to 6 months. Figure 5.35 shows the pass-through of all the Doppler data after the UBO008 delivery up to November 29, 2022.

5.3.12 Solution UBO010

The pre-fit residuals after the fly-by were much better than the ones before meaning that the S/C dynamics was more stable, and no other critical events occurred. Then, a UBO010 solution was computed using all the good tracking data after the fly-by of the Moon and the resulting post-fit residuals are presented in Figure 5.36. As for UBO008-9, the estimated parameters were only the S/C's initial state and the SRP scale factor. The angle between the UBO009 and the UBO010 solutions as seen from the DSN is reported in Figure 5.37. The angle between the two solutions and its related uncertainty were well below the HPBW of the 34 m antennas meaning that the NAVREQ-3 was fulfilled with all the three solutions UBO008, UBO009 and UBO010. In fact, the DSN did not encountered particular problems in track and lock the S/C's carrier signal after the UBO008 delivery. UBO010 has been the last OD delivery performed and it is still considered as the best solution for the proper pointing of the 34 m antennas towards ArgoMoon up to June 6, 2023.

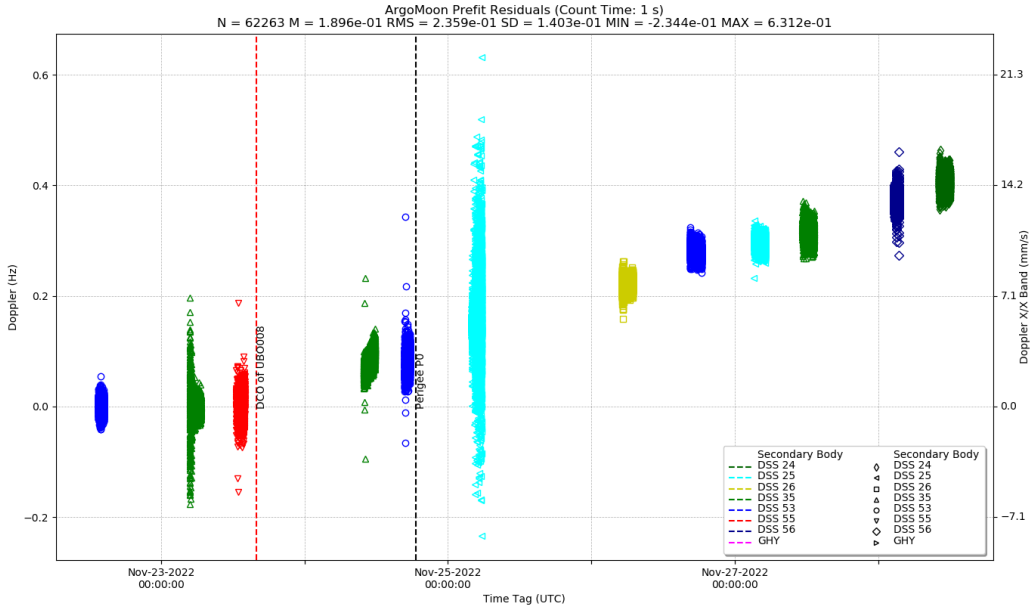

Figure 5.35: Pre-fit two-way Doppler residuals (CT = 1 s) up to November 29, 2022, using the UBO008 solution.

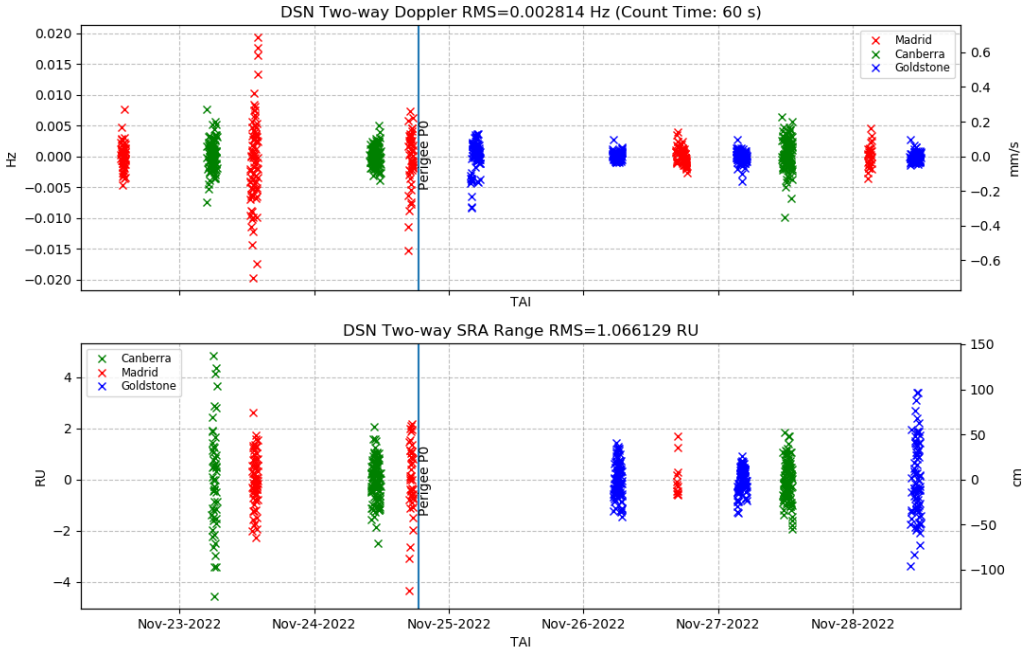

Figure 5.36: Two-way Doppler (top) and range (bottom) post-fit residuals of the UBO010 solution.

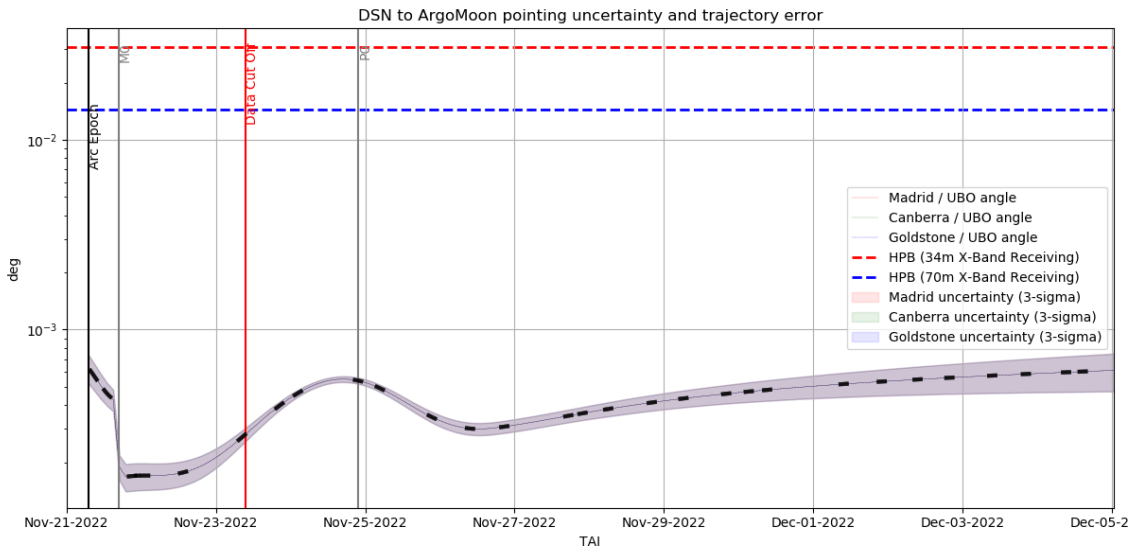

Figure 5.37: Angle between UBO010 and UBO009 trajectories as seen from the DSN with the associated pointing uncertainty shaded above the angle line. The black rectangles above the angle line represents the past and future tracking passes.

5.4 Summary

ArgoMoon was successfully launched and released in space by the SLS on November 16, 2022. The S/C performed 4 orbital maneuvers for a total of 9 independent partial burns. The fly-by of the Moon was successfully performed at 16:07 UTC of November 21, approximately 48 minutes before the planned epoch. Due to the different ΔV provided by the S/C, the error on the B-plane with respect to the reference trajectory was ∼5000 km. After the fly-by, ArgoMoon passed close to the Earth at 18:38 UTC of November 24 at 165880 km. Due to the different geometry of the Moon's fly-by, ArgoMoon was unable to remain in a geocentric orbit and after the C/A with the Earth it was following a path towards an heliocentric orbit. Based on the last OD solution UBO010, ArgoMoon entered the interplanetary space after leaving the Earth's SOI on December 10, 2022.

ArgoMoon navigation operations lasted for 13 days, from the launch of the S/C up to the last contact after overtaking the orbit of the Moon on November 28, 2022, on its way to a heliocentric orbit. However, mission operations still continued for a while in an intense search for the S/C signal in collaboration with the DSN, after the loss of the lock on 28 November 2022. The latter research operations performed by the DSN confirmed that the loss of communication was not related to the navigation. During the operations, the navigation team worked night and day for very long shifts trying to solve all the encountered problems in the best possible way. The navigation team delivered a total of 10 OD solutions and 5 orbital maneuvers by successfully fulfilling the NAVREQ-3. The latter was the last applicable navigation requirement as the others were no longer compatible with the mission after the technical problems occurred in the PS.

During the flight activities a total of 13 tracking passes were provided, 10 of which by DSN and the other 3 by ESTRACK. All the tracking passes had two-way Doppler data with 1 s of CT while only 9 of them also provided the range observables. The quality of the ArgoMoon radiometric data was mostly affected by the S/C's rotational dynamics, the IRIS radio design and configuration, and the frequently reboots of the S/C. The range

data had frequent significant biases whose origin is still under investigation. A summary timeline of all the tracking passes and relevant events related to the navigation operations is reported in Figure 5.38.

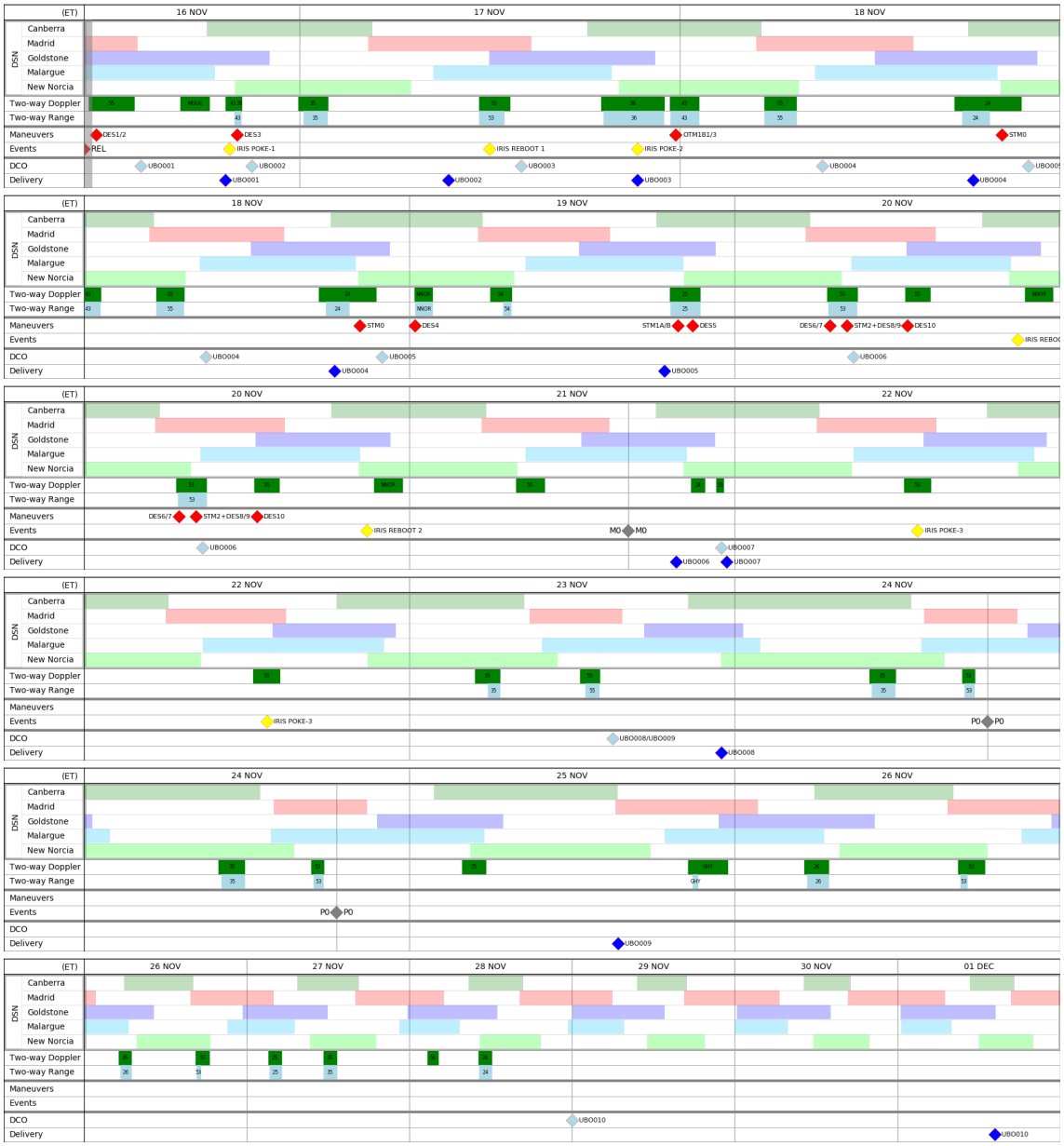

Figure 5.38: ArgoMoon navigation operations timeline showing the DSN coverage on the first row, the actual tracking passes on the second and third row (Doppler and range data), the performed orbital maneuvers on the fourth row, DCOs of the OD solutions on the fifth row, and the fundamental trajectory events on the last row.

Chapter 6

Conclusions and Future Works

CubeSats are already gaining access to cis-lunar and interplanetary space as happened in the MarCO, LICIACube, and ArgoMoon missions. Breakthrough miniaturized technologies are already being developed to solve the significant technological challenges of deep space missions. However, using CubeSats in deep space also requires addressing many operational challenges, particularly those related to the navigation. The achievement of complex objectives as in a regular deep space mission, given the limitations of the CubeSats platform, requires navigation as precise as that adopted for interplanetary exploration missions. Therefore, extensive investigations, analysis, and experimentation are required to properly navigate and operate a CubeSat in deep space.

This dissertation covers the design and execution of the navigation for the ArgoMoon mission. The conducted work has been described in this thesis in a part dedicated to the pre-launch analysis and a comprehensive description of the actual navigation operations and obtained results. All the software and numerical models used for navigation design and execution has been developed using the NASA/JPL's signature astrodynamic computing platform named MONTE.

In order to follow the reference ArgoMoon's trajectory and fulfill the mission objectives, the navigation procedure has been designed with the goal of reconstructing the S/C trajectory and computing the correction maneuvers. The estimation of the trajectory is performed on ground by the navigation team through a single-arc batch-sequential OD process using the radiometric observables Doppler and range. The tracking of the S/C is performed alongside the telecommunications by the DSN using the 34 m antennas located in the complexes of Madrid, Goldstone and Canberra. The estimated trajectory is then compared with the reference one to evaluate if correction maneuvers have to be computed. The correction maneuvers were scheduled by means of an optimal control strategy designed before the launch.

The designed trajectory control strategy allows to minimize the error with respect to the reference trajectory, as well as the statistical Δv, by using the following targets: the nominal B-plane coordinates $(B.R, B.T, LTOF)$ for the fly-bys with the Moon, the position at the apogee and the velocity at the perigee when orbiting the Earth. The search of the norm's local minima of the K-inverse matrix for each target allowed to find the optimal maneuvers location that minimizes the Δv. The position at the apogee is optimally targeted with a maneuver placed two days after the preceding perigee, whereas a maneuver at the apogee targets the velocity at the following perigee. Through a non-linear Monte Carlo simulation, the optimal control strategy has been validated giving that the reference trajectory can be flown with a Δv of 49.5 m/s at the 99^{th} percentile.

Examining the OD analysis' results identified the optimal schedule for delivering the

estimated trajectory to the DSN required to properly point the antennas towards the S/C. To ensure a pointing uncertainty from the Earth to the S/C within the beamwitdh of the DSN's 34 m antennas, a new estimated trajectory should be provided to DSN at least once each REV. To meet the pointing requirement, the delivery to DSN during the REV0 should be carried out at least three times. Additionally, due to the high level of uncertainty during the launch phases, the first two tracking passes should be supported by an X-Band aided acquisition antenna with a wider beamwidth in order to fulfill the pointing requirement. The S/C ephemeris uncertainty mapped on the B-plane of the last Moon encounter shows that the selected trajectory and navigation strategy can fulfill the disposal requirement at the 99% of confidence.

The sensitivity study revealed that the orbital propulsion system's performance and the injection inaccuracy have a significant impact on the trajectory controllability. The DSN pointing requirement is instead impacted by uncertainties in stochastic accelerations, orbital maneuvers, and tracking data shortages. However, by varying the schedule of the deliveries to DSN, the degradation of the S/C pointing uncertainty can be controlled. Finally, all the tested cases of the sensitivity analysis have widely satisfied the impact's risk and disposal requirements.

The pre-launch analysis demonstrated that the navigation of ArgoMoon was feasible, under realistic assumptions on the mission scenario and the technological capabilities of the space and ground segment. The main challenges were expected to be the performance of the propulsion system as well as the injection accuracy provided by SLS.

The navigation operations of the ArgoMoon were under the responsibility of the flight dynamics team of the University of Bologna. The team has been composed by five aerospace engineers with experience in deep space navigation, in particular for the OD. The operations were organized taking inspiration from the heritage of ESA and JPL deep space missions activities. The navigation facility was at the Radio Science and Planetary Exploration Laboratory of the UNIBO, in Forli' (Italy) where the flight dynamics team had its own control room in loop with the ArgoMoon's MCC in Turin (Italy).

ArgoMoon was then launched on November 16, 2022, at 06:47:44 UTC by the SLS as secondary payload in the context of the Artemis-1 mission. According to the DSN, ArgoMoon was released by ICPS at 10:36 UTC and the first signal acquisition was successfully occurred at 10:37 UTC. The first received Doppler data was noisy due to a tumbling motion of the S/C induced by the spin of ICPS plus a contribution from the dispenser mechanism. However, using the designed navigation process and strategy the UNIBO team has fitted the Doppler data delivering the first solution just 12 hours after the launch. The day after the launch ArgoMoon performed the first orbital maneuver named OTM1B. The pass-through analysis of the Doppler data acquired in correspondence of the maneuver revealed an underperforming PS not capable of executing the commanded Δv. After that event, the navigation team delivered 5 reliable OD solutions and three correction maneuvers to bring ArgoMoon on its designed path. Unfortunately, the PS failed all the commanded maneuvers preventing ArgoMoon to reach the desired aimpoint on the B-plane. Moreover, several reset of the IRIS transponder and a leakage of the engine further increased the complexity of the OD. On November 21, at 16:07 UTC, ArgoMoon successfully performed the fly-by of the Moon, taking some spectacular pictures of the Moon's surface. After the encounter with the Moon, the navigation team reconstructed the trajectory and delivered another set of 5 OD solutions verifying that the S/C was leaving the Earth-Moon system, entering a heliocentric orbit.

The operations results proved the reliability and accuracy of the designed navigation process and strategy. Despite the critical events occurred during the flight, the postfit

residuals after the fly-by shown a Root Mean Square (RMS) of 0.1 mm/s for Doppler and 30 cm for range, better than assumed in the pre-launch analysis. Due to the lack of a proper orbital propulsion, the only applicable navigation requirements were the DSN pointing and the impact risk. The navigation team was capable of met both of them even with a very stringent contingency timeline. As expected during the design phase, the DSN pointing requirement was a major challenge requiring a constant monitoring of the angle between the last delivered solution to DSN and the actual estimated orbit. The optimal organization of the navigation team and activities was a key factor in the successfully determination of the ArgoMoon's trajectory. Even if not fully employed and tested during the operations, the FPC strategy always provided optimal maneuvers capable of retargeting the ArgoMoon's trajectory towards the reference one.

In the context of the ArgoMoon mission, future works will include a complete reconstruction of the trajectory using all the data since the deployment of the S/C. Through this analysis would be possible to reconstruct the leakage events as well as confirm the reliability of the delivered solutions and the robustness of the designed navigation process. Also, the reconstruction will help find potential flaws in the navigation setup and software to provide a relevant heritage for the upcoming deep space CubeSats missions.

Appendix A

B-plane

The *B-plane* is defined as the plane orthogonal to the inbound asymptote of a hyperbolic osculating orbit with respect to a chosen target [99]. The trajectory of a S/C that is performing a fly-by of a planet can be approximated to the motion of a particle that is traveling along the asymptotes of a hyperbola. The only factors that affect the angle of deflection between the asymptotes are the particle's energy, the central force, and the distance of the inbound asymptote from the center of motion.

Let's now assume that a S/C is approaching a planet (whose gravitational parameter is $\mu = GM$) on an hyperbolic trajectory with an inbound excess velocity vector $\mathbf{v}_\infty$. Then, the inbound asymptote direction is defined as

$$\hat{\mathbf{S}} = \frac{\mathbf{v}_\infty}{|\mathbf{v}_\infty|} = \frac{1}{e}\hat{\mathbf{P}} + \frac{\sqrt{e^2-1}}{e}\hat{\mathbf{Q}} \tag{A.1}$$

where $\hat{\mathbf{P}} = \mathbf{e}/e$ and $\hat{\mathbf{Q}} = \mathbf{h} \times \hat{\mathbf{P}}/h$ are the unit vectors pointing to the periapsis position and velocity, $h = |\mathbf{h}| = |\mathbf{r} \times \mathbf{v}|$ is the orbit's angular momentum, and

$$e = |\mathbf{e}| = \frac{\mathbf{v} \times \mathbf{h}}{\mu} - \frac{\mathbf{v}}{|\mathbf{r}|} \tag{A.2}$$

is the orbital eccentricity.

The B-plane is orthogonal to the vector $\hat{\mathbf{S}}$ where his origin is at the planet's center. The vector $\mathbf{B}$ is defined as that vector which departs from the origin and arrives at the point of intersection between the B-plane and the incoming asymptote:

$$\mathbf{B} = \frac{\hat{\mathbf{S}} \times \mathbf{h}}{|\mathbf{v}_\infty|} \tag{A.3}$$

By using a third vector $\mathbf{k}$ not parallel to $\hat{\mathbf{S}}$ (i.e., the planet's spinning pole), it is possible to define an orthonormal base in which project the vector $\mathbf{B}$ and visualize it as looking at the B-plane along the $\hat{\mathbf{S}}$ direction. This orthonormal frame is defined by the vectors $\hat{\mathbf{S}}$, and

$$\hat{\mathbf{T}} = \frac{\hat{\mathbf{S}} \times \mathbf{k}}{|\hat{\mathbf{S}} \times \mathbf{k}|}, \qquad \hat{\mathbf{R}} = \hat{\mathbf{S}} \times \hat{\mathbf{T}}. \tag{A.4}$$

Then, since the $\mathbf{B}$ vector lies on the B-plane, it can be expressed in the defined frame as a combination of the B-plane coordinates $(B.R, B.T)$ defined as follows:

$$B.T = \mathbf{B} \cdot \hat{\mathbf{T}} = \frac{\hat{\mathbf{T}} \cdot \mathbf{h}}{|\mathbf{v}_\infty|}, \qquad B.R = \mathbf{B} \cdot \hat{\mathbf{R}} = -\frac{\hat{\mathbf{R}} \cdot \mathbf{h}}{|\mathbf{v}_\infty|} \tag{A.5}$$

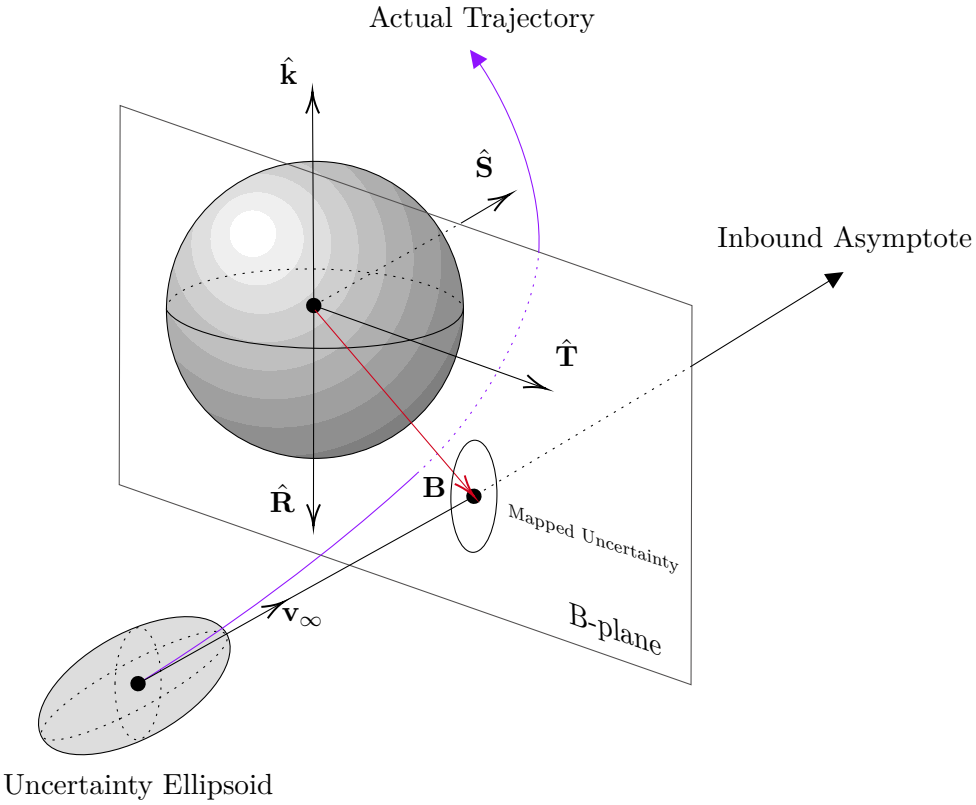

Figure A.1: Representation of the B-plane structure and the mapping of the uncertainty ellipsoid on the plane.

The schematic representation of the B-plane and the described quantities can be depicted from Figure A.1.

As can be seen from the scheme, the actual trajectory of the S/C is obviously bent due to the central body's gravity. Therefore, the $(B.R, B.T)$ coordinates may provide a misleading information if an impact assessment has to be performed. In fact, one may erroneously think that if the **B** point is outside the surface of the central body then also the actual trajectory is without impact. To avoid this problem, an impact parameter related to the B-plane coordinates can be computed. By exploiting the conservation of angular momentum

$$h = r_p v_p = |\mathbf{B}| v_\infty \tag{A.6}$$

and the conservation of the energy

$$\frac{v_p^2}{2} - \frac{\mu}{r_p} = \frac{v_\infty^2}{2} \tag{A.7}$$

a relation between $B = |\mathbf{B}|$ and the radius at the C/A is found

$$B = r_p \sqrt{1 + \frac{2\mu}{r_p v_\infty^2}}. \tag{A.8}$$

The impact is verified when $r_p \leq R_{cb}$, where R_{cb} is the radius of the central body. Therefore, the B-plane impact condition can be defined as

$$B \leq R_{cb} \sqrt{1 + \frac{2\mu}{R_{cb} v_\infty^2}}. \tag{A.9}$$

which practically identify the radius of the central body enlarged by a factor dependent on its own gravitational field.

Another important quantity, that is frequently used to complete the B-plane coordinates set, is the Linearized Time of Flight (LTOF) [100]. This parameter can be seen as the time to periapsis for a rectilinear trajectory coincident with the incoming asymptote and traveled with a velocity v_∞. The time to periapsis, or Time of Closest Approach (TCA), for an osculating hyperbolic trajectory can be computed as

$$t_p = t - \frac{1}{n}(e \sinh F - F) \tag{A.10}$$

where n is the hyperbolic mean motion, F is the hyperbolic eccentric anomaly and t is the reference epoch from which the t_p is computed. Then, for $t \to -\infty$, also $F \to -\infty$, $r \to \infty$, and

$$\cosh F \simeq -\frac{r}{ae}, \qquad \sinh F \simeq \frac{r}{ae}, \qquad F \simeq -\log\left(\frac{-2r}{ae}\right) \tag{A.11}$$

such that the Equantion A.10 can be approximated to

$$t_p \simeq t - \frac{1}{n}\left[\frac{r}{a} + \log\left(\frac{-2r}{ae}\right)\right] \tag{A.12}$$

where a is the semi-major axis of the hyperbolic orbit. Then, for a rectilinear trajectory $e = 1$ and the previous equation becomes

$$t_L \simeq t - \frac{1}{n}\left[\frac{r}{a} + \log\left(\frac{-2r}{a}\right)\right] \to t_L = t_p - \frac{\log e}{n} \tag{A.13}$$

where t_L is the LTOF. However, this parameter may be complex to be rapidly understood in certain cases and therefore the TCA can be used as the third coordinate of the B-plane system.

In conclusion, by using the triplet of coordinates $(B.T, B.R, LTOF)$, or $(B.T, B.R, TCA)$, it is possible to uniquely determine the geometry of an encounter with an intuitive visualization of the desired aimpoint on the B-plane.

List of Figures

List of Tables

Bibliography

[1] M. Lombardo, M. Zannoni, I. Gai, L. Gomez Casajus, E. Gramigna, R. L. Manghi, P. Tortora, V. Di Tana, B. Cotugno, S. Simonetti, et al. "Design and Analysis of the Cis-Lunar Navigation for the ArgoMoon CubeSat Mission". In: *Aerospace* 9.11 (2022), p. 659.

[2] S. Evans, W. Taber, T. Drain, J. Smith, H. Wu, M. Guevara, R. Sunseri, and J. Evans. "MONTE: The next generation of mission design and navigation software". In: *CEAS Space Journal* 10.1 (2018), pp. 79–86.

[3] A. Johnstone. *CubeSat Design Specification*. 14.1. The CubeSat Program, Cal Poly San Luis Obispo. Feb. 2022.

[4] H. Heidt, J. Puig-Suari, A. Moore, S. Nakasuka, and R. Twiggs. "CubeSat: A new generation of picosatellite for education and industry low-cost space experimentation". In: *Proceedings of the AIAA/USU Conference on Small Satellites*. Logan UT, USA, 11-26 September, 2000.

[5] J. Puig-Suari, C. Turner, and W. Ahlgren. "Development of the standard CubeSat deployer and a CubeSat class PicoSatellite". In: *2001 IEEE Aerospace Conference Proceedings (Cat. No.01TH8542)*. Vol. 1. 2001, 1/347–1/353 vol.1. DOI: 10.1109/AERO.2001.931726.

[6] E. Kulu. "Nanosatellite Launch Forecasts-Track Record and Latest Prediction". In: *Proceedings of the 36th Annual Small Satellite Conference*. Swifty Session 1, Utah State University, Logan, UT, 2022.

[7] C. Cappelletti, S. Battistini, and B. Malphrus. *CubeSat Handbook: From Mission Design to Operations*. Academic Press, 2020.

[8] S. Asmar and S. Matousek. "Mars Cube One (MarCO) shifting the paradigm in relay deep space operation". In: *14th International Conference on Space Operations*. 2016, p. 2483.

[9] T. Martin-Mur and B. Young. "Navigating (MarCO), the first interplanetary CubeSats". In: *27th International Symposium on Space Flight Dynamics*. Melbourne, Australia, 2019, pp. 24–26.

[10] E. Dotto, V. Della Corte, M. Amoroso, I. Bertini, J. Brucato, A. Capannolo, B. Cotugno, G. Cremonese, V. Di Tana, I. Gai, S. Ieva, G. Impresario, S. Ivanovski, M. Lavagna, A. Lucchetti, E. Mazzotta Epifani, A. Meneghin, F. Miglioretti, D. Modenini, M. Pajola, P. Palumbo, D. Perna, S. Pirrotta, G. Poggiali, A. Rossi, E. Simioni, S. Simonetti, P. Tortora, M. Zannoni, G. Zanotti, A. Zinzi, A. Cheng, A. Rivkin, E. Adams, E. Reynolds, and K. Fretz. "LICIACube - The Light Italian Cubesat for Imaging of Asteroids In support of the NASA DART mission towards asteroid (65803) Didymos". In: *Planetary and Space Science* 199 (2021), pp. 105–185. DOI: https://doi.org/10.1016/j.pss.2021.105185.

[11] M. Amoroso, S. Pirrotta, V. Della Corte, E. Dotto, I. Bertini, J. Brucato, A. Capannolo, G. Zanotti, B. Cotugno, J. Deshapriya, V. Di Tana, M. Dall'Ora, I. Gai, G. Impresario, S. Ieva, S. Ivanovski, M. Lavagna, M. Lombardo, A. Lucchetti, E. Mazzotta Epifani, P. Hasselmann, A. Meneghin, F. Miglioretti, D. Modenini, M. Pajola, D. Perna, G. Poggiali, A. Rossi, E. Simioni, S. Simonetti, M. Zannoni, A. Zinzi, and P. Tortora. "LICIACube: a Deep Space CubSat to Witness the First Asteroid Kinetic Impactor Test". In: *International Astronautical Congress: IAC Proceedings*. 2022, pp. 1–10.

[12] M. Amoroso, S. Pirrotta, G. Impresario, A. Zinzi, F. Miglioretti, V. Di Tana, S. Simonetti, B. Cotugno, V. Della Corte, E. Dotto, M. Zannoni, I. Gai, M. Lombardo, G. Zanotti, and A. Capannolo. "Italian Cubesats for Moon and Asteroid imaging". In: *International Astronautical Congress: IAC Proceedings*. 2022, pp. 1–10.

[13] A. Rivkin, N. Chabot, A. Stickle, C. Thomas, D. Richardson, O. Barnouin, E. Fahnestock, C. Ernst, A. Cheng, S. Chesley, S. Naidu, T. Statler, B. Barbee, H. Agrusa, N. Moskovitz, R. T. Daly, P. Pravec, P. Scheirich, E. Dotto, V. Della Corte, P. Michel, M. Küppers, J. Atchison, and M. Hirabayashi. "The Double Asteroid Redirection Test (DART): Planetary Defense Investigations and Requirements". In: *The Planetary Science Journal* 2.5 (Aug. 2021), p. 173. DOI: 10.3847/psj/ac063e.

[14] P. Pravec, L. Benner, M. Nolan, P. Kusnirak, D. Pray, J. Giorgini, R. Jurgens, S. Ostro, J. Margot, C. Magri, A. Grauer, and S. Larson. "(65803) 1996 GT". In: *IAU Circ.* 8244 (Nov. 2003), p. 2.

[15] I. Gai, M. Lombardo, and M. Zannoni. "Challenges in Orbit Determination for Deep-Space Science CubeSat: the case of LICIACube". In: *14th Europlanet Science Congress*. Sept. 2020. DOI: 10.5194/epsc2020-885.

[16] S. Pirrotta, G. Impresario, B. Cotugno, F. Cavallo, E. Bruno, P. Tortora, M. Zannoni, I. Gai, M. Lombardo, L. A. Gomez Casajus, E. Gramigna, G. Zanotti, M. Ceresoli, M. Lavagna, D. Lubey, and M. Smith. "ArgoMoon and LICIACube: Italian first missions operated in Deep Space". In: *17th International Conference on Space Operations*. Dubai, United Arab Emirates, 2023.

[17] B. Cheetham, T. Gardner, A. Forsman, E. Kayser, and M. Clarkson. "CAPSTONE: A Unique CubeSat Platform for a Navigation Demonstration in Cislunar Space". In: *ASCEND 2022*. 2022, p. 4382.

[18] F. De Grossi, P. Marzioli, M. Cho, F. Santoni, and C. Circi. "Trajectory optimization for the Horyu-VI international lunar mission". In: *Astrodynamics* 5.3 (2021), pp. 263–278.

[19] R. Smith, N. Merancy, and J. Krezel. "Exploration Missions 1, 2, and Beyond: First Steps Toward a Sustainable Human Presence at the Moon". In: *2019 IEEE Aerospace Conference*. 2019, pp. 1–12. DOI: 10.1109/AERO.2019.8742118.

[20] K. Robinson, A. Schorr, and D. Smith. "NASA's space launch system: Opportunities for small satellites to deep space destinations". In: *Proceedings of the 32nd Annual AIAA/USUConference on Small Satellites*. Session 9: Space Access, Logan, UT, USA, 2018.

[21] D. McIntosh, J. Baker, and J. Matus. "The NASA Cubesat Missions Flying on Artemis-1". In: *Proceedings of the 34th Annual Small Satellite Conference*. Pre-Conference Workshop Session VII: Instruments/Science II, Utah State University, Logan, UT, 2020.

[22] V. Di Tana, B. Cotugno, S. Simonetti, G. Mascetti, E. Scorzafava, and S. Pirrotta. "ArgoMoon: There is a Nano-Eyewitness on the SLS". In: *IEEE Aerospace and Electronic Systems Magazine* 34.4 (2019), pp. 30–36.

[23] S. Massaro Tieze, L. Liddell, S. Santa Maria, and S. Bhattacharya. "BioSentinel: A Biological CubeSat for Deep Space Exploration". In: *Astrobiology* 0.0 (0). PMID: 32282239, null. DOI: 10.1089/ast.2019.2068.

[24] T. Lockett, J. Castillo-Rogez, L. Johnson, J. Matus, J. Lightholder, A. Marinan, and A. Few. "Near-Earth Asteroid Scout Flight Mission". In: *IEEE Aerospace and Electronic Systems Magazine* 35.3 (2020), pp. 20–29. DOI: 10.1109/MAES.2019.2958729.

[25] M. Desai, F. Allegrini, R. Ebert, K. Ogasawara, M. Epperly, D. George, E. Christian, S. Kanekal, N. Murphy, and B. Randol. "The CubeSat Mission to Study Solar Particles". In: *IEEE Aerospace and Electronic Systems Magazine* 34.4 (2019), pp. 16–28. DOI: 10.1109/MAES.2019.2917802.

[26] R. Funase, S. Ikari, K. Miyoshi, Y. Kawabata, S. Nakajima, S. Nomura, N. Funabiki, A. Ishikawa, K. Kakihara, S. Matsushita, R. Takahashi, K. Yanagida, D. Mori, Y. Murata, T. Shibukawa, R. Suzumoto, M. Fujiwara, K. Tomita, H. Aohama, K. Iiyama, S. Ishiwata, H. Kondo, W. Mikuriya, H. Seki, H. Koizumi, J. Asakawa, K. Nishii, A. Hattori, Y. Saito, K. Kikuchi, Y. Kobayashi, A. Tomiki, W. Torii, T. Ito, S. Campagnola, N. Ozaki, N. Baresi, I. Yoshikawa, K. Yoshioka, M. Kuwabara, R. Hikida, S. Arao, S. Abe, M. Yanagisawa, R. Fuse, Y. Masuda, H. Yano, T. Hirai, K. Arai, R. Jitsukawa, E. Ishioka, H. Nakano, T. Ikenaga, and T. Hashimoto. "Mission to Earth-Moon Lagrange Point by a 6U CubeSat: EQUULEUS". In: *IEEE Aerospace and Electronic Systems Magazine* 35.3 (2020), pp. 30–44. DOI: 10.1109/MAES.2019.2955577.

[27] T. Hashimoto, T. Yamada, M. Otsuki, T. Yoshimitsu, A. Tomiki, W. Torii, H. Toyota, J. Kikuchi, N. Morishita, Y. Kobayashi, T. Ito, H. Tanno, A. Nagamatsu, and H. Morimoto. "Nano Semihard Moon Lander: OMOTENASHI". In: *IEEE Aerospace and Electronic Systems Magazine* 34.9 (2019), pp. 20–30. DOI: 10.1109/MAES.2019.2923311.

[28] C. Hardgrove, J. DuBois, L. Heffern, E. Cisneros, J. Bell, T. Crain, R. Star, T. Prettyman, I. Lazbin, B. Roebuck, et al. "The Lunar Polar Hydrogen Mapper (LunaH-Map) Mission". In: *Proceedings of the 33rd Annual AIAA/USUConference on Small Satellites*. Session V: Upcoming Missions, Utah State University, Logan, UT, USA, 2019.

[29] B. K. Malphrus, K. Z. Brown, J. Garcia, C. Conner, J. Kruth, M. S. Combs, N. Fite, S. McNeil, S. Wilczweski, K. Haught, A. Zucherman, P. Clark, K. Angkasa, N. Richard, T. Hurford, D. Folta, C. Brambora, R. MacDowall, P. Mason, S. Hur-Diaz, J. Breeden, R. Nakamura, A. Martinez, and M. M. Tsay. "The Lunar IceCube EM-1 Mission: Prospecting the Moon for Water Ice". In: *IEEE Aerospace and Electronic Systems Magazine* 34.4 (2019), pp. 6–14. DOI: 10.1109/MAES.2019.2909384.

[30] M. Tsay, J. Frongillo, J. Model, J. Zwahlen, and B. Malphrus. "Flight development of iodine BIT-3 RF ion propulsion system for SLS EM-1 CubeSats". In: *Proceedings of the 30th Annual AIAA/USUConference on Small Satellites*. Session VI:Propulsion, North Logan, UT, USA, 2016.

[31] G. Williams and J. Crusan. "Pioneering space: the evolvable mars campaign". In: *NASA Headquarters, Washington, 20150408-NAC-Crusan-EMC-v7a*. 2015.

[32] L. Hyde and J. Cockrell. "NASA's CubeQuest Challenge: Ground Tournament 4 Results and Technology". In: *Annual Conference on Small Satellites*. ARC-E-DAA-TN45532. 2017.

[33] A. Cervone, F. Topputo, S. Speretta, A. Menicucci, E. Turan, P. Di Lizia, M. Massari, V. Franzese, C. Giordano, G. Merisio, D. Labate, G. Pilato, E. Costa, E. Bertels, A. Thorvaldsen, A. Kukharenka, J. Vennekens, and R. Walker. "LUMIO: A CubeSat for observing and characterizing micro-meteoroid impacts on the Lunar far side". In: *Acta Astronautica* 195 (2022), pp. 309–317. DOI: https://doi.org/10.1016/j.actaastro.2022.03.032.

[34] P. Michel, M. Kueppers, H. Sierks, I. Carnelli, A. Cheng, K. Mellab, M. Granvik, A. Kestilä, T. Kohout, K. Muinonen, A. Näsilä, A. Penttila, T. Tikka, P. Tortora, V. Ciarletti, A. Hérique, N. Murdoch, E. Asphaug, A. Rivkin, O. Barnouin, A. Campo Bagatin, P. Pravec, D. Richardson, S. Schwartz, K. Tsiganis, S. Ulamec, and O. Karatekin. "European component of the AIDA mission to a binary asteroid: Characterization and interpretation of the impact of the DART mission". In: *Advances in Space Research* 62.8 (2018), pp. 2261–2272. DOI: https://doi.org/10.1016/j.asr.2017.12.020.

[35] F. Topputo, Y. Wang, C. Giordano, V. Franzese, H. Goldberg, F. Perez-Lissi, and R. Walker. "Envelop of reachable asteroids by M-ARGO CubeSat". In: *Advances in Space Research* 67.12 (2021), pp. 4193–4221. DOI: https://doi.org/10.1016/j.asr.2021.02.031.

[36] H. Goldberg, Ö. Birgin Ritter, A. Henrique, P. Tortora, C. Prioroc, B. Garcia Gutierrez, P. Martino, and I. Carnelli. "The Juventas CubeSat in Support of ESA's Hera Mission to the Asteroid Didymos". In: *33rd Annual AIAA/USU Conference on Small Satellites*. 2019.

[37] F. Ferrari, V. Franzese, M. Pugliatti, C. Giordano, and F. Topputo. "Preliminary mission profile of Hera's Milani CubeSat". In: *Advances in Space Research* 67.6 (2021), pp. 2010–2029. DOI: https://doi.org/10.1016/j.asr.2020.12.034.

[38] L. Wood. "The Evolution of Deep Space Navigation: 1962-1989". In: (2008), pp. 285–308.

[39] G. J. Bierman. *Factorization methods for discrete sequential estimation*. Courier Corporation, 2006.

[40] C. L. Thornton and J. S. Border. *Radiometric tracking techniques for deep-space navigation*. John Wiley & Sons, 2003.

[41] B. Tapley, B. Schutz, and G. Born. "Fundamentals of Orbit Determination". In: *Statistical Orbit Determination*. Burlington: Academic Press, 2004. Chap. 4, pp. 159–284. DOI: https://doi.org/10.1016/B978-012683630-1/50023-0.

[42] T. D. Moyer. *Formulation for observed and computed values of Deep Space Network data types for navigation*. John Wiley & Sons, 2005.

[43] D. Allan. "Statistics of atomic frequency standards". In: *Proceedings of the IEEE* 54.2 (1966), pp. 221–230. DOI: 10.1109/PROC.1966.4634.

[44] S. Asmar, D. Atkinson, M. Bird, and G. Wood. "Ultra-stable oscillators for planetary entry probes". In: *Proceedings of the International Workshop Planetary Probe Atmospheric Entry and Descent Trajectory Analysis and Science*. Lisbon, Portugal, Oct. 2003.

[45] P. F. Kuhnle. "NASA/JPL Deep Space Network frequency and timing". In: *Proceedings of the 21th Annual Precise Time and Time Interval Systems and Applications Meeting*. 1989, pp. 479–490.

[46] B. Bertotti, G. Comoretto, and L. Iess. "Doppler tracking of spacecraft with multi-frequency links". In: *Astronomy and Astrophysics* 269 (1993), pp. 608–616.

[47] R. Treuhaft and G. Lanyi. "The effect of the dynamic wet troposphere on radio interferometric measurements". In: *Radio Science* 22.02 (1987), pp. 251–265.

[48] Y. E. Bar-Sever, C. S. Jacobs, S. Keihm, G. E. Lanyi, C. J. Naudet, H. W. Rosenberger, T. F. Runge, A. B. Tanner, and Y. Vigue-Rodi. "Atmospheric media calibration for the deep space network". In: *Proceedings of the IEEE* 95.11 (2007), pp. 2180–2192.

[49] R. L. Manghi, M. Zannoni, P. Tortora, A. Martellucci, J. De Vicente, J. Villalvilla, M. Mercolino, G. Maschwitz, and T. Rose. "Performance characterization of ESA's tropospheric delay calibration system for advanced radio science experiments". In: *Radio Science* 56.10 (2021), pp. 1–14.

[50] T. Wang, R. Stanford, and P. Sunseri R.and Breckheimer. "Survey of optimization techniques for nonlinear spacecraft trajectory searches". In: *Astrodynamics Conference*. 1988, p. 4285.

[51] R. Hanson and F. Krogh. "A Quadratic-Tensor Model Algorithm for Nonlinear Least-Squares Problems with Linear Constraints". In: *ACM Trans. Math. Softw.* 18.2 (June 1992), pp. 115–133. DOI: 10.1145/146847.146857.

[52] P. N. Valerino, P. Thompson, D. Jones, T. Goodson, M.-K. Chung, and N. Mottinger. "Flight Path Control Analysis for Parker Solar Probe". In: *Proceedings of the 2017 AAS/AIAA Astrodynamics Specialists Conference*. 2017, pp. 17–631.

[53] L. Deutsch. "Resolving the Cassini/Huygens relay anomaly". In: *Proceedings of the Aerospace Conference*. Big Sky, MT, USA, Sept. 2002.

[54] D. Roth, S. Hernandez, and S. Wagner. *Cassini Navigation Performance Assessment*. Tech. rep. Descanso-17. 4800 Oak Grove Drive, Pasadena, CA 91109: Jet Propulsion Laboratory, California Institute of Technology, Mar. 2021.

[55] B. A. Conway. *Spacecraft trajectory optimization*. Vol. 29. Cambridge University Press, 2010.

[56] R. Broucke. "The celestial mechanics of gravity assist". In: *Proceedings of the Astrodynamics Conference*. 1988, p. 4220. DOI: 10.2514/6.1988-4220.

[57] D. Izzo, V. M. Becerra, D. R. Myatt, S. J. Nasuto, and J. M. Bishop. "Search space pruning and global optimisation of multiple gravity assist spacecraft trajectories". In: *Journal of Global Optimization* 38.2 (2007), pp. 283–296.

[58] P. E. Gill, W. Murray, and M. A. Saunders. "SNOPT: An SQP algorithm for large-scale constrained optimization". In: *SIAM review* 47.1 (2005), pp. 99–131.

[59] D. Roth, Y. Hahn, B. Owen, and S. V. Wagner. "Cassini In-Flight Navigation Adaptations". In: *2018 SpaceOps Conference*. 2018, p. 2647.

[60] S. Ardalan, J. Bordi, N. Bradley, D. Farnocchia, Y. Takahashi, and P. Thompson. "Juno Orbit Determination Experience During First Year at Jupiter". In: (Aug. 2017).

[61] L. G. Casajus, M. Zannoni, D. Modenini, P. Tortora, F. Nimmo, T. Van Hoolst, D. Buccino, and K. Oudrhiri. "Updated Europa gravity field and interior structure from a reanalysis of Galileo tracking data". In: *Icarus* 358 (2021), p. 114187.

[62] P. Tortora, M. Zannoni, D. Hemingway, F. Nimmo, R. A. Jacobson, L. Iess, and M. Parisi. "Rhea gravity field and interior modeling from Cassini data analysis". In: *Icarus* 264 (2016), pp. 264–273.

[63] M. Zannoni, D. Hemingway, L. G. Casajus, and P. Tortora. "The gravity field and interior structure of Dione". In: *Icarus* 345 (2020), p. 113713.

[64] I. Gai. "Deep space orbit determination and guidance of the LICIACube microsatellite mission". PhD thesis. Via Zamboni 33, Bologna, Italy: University of Bologna, Department of Industrial Engineering, 2022.

[65] J. Smith, W. Taber, T. Drain, S. Evans, J. Evans, M. Guervara, W. Schulze, R. Sunseri, and H.-C. Wu. "MONTE python for deep space navigation". In: *Proceedings of the 15th Python in Science Conference (SciPy)*. Austin, Texasl, July 2016.

[66] S. Simonetti, V. D. Tana, G. Mascetti, S. Pirrotta, and E. Scorzafava. "ArgoMoon: Italian CubeSat Technology to Record the Maiden Flight of SLS Towards the Moon". In: *Proceedings of the 34th Annual Small Satellite Conference*. Utah State University, Logan, UT, Aug. 2020.

[67] V. Di Tana, B. Cotugno, G. Mascetti, S. Pirrotta, C. Fiori, R. Rinaldi, and S. Simonetti. "ArgoMoon: Challenges and design solutions for the development of a deep space small satellite". In: *IAC-18 B* 4 (2018), pp. 8–1.

[68] W. A. Imbriale. *Large antennas of the deep space network*. John Wiley & Sons, 2005.

[69] S. Pirrotta, B. Cotugno, V. di Tana, S. Patruno, F. Ingiosi, and S. Simonetti. "ArgoMoon: the Italian cubesat for Artemis1 mission". In: *Proceedings of the European Planetary Science Congress*. 2021, EPSC2021–879.

[70] M. M. Kobayashi, S. Holmes, A. Yarlagadda, F. Aguirre, M. Chase, K. Angkasa, B. Burgett, L. McNally, T. Dobreva, and E. Satorius. "The Iris Deep-Space Transponder for the SLS EM-1 Secondary Payloads". In: *IEEE Aerospace and Electronic Systems Magazine* 34.9 (2019), pp. 34–44. DOI: 10.1109/MAES.2019.2905923.

[71] J. Cardin, K. Coste, D. Williamson, and P. Gloyer. "A cold gas micro-propulsion system for cubesats". In: *Proceedings of the 17th Annual AIAA/USU Conference on Small Satellites*. Advanced Technologies, Subsystems, and components for Small Satellites: Section II, Utah State University, Logan, UT, Aug. 2003.

[72] A. L. Batcha, J. Williams, T. F. Dawn, J. P. Gutkowski, M. V. Widner, S. L. Smallwood, B. J. Killeen, E. C. Williams, and R. E. Harpold. "Artemis I Trajectory Design and Optimization". In: *Proceedings of the 2020 AAS/AIAA Astrodynamics Specialist Conference*. AAS 20-649. 2020.

[73] W. Rafferty, S. Slobin, C. Stelzried, and M. Sue. "Ground antennas in NASA's deep space telecommunications". In: *Proceedings of the IEEE* 82.5 (1994), pp. 636–645. DOI: 10.1109/5.284731.

[74] L. Iess, F. Budnik, C. Colamarino, A. Corbelli, M. Di Benedetto, V. Fabbri, A. Graziani, R. Hunt, N. James, M. Lanucara, R. Maddé, M. Marabucci, G. Mariotti, M. Mercolino, P. Racioppa, L. Simone, P. Tortora, M. Westcott, and M. Zannoni. "ASTRA: Interdisciplinary study on enhancement of the end-to-end accuracy for spacecraft tracking techniques". In: *Proceedings of the International Astronautical Congress, IAC*. Vol. 5. Jan. 2012.

[75] R. Ionasescu, T. Martin-Mury, P. Valerinoy, K. Criddley, B. Buffington, and T. McElrath. "Orbit determination covariance analysis for the Europa Clipper mission". In: *Proceedings of the American Institute of Aeronautics and Astronautic (AIAA) Space*. August 5-7, San Diego, California, Aug. 2014.

[76] *DSN Telecommunications Link Design Handbook, 104 34-m BWG Stations Telecommunications Interfaces, Rev. L*. DSN No. 810-005. Jet Propulsion Laboratory - California Institute of Technology. Oct. 2019.

[77] B. J. Clement and M. D. Johnston. "The Deep Space Network Scheduling Problem". In: *Proceedings of the 17th Conference on Innovative Applications of Artificial Intelligence*. July 9-13, Pittsburgh, Pennsylvania, 2005.

[78] M. D. Johnston. "Scheduling NASA's Deep Space Network: Priorities, Preferences, and Optimizationn". In: *Proceedings of the 30th International Conference on Automated Planning and Scheduling*. October 26-30, Nancy, France, 2020.

[79] *Deep Space Network Services Catalog, Rev. F*. DSN No. 820-100. Jet Propulsion Laboratory - California Institute of Technology. Jan. 2015.

[80] B. J. Giovannoni and D. Abraham. *DSN Mission Briefing 16-Upcoming DSN Contention Period*. Tech. rep. Deep Space Network Project. 4800 Oak Grove Drive, Pasadena, CA 91109: Customer Interface Management Office, Jet Propulsion Laboratory, California Institute of Technology, Feb. 2021.

[81] C. Foerste, R. Schmidt, R. Stubenvoll, F. Flechtner, U. Meyer, R. Kanig, H. Neumayer, R. Biancale, J.-M. Lemoine, S. Bruinsma, S. Loyer, F. Barthelmes, and S. Esselborn. "The GeoForschungsZentrum Potsdam/Groupe de Recherche de Geodesie Spatiale satellite-only and combined gravity field models: EIGEN-GL04S1 and EIGEN-GL04C". In: *Journal of Geodesy* 82.5 (2008), pp. 331–346. DOI: 10.1007/s00190-007-0183-8.

[82] A. S. Konopliv, R. S. Park, D. N. Yuan, S. W. Asmar, M. M. Watkins, J. G. Williams, E. Fahnestock, G. Kruizinga, M. Paik, D. Strekalov, N. Harvey, D. E. Smith, and M. T. Zuber. "The JPL lunar gravity field to spherical harmonic degree 660 from the GRAIL Primary Mission". In: *Journal of Geophysical Research: Planets* 118.7 (2013), pp. 1415–1434. DOI: https://doi.org/10.1002/jgre.20097.

[83] W. M. Folkner, J. G. Williams, D. H. Boggs, R. S. Park, and P. Kuchynkad. *The Planetary and Lunar Ephemerides DE430 and DE431*. Tech. rep. Interplanetary Network Progress Report 42-196. 4800 Oak Grove Drive, Pasadena, CA 91109: Jet Propulsion Laboratory, California Institute of Technology, Feb. 2014.

[84] *Space engineering, Space environment, Rev. 1*. ECSS-E-ST-10-04C. European Space Agency (ESA), European Cooperation for Space Standardization (ECSS). June 2020.

[85] G. Petit and B. Luzum. *IERS Technical Note*. Tech. rep. 36. Verlag des Bundesamts fur Kartographie und Geodasie, Frankfurt am Main: International Earth Rotation and Reference Systems Service, 2010.

[86] A. E. H. Love. "The yielding of the Earth to disturbing forces". In: *Proceedings of the Royal Society of London. Series A, Containing Papers of a Mathematical and Physical Character* 82.551 (1909), pp. 73–88. DOI: 10.1098/rspa.1909.0008.

[87] C. M. Will and J. Nordtvedt Kenneth. "Conservation Laws and Preferred Frames in Relativistic Gravity. I. Preferred-Frame Theories and an Extended PPN Formalism". In: *ApJ* 177 (Nov. 1972), p. 757. DOI: 10.1086/151754.

[88] T.-H. You, P. Antreasian, S. Broschart, K. Criddle, E. Higa, D. Jefferson, E. Lau, S. Mohan, M. Ryne, and M. Keck. "Gravity Recovery and Interior Laboratory Mission (GRAIL) Orbit Determination". In: *Proceedings of the International Symposium on Space Flight Dynamics, IN-2: Interplanetary Navigation Session 2*. Pasadena, California, Oct. 2012.

[89] J. Bellerose, D. Roth, Z. Tarzi, and S. Wagner. "The Cassini Mission: Reconstructing Thirteen Years of the Most Complex Gravity-Assist Trajectory Flown to Date". In: *SpaceOps 2018 Conference, Marseille, France*. May 2019, pp. 575–588. DOI: 10.1007/978-3-030-11536-4_22.

[90] P. Valerino, P. Thompson, D. Jones, T. Goodson, M.-K. Chung, and N. Mottinger. "Flight Path Control Analysis for Parker Solar Probe". In: *Proceedings of the AAS/AIAA Astrodynamics Specialist Conference*. Code 17-631, Stevenson, Washington, Aug. 2017.

[91] T. Williams, K. M. Hughes, A. K. Mashiku, and J. M. Longuski. "Orbit Stability of OSIRIS-REx in the Vicinity of Bennu Using a High-Fidelity Solar Radiation Model". In: *Proceedings of the AAS/AIAA Astrodynamics Specialist Conference*. Code 15-690, Vail, Colorado, Aug. 2015.

[92] M. Vaquero, Y. Hahn, D. Roth, and M. Wong. "A Linear Analysis for the Flight Path Control of the Cassini Grand Finale Orbits". In: *Proceedings of the International Symposium on Space Flight Dynamics*. Matsuyama, Japan, June 2017.

[93] E. H. Maize. "Linear statistical analysis of maneuver optimization techniques". In: *Proceedings of the AIAA/AAS Astrodynamics Specialist Conference*. Kalispell, Montana, United States, Aug. 1987, pp. 1005–1022.

[94] P. Kallemeyn, D. Spencer, R. Vaughan, and C. Helfrich. "The Mars Pathfinder navigation system". In: *Proceedings of the AAS/AIA Astrodynamics Conference*. San Diego, California, United States, July 1996, pp. 733–746. DOI: 10.2514/6.1996-3656.

[95] P. N. Valerino, B. Buffington, K. Criddle, Y. Hahn, R. Ionasescu, J. A. Kangas, T. Martin-Mur, R. B. Roncoli, and J. A. Sims. "Preliminary Maneuver Analysis for the Europa Clipper Multiple-Flyby Mission". In: *Proceedings of the AIAA/AAS Astrodynamics Specialist Conference*. Aug. 2014. DOI: 10.2514/6.2014-4461.

[96] T. D. Goodson. "Monte-carlo maneuver analysis for the microwave anisotropy probe". In: *Proceedings of the AIAA/AAS Astrodynamics Specialist Conference*. Quebec City, Quebec, Canada, July 2001.

[97] S. V. Wagner and T. D. Goodson. "Execution-error modeling and analysis of the Cassini-Huygens spacecraft through 2007". In: *Proceedings of the AAS/AIAA Space Flight Mechanics Meeting*. Galveston, Texas, United States, Jan. 2008.

[98] Z. Tarzi, D. Boone, N. Mastrodemos, S. Nandi, and B. Young. "Orbit determination sensitivity analysis for th Europa Clipper Mission tour". In: Ka'anapali, Hawaii, United States, Jan. 2019.

[99] D. Farnocchia, S. Eggl, P. W. Chodas, J. D. Giorgini, and S. R. Chesley. "Planetary encounter analysis on the B-plane: a comprehensive formulation". In: *Celestial Mechanics and Dynamical Astronomy* 131.8 (2019), pp. 1–16.

[100] M. Jah. "Derivation of the B-Plane (Body Plane) and its associated parameters". In: *A Lecture Series on Orbit Mechanics and Interplanetary Mission Design*. University of Colorado, 2002.